

DNA-Interactions, Self-Assembly and Photophysical Properties of DNA Three-way Junction Templated Fluorescent Silver Nanoclusters and Functional Tetraphenylethylene Derivatives

By

SAJENA K. S.

10CC15A39003

A thesis submitted to the
Academy of Scientific and Innovative Research
for the award of the degree of
DOCTOR OF PHILOSOPHY
in
SCIENCE

Under the supervision of
Dr. JOSHY JOSEPH



**CSIR-National Institute for Interdisciplinary
Science and Technology (CSIR-NIIST),
Thiruvananthapuram - 695 019**



Academy of Scientific and Innovative Research
AcSIR Headquarters, CSIR-HRDC campus
Sector 19, Kamla Nehru Nagar,
Ghaziabad, U.P. - 201 002, India

April 2021

Dedicated to

My Mother

&

All Women in Science

National Institute for Interdisciplinary Science and Technology (CSIR-NIIST)



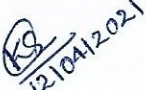
Council of Scientific & Industrial Research (CSIR)
Industrial Estate P. O., Trivandrum - 695 019
Kerala, INDIA


Dr. Joshy Joseph
Principal Scientist & Associate Professor
Chemical Sciences and Technology Division

Tel: +91-471-2515 476
Fax: +91-471-2491 712
E-mail: joshyja@gmail.com, joshy@niist.res.in

CERTIFICATE

This is to certify that the work incorporated in this Ph.D. thesis entitled, "*DNA-Interactions, Self-Assembly and Photophysical Properties of DNA Three-way Junction Templated Fluorescent Silver Nanoclusters and Functional Tetraphenylethylene Derivatives*", submitted by *Ms. Sajena K. S.* to the Academy of Scientific and Innovative Research (AcSIR) in fulfilment of the requirements for the award of the Degree of *Doctor of Philosophy in Sciences*, embodies original research work carried-out by the student. We further certify that this work has not been submitted to any other University or Institution in part or full for the award of any degree or diploma. Research materials obtained from other sources and used in this research work have been duly acknowledged in the thesis. Images, illustrations, figures, tables etc., used in the thesis from other sources, have also been duly cited and acknowledged.


12/04/2021
Sajena K. S.


12/04/2021
Dr. Joshy Joseph
(Thesis Supervisor)

STATEMENTS OF ACADEMIC INTEGRITY

I Sajena K. S., a Ph.D. student of the Academy of Scientific and Innovative Research (AcSIR) with Registration No. 10CC15A39003 hereby undertake that, the thesis entitled ***“DNA-Interactions, Self-Assembly and Photophysical Properties of DNA Three-way Junction Templated Fluorescent Silver Nanoclusters and Functional Tetraphenylethylene Derivatives”*** has been prepared by me and that the document reports original work carried out by me and is free of any plagiarism in compliance with the UGC Regulations on *“Promotion of Academic Integrity and Prevention of Plagiarism in Higher Educational Institutions (2018)”* and the CSIR Guidelines for *“Ethics in Research and in Governance (2020)”*.

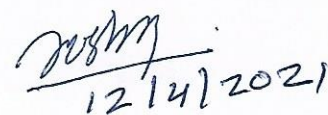

12/04/21

Sajena K. S.

April 12, 2021

Thiruvananthapuram

It is hereby certified that the work done by the student, under my supervision, is plagiarism-free in accordance with the UGC Regulations on *“Promotion of Academic Integrity and Prevention of Plagiarism in Higher Educational Institutions (2018)”* and the CSIR Guidelines for *“Ethics in Research and in Governance (2020)”*.


12/4/2021

Dr. Joshy Joseph

April 12, 2021

Thiruvananthapuram

DECLARATION

I, Sajena K.S., bearing AcSIR Registration No. 10CC15A39003 declare that my thesis entitled, ***“DNA-Interactions, Self-Assembly and Photophysical Properties of DNA Three-way Junction Templated Fluorescent Silver Nanoclusters and Functional Tetraphenylethylene Derivatives”*** is plagiarism free in accordance with the UGC Regulations on *“Promotion of Academic Integrity and Prevention of Plagiarism in Higher Educational Institutions (2018)”* and the CSIR Guidelines for *“Ethics in Research and in Governance (2020)”*.

I would be solely held responsible if any plagiarised content in my thesis is detected, which is violative of the UGC regulations 2018.


Sajena K. S.

April 12, 2021

Thiruvananthapuram

ACKNOWLEDGEMENTS

I have great pleasure in placing on record my deep sense of gratitude to Dr. Joshy Joseph, my thesis supervisor, for suggesting the research problem and for his constant guidance, endearing care, valuable support, and encouragement, leading to the successful completion of this work.

I would like to express my gratitude to Prof. M. V. George for being an inspiration.

I wish to thank Dr. A. Ajayaghosh, Director and Dr. Gangan Pratap and Dr. Suresh Das, former Directors of CSIR-National Institute for Interdisciplinary Science and Technology (CSIR-NIIST), Thiruvananthapuram, for providing the necessary facilities for carrying out this work.

My sincere thanks to:

- *Dr. Kaustabh Kumar Maiti, Dr. Vijayakumar C. Nair and Dr. Jayamurthy P., Doctoral Advisory Committee (DAC) members for their informative discussions in the DAC meetings and the whole AcSIR faculties for their help in the successful completion of my AcSIR course work.*
- *Dr. V. Karunakaran, Dr. C. H. Suresh, Dr. R. Luxmi Varma and Dr. Mangalam S. Nair, present and former AcSIR co-ordinators.*
- *Dr. P. Sujatha Devi, Dr. R. Luxmi Varma, Dr. K. R. Gopidas, present and former Heads of the Division, Chemical Sciences and Technology Division (CSTD).*
- *Dr. Narayanan Unni K. N., Head of the Section and Dr. D. Ramaiah, Dr. K. Yoosaf, Dr. Biswapriya Deb, Dr. Suraj Soman, Dr. Sreejith Shankar, former and present Scientists, Photosciences and Photonics Section, CSTD.*
- *Dr. V. K. Praveen, Senior Scientist (CSTD) for the fruitful discussions on self-assembly, and for his encouragement and motivation in the final stages of my Ph.D. work.*
- *Dr. E. Bhoje Gowd, Principal Scientist (MSTD) for his informative discussions and suggestions in the XRD studies.*
- *Dr. Saju Pillai, Senior Scientist (MSTD) for the XPS analysis and discussions.*
- *Mr. Kiran Mohan for TEM analysis, Mr. Harish Raj V. for SEM analysis, Mrs. Soumini Mathew, Mr. Saran P. and Mr. R. Gokul for NMR spectral analysis, Mrs. Viji S., and Ms. Athira for mass spectral analysis, Mr. Peer Mohamed for Rheological experiments, Mr. Amal Raj for XRD analysis and Mr. Robert Philip for the general help.*
- *Mr. Rajeev V. R. and Mr. Vibhu Darshan for their help with the conductivity measurements.*

- *Mr. Gourab Das for his help in the self-assembly studies and Ms. Drishya Elizebath and Mr. Akhil P. for their help in the optical microscopic studies.*
- *Dr. Varsha Karunakaran for performing cytotoxicity studies.*
- *M.Sc. Project students; Navaneetha P., Kavya J. M., Krishnapriya E., Sneha S. Kumar, Nivya K., Anju A. K., Kripa M. Joseph and Aishwarya P. for their help.*
- *Dr. Divya K. P., my teacher at PSMO College for being an inspiration and showing me a way to pursue my interest of doing research.*
- *Dr. Adarsh N. and Dr. Divya Susan Philips for their constant care, support, and affection from the beginning of my stay at NIIST.*
- *Dr. Sreejith M., and Dr. Sandeepa K. V., Senior colleagues of our group for their help, in understanding the instrumental techniques, organic synthesis, and the informative scientific discussions in the initial stages of my Ph.D., which throughout helped me a lot for the successful completion of my Ph.D. work.*
- *Mr. Mathews K. M., and Dr. Silja Abraham, Senior colleagues of our group for their help in the initial stages of my Ph.D. work, in learning DNA synthesis, HPLC and wet lab synthesis.*
- *Dr. Shanthi Krishna A., Ms. Anjali B. R., Mrs. Shibna Balakrishnan, Mrs. Nishna N., Ms. Pavithra V. Prabhu, Mr. Arjun V. Prakash, Ms. Ashwathi H., Ms. Anagha Thomas, Mr. Jomon George Joy and all other former group members for their good cooperation and companionship in the lab.*
- *Ms. Sumitha Paul, Mr. Jayadev V., Mr. Manuraj M., Mr. Shaiju S. S., Dr. Jayanthi S. P., Dr. Arun Gopi, Dr. Samrat Ghosh and Mrs. Vindhya Sarumi for their good companionship, care, love, and support throughout my stay in NIIST.*
- *Our Twin lab members; Dr. Biswapriya Deb's lab for their cooperative and smooth give and take polices between the labs.*
- *Former and present members of CSTD and friends at CSIR-NIIST, for their help and support.*
- *All my teachers and friends for their care and support.*
- *University Grant Commission (UGC) for the Research fellowship.*

I am deeply and forever indebted to my family, especially my mother Saraswathi K. P., my brother Mr. Sajeesh K. S. and my sister-in-law Mrs. Prabija B. for their constant source of support, love, care, and trust. Above all, I thank Almighty for all his blessings.

Sajena K. S.

TABLE OF CONTENTS

Certificate		i
Statements of Academic Integrity		ii
Declaration		iii
Acknowledgements		iv
Table of Contents		vi
List of Abbreviations		x
Preface		xiii
CHAPTER 1	Self-Assembled Architectures of DNA and DNA Building Blocks: An Overview	1-54
1.1	Abstract	1
1.2	Introduction	2
1.3	DNA: Structure, Properties and Functions	4
1.4	Self-Assembly of DNA-Nanostructures	8
1.4.1	DNA-Tile Based Self-Assembly	8
1.4.2	DNA-Origami Based Self-Assembly	11
1.5	Supramolecular DNA Assembly	15
1.5.1	Covalently Modified DNA Assemblies	15
1.5.2	Non-Covalent Interaction Directed DNA Assemblies	25
1.6	Self-Assembly Directed by Nucleobase Derivatives	34
1.6.1	Nucleotide Directed Assemblies	35
1.6.2	Nucleoside Directed Assemblies	38
1.6.3	Nucleobase Directed Assemblies	39
1.7	Perspectives and Challenges in Supramolecular DNA Assembly	41
1.8	Objectives of the Present Investigation	43
1.9	References	44

CHAPTER 2	Design and Synthesis of DNA Three-way Junction Templated Fluorescent Silver Nanoclusters: Sequence Programming and Metal ion Sensing	55-90
2.1	Abstract	55
2.2	Introduction	56
2.3	Results and Discussion	61
2.3.1	Synthesis of Short ssDNA Sequences	61
2.3.2	Fluorescent AgNCs Templated by ssDNA Sequences	62
2.3.3	Design, Synthesis and Characteristics of DNA Three-way Junctions	65
2.3.4	Fluorescent AgNCs Templated by DNA-3WJs	67
2.3.5	Morphology and Elemental Analysis of 3WJ20-C12/AgNCs	71
2.3.6	Sequence Programming and Influence on 3WJN-CX/AgNC Formation	74
2.3.7	Metal ion Interaction Studies of 3WJ20-C12/AgNCs	76
2.4	Conclusions	79
2.5	Experimental Section	80
2.5.1	Materials and Methods	80
2.5.2	Synthesis of Sequence Specific DNA-3WJs	82
2.5.3	Synthesis of 3WJ/AgNCs.	83
2.5.4	Selectivity and Sensitivity Measurements of 3WJ20-C12/AgNCs	84
2.6	References	85
CHAPTER 3: PART A	1D-Organization and Thymine Induced Transition of Molecular Aggregates in a Diaminotriazine Functionalized Tetraphenylethylene Derivative	91-138
3A.1	Abstract	91
3A.2	Introduction	92
3A.3	Results and Discussion	100
3A.3.1	Synthesis of TPE-1 and T-C12	100
3A.3.2	Aggregation Induced Emission Properties of TPE-1	101

3A.3.3	Self-Assembly of TPE-1	103
3A.3.4	Thermodynamic and Morphological Features of TPE-1 Self-Assembly	107
3A.3.5	T-C12 Directed Changes in the TPE-1 Self-Assembly	109
3A.3.6	Morphological Studies of TPE-1 \equiv T-C12 Assembly	112
3A.3.7	Fluorescence Lifetime and Optical Microscopic Analysis	113
3A.3.8	Organogels of TPE-1 and TPE-1 \equiv T-C12	116
3A.3.9	Gel Characterizations: FT-IR and Rheology	119
3A.3.10	Mechanism of Self-Assembly	121
3A.4	Conclusions	124
3A.5	Experimental Section	125
3A.5.1	Materials and Methods	125
3A.5.2	AFM/TEM/OFM Sample Preparations	126
3A.5.3	Gelation Studies and Xerogel Sample Preparations	127
3A.5.4	Synthetic Procedures and Characterizations	128
3A.6	References	133
CHAPTER 3: PART B	Effect of Different Alkoxy Substitutions on the Self-Assembly Properties of Tetraphenylethylene-Diaminotriazine Derivatives: Photophysical and Morphological Studies	139-184
3B.1	Abstract	139
3B.2	Introduction	140
3B.3	Results and Discussion	145
3B.3.1	Design and Synthesis of TPE-DAT derivatives	145
3B.3.2	Photophysical Properties	147
3B.3.3	Aggregation: Optical and Morphological Properties	148
3B.3.4	Self-Assembly of TPE-2 and TPE-3	150
3B.3.5	Thermodynamic and Chiroptical Properties of Self-Assembly	155
3B.3.6	Microscopic Studies	158
3B.3.7	Self-Assembly of TPE-4 with dT ₂₀ Template	160
3B.3.8	Supramolecular Gels of TPE-2 and TPE-3	163
3B.3.9	FT-IR and Rheology Studies of Xerogels	165

3B.3.10	XRD and Mechanism of Self-Assembly	168
3B.4	Conclusions	171
3B.5	Experimental Section	172
3B.5.1	Materials and Methods	172
3B.5.2	Synthetic Procedures and Characterizations	172
3B.6	References	180
CHAPTER 4	Tetraphenylethylene-Viologen Derivatives: Synthesis and Study of their DNA Interaction and Condensation Properties	185-238
4.1	Abstract	185
4.2	Introduction	187
4.3	Results and Discussion	191
4.3.1	Molecular Design and Synthesis	191
4.3.2	Photophysical and Morphological Properties	194
4.3.3	Interactions of TPE-V Derivatives with CT-DNA	198
4.3.4	Thermal Denaturation and Circular Dichroism Studies	203
4.3.5	Ethidium Bromide Displacement Assay	206
4.3.6	Morphological Studies	210
4.3.7	Interactions of Cucurbit[8]uril/TPE-V Complexes with CT-DNA	216
4.3.8	Cytotoxicity Studies	217
4.4	Conclusions	220
4.5	Experimental Section	221
4.5.1	Materials and Methods	221
4.5.2	AFM/TEM Sample Preparations	223
4.5.3	MTT Assay	223
4.5.4	Synthetic Procedures and Characterization Details	224
4.6	References	233
	Abstract of the Thesis	239
	List of Publications	241
	List of Posters and Papers Presented in Conference	243

LIST OF ABBREVIATIONS

Å	Angstrom
Ag	Silver
AgNPs	Silver nanoparticles
AgNCs	Silver nanoclusters
Al	Aluminium
AFM	Atomic force microscopy
AIE	Aggregation induced emission
CT-DNA	Calf thymus - Deoxyribonucleic acid
CDCl ₃	Deuterated chloroform
CH ₃ CN	Acetonitrile
calcd.	Calculated
CD	Circular dichroism
CGC	Critical gelator concentration
CB[8]	Cucurbit[8]uril
DAT	Diaminotriazine
DLS	Dynamic light scattering
DNA	Deoxyribonucleic acid
dsDNA	Double strand DNA
EB	Ethidium bromide
equiv.	Equivalent
EDAX	Energy dispersive X-ray spectroscopy
EQ	Equilibrium
ESI	Electrospray ionization
FT-IR	Fourier transform-infrared
g	Gram
G'	Storage modulus
G''	Loss modulus
hrs	Hours
Hg	Mercury
HOMO	Highest occupied molecular orbital
HRMS	High resolution mass spectrometry
I _{em}	Intensity of emission

ICD	Induced circular dichroism
K	Kelvin
k	Kilo
KBr	Potassium bromide
LVR	Linear viscoelastic region
LOD	Limit of detection
LUMO	Lowest unoccupied molecular orbital
M	Molar
mm	Millimeter
MHz	Mega hertz
min	Minute
mL	Millilitre
mM	Millimolar
mol	Mole
nm	Nanometer
NMR	Nuclear magnetic resonance
ns	Nanosecond
OPM	Optical polarizing microscopy
PBS	Phosphate buffered saline
PBI	Perylene bisimide
pH	Hydrogen ion concentration at logarithmic scale
Fl	Fluorescence
ps	Picosecond
ppm	Parts per million
RNA	Ribonucleic acid
RP-HPLC	Reverse phase - High performance liquid chromatography
s	Second
ssDNA	Single strand DNA
SEM	Scanning electron microscopy
t	Time
T	Temperature
TCSPC	Time correlated single photon counting
Te	Elongation temperature
Tm	Melting temperature

TEM	Transmission electron microscopy
TEG	Triethylene glycol
TPE	Tetraphenylethylene
THF	Tetrahydrofuran
TLC	Thin layer chromatography
TRES	Time resolved emission spectroscopy
TEAA	Triethylammonium acetate
TMS	Tetramethylsilane
UV-vis	Ultra Violet-visible
WAXS	Wide angle X-ray scattering
XRD	X-ray diffraction
XPS	X-ray photoelectron spectroscopy
ε	Molar extinction coefficient
%	Percentage
λ	Wavelength
θ	Reflection
ΔH°	Standard enthalpy
ΔS°	Standard entropy
ΔG°	Standard Gibbs free energy
Φ_F	Fluorescence quantum yield
α_{agg}	Fraction of aggregate / Degree of aggregation
λ_{em}	Wavelength of emission
λ_{ex}	Wavelength of excitation
λ_{max}	Maxima of wavelength
τ	Lifetime
μm	Micrometer
μM	Micromolar
μL	Microliter
$^\circ\text{C}$	Degree Celsius
cm	Centimeter
1D	One-dimensional
2D	Two-dimensional
3WJ	Three-way junction

PREFACE

The development of DNA nanotechnology using the structural and supramolecular properties of DNA was a major breakthrough in the area of bottom-up construction of functional nanostructures.^{1,2} The unique properties of DNA double helical structure and the simple hydrogen bonding interactions of complementary nucleobases add extra features like stimuli responsive behaviour, information storage and information transfer capacity to the self-assembled materials. Although great progress has been made in the field of bottom-up self-assembly using DNA and nucleobase derivatives, the potential of DNA in templating functional materials is not yet completely explored. Introduction of site-specific groups, careful optimization of non-covalent assembly conditions and more insights into the random oligonucleotide directed assemblies are required. In this regard, the current thesis makes an effort to use the non-covalent interaction potentials of DNA to develop supramolecularly self-assembled metal/organic-DNA/nucleobase hybrid systems with less structural complexity, tuneable morphological and optical properties, and biocompatibility.

The thesis is organized into four chapters. **Chapter 1** gives an overview of the self-assembled architectures constructed from DNA and DNA building blocks. The development of DNA nanotechnology, classifications and important outcomes are described in this chapter. Finally, we also highlight the perspectives and current challenges in the area of DNA mediated, supramolecular self-assembly. To overcome these challenges, we present the use of various non-covalent interaction possibilities of DNA to construct functional materials for applications in material and biomedical science. The results are summarized in the following chapters.

In **Chapter 2**, we describe a design strategy for sequence programmed, DNA three-way junctions (**DNA-3WJ**), comprising of unhybridized cytosine nucleobases in the 3WJ-center, capable of binding to silver ions and stabilizing the AgNCs. The formations of AgNCs in these **DNA-3WJs** were confirmed by various spectroscopic and microscopic techniques. **3WJ20-C12** comprising of 12 cytosine bases in the center of the **DNA-3WJ**, form fluorescent nanoclusters with an emission maximum around 630 nm and 12% fluorescence quantum yield. Control **DNA-3WJs** with six cytosine bases in the center (**3WJ20-C6**) and ones without cytosine bases (**3WJ20**) failed to form

fluorescent AgNCs confirming the requirement of central, unhybridized cytosine bases for the stabilization of the nanoclusters. Further, the duplex arms of **DNA-3WJs** were shown to influence the fluorescent properties of AgNCs by varying the size and stability of the cytosine-loop structure of **DNA-3WJs**. Metal ion interaction studies show the selectivity of the **3WJ20-C12/AgNCs** towards Hg^{2+} with sensitivity in the nanomolar range (*J. Photochem. Photobiol. B, Biol.*, **2020**, 207, 111886).

The construction of 1D supramolecular assemblies of **TPE-DAT** molecules and tuning of the photophysical and morphological properties using competitive H-bonding interactions were discussed in **Chapter 3**. This chapter is separated into two parts. **Chapter 3: Part A** describes the H-bonding directed self-assembly of **TPE-1** to highly ordered flexible fibers in dodecane with a characteristic 307 nm absorption and 430 nm emission band. The cooperative pathway and thermodynamic features of the self-assembly were deduced by performing temperature dependent absorption measurements at 307 nm. Addition of thymine derivative, **T-C12** with superior complimentary H-bonding ability with DAT units in **TPE-1** and subsequent annealing transforms the ordered blue emissive assembly in to green emissive assembly. At higher concentrations, both these assemblies give rise to the formation of supramolecular gels in dodecane with similar absorption, emission and morphological characteristics observed at low concentration. Role of H-bonding in these assemblies were confirmed by solid state FT-IR studies of xerogels. Further, we propose a plausible mechanism for these assemblies based on the results obtained from the XRD of xerogels and energy minimized molecular size measurements.

Literature reports on the 1D assemblies of TPE molecules with precise mechanistic insights about the self-assembly are very rare. So, in **Chapter 3: Part B** we studied the self-assembly properties of **TPE-DAT** in detail by changing the alkoxy substitution with racemic (**TPE-2**), chiral (**TPE-3**) and triethylene glycol units (**TPE-4**). **TPE-2** and **TPE-3** displayed similar 1D assembly in dodecane with characteristic 430 nm blue emission, which transforms to green emissive assemblies in presence of **T-C12**. The chiral derivative, **TPE-3** displayed a bisignated CD signal centered at 307 nm, indicating the initial, ordered chiral assembly of the monomeric units in the molecular packing. On the other hand, morphological studies using microscopic techniques did not show any visible structural features of supramolecular chirality. Investigation of their

gelation behaviour and characteristics of xerogels confirmed, similar H-bonding directed columnar packing of homo-dimers in blue emissive assembly and hetero-dimers in green emissive assembly, as observed in **TPE-1**. These results further validate the mechanism of 1D assemblies of TPE, proposed in Part A and suggest the secondary molecular packing directed masking of structural chirality in chiral TPE derivative, **TPE-3**. The triethylene glycol derivative, **TPE-4** was insoluble in dodecane and therefore we conducted similar experiments in 20% THF-PB with dT₂₀. In presence dT₂₀, the formation of uniformly distributed spherical nanostructures of **TPE-4/dT₂₀** was observed instead of the flower like morphology of **TPE-4** alone. All these results clearly confirm the role of alkoxy substitutions in directing the self-assembly of **TPE-DAT** molecules.

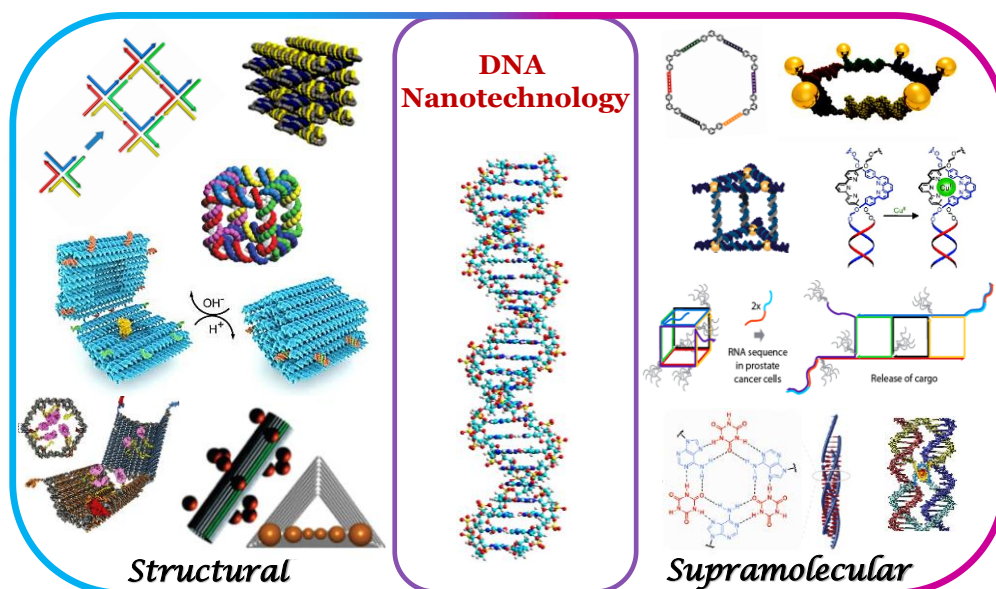
In **Chapter 4**, we describe the rational design and synthesis of four cationic **TPE-V** molecules (**TPE-V1-4**), varying their chemical structure by the number of viologen units present or by difference in the spacer length between TPE and viologen units. Their electrostatic interaction prompted synergistic self-assembly with CT-DNA and subsequent DNA condensation studies are explained in this chapter. The DNA-binding process was monitored in detail by UV-visible absorption, fluorescence emission, thermal melting, CD, EB-intercalation, CB [8] encapsulation and morphology analysis experiments. The aggregates of **TPE-V** molecules in Triz buffer, interacts and disassembles the long fibrous network structure of CT-DNA into weakly condensed 'beads on a string' type assembly and completely condensed 40-50 nm sized spherical compact structures at 1:1 and 1:2 ratios, respectively. Among the four derivatives, **TPE-V2** displayed better DNA condensation abilities attributed to presence of two viologen units and comparatively better solubility in water. Further, cytotoxicity studies reveal the non-toxic nature of the **CT-DNA** condensates of **TPE-V1**, **TPE-V2** and **TPE-V3** towards both normal and cancer cell lines and hence these derivatives could be potential candidates as biocompatible non-viral gene-delivery vectors.

References

- 1) Aldaye, F. A.; Palmer, A. L.; Sleiman, H. F. Assembling Materials with DNA as the Guide. *Science*. **2008**, *321*, 1795-1799.
- 2) Rothmund, P. W. K. Folding DNA to create nanoscale shapes and patterns. *Nature*. **2006**, *440*, 297-302.

Note: The abbreviations of various compounds used here correspond to those given under respective chapters.

SELF-ASSEMBLED ARCHITECTURES OF DNA AND DNA BUILDING BLOCKS: AN OVERVIEW



1.1. ABSTRACT

Nature follows a method of spontaneous association of constituents into well-organized structures using non-covalent interactions to achieve complexity. For example, hydrogen bonding, π -stacking, electrostatic and hydrophobic interactions allow the self-association of single strand DNA into its double helical structure found in the nucleus. DNA with its unique double helical structure and the exceptional molecular recognition nature of nucleobases permits the programmable hierarchical organization of functional organic and inorganic structures. The idea of using DNA as a template introduced by Seeman in 1982 was a major breakthrough in the area of bottom-up construction of functional nanostructures, which resulted in the entire identity change of DNA from its common name of “Genetic blueprint of life” to the

building block of "DNA nanotechnology". These self-assembled structures of organic and inorganic materials using DNA and its constituents find various applications in the field of sensing, optoelectronics, light harvesting, drug delivery and DNA condensation. Though there is a great progress in material DNA research, high cost of modified nucleobases, construction of smart DNA templates with less structural complexity, improving the specificity of supramolecular interactions and development of better strategies for constructing random DNA templated assemblies, etc., remains as key challenges to address. In this introductory chapter, the recent progress in the construction of self-assembled structures using DNA and nucleobase derivatives, their properties and applications are discussed. Finally, the chapter concludes with a discussion on the challenges and prospects of DNA nanotechnology, origin of the current research work and its major objectives.

1.2. INTRODUCTION

Construction of highly ordered functional structures with precision in the nanometer scale has been one of the major intellectual searches of the research community for the last few decades. Top-down and bottom-up approaches are the two basic methods used for the fabrication of nano- to micro-meter scale structures (Figure 1.1).¹ A typical approach in manufacturing is the top-down method, which finds it increasingly difficult when we go for the construction of molecular level assemblies. However, the bottom-up approach exploits the hidden molecular level information to self-assemble nanostructures and offers the use of enormous chemical diversity and highly parallel synthesis.² Although numerous self-assembled constructs were developed by this technique,³⁻⁵ they lack the control over resultant geometry and positioning of functional components. It was in this scenario, the DNA

based self-assembly, using the nature's perception of non-covalent interactions for hierarchical organization of complex functional structures came into vicinity.⁶ Among the various biomolecules present in nature, DNA is probably the most promising template with predictable and programmable control over the self-assembled structures using its unique double helical structure and the simple hydrogen bonding interactions of complementary nucleobases.

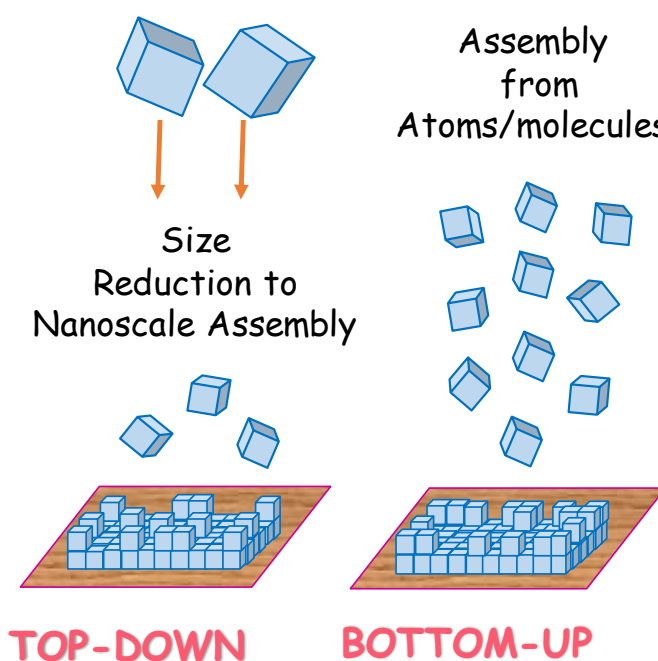


Figure 1.1. Schematic representation of the top-down and bottom-up approaches in nanotechnology.

DNA nanotechnology is a branch of nanoscience which deals with the construction, investigation, and applications of higher ordered DNA-structures using the physiochemical properties of DNA. DNA-tile assembly introduced by Nadrian C. Seeman (1982) and DNA-origami based assembly introduced by Paul W. K. Rothemund (2006) are the two important strategies used in DNA nanotechnology.^{6,7} Soon after, combining the programmability of DNA with the chemical diversity and concepts of supramolecular chemistry, a new area got emerged in 2008 called “supramolecular DNA assembly”.⁸ Subsequently, organic molecules with specific

geometries and functionalities,^{9,10} modified single strand DNA sequences¹¹ and transition metal complexes¹² were incorporated into DNA to achieve better control over its hybridization, self-assembly and structure. Further, for the construction of various DNA-organic/inorganic hybrid structures, many research groups have employed the electrostatic,^{13,14} hydrogen bonding,¹⁵ π -stacking and intercalative mode of interactions.¹⁶ Another alternative method for developing self-assembled system without losing the programmability is to use DNA building blocks such as nucleotides,¹⁷ nucleosides¹⁸ and nucleobases¹⁹ as templates. Such self-assembled system possesses small size, low cost compared to DNA and avoids the complexity associated with geometry. These unique properties of the self-assembled system with DNA and its building blocks, makes it an extraordinarily irreplaceable approach to construct functional materials for applications in the fields of material science, biomedical science, and optoelectronics.^{20,21}

1.3. DNA: STRUCTURE, PROPERTIES AND FUNCTIONS

DNA, deoxyribonucleic acid is the basic structural and functional unit of all living organisms and carries the hereditary information inside chromosomes of the cell. Ever since the discovery of DNA as a genetic carrier,²² the biological role of DNA has been extensively investigated without much knowledge about the structure of DNA. It was in 1953, Watson and Crick established the structure of DNA as the double helix (Figure 1.2A).²³ The ladder-like double helix comprises two polynucleotide strands twisted around each other in an antiparallel direction (Figure 1.2B). Polynucleotides are formed from monomeric nucleotide monophosphate units, which contains phosphate group, 2'-deoxyribose sugar and nucleobase (Figure 1.2C). Nucleobase attached to the sugar unit is termed as

nucleoside, and they are connected through phosphodiester bond to form polynucleotides. The sugar units and phosphate groups constitute the backbone of double helix and the Watson-Crick hydrogen bonding between nucleobases from opposite strands holds together the polynucleotides. Purines and pyrimidines are the two types of nucleobases present in DNA. Adenine and guanine nucleobases are derived from purines whereas cytosine and thymine are derived from pyrimidines (Figure 1.3A). The analogue of DNA, in which the nucleobase thymine replaced with uracil and deoxyribose sugar unit replaced with ribose is called RNA. Shapes and hydrogen bonding sites of nucleobases prefers the binding between adenine and thymine and between guanine and cytosine, known as the complementary relationship, a fundamental property of double helix contributing to the thermodynamic stability and information storage.

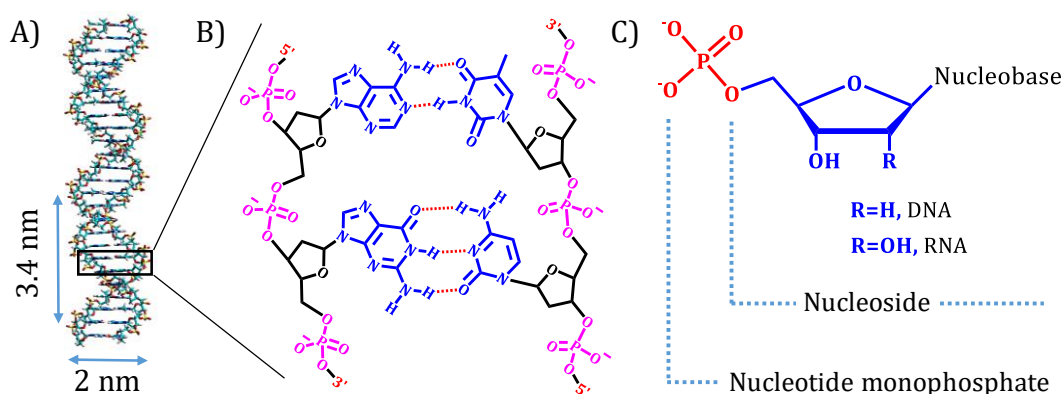


Figure 1.2. A) Schematic representation of DNA Double helix structure, B) Watson-Crick hydrogen bonding between antiparallel polynucleotide strands and C) representative structure of the nucleotide monophosphate.

DNA double helix exists in three forms; A, B and Z. Common form of DNA double helix under physiological condition is B-form with right-handed helicity. The diameter of the B-form of DNA is ~ 2 nm with 10.5 base pairs in a helical turn. The distance and angle of rotation between two base pairs in the B-form of DNA is 0.34 nm and 35.9° , respectively. The helical structure of DNA gives rise to two

grooves with unequal sizes; major grooves (1.17 nm width with sides of nucleobases are away from sugar units) and minor grooves (0.57 nm width with sides of nucleobases are near to sugar units).²⁴ The major grooves are rich with chemical information, whereas minor grooves are rich in charge density leading to differential mode of interactions with different DNA binding ligands and biomolecules.

Nucleobases present in the DNA absorbs 260 nm UV light and therefore absorption measurements are used to obtain the concentration of DNA. Melting temperature (T_m) and Circular Dichroism (CD) are the two key characteristics of double strand DNA (dsDNA). The temperature at which dsDNA separates into single strand DNA (ssDNA) is defined as T_m , which completely depends on the structure and sequences of dsDNA. Differential scanning calorimetry (DSC) and UV absorption spectroscopy are used to determine T_m values. Presence of chiral sugar units and helical twist of dsDNA leads to the differential absorption of right and left circularly polarized light, resulting in characteristic CD signals for various dsDNA structures. For example, CD signal of B-DNA has a positive band at 275 nm and negative band at 245 nm with a zero-crossover at 260 nm, while for Z-DNA, the CD signal is centered at 280 nm, with a positive band at 263 nm and a negative band at 293 nm. In addition to the above-mentioned properties, DNA is reported to have electronic conducting properties with magnitudes ranging from semiconductor to conductor based on its assembled structure and analyzing conditions.²⁵ Furthermore, the programmable self-assembly and reported conducting properties in conjugation with other conducting polymers and metal nanoclusters project DNA as a promising building block for nano-electronic devices. Short ssDNA sequences used for the application in DNA nanotechnology are synthesized via solid-phase phosphoramidite chemistry. This method is particularly very useful among the

existing laboratory oligonucleotide synthetic strategies, as it offers easy and fast access to custom-built DNA sequences.

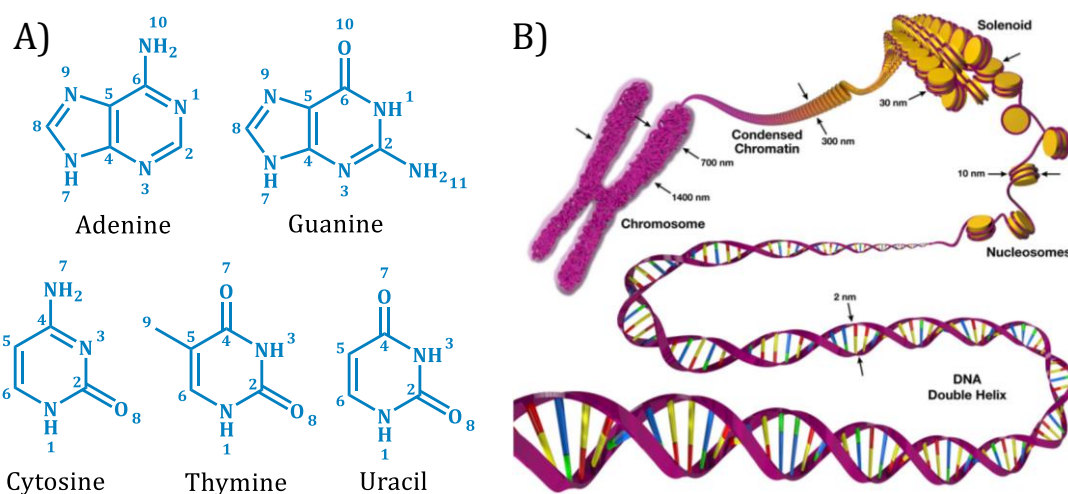


Figure 1.3. A) Structure of nucleobases and B) schematic representation of DNA and histone packing in the formation of chromosomes (Adapted from reference 26).

The two important biological functions of DNA are DNA-replication and transcription. The long chains of dsDNA are tightly bound over positively charged histone proteins to form chromosomes (Figure 1.3B).²⁶ In eukaryotes, chromosomes are present in the nucleus of the cell. The total length of DNA in the nucleus of a cell is around 1.8 meters. The first and foremost function of DNA is to transfer the hereditary information and it is achieved by DNA replication process inside the nucleus of the cell. Initially, the dsDNA in chromosomes unwinds and the resulting ssDNA acts as templates to synthesize the corresponding complementary ssDNA with the help of a set of enzymes including DNA polymerase. Similar to DNA replication, the synthesis of a specific messenger RNA (mRNA) from DNA, with the help of RNA polymerase is called transcription. The mRNA formed contains genetic information in the form of groups of three nucleotides (codons), which represents a specific amino acid for protein synthesis. In addition to this biological function, the structural programmability and predictable non-covalent interactions of DNA,

marks it as a distinctive template for the bottom-up construction of functional materials.

1.4. SELF-ASSEMBLY OF DNA-NANOSTRUCTURES

As mentioned earlier, the first attempt to use DNA as template was introduced by Nadrian C. Seeman and co-workers in 1980's.⁶ Inspired from the naturally occurring Holliday junctions, they developed branched nucleic acid junctions for the construction of lattices in bimolecular crystallography.⁶ And this was the groundwork of a new platform called DNA-nanotechnology for developing functional materials. Based on the strategies of constructing DNA nanostructures from DNA, the self-assembly is classified into two: (i) DNA-tile based self-assembly and (ii), DNA-origami based self-assembly.

1.4.1. DNA-tile based self-assembly

Branched oligonucleotide junctions with sticky ends or single complementary strands are the basic units in DNA-tile based self-assembly to construct higher-ordered 1D, 2D, and 3D structures. Seeman and coworkers developed artificial branched DNA junctions by modifying the naturally occurring Holliday junction tiles with different asymmetric strands and complementary sticky end sequences in the arms.⁶ Using this type of artificial branched DNA junctions, they have assembled 2D and 3D DNA lattices (Figures 1.4A and 1.4B) for organizing biomacromolecules.²⁷ Subsequently, to avoid the structural flexibility and strand migration at the branch points, more rigid DNA-tile based building blocks were constructed.²⁸ For example, two DNA double helices were joined together by two strand exchange and developed double crossover (DX) molecules with better rigidity and stability to

construct higher order DNA nanostructures.²⁹ Following this development, several research groups have assembled different types of DNA-tile based constructs like 4×4 , 6×4 , triangular DNA-tiles and isolated polyhedral DNA nanostructures (Figures 1.4C-E) using the idea of cross over variations.^{30,31}

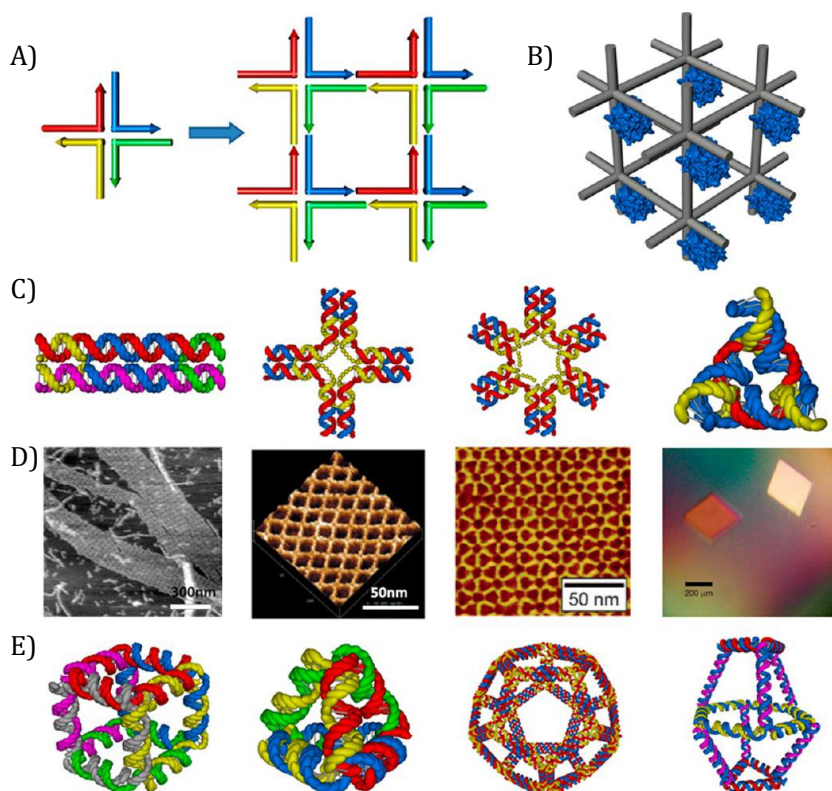


Figure 1.4. Seeman's artificial branched DNA junctions assembling into A) 2D and B) 3D lattices. C) DX and various crossover-based DNA-tiles; 4×4 , 6×4 and triangular assemblies, D) corresponding AFM images and E) isolated polyhedral 3D DNA assemblies (Adapted from reference 30).

Subsequently, extended 2D tiles were assembled from small DNA-tiles by incorporating sticky ends and used for the controlled organization of proteins,³² aptamers,³³ antibodies,³⁴ and nanoparticles.³⁵ Atomic force microscopy (AFM) is one of the important microscopic techniques used to visualize these self-assembled structures. Figures 1.5A-C shows the 1D and 2D-DNA tile structures, and the corresponding AFM images reported by Seeman *et al.* in 1990's.³¹ Yan *et al.* demonstrated the organization of streptavidin on to biotin functionalized 2D DNA-

tile assembly (Figure 1.5D).³² Later, from the same group, they have shown the periodic organization of 5 nm gold nanoparticles (AuNPs) on the 2D DNA nanogrids (Figure 1.5E) for nano-electronic applications.³⁵

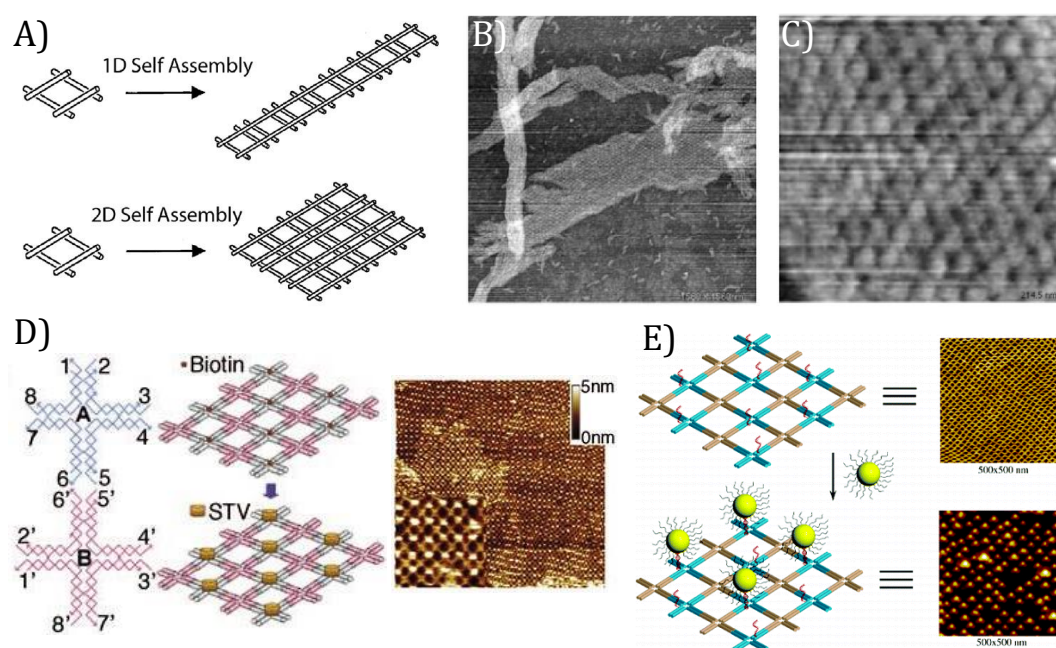


Figure 1.5. A) Assembly of 1D and 2D DNA-tiles from DX motifs and corresponding AFM images of B) 1D and C) 2D DNA nanostructures (Adapted from reference 31). Organization of D) streptavidin on biotin labeled 2D DNA network structures and E) 5 nm AuNPs on 2D nanogrids (Adapted from reference 32 and 35).

In order to address the challenge of reducing the number of DNA strands used to construct DNA-tiles, Mao *et al.* in 2006 developed a DX tile from self-complementary ssDNA and assembled into extended nanotubes,³⁶ which was another important glory in the DNA-tile based self-assembly. Later using the same concept, a T-junction DNA was assembled into Z and C-tiles, which further self-assembled into 1D and 2D DNA nanostructures (Figure 1.6A).³⁷ Subsequently, 3D DNA networks were assembled by combining the cross-over tiles and single strands in various assembly conditions.³⁸ Combined effort of Seeman and Mao group has led to the assembly of a 3D network of crystalline lattice using a rigid tensegrity triangle (Figure 1.6B).³⁹ Sleiman *et al.* in 2012, developed a 3D DNA cube with the least

number of strands and the single strand part was hybridized with complementary DNA block copolymers to assemble bio-hybrid cages (Figure 1.6C).⁴⁰ These bio-hybrid cages showed enhanced resistance towards nucleases compared to bare DNA cages. Recently, in 2017 Liu *et al.* studied the kinetic and thermodynamic parameters of DNA-tile based assemblies and found that these type of assemblies with a higher number of sticky ends are more thermodynamically stable accompanied by the decrease in free energy.⁴¹ Their results are inevitably important in the future development of DNA-tile based structural DNA nanotechnology.

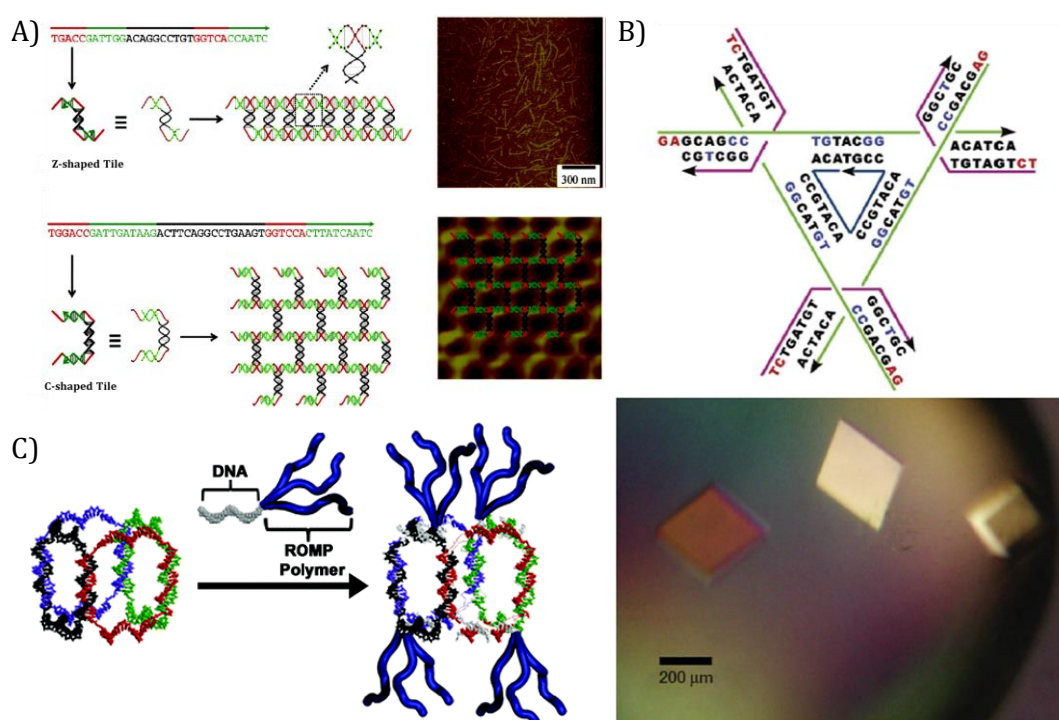


Figure 1.6. A) Single stranded DNA assembling into Z and C tile motifs and extended self-assembly into linear and 2D networks (Adapted from reference 37), B) tensegrity triangle constructed to assemble 3D crystalline structures and the figure below shows an optical image of crystals (Adapted from reference 39). C) Bio-hybrid cages assembled from 3D DNA cubes and DNA block copolymers (Adapted from reference 40).

1.4.2. DNA-origami based self-assembly

Rothemund's method of DNA-origami for the assembly of DNA nanostructures was based on a very long genomic ssDNA (>1000 nucleotides) folded

into desired shapes using small staple strands (Figure 1.7A).⁷ This is a one-pot method in which the long ssDNA strand and short single strands are mixed together to self-assemble the desired shapes with approximately 100 nm size and 6 nm spatial resolution. This method involves two important steps. Initially, a desired shape is constructed by raster-progression of a long ssDNA sequence, which is further fixed in the appropriate position's using staple strands.

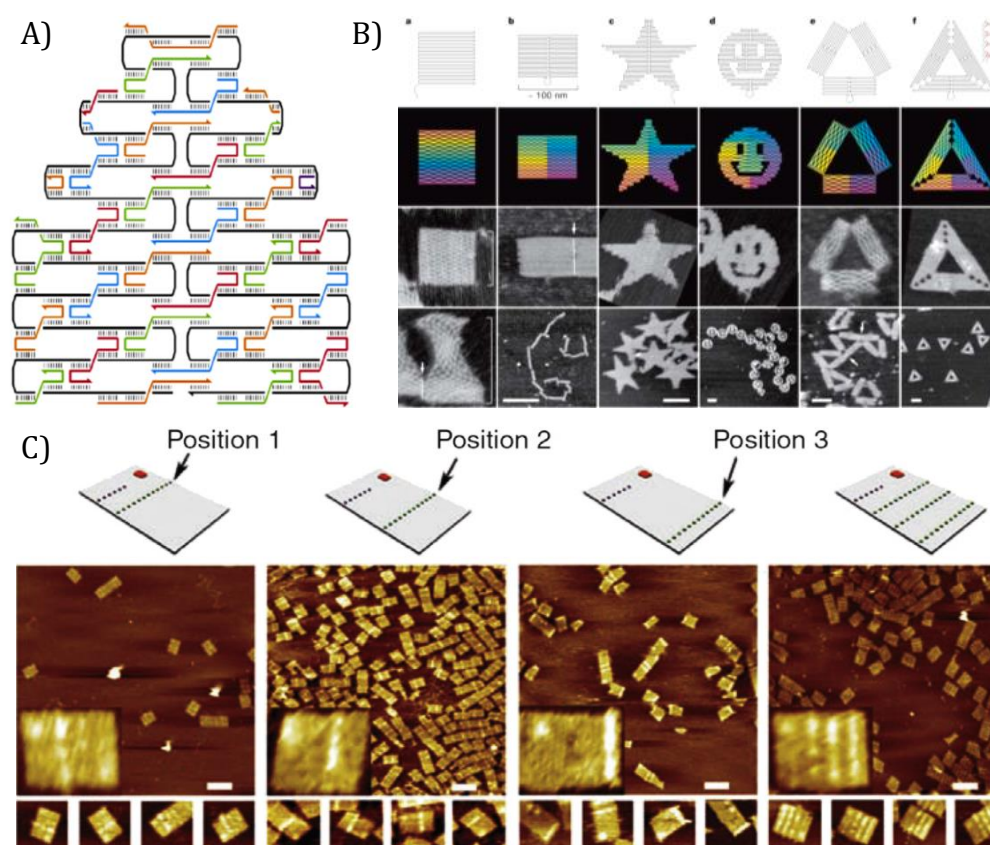


Figure 1.7. A) Structure of DNA-origami formed from a long ssDNA and short staple strands (Adapted from reference 7). B) examples of few shapes; square, rectangle, star, smile face and prismatic structures assembled using DNA-origami approach and the corresponding AFM images (Adapted from reference 7), and C) 2D DNA-origami tiles for the precise positioning of DNA strands as capture probes of RNA and the corresponding AFM images of assemblies (Adapted from reference 42).

These small staple strands required for the specific designs are selected by the careful computer programming (Candnano Software). The cooperativity of staple strands to assemble into complex non-periodic shapes with comparatively good

yields make them a versatile strategy over the so far mentioned DNA-tile based assemblies. Accordingly, several arbitrary structures like squares, stars, smiley faces, etc., were constructed to demonstrate the vast applicability of DNA-origami based self-assembly (Figure 1.7B).⁷

Later, Yonggang *et al.* in 2008 developed 2D assemblies from a DNA-origami tile motif for the precise positioning of RNA capture probes.⁴² Here, a rectangular shaped DNA-origami with three, pre-positioned dissimilar capture-DNA sequences corresponding to three genes *C-myc*, *β -actin* and *Rag-1* resulted in efficient target binding compared to bare-templates (Figure 1.7C). Subsequently, a wide variety of higher ordered DNA assemblies like 3D DNA box with lid, tetrahedron and elongated prismatic structures were designed from 2D DNA-origami tiles.⁴³⁻⁴⁵ Recently, in 2019 Hyungmin and coworkers published a fully automated strategy to design staple strands to fold any free-form of 2D framework using PERDIX algorithm.⁴⁶ They have incorporated DX based staple strands instead of ssDNA sequences to achieve better flexibility without losing control over the required geometry. And this method eliminates the tedious design of ssDNA sequences manually.

As mentioned earlier, 3D DNA nanostructures can be constructed either from DNA-tile based assemblies or from 2D DNA-origami based assemblies. Shih *et al.* reported the first DNA-origami based 3D DNA nanostructure from helices assembled into honey-comb lattice like structure.⁴⁷ Initially staple strands spirals around bigger strand in an anti-parallel direction and assembles into helices with diameter around 2 nm. These helices are further joined using crossover staple sequences to make extended 3D structures (Figure 1.8A). Using this principle, researchers were able to develop 3D objects by twisting and bending the DNA rod like structures.^{48,49}

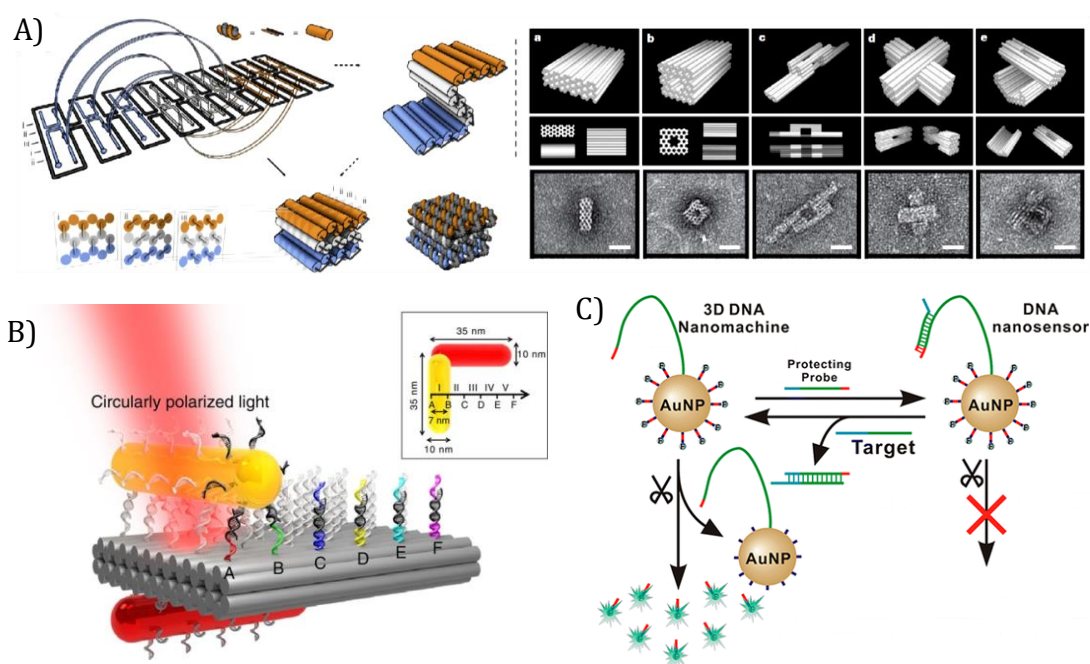


Figure 1.8. A) Construction of 3D DNA-origami structures using cross over strands from DNA-helices and corresponding TEM images (Adapted from reference 47). B) Design of DNA walker, a plasmonic Au nanorod moving along a 3D double layered DNA-origami structure. (Adapted from reference 54) and C) DNA walker moving around a 3D DNA-AuNP for drug delivery (Adapted from reference 55).

DNA-walkers are another important innovation in the field of DNA nanotechnology.⁵⁰ Seeman in 2010 reported a DNA-origami based DNA walker, which can move around the DNA-tile and gather, transport AuNP cargos.⁵¹ Soon after, numerous dynamic DNA nanostructures were designed to perform various applications.^{52,53} Liu and coworkers in 2015, designed a plasmonic nanorod which can move along a 3D DNA-origami platform for application in smart nanophotonics.⁵⁴ Here, a 35 nm gold nanorod functionalized with ssDNA sequences acts as the plasmonic system and a double layer 3D DNA-origami with precisely organized complementary sequences as platforms. Upon addition of selected blocking strands, strand displacement reaction occurs and gold nanorod starts moving over the surface and carries the optical information along its direction of movement (Figure 1.8B). Likewise, Feng and associates designed a DNA

nanomachine with a DNA walker moving around a 3D DNA-AuNP construct for efficient drug delivery.⁵⁵ Initially, a AuNP of 20 nm diameter was modified with DNA substrates (DS) to carry payloads and DNA walkers (DW). In presence of an enzyme termed nicking endonuclease, the DNA walker moves over the 3D AuNP by cleaving the nearest DS and thereby releasing the payloads (Figure 1.8C). In addition, they have demonstrated the controlled delivery of payloads by introducing a complementary sequence corresponding to DW.

1.5. SUPRAMOLECULAR DNA ASSEMBLY

Combining the programmable and predictive DNA assembly with synthetic molecules and ideas of supramolecular chemistry, the field of supramolecular DNA assembly got established.⁸ This method imparts benefits to both DNA assemblies and supramolecular assemblies by introducing functionalities on to DNA assemblies and improved programmability to the supramolecular assemblies. As a result, the number of DNA strands required for the construction of DNA assemblies is less compared to the assemblies formed from DNA alone, which further reduces the complexity in the design of DNA strands. For a better understanding, the assemblies can be classified into two; (i) DNA strands covalently modified with synthetic moieties and their assemblies, and (ii) assemblies formed by the non-covalent interactions of DNA with organic or inorganic molecules.

1.5.1. Covalently modified DNA assemblies

Synthetic organic fragments, transition metal complexes, polymers and lipids were introduced into DNA assemblies by replacing the crossover motifs used in DNA-tile and origami assemblies. These assemblies were achieved by the covalent

modification of ssDNA strands with synthetic motifs. The first report on this type of assembly was from Bergstrom group, where a tetrahedral carbon is covalently linked to two similar self-complementary strands via *p*-(2-hydroxyethyl)phenylethynylphenyl units, which assembles into cyclic oligomers of various size through hybridization (Figure 1.9A).⁵⁶ In this strategy, the flexibility in forming different sized cyclic structure was controlled by the use of dissimilar ssDNAs.

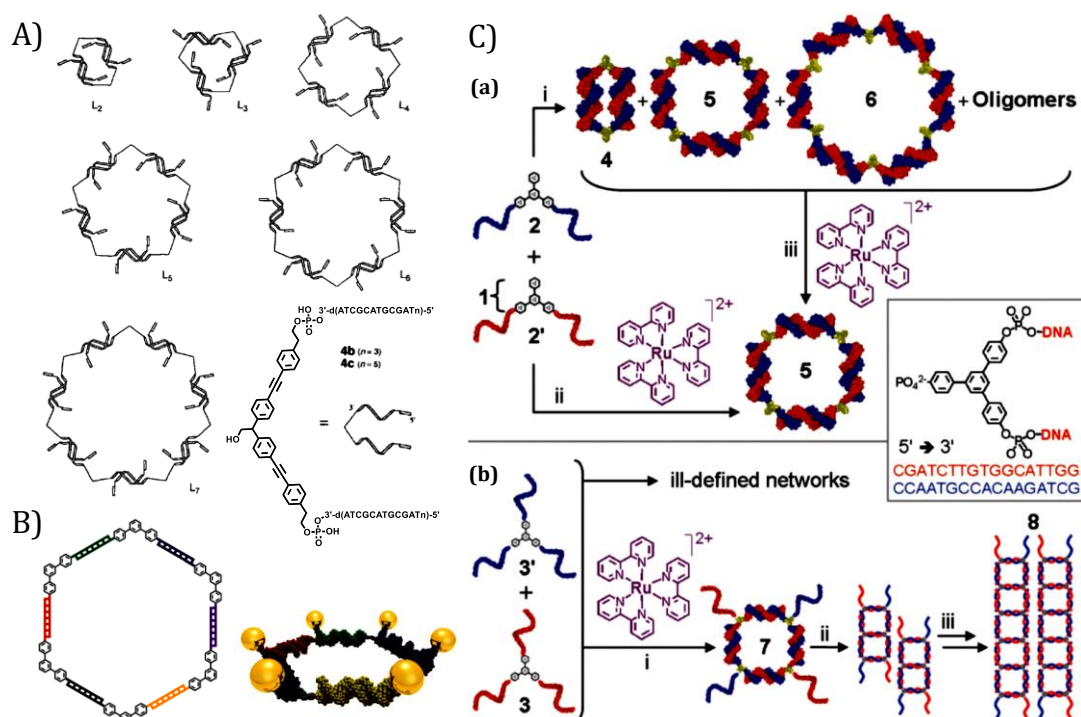


Figure 1.9. Structures of synthetic vertex incorporated A) cyclic DNA assemblies (Adapted from reference 56), B) DNA hexagon and AuNP modified DNA hexagon (Adapted from reference 57) and C) cyclic oligomers and nanofiber formation in presence of a Tris(bipyridine)ruthenium(II) complex (Adapted from reference 58).

Sleiman and coworkers extended this work by introducing rigid vertices and asymmetric ssDNA strands into DNA-assemblies and established the construction of 2D DNA assemblies for organizing nanoparticles.^{57,58} Initially, a rigid organic moiety like *m*-terphenyl system was covalently attached to two asymmetric ssDNA strands and sequentially assembled into a DNA hexagon. Similarly, by replacing one of the ssDNA with AuNP modified ssDNA, DNA hexagons with precisely organized AuNP

assemblies were fabricated (Figure 1.9B) and the formation of these assemblies were confirmed primarily using gel electrophoresis technique.⁵⁷ Likewise, using triphenylbenzene as the vertex unit, cyclic and 1D DNA nanofibers were reported by the same group.⁵⁸ Modification of two phenyl units of organic vertex lead to the formation of three different cyclic assemblies (Figure 1.9Ca.i). Whereas, modifying all the three phenyls groups resulted in micrometer sized 1D DNA nanofibers (Figure 1.9Cb). Also, they have shown the guest induced selectivity and the selective formation of cyclic assembly, 5 (Figures 1.9Ca.ii, iii and 1.9Cb.i). This selectivity in presence of the guest, Tris(bipyridine)ruthenium(II) complex is ascribed to suitable size of cavity to accommodate the complex compared to other cyclic structures and represent a fine example for controlling the assembly through selective host-guest interactions.

The formation of macrocyclic oligomers was further extended into 3D structures by inserting complementary ssDNA between these structures.⁵⁹ Using this strategy various 2D polygon assemblies were converted into 3D cage like structures and used to encapsulate nanoparticles, proteins, drug molecules, etc.^{60,61} In 2010, a DNA nanotube with cages to precisely organize AuNPs and subsequent, stimuli responsive release in presence of added ssDNA was reported (Figure 1.10A).⁶⁰ Initially, different sized trigonal 2D nanostructures were assembled into longitudinal nanotubes with dissimilar sized cages, by linking ssDNA between these triangular units. These cages encapsulate citrate stabilized AuNPs at specific sites with regular spacing of 65 nm and were characterized by UV-visible absorption, AFM and confocal imaging techniques. The selective and efficient release of nanoparticle cargo was achieved by the addition of specific, completely complementary ssDNA sequence to the closing ssDNA strand in nanotubes, which

upon hybridization removes the closing DNA strand as dsDNA and triggers the release of AuNP by leaving the partially single stranded-DNA nanotube.

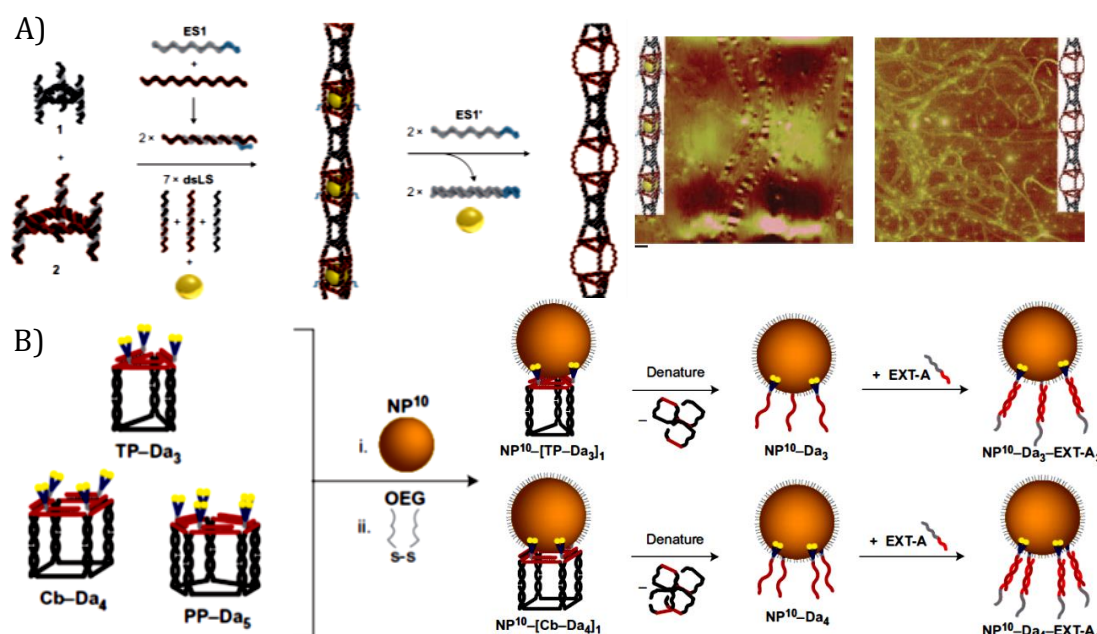


Figure 1.10. A) Encapsulation and selective release of AuNPs using 3D DNA nanotube, corresponding AFM images (Adapted from reference 60) and B) schematic representation of the functionalization of ssDNA onto AuNP using 3D DNA polygonal structures (Adapted from reference 61).

Recently, in 2016 Sleiman *et al.* reported a method to chemically transfer the molecular level information from 3D DNA nanostructures to AuNPs (Figure 1.10B).⁶¹ In this approach they have modified the long ssDNA sequences with hexyloxyglycol spacers and assembled 3D nanostructures having various polygonal faces. And the chemical information, that is the specific ssDNA sequences were effectively transferred into AuNPs. The success of this method was confirmed using agarose gel electrophoresis (AGE) analysis, transmission electron microscopy (TEM), UV-visible absorption and fluorescence emission studies. The benefit of this method over other strategies in transferring the information are, control over the number of binding strands, controlled spacing and regioselective positioning of strands onto

nanoparticles. This is considered as a promising strategy, which finds remarkable applications in the areas of information storage and biomedical technologies.

Another approach to construct functional structures using DNA is by covalent modification of ssDNA sequences with transition metals, polymers and organic molecules. Inspired from the transition metal complexes in biological system, Sleiman and McLaughlin developed various branched DNA-transition metal complex assemblies by covalently attaching transition metal complexes with ssDNA as well as nucleobases of ssDNA.^{62,63} Using this strategy, McLaughlin and coworkers reported selective encapsulation of different metal ions by varying the ligand units attached to DNA (Figure 1.11A).⁶⁴ For this purpose, a ssDNA and its complementary DNA sequences were covalently modified with terpyridine (tpy) and diphenylphenanthroline (dpp) ligands separately. Combination of two tpy appended dsDNA and two dpp appended dsDNA were highly selective towards Fe(II) and Cu(I), respectively. On the other hand, dsDNA formed by the combination of tpy and dpp was selective towards Cu(II). This differential selectivity towards various metal ions was accompanied by the increased stability of dsDNA compared to the hybrids without metal coordination. Moreover, this was an important achievement for the selective positioning of various metal ions at specific locations of DNA-nanostructures.

Herrmann and coworkers reported amphiphilic self-assembly of DNA-block copolymer micelles into rod-like aggregates, similar to the assembly of amphiphilic polymers in aqueous solutions.⁶⁵ Afterwards, other research groups also started exploring this assembly for applications in controlled drug delivery. Recently, Serpell and Sleiman reported a hydrophobic polymer conjugated to 3D DNA prism with multiplex application's in light harvesting and controlled release and

aggregation of substituents (Figure 1.11B).⁵⁹ By changing the position, number and length of hydrophobic polymers attached to the cage DNA, the structure and aggregation behavior of resultant assembly was evaluated. With increase in the size of polymer chain, dimeric and higher order assemblies were formed. After a particular length, the assembly becomes monodisperse with micelle structures.

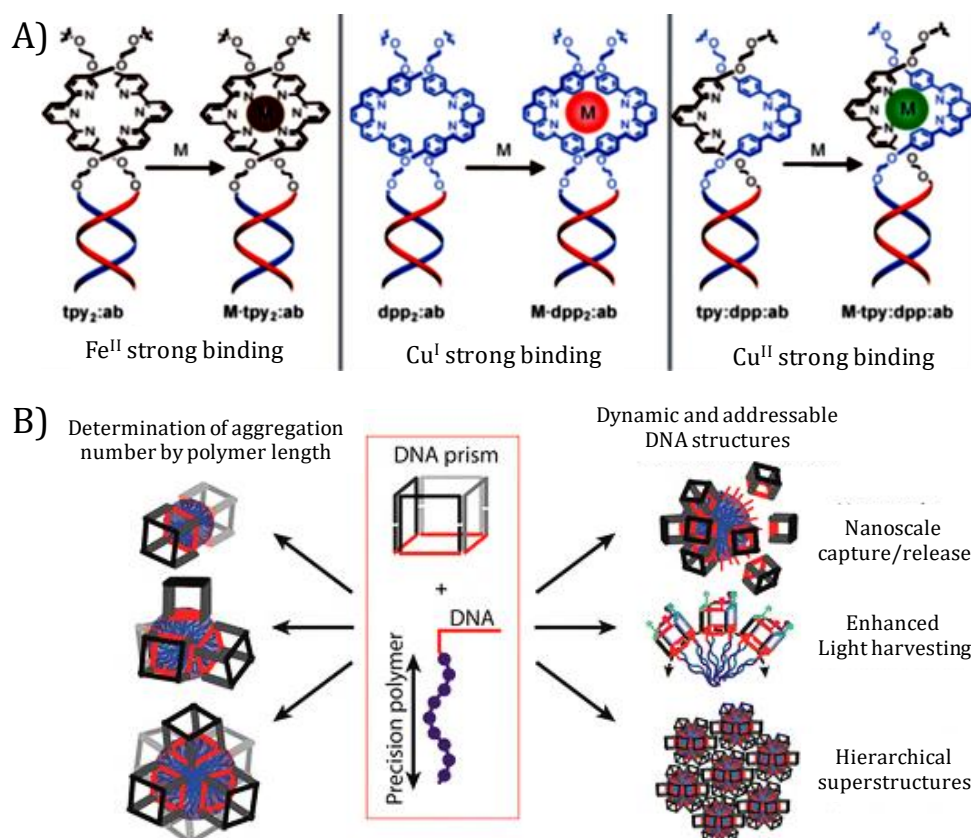


Figure 1.11. A) Selective detection of different transition metals in different DNA-ligand environment (Adapted from reference 64). B) 3D DNA-polymer conjugates used for light harvesting and controlled release and aggregation of constituents (Adapted from reference 59).

These micellar structures are of appropriate size for targeted cancer therapy. Therefore, they have explored the controlled release of DNA cages by strand displacement reactions. In addition, the potential of this assembly in light harvesting was demonstrated by modifying the outer surface of DNA cages in the micellar form with different fluorophores which can undergo Förster resonance energy transfer (FRET).

Exploiting the amphiphilicity directed bottom-up self-assembly, DNA-organic conjugates have been constructed and used as templates for organizing functional materials. Mirkin and Herrmann's research group are pioneers in this area and have developed several self-assembled systems from DNA-organic conjugates.^{66,67} R. Varghese's research group are extensively working based on this strategy and have shown the formation of self-assembled vesicles and 2D nanosheets from DNA-organic chromophore conjugates.^{68,69} Recently in 2019, they have reported the formation of helically twisted nanoribbon like assemblies by wisely choosing the organic part as hexaphenylbenzene (HPB).⁷⁰

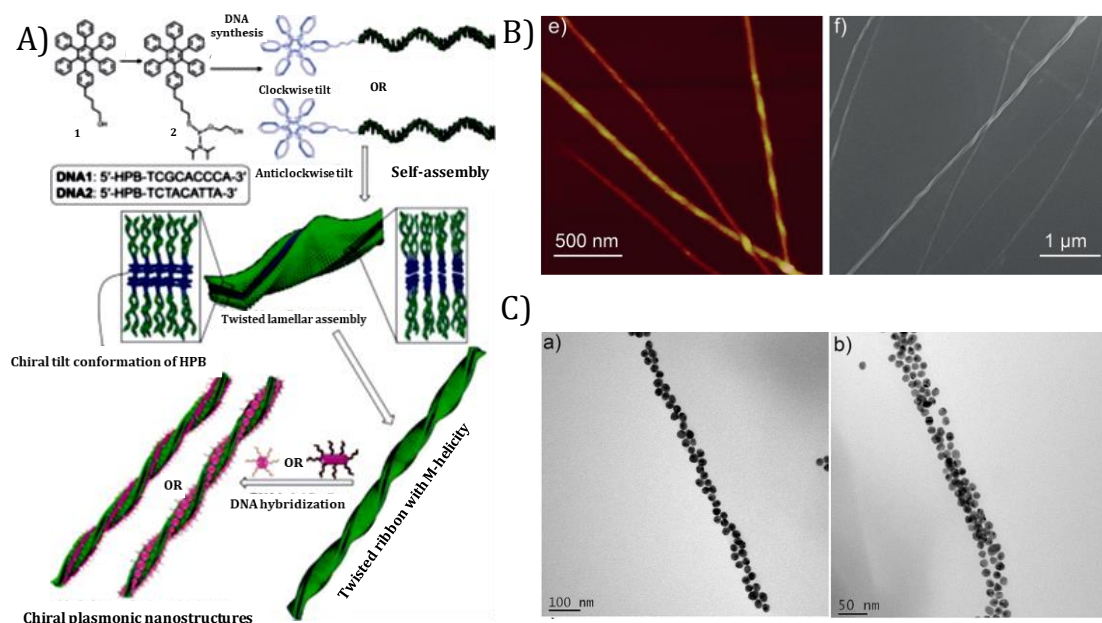


Figure 1.12. A) Schematic representation of the self-assembly of DNA-HPB conjugate into helically twisted ribbon like structures, corresponding B) AFM and SEM images, and C) TEM images of AuNP decorated DNA-HPB assembly (Adapted from reference 70).

HPB, with propeller structure is well known for its atrop-isomerism property associated with the hindered rotation of six $C(sp^2)$ - $C(sp^2)$ bonds attached to the central benzene ring. As a result, a helical twist was incorporated into the amphiphilicity driven self-assembly (Figure 1.12A). Microscopic analysis showed the successful formation of twisted helical ribbons with approximately 12 nm thickness

and several micrometers in length (Figure 1.12B). Further, the ability of this chiral assembly to template the organization of nanoparticle was studied by inserting a AuNP modified with ssDNA complementary to the strand over the surface of ribbon and verified using UV-visible absorption, CD and TEM analysis (Figure 1.12C).

Organic chromophores can also be introduced into DNA by using phosphoramidites of organic chromophores in solid phase oligonucleotide synthesis or by inserting artificial nucleobases conjugated with organic moieties. Inserting artificial nucleobases into DNA requires the post synthetic modification of nucleobases with chromophores, which was earlier achieved using copper-catalyzed cycloaddition reactions. Wagenknecht and Haner research groups are using this strategy of post synthetic modification to develop self-assembled DNA-organic light harvesting systems.⁷¹⁻⁷³ Wagenknecht *et al.* in 2015 reported the assembly of three chromophores based on DNA, and demonstrated the self-assembly and photophysical properties in the context of their applications in light harvesting.⁷² The chromophores, pyrene, perylene and Nile red were initially attached to nucleobases (Figure 1.13A) using acetylene linkages and assembled into different dsDNA using solid phase phosphoramidite chemistry (Figure 1.13B). The absorption spectra of dsDNA with all the three chromophores covers the entire UV-visible range compared to dsDNA with single chromophores (Figure 1.13C). Here, an energy transfer followed by an electron transfer in the opposite direction takes place upon excitation and results in a charge separated state. Along with this, they have studied the efficiencies of these transfers by varying the distance between the chromophores and showed that any wavelength between 350 and 700 nm can accomplish this energy/electron transfer processes signifying the potential of these assemblies in light harvesting.

Recently, from Haner group, they have constructed a similar light harvesting system by the self-assembly of phenanthrene polymers and DNA functionalized with three chromophores (Figure 1.13D).⁷³ Here, a stepwise energy transfer from light-harvesting phenanthrene polymers to Cy5.5 chromophore occurs through Cy3 and Cy5 intermediates via Forster resonance energy transfer (FRET), with 59% efficiency. They have evaluated the FRET efficiencies by varying the inter chromophore distances, which was accomplished by incorporating normal nucleobases between chromophores.

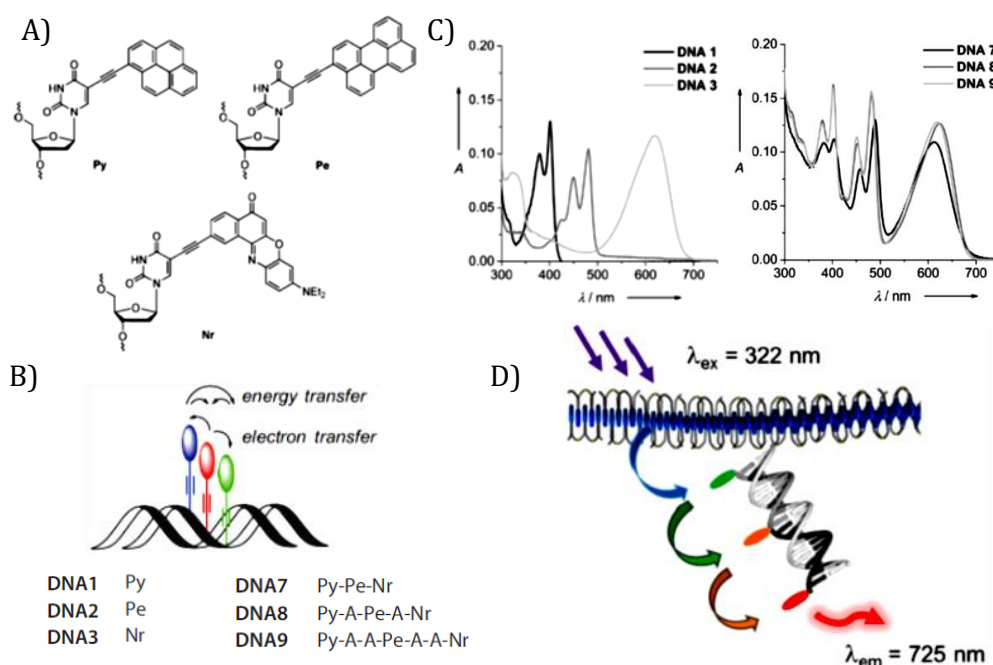


Figure 1.13. A) Chemical structures of Py, Pe and Nr, B) schematic representation of energy, electron transfer processes and ds DNA sequences, and C) absorption spectra of chromophore functionalized dsDNAs used in this work (Adapted from reference 72). D) Schematic representation of FRET in a self-assembled system of supramolecular phenanthrene polymers and multiple chromophore functionalized DNA (Adapted from reference 73).

Nucleic acid-based hydrogels are another promising candidate in supramolecularly assembled functional materials. There are mainly two types of nucleic acid-based hydrogels; i) hydrogels formed by the sequence selective hybridization of long ssDNA sequences and ii) hydrogels derived from

functionalized oligonucleotides. Among these, functional nucleic acid based hydrogels with catalytic, molecular recognition, encapsulation, storage and stimuli responsive properties are extensively used in biomedical fields.⁷⁴ Functional nucleic acids include chromophore modified oligonucleotides, siRNAs, aptamers, i-motif structures, DNazymes, etc.⁷⁵ For example, Willner *et al.* demonstrated pH and ligand responsive release of substrates from microcapsule like structures of acrylamide-DNA hydrogels.⁷⁶ For this study, nucleic acid functionalized CaCO₃ substrates and polyacrylamide functionalized hairpin oligonucleotides were assembled into microcapsule like structures via hybridization chain reactions. In the assembled state the substrates are encapsulated in the microcapsules, which were designed with aptamers sensitive towards pH and ATP/cocaine. As a result, the presence of stimuli's like ATP, cocaine or pH=5 releases the substrate via changing the DNA hybridization pattern from hairpin structures to i-motif structures in the microcapsule assembly (Figure 1.14). In addition, they have verified the applicability of this strategy by performing permeability studies using microcapsules loaded with fluorescent quantum dots and drug release using DOX-D loaded microcapsules on MDA-MB-231 cancer cells.

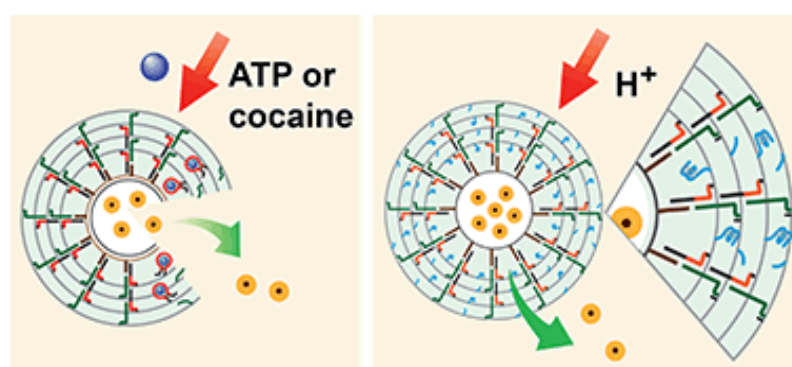


Figure 1.14. Stimuli responsive release of substrates from polyacrylamide functionalized nucleic acid-hydrogels (Adapted from reference 76).

1.5.2. Non-covalent interaction directed DNA assemblies

Apart from the structural modification of DNA, the available supramolecular interaction sites of DNA were also used to assemble small organic molecules and metal ions. Supramolecular interactions include, conventional or unconventional hydrogen bonding, groove binding, intercalation, electrostatic and metal-base pair interactions. These types of assemblies were usually demonstrated using short ssDNA and dsDNA sequences with <40-50 nucleobases. The presence of multiple interaction sites in ssDNA and its ability to assemble into helical structures are the two driving forces used in the assembly of ssDNA with small functional organic molecules and metal ions. In such assemblies, small functional organic molecules interact with dsDNA through major/minor groove binding, intercalation between nucleobases and/or electrostatic binding with sugar phosphate back-bone. Also, such assemblies avoid the difficulties with complex structural design and covalent modification of DNA for self-assembly.

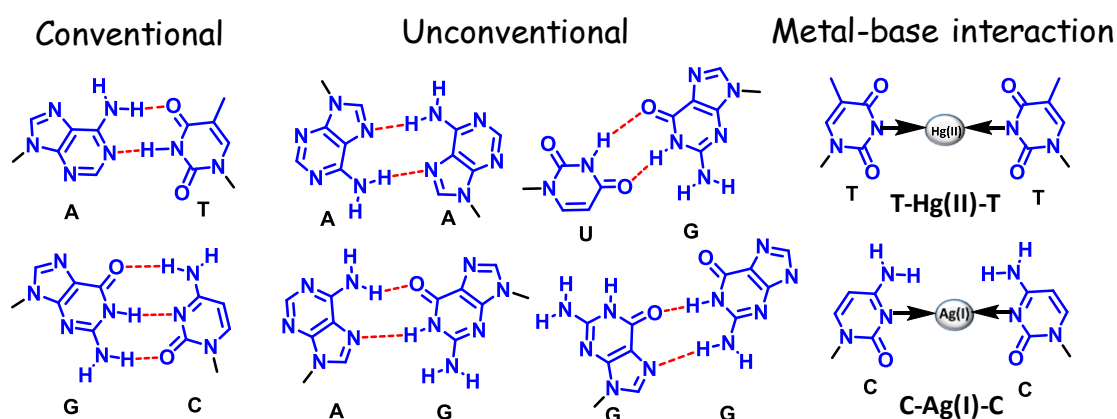


Figure 1.15. Different types of conventional and unconventional hydrogen bonding between nucleobases and metal-nucleobase interactions.

Non-covalent interactions of nucleobases include, conventional or unconventional hydrogen bonding interactions of ssDNA with small molecules having nucleobase partners and metal-base pair interactions (Figure 1.15). For

example, in 2015 Govindaraju and coworkers described a mutually templated helical double zipper assembly of DNA-Perylene hybrid system by exploiting the conventional and unconventional hydrogen bonding property of nucleobases.⁷⁷

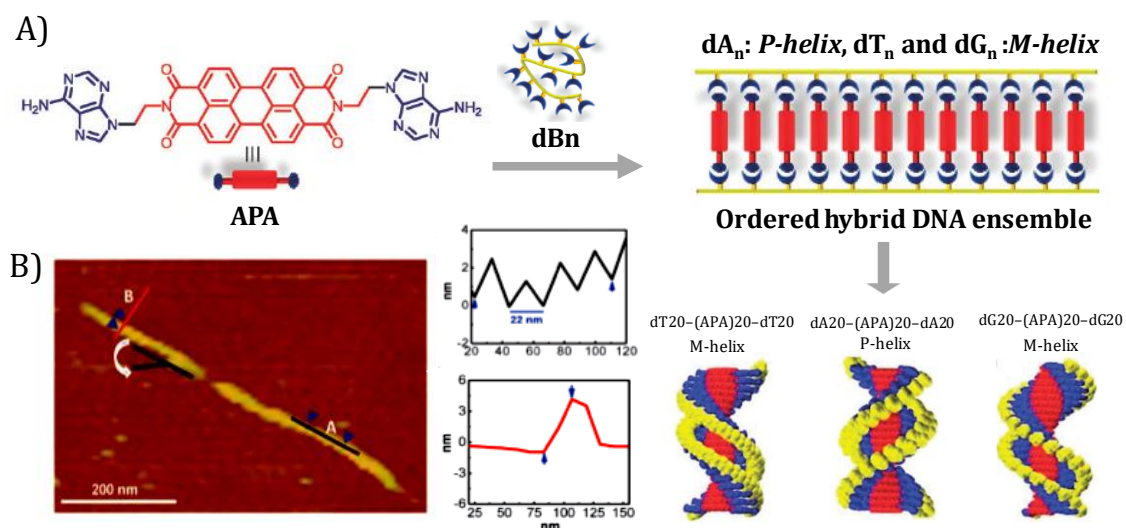


Figure 1.16. A) Chemical structure of APA, its assembly in presence of different oligonucleotides into ordered double zipper structures followed by helical assemblies. B) AFM image of M-helical dT20-(APA)20-dT20 assembly with width and height profile (Adapted from reference 77).

Primarily, an adenine functionalized perylenebisimide derivative (APA) was designed and synthesized. This APA derivative in PBS (phosphate buffered saline, pH=7) buffer, initially self-assembles into ordered double zipper like structures and further into helical assemblies in presence of deoxyoligonucleotides, dBn (Figure 1.16A). The anti-clockwise direction of transition moments of APA and conventional hydrogen bonding interactions leads to the assembly of APA in presence of dT20 (10:2) into M-helical structures. On the other hand, the unconventional hydrogen bonding between APA and dA20, APA and dG20 results in the formation of P-helix and M-helix respectively. They have used AFM and CD studies to confirm the formation of helical assemblies. Figure 1.16B shows the AFM image of their M-helical dT20-(APA)20-dT20 assembly with ~22 nm helical pitch and ~5 nm height, which was in agreement with the theoretically calculated values. Also, they have

demonstrated the stimuli responsive (pH <6) collapse of double zipper structures for application in delivery of therapeutic small molecules and ssDNA sequences. There are several other reports from Schenning, Iizawa, and Shimizu's research groups, where they have employed the different hydrogen bonding possibilities of nucleobases in the oligonucleotides to assemble helical structures of small molecules.⁷⁸⁻⁸⁰

As mentioned earlier, nanoparticles can be precisely organized using the structural programmability of DNA and in most of these cases, modified ssDNA sequences with functional groups capable to bind with metal ions are used to locate metal atoms in fixed positions. Apart from this strategy, a supramolecular approach to construct DNA-inorganic hybrid assembly is by using the metal-base pair interaction. It is well known that, the binding affinity of Hg(II) between two thymine's and Ag(I) between two cytosines are high compared to other metal-base pair interactions.^{81,82} Exploiting this property, numerous thymine and DNA based fluorometric and colorimetric sensors with high sensitivity were developed for detecting Hg²⁺ ions in aqueous medium.^{83,84} For example, M. Pandeewar *et al.* developed a DNA-organic ensemble for the detection of Hg with 0.1 nM limit of detection (LOD).⁸⁵ A DNA-organic hybrid 2D nanosheets were assembled from a semiconducting adenine functionalized naphthalenediimide (BNA) and dTn via conventional hydrogen bonding. Upon adding Hg(II) to this system, BNA were replaced by Hg and forms [dT-Hg-dT]_n assemblies with lower lateral dimensions compared to the 2D sheets of BNA-dTn (Figure 1.17A). Further, they have transformed this assembly into a field effect transistor (FET) device for the sensitive detection of Hg in water by measuring the conductivity changes.

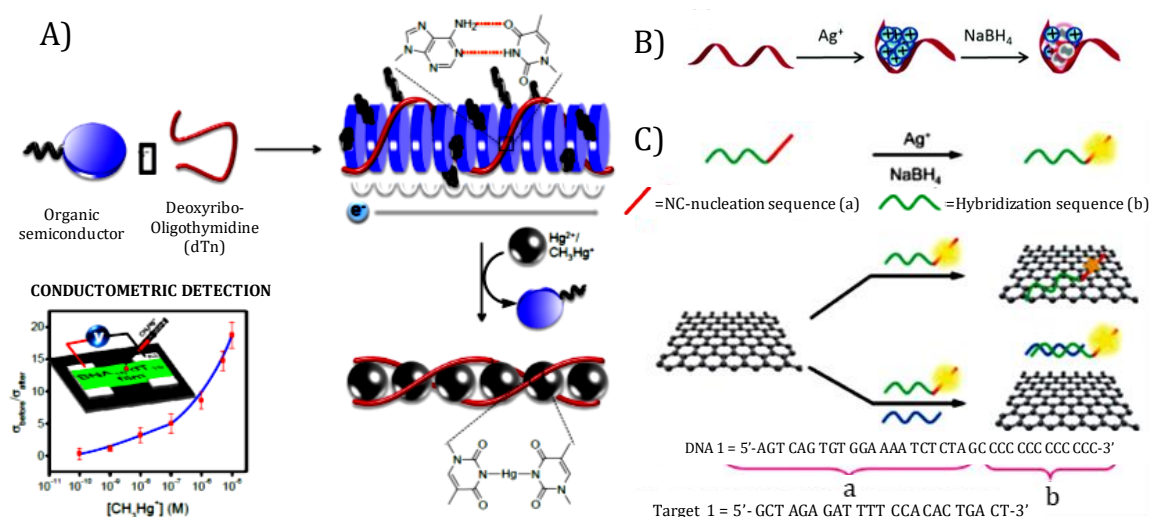


Figure 1.17. Schematic representation of A) the BNA and dTn self-assembly, following transformation into [dT-Hg-dT]_n assemblies, conductometric measurements of FET device with addition of methylmercury (Adapted from reference 85), B) DNA templated fluorescent silver nanocluster formation (Adapted from reference 86) and C) DNA detection strategy using GO and DNA-AgNCs (Adapted from reference 87).

Similarly, the cytosine-Ag(I)-cytosine interaction is used to develop fluorescent silver nanoclusters stabilized by cytosine rich oligonucleotides (Figure 1.17B).^{82,86} Ever since the first report by Robert M Dickson,⁸⁶ these label free fluorophores were broadly used in bioimaging and sensing applications.^{87,88} In this strategy, as a result of the interaction of cytosine with Ag(I), only few of the ions gets reduced to Ag atoms upon reduction. And the reduced ions will be stabilized inside the cytosine rich sequence, which results in fluorescent Ag nanoclusters with sub-nanometer size. The advantages of this strategy compared to other stabilizing agents include, the controlled reduction of Ag(I) and the stabilization of nanoclusters formed inside the oligonucleotide template from further reduction to higher sized non-fluorescent nanoparticles.

Using this method, Qu *et al.* reported an efficient strategy for the detection of multiple DNA strands using graphene oxide (GO) and DNA-silver nanocluster (DNA-AgNC) systems (Figure 1.17C).⁸⁷ The fluorescence quenching property of GO and

monitoring the optical properties of DNA-AgNC supported the selective detection of specific DNA strands. Though it looks simple, the importance lies in the easy synthesis, cost effectiveness, biocompatibility and multiple target analysis. This area of DNA templated fluorescent silver nanoclusters will be further discussed in detail as a part of Chapter 2. In addition to the above mentioned metal-base pair interactions, there are also reports on DNA-inorganic assemblies formed from Zn(II) or Cu(II)-nucleobase interactions.^{89,90}

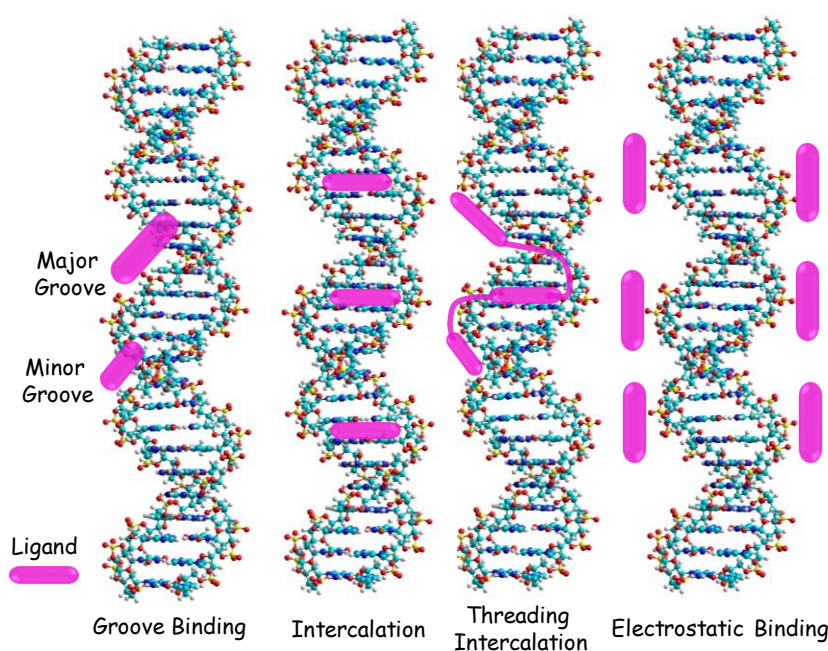


Figure 1.18. Illustration of the different supramolecular interactions of ligand with dsDNA.

As discussed previously, small molecules and biomolecules (collectively mentioned as ligand) interact with dsDNA through groove binding, intercalation and electrostatic interactions (Figure 1.18). Groove binders are usually biomolecules or small molecules, which plays important role in drug development. There are two types of grooves in dsDNA: major and minor grooves. As the name implies the size of grooves are different and so the binding molecules are also dissimilar. Typically, larger molecules like sequence specific proteins, peptide nucleic acids, etc., binds to major grooves via hydrogen bonding or by intercalative interactions and thereby

regulates the biological processes.^{91,92} Whereas, small molecules binding to major groove of DNA are developed by covalently modifying the nucleobases.^{93,94}

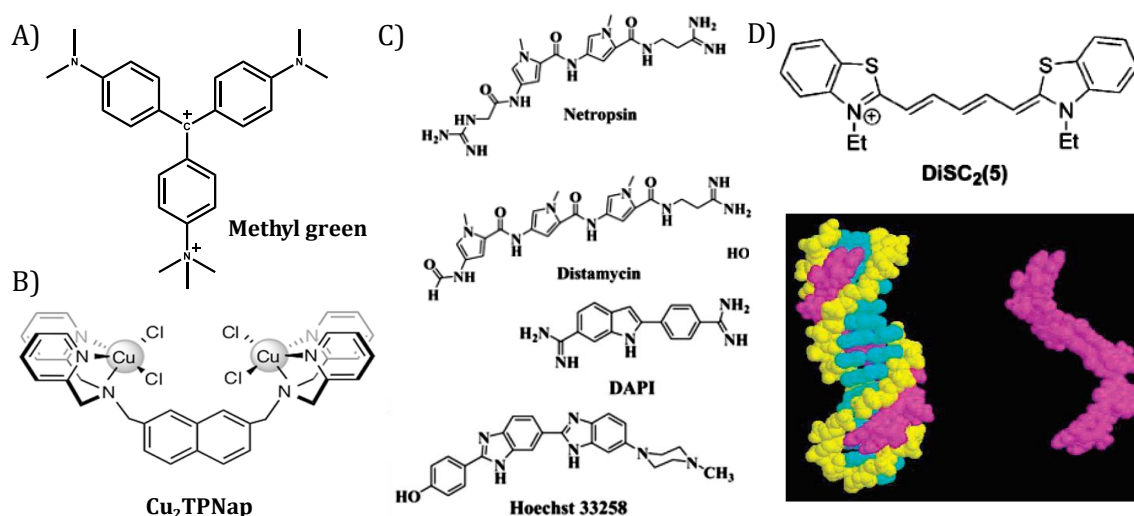


Figure 1.19. Chemical structures of A), B) major, C) minor groove binders (Adapted from reference 95, 97 and 98), and D) DiSC₂(5) and the molecular modelling showing the assembly of three DiSC₂(5) dimers along the minor grooves of DNA (Adapted from reference 99).

To date there are only very few reports on small molecules (For example methyl green, Figure 1.19A) binding to major grooves of DNA without any covalent modifications.⁹⁵⁻⁹⁷ Recently, Kellett *et al.* reported a di-Cu(II) complex, Cu₂TPNap (Figure 1.19B) which exclusively binds to major grooves without any intercalation and displays efficient oxidative DNA damage.⁹⁷ On the other hand, minor groove binding small molecules uses electrostatic, hydrophobic, hydrogen bonding and van der Waals forces to bind with dsDNA. Netropsin, distamycin, DAPI29 and Hoechst 33258 are examples of extensively studied DNA-minor groove binders (Figure 1.19C).⁹⁸ Armitage and coworkers in 2014 demonstrated the formation of three self-assembled dimers of benzothiazole based symmetrical cyanine dye (DiSC₂(5)) along the minor grooves of dsDNA (Figure 1.19D). This was one of the first reports, which employed the groove binding property of DNA to template the assembly of small organic dyes.⁹⁹

Recently, our research group has shown the ordered assembly of short dsDNA and three-way junction (TWJ) DNA structures into 1D and 2D functional materials using multiple non-covalent interactions.^{100,101} An aniline modified fullerene derivative (**FAn**) with amphiphilic structure was designed and synthesized. **FAn** assembles into 3-5 nm sized fullerene clusters in 10% DMSO-PBS and these clusters interact with short dsDNA, primarily through DNA-groove binding and forms micrometer long nanowires with 80-120 nm thickness and ~2 nm height (Figure 1.20A). Similarly in presence of TWJ-DNA, micrometer sized layered nanosheets with ~2 nm height was observed (Figure 1.20B).¹⁰¹ The potential of these non-covalently assembled 2D-nanosheets to template functional nanomaterials was also demonstrated by introducing a cytosine rich overhang into the TWJ-DNA structure. Successful formation of fluorescent AgNC decorated 2D nano-networks further supports the possibility of our strategy to construct higher order functional materials for application in nanoelectronics.

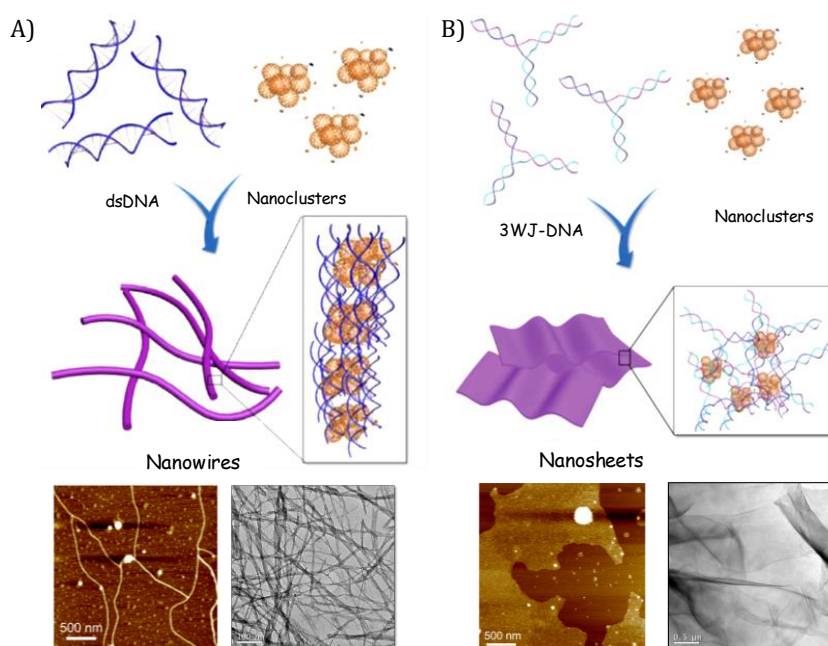


Figure 1.20. Schematic representation and corresponding AFM, TEM images of the supramolecular assembly of **FAn** nanoclusters with A) dsDNA into nanowires and B) 3WJ-DNA into 2D nanosheets (Adapted from reference 100 and 101).

On the other hand, insertion of the planar aromatic part of cationic molecules between bases pairs of DNA is termed as intercalation. Intercalative binding consumes energy to unwind, as a result the binding is comparatively stronger than other non-covalent interactions. There are two types of intercalative binding: classical intercalation and threading intercalation. Classical is the standard kind of intercalation with free planar aromatic units, whereas threaded interaction involves planar structures with two opposite side chains. These two opposite chains further interact with DNA through groove binding and stabilizes the assembly. G/C rich sequences are superior intercalation sites in a dsDNA, as they unstacks easily.⁹⁸ Ethidium bromide (EB), methylviologen (MV) and acridine (Acr) are some of the extensively studied organointercalators (Figure 1.21A).

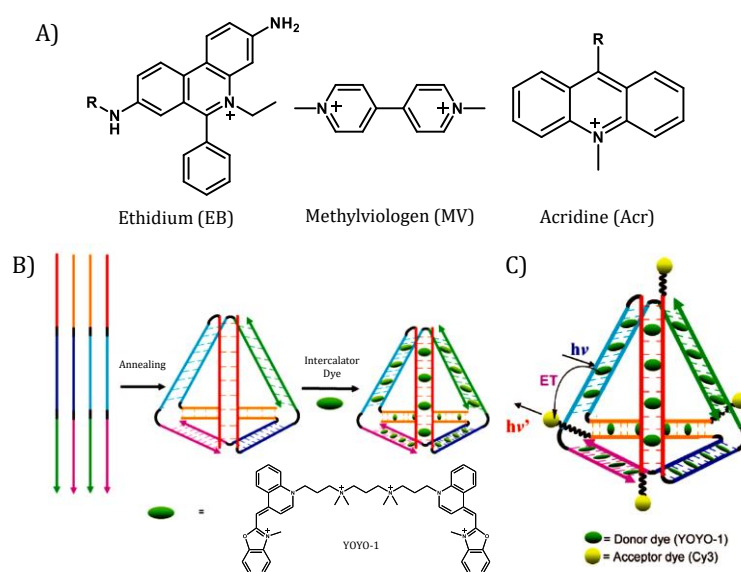


Figure 1.21. A) Chemical structures of organo-intercalators EB, MV and Acr. B) Schematic representation of DNA tetrahedron formation, YOYO-1 intercalation and C) electron transfer (ET) in the DNA tetrahedron with intercalated YOYO-1 and covalently modified Cy3 acceptor dyes (Adapted from reference 102).

Several light harvesting multi chromophore arrays have been constructed with different DNA nanostructures using this method of DNA intercalation.^{16,102} Armitage *et al.* reported a 3D DNA-tetrahedron structure capable of templating the

intercalation of a bis-intercalating YOYO-1 dye at defined positions.¹⁰² Around 25 YOYO-1 molecules were incorporated into the DNA-tetrahedron, with all the dye molecules coming inside a diameter of 10 nm. The assembled structure displayed improved optical properties and better photostability compared to the monomer (Figure 1.21B). They have also demonstrated the efficient electron transfer (ET) properties of this system by selectively modifying the 5'-terminus of DNA-tetrahedron with Cy3 acceptor dyes (Figure 1.21C).

Electrostatic interactions of hard, electron rich and negatively charged sugar-phosphate back bone of DNA with cationic molecular structures are also exploited for the assembly of functional materials. Cationic molecular structures include polycationic polymers and positively charged small asymmetric and symmetric organic molecules.^{14,103,104} Purrello *et al.* described a selective sensing strategy for spermine directed Z-form of DNA using the electrostatic interactions of DNA, spermine and a metal organic complex.¹⁴ A tetraanionic nickel(II) porphyrin complex was used to monitor the pH depended structural changes in DNA (Figure 1.22A). At lower pH, an organized reversible supramolecular assembly of porphyrin-spermine-Z-DNA complex with the ability to store chemical information was reported.

Recently, from Myongsoo Lee's group, a pH responsive hierarchical assembly of two small molecules with dsDNA was reported.¹⁰⁴ Two bent shaped molecules (Figure 1.22B) were synthesized and assembled into helical, hollow cylindrical structures. These assemblies encapsulate dsDNA via simple electrostatic interactions. Interestingly, by mixing these two molecules in a particular ratio, pH driven switching of the helicity between B-form and Z-form of DNA was observed (Figure 1.22C). At pH 7.4, the outer diameter of cylindrical structure is ~8 nm,

whereas it is only 7 nm at 5.5 pH. This phenomenon was explained by the molecular rearrangement between the protonated and deprotonated forms of two molecules in the assembly at different pH conditions, leading to changes in the size of cylindrical structures. As a result of fluctuations in the electrostatic interaction between DNA and molecular assembly, the helicity of DNA also changes with the reversible helical motion of surrounding molecular assembly. They also have demonstrated these structural changes in DNA by taking it into the intracellular sections. In nutshell, this was a very intriguing work, which took the simple non-covalent electrostatic interaction of DNA and small molecules into higher levels for application in DNA-based nanomachines.

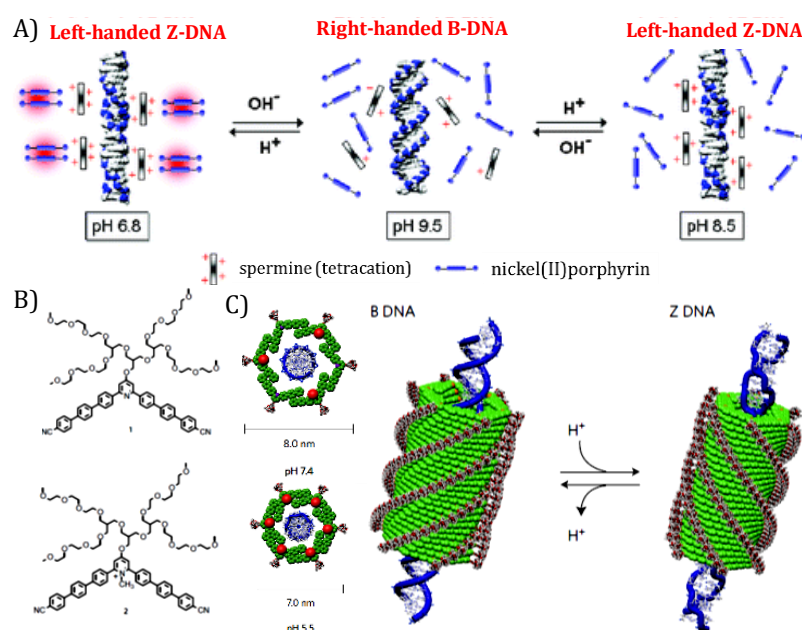


Figure 1.22. A) pH dependent arrangement of Ni-porphyrin complexes and structural changes in DNA (Adapted from reference 14). B) Molecular structures and C) schematic representation of the reversible helicity changes in the DNA incorporated molecular assembly at pH 7.4 and 5.5 (Adapted from reference 104).

1.6. SELF-ASSEMBLY DIRECTED BY NUCLEOBASE DERIVATIVES

Approaching the building blocks of nucleic acids individually and utilizing the above-mentioned supramolecular interactions of DNA, numerous self-assembled

materials have been fabricated. As the components of nucleic acid, nucleobases and their derivatives also possess good recognition, organization, biocompatibility and information storage properties. Nucleobase derivatives include nucleosides and mono, di, tri-phosphate nucleotides. Compared to other bimolecular templates, they are smaller in size, reasonably low cost and stable. In addition to its templating action, they can also modulate the physical and morphological properties of supramolecular assemblies. In the following section, we have described the latest developments in this field by appropriately classifying the self-assembly utilizing nucleosides and nucleobases separately.

1.6.1. Nucleotide directed assemblies

Among the other nucleobase derivatives, nucleotides with improved biocompatibility are more employed in the construction of self-assembled materials from small molecules and metal ions. Supramolecular polymers of small molecules, metal encapsulated hydrogels and coordination polymer nanoparticles were assembled from various nucleotide templates and employed for applications in energy and/or information transfer, light harvesting, sensing, nanoelectronics and biomedical applications.²¹ S. J. George and coworkers in 2014 described the formation of self-assembled nanofibers from naphthalene diimide (NDI) with tunable chirality using adenosine nucleotides (AP).¹⁰⁵ Dipicolylethylenediamine capable of coordinating with Zn were attached to the two ends of naphthalenediimide resulting in the formation of cationic complexes (APDI). These cationic molecules interact with negatively charged adenosine nucleotides; ATP, ADP and AMP in different ways and assemble into helical fibers with differential chirality. As the number of negative charges in ATP, ADP and AMP are different, the

equality in electrostatic interactions are also dissimilar. ATP assembles APDI into right-handed helical fibers whereas ADP and AMP assemble into left-handed helical fibers (Figure 1.23A). These interesting stimuli responsive chiral changes were used to monitor the real time enzymatic hydrolysis of APs (Figure 1.23B). The same group extended this strategy into perylenebisimide derivatives and demonstrated the AP responsive transformation of self-assembled 2D nanosheets into 1D nanofibers.¹⁰⁶

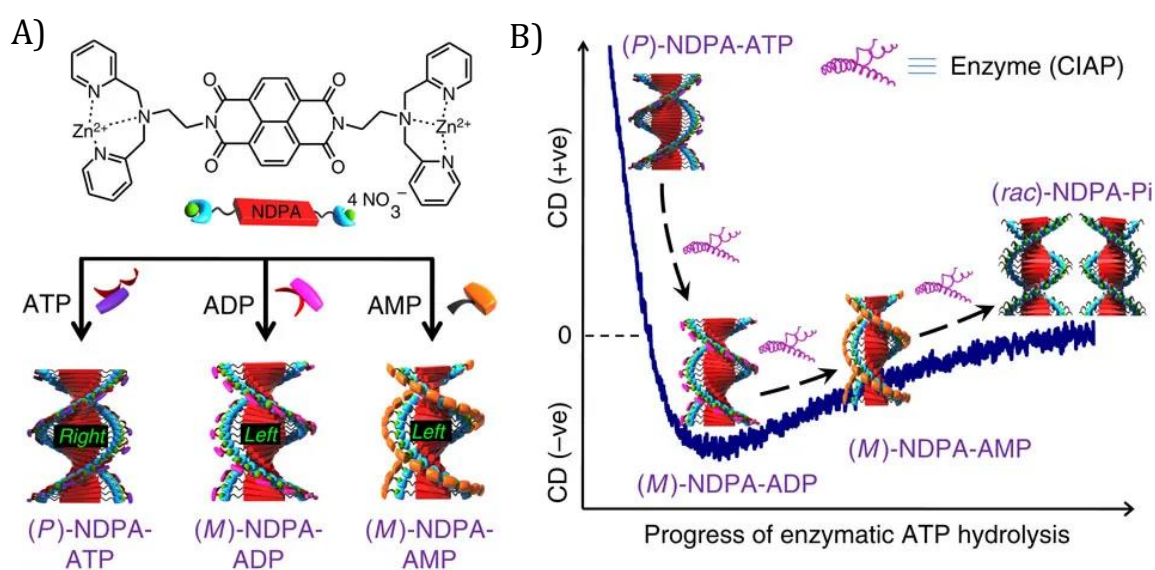


Figure 1.23. A) Molecular structure of APDI and illustration of different self-assemblies of helical fibers in presence of three APs. B) Schematic representation and corresponding chiroptical properties of helical assemblies during the enzymatic AP hydrolysis (Adapted from reference 105).

As in DNA, nucleobases in nucleotide also interacts with metals (Ag, Hg, Cu, etc.) via coordination bonds leading to supramolecular assemblies of metal nanoparticles.²¹ Apart from the reports on interactions with common metals, Liu *et al.* used isothermal scanning calorimetry techniques and studied the interactions of nucleotides with lanthanide ions.¹⁰⁷ They suggested the pyrimidine nucleotides interacts with lanthanide ions mainly through phosphate groups whereas purine nucleotides use both phosphate and nucleobase interactions. Similar to this assembly, Liang *et al.* in 2017 described the formation of laccase imitating

nanoenzyme metal organic frameworks (MOF) using GMP and Cu(II) ions.¹⁰⁸ Laccase is an enzyme commonly used for catalyzing the oxidation reactions. These MOFs are efficient replacements for laccase enzyme (Figures 1.24A and 1.24B) with ~2400-fold enhanced activity and better shelf-life.

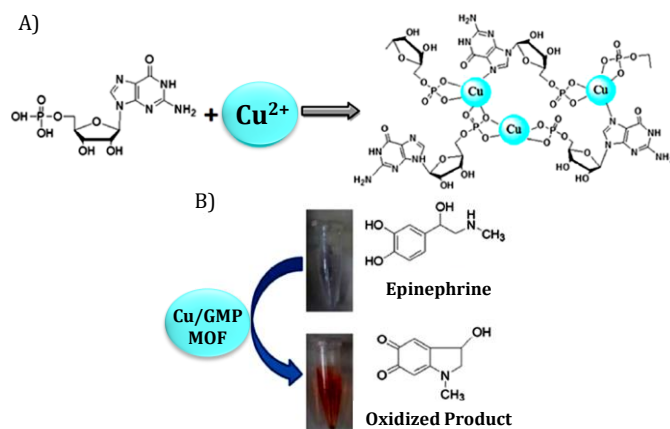


Figure 1.24. A) Schematic depiction of enzyme mimic MOF assembly from GMP and Cu(II) ions, and B) example of an oxidation reaction catalyzed by Cu/GMP MOF (Adapted from reference 108).

Supramolecular organo and hydrogels gels formed from nucleotides using non-covalent hydrogen bonding, π - π stacking and nucleobase-metal interactions are another class of self-assembled architectures, which finds applications mainly in the field of biomedical science.^{21,109} In all such assemblies, small molecules with hydrogen bonding motifs and metal ions are used as the guest molecules to direct the assembly. Hao *et al.* in 2017 demonstrated the Ag (I) and pH modulated enhanced gelation properties of AMP.¹¹⁰ They proposed, π - π stacking and nucleobase-Ag (I) interactions as the main appealing forces for this assembly. Rheology, atomic absorption spectroscopy and morphological analysis were employed to support their proposed mechanism and self-assembly. More interestingly, they have used these gels for the effective encapsulation of biomolecules using the interaction of Ag(I) ions with guest molecules.

1.6.2. Nucleoside directed assemblies

Nucleoside assisted assemblies yet reported mainly include nucleoside templated fluorescent metal nanoclusters (NCs) and supramolecular hydrogels. Metal-nucleobase interactions and canonical or non-canonical hydrogen bonding interactions are the key driving forces in such assemblies. Wang and coworkers prepared fluorescent metal clusters of Au, Ag and Cu.^{21,111} They reported that cytidine and adenosine can template the formation of fluorescent AuNCs and AuAgNCs,²¹ whereas, thymidine, uridine, and guanosine failed to generate fluorescent clusters. Later the same group, reported the formation of nucleoside templated fluorescent water soluble CuNCs using a one-pot synthetic strategy.¹¹¹ Fluorescence quantum yield obtained with different nucleoside templated CuNCs suggested the differential binding affinity of nucleosides towards Cu. In this case, guanosine, cytidine, and adenosine were able to assist the formation of CuNCs, whereas thymidine failed.

Supramolecular hydrogels derived from nucleosides and nucleoside derivatives are another important functional assembly, extensively studied and used in therapeutic applications. Among the various nucleoside assisted supramolecular gels,¹¹² the ones formed from guanosine and guanosine analogues are given more importance because of its G-quartet forming ability. Upon G-quartet formation, they can encapsulate various biomolecules and drug molecules. Recently, Apurba K Das and coworkers synthesized a novel G-quadruplex hydrogel from guanosine, 2-formylphenylboronic acid (2-FPBA) and 4-arm amine-functionalized (PEG) polyethylene glycol (Figure 1.25A).¹¹³ Initially, G-quartet was formed in the presence of K⁺ ions, which results in the formation of hydrogels with G-quadruplex structure.

The imino-borate bond formed during the gelation provides dynamic, stimuli responsive and injectable properties to the gels. The initially formed G-quartet further assembles into hydrogels with G4 structures through polyethylene glycol units. The hydrogels thus formed showed self-healing properties and pH responsive dissolution of gels and the pH dependent drug delivery was demonstrated by incorporating anticancer doxorubicin drug into nano-fibrillar hydrogel assemblies (Figure 1.25B). The slow and steady release of drugs from hydrogels offers the practicability of this assembly for the controlled release of drugs into infected tissues.

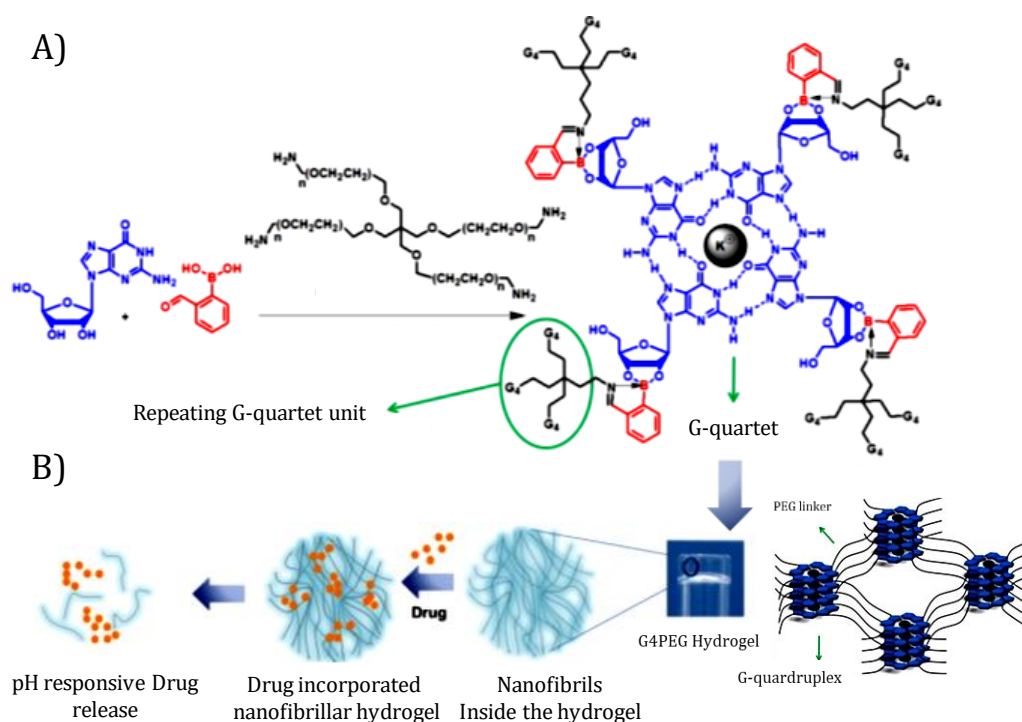


Figure 1.25. A) Schematic illustration of the formation of G-quartet and B) corresponding assembly into hydrogel and mechanism of drug delivery (Adapted from reference 113).

1.6.3. Nucleobase directed assemblies

Compared to nucleotides and nucleosides the use of nucleobases as building materials is less employed. This is because of the limited non-covalent interaction possibilities in nucleobases, thereby limiting its application in biomolecular studies.

But still, there are some reports which describe the use of adenine as a stabilizing agent in the formation of inorganic nanomaterials.²¹ Liu and his coworkers demonstrated the use of purine nucleobases to assemble protected chiral glutamic acid derivatives (protection; Fmoc, N-(9-fluorenylmethoxycarbonyl)) into helical fibers.¹¹⁴ They described that the chiral molecules itself cannot self-assemble, but in presence of achiral nucleobases they self-assembles into hydrogels with helical structures. This chirality was further transferred into achiral fluorescent guest molecules (Figure 1.26A). Opaque gels are formed in the presence of G and translucent gels are formed in the presence of A. However, pyrimidine nucleobases couldn't trigger the formation of helical assemblies. Visualization of assemblies using AFM showed the formation of fibers with 90 nm width and 125 nm helical pitch before the addition of achiral guest molecules (Figure 1.26B). Whereas, after guest incorporation the width and helical pitch increased by 20 and 25 nm, respectively (Figure 1.26C).

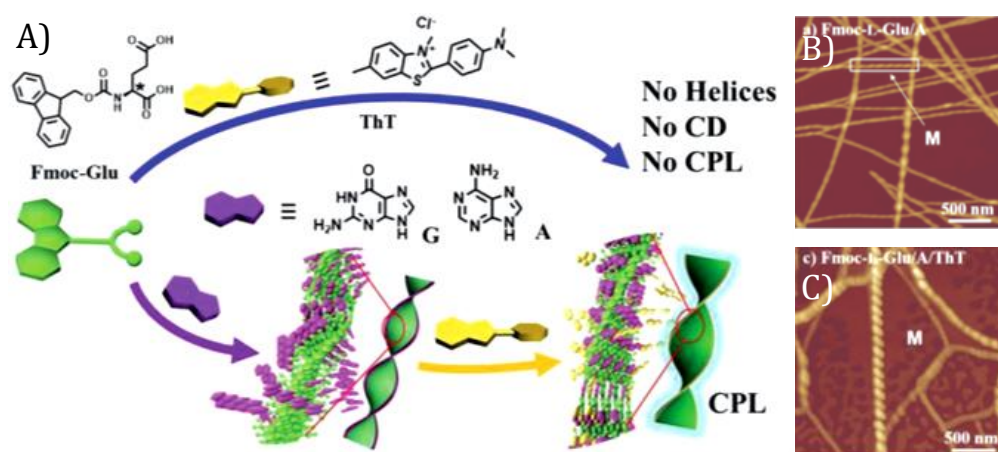


Figure 1.26. A) Schematic representation of purine directed self-assembly of Fmoc-glutamic acid molecules into chiral nanofibers, B) corresponding AFM images of helical fibers before and C) after the addition of fluorescent guest molecules (Adapted from reference 114).

As mentioned in section 1.5.2., supramolecular functional assemblies can also be developed by incorporating nucleobases or nucleobase analogs into organic

molecules.¹¹⁵ Instead of introducing complementary ssDNA, complementary nucleobases or nucleobase analogs were also employed to direct the self-assembly of small molecules and polymers.^{116,117}

1.7. PERSPECTIVES AND CHALLENGES IN SUPRAMOLECULAR DNA ASSEMBLY

Extensive diversities of hierarchically self-assembled functional architectures for specific applications were achieved using DNA, nucleotides, nucleosides, nucleobases, and its analogues as templates. As described in the above sections, the interesting structural programmability, molecular recognition properties, and supramolecular interaction possibilities are the key intriguing features, which makes DNA and its constituents as the distinctive and promising building blocks in the bottom-up self-assembly. These unique properties add extra features like stimuli responsive behavior, information storage and information transfer capacity to the self-assembled materials. The last four decades have witnessed tremendous developments in this field and their potential applications grew substantially across scientific disciplines. Applications include the templated synthesis of small fluorescent nanoparticles to higher ordered self-assembled materials for practice in biomedical, photonic, and nanoelectronic fields.

Even though great progress has been made in the field of bottom-up self-assembly using DNA and its constituents, challenges still remain to be addressed. (i) Modified oligonucleotides are quite costly and the synthesis yields using solid-phase oligonucleotide synthesizer is comparatively very low. As a result, self-assembly also becomes very expensive. In order to address this problem, instead of modifying oligonucleotides covalently, the non-covalent interaction possibilities of DNA need to be explored. Smart design of simple DNA nanostructures with less structural

complexity and improved non-covalent templating properties are required. (ii) The specificity over supramolecular interactions is less compared to covalently modified assemblies. As a result, a combination of assemblies will be formed and at present there are only very few reports on controlled DNA-supramolecular assembly compared to covalently modified DNA assemblies. So, introduction of site-specific groups and careful optimization of non-covalent assembly conditions are required in such supramolecular approaches. (iii) More insights into the random oligonucleotide directed assemblies are required. This can avoid the complexity with sequence specific design and assembly. (iv) Templating action of DNA requires water as medium. As a result, incorporation of several extended π -conjugated organic molecules is difficult to achieve. Though there are some reports using water-organic solvent system for constructing such assemblies, better strategies and conditions need to be introduced. (v) Nucleobase, nucleoside and nucleotide templated self-assemblies are in the initial stages. Therefore, a better understanding about the fundamental aspects and mechanism of such assemblies need to be gathered.

The potential of DNA and nucleobase derivatives in templating functional architectures are not yet completely explored and addressing the above-mentioned challenges are the current focus of research community. Along with this, tailoring the properties of self-assembled materials using DNA and nucleobase derivatives are another area of research currently ongoing in this field. Beyond this, demonstrating the applicability of these self-assembled materials into practical applications is the main task in the current scenario. Application dependent specific alterations and modifications are required in these assembled systems, to transfer the assembly into real-time analysis of targeted drug or DNA delivery in biomedical field and smart devices in nanoelectronics.

1.8. OBJECTIVES OF THE PRESENT INVESTIGATION

A survey of the recent literatures in functional supramolecular DNA assemblies indicate that there exist very few strategies which use the non-covalent interaction possibilities of DNA and DNA-building blocks like nucleobase, nucleoside and single nucleotide derivatives. In this context, we set our objective of the present study as to employ the non-covalent interaction possibilities of DNA, which includes the metal-base interaction, hydrogen bonding and electrostatic interactions to construct functional assemblies. Our first objective was to develop a smart DNA nanostructure which can be used for multifunctional applications. To achieve this objective, we synthesized branched DNA three-way junction structures with a central cytosine loop and used the non-covalent cytosine - Ag⁺ interactions to construct fluorescent DNA biolabels (**Chapter 2**).

The second objective of our study is to employ the non-covalent hydrogen bonding properties of nucleobase and nucleobase analogues to get a control over the assemblies of Tetraphenylethylene (TPE) derivatives, which typically gives rise to the formation of random aggregated structures with aggregation induced emission property. In order to study this objective, we synthesized four diaminotriazine functionalized TPE molecules and their self-assembly properties were investigated using a thymine derivative and oligo-thymidine DNA sequence (**Chapter 3A and 3B**). We further attempted to utilize the non-covalent electrostatic interaction possibility of DNA backbone having negatively charged phosphate group with positively charged TPE-viologen derivatives to achieve DNA condensation (**Chapter 4**). For this study, we synthesized four viologen functionalized TPE derivatives varying in their chemical structure and investigated their interactions with long

duplex calf-thymus DNA (CT-DNA). Detailed insights in to the strategies described in each chapter were achieved by systematic studies using photophysical and morphological techniques. In brief, the present thesis outlines three different strategies using the supramolecular interactions of DNA to attain the initially-mentioned objectives and the results of which are described in detail.

1.9. REFERENCES

- 1) Iqbal, P.; Preece, J. A.; Mendes, P. M.: Nanotechnology: The “Top-Down” and “Bottom-Up” Approaches. *Supramolecular Chemistry: From Molecules to Nanomaterials*. **2012**.
- 2) Seeman, N. C.; Belcher, A. M. Emulating biology: Building nanostructures from the bottom up. *PNAS*. **2002**, *99*, 6451-6455.
- 3) Zhang, S.; Lockshin, C.; Cook, R.; Rich, A. Unusually stable β -sheet formation in an ionic self-complementary oligopeptide. *Biopolymers*. **1994**, *34*, 663-672.
- 4) Zelzer, M.; Ulijn, R. V. Next-generation peptide nanomaterials: molecular networks, interfaces and supramolecular functionality. *Chem. Soc. Rev.* **2010**, *39*, 3351-3357.
- 5) Ikeda, M.; Ochi, R.; Hamachi, I. Supramolecular hydrogel-based protein and chemosensor array. *Lab on a Chip*. **2010**, *10*, 3325-3334.
- 6) Seeman, N. C. Nucleic acid junctions and lattices. *J. Theor. Biol.* **1982**, *99*, 237-247.
- 7) Rothmund, P. W. K. Folding DNA to create nanoscale shapes and patterns. *Nature*. **2006**, *440*, 297-302.
- 8) Aldaye, F. A.; Palmer, A. L.; Sleiman, H. F. Assembling Materials with DNA as the Guide. *Science*. **2008**, *321*, 1795-1799.
- 9) Aldaye, F. A.; Sleiman, H. F. Sequential Self-Assembly of a DNA Hexagon as a Template for the Organization of Gold Nanoparticles. *Angew. Chem. Int. Ed.* **2006**, *45*, 2204-2209.
- 10) Aldaye, F. A.; Sleiman, H. F. Modular Access to Structurally Switchable 3D Discrete DNA Assemblies. *J. Am. Chem. Soc.* **2007**, *129*, 13376-13377.
- 11) Choi, J. S.; Kang, C. W.; Jung, K.; Yang, J. W.; Kim, Y.-G.; Han, H. Synthesis of DNA Triangles with Vertexes of Bis(terpyridine)iron(II) Complexes. *J. Am. Chem. Soc.* **2004**, *126*, 8606-8607.

- 12) Mitra, D.; Di Cesare, N.; Sleiman, H. F. Self-Assembly of Cyclic Metal–DNA Nanostructures using Ruthenium Tris(bipyridine)-Branched Oligonucleotides. *Angew. Chem. Int. Ed.* **2004**, *43*, 5804-5808.
- 13) Garoff, R. A.; Litzinger, E. A.; Connor, R. E.; Fishman, I.; Armitage, B. A. Helical Aggregation of Cyanine Dyes on DNA Templates: Effect of Dye Structure on Formation of Homo- and Heteroaggregates. *Langmuir.* **2002**, *18*, 6330-6337.
- 14) D’Urso, A.; Mammana, A.; Balaz, M.; Holmes, A. E.; Berova, N.; Lauceri, R.; Purrello, R. Interactions of a Tetraanionic Porphyrin with DNA: from a Z-DNA Sensor to a Versatile Supramolecular Device. *J. Am. Chem. Soc.* **2009**, *131*, 2046-2047.
- 15) Janssen, P. G. A.; Meeuwenoord, N.; van der Marel, G.; Jabbari-Farouji, S.; van der Schoot, P.; Surin, M.; Tomović, Ž.; Meijer, E. W.; Schenning, A. P. H. J. ssPNA templated assembly of oligo(p-phenylenevinylene)s. *Chem. Commun.* **2010**, *46*, 109-111.
- 16) Benvin, A. L.; Creeger, Y.; Fisher, G. W.; Ballou, B.; Waggoner, A. S.; Armitage, B. A. Fluorescent DNA Nanotags: Supramolecular Fluorescent Labels Based on Intercalating Dye Arrays Assembled on Nanostructured DNA Templates. *J. Am. Chem. Soc.* **2007**, *129*, 2025-2034.
- 17) Liang, H.; Zhang, Z.; Yuan, Q.; Liu, J. Self-healing metal-coordinated hydrogels using nucleotide ligands. *Chem. Commun.* **2015**, *51*, 15196-15199.
- 18) Adhikari, B.; Shah, A.; Kraatz, H.-B. Self-assembly of guanosine and deoxyguanosine into hydrogels: monovalent cation guided modulation of gelation, morphology and self-healing properties. *J. Mater. Chem. B.* **2014**, *2*, 4802-4810.
- 19) Shimizu, T.; Iwaura, R.; Masuda, M.; Hanada, T.; Yase, K. Internucleobase-Interaction-Directed Self-Assembly of Nanofibers from Homo- and Heteroditopic 1,ω-Nucleobase Bolaamphiphiles. *J. Am. Chem. Soc.* **2001**, *123*, 5947-5955.
- 20) Seeman, N. C.; Sleiman, H. F. DNA nanotechnology. *Nat. Rev. Mater.* **2017**, *3*, 17068.
- 21) Pu, F.; Ren, J.; Qu, X. Nucleobases, nucleosides, and nucleotides: versatile biomolecules for generating functional nanomaterials. *Chem. Soc. Rev.* **2018**, *47*, 1285-1306.
- 22) McCarty, M. Discovering genes are made of DNA. *Nature.* **2003**, *421*, 406-406.
- 23) CRICK, F. H. C. DNA: A Cooperative Discovery. *Ann. N. Y. Acad. Sci.* **1995**, *758*, 198-198.

- 24) Dickerson, R. E.; Drew, H. R.; Conner, B. N.; Kopka, M. L.; Pjura, P. E. Helix geometry and hydration in A-DNA, B-DNA, and Z-DNA. *Cold Spring Harb Symp Quant Biol.* **1983**, *47 Pt 1*, 13-24.
- 25) Dai, X.; Li, Q.; Aldalbahi, A.; Wang, L.; Fan, C.; Liu, X. DNA-Based Fabrication for Nanoelectronics. *Nano Lett.* **2020**, *20*, 5604-5615.
- 26) Silberstein, S.; Dodick, D. Migraine Genetics - A Review: Part I. **2013**.
- 27) Kallenbach, N. R.; Ma, R.-I.; Seeman, N. C. An immobile nucleic acid junction constructed from oligonucleotides. *Nature.* **1983**, *305*, 829-831.
- 28) Chen, J.; Seeman, N. C. Synthesis from DNA of a molecule with the connectivity of a cube. *Nature.* **1991**, *350*, 631-633.
- 29) Fu, T. J.; Seeman, N. C. DNA double-crossover molecules. *Biochemistry.* **1993**, *32*, 3211-3220.
- 30) Zhang, F.; Nangreave, J.; Liu, Y.; Yan, H. Structural DNA Nanotechnology: State of the Art and Future Perspective. *J. Am. Chem. Soc.* **2014**, *136*, 11198-11211.
- 31) Conway, J. W.; Sleiman, H.: 5.19 - Supramolecular DNA Nanotechnology. In *Comprehensive Supramolecular Chemistry II*; Atwood, J. L., Ed.; Elsevier: Oxford, **2017**; pp 441-486.
- 32) Park, S. H.; Yin, P.; Liu, Y.; Reif, J. H.; LaBean, T. H.; Yan, H. Programmable DNA Self-Assemblies for Nanoscale Organization of Ligands and Proteins. *Nano Lett.* **2005**, *5*, 729-733.
- 33) Chhabra, R.; Sharma, J.; Ke, Y.; Liu, Y.; Rinker, S.; Lindsay, S.; Yan, H. Spatially Addressable Multiprotein Nanoarrays Templated by Aptamer-Tagged DNA Nanoarchitectures. *J. Am. Chem. Soc.* **2007**, *129*, 10304-10305.
- 34) He, Y.; Tian, Y.; Ribbe, A. E.; Mao, C. Antibody Nanoarrays with a Pitch of ~20 Nanometers. *J. Am. Chem. Soc.* **2006**, *128*, 12664-12665.
- 35) Zhang, J.; Liu, Y.; Ke, Y.; Yan, H. Periodic Square-Like Gold Nanoparticle Arrays Templated by Self-Assembled 2D DNA Nanogrids on a Surface. *Nano Lett.* **2006**, *6*, 248-251.
- 36) Liu, H.; Chen, Y.; He, Y.; Ribbe, A. E.; Mao, C. Approaching The Limit: Can One DNA Oligonucleotide Assemble into Large Nanostructures? *Angew. Chem. Int. Ed.* **2006**, *45*, 1942-1945.
- 37) Tian, C.; Zhang, C.; Li, X.; Hao, C.; Ye, S.; Mao, C. Approaching the Limit: Can One DNA Strand Assemble into Defined Nanostructures? *Langmuir.* **2014**, *30*, 5859-5862.

-
- 38) He, Y.; Ye, T.; Su, M.; Zhang, C.; Ribbe, A. E.; Jiang, W.; Mao, C. Hierarchical self-assembly of DNA into symmetric supramolecular polyhedra. *Nature*. **2008**, *452*, 198-201.
- 39) Zheng, J.; Birktoft, J. J.; Chen, Y.; Wang, T.; Sha, R.; Constantinou, P. E.; Ginell, S. L.; Mao, C.; Seeman, N. C. From molecular to macroscopic via the rational design of a self-assembled 3D DNA crystal. *Nature*. **2009**, *461*, 74-77.
- 40) McLaughlin, C. K.; Hamblin, G. D.; Hänni, K. D.; Conway, J. W.; Nayak, M. K.; Carneiro, K. M. M.; Bazzi, H. S.; Sleiman, H. F. Three-Dimensional Organization of Block Copolymers on "DNA-Minimal" Scaffolds. *J. Am. Chem. Soc.* **2012**, *134*, 4280-4286.
- 41) Jiang, S.; Hong, F.; Hu, H.; Yan, H.; Liu, Y. Understanding the Elementary Steps in DNA Tile-Based Self-Assembly. *ACS Nano*. **2017**, *11*, 9370-9381.
- 42) Ke, Y.; Lindsay, S.; Chang, Y.; Liu, Y.; Yan, H. Self-assembled water-soluble nucleic acid probe tiles for label-free RNA hybridization assays. *Science*. **2008**, *319*, 180-183.
- 43) Andersen, E. S.; Dong, M.; Nielsen, M. M.; Jahn, K.; Subramani, R.; Mamdouh, W.; Golas, M. M.; Sander, B.; Stark, H.; Oliveira, C. L.; Pedersen, J. S.; Birkedal, V.; Besenbacher, F.; Gothelf, K. V.; Kjems, J. Self-assembly of a nanoscale DNA box with a controllable lid. *Nature*. **2009**, *459*, 73-76.
- 44) Kuzuya, A.; Komiyama, M. Design and construction of a box-shaped 3D-DNA origami. *Chem Commun*. **2009**, 4182-4184.
- 45) Endo, M.; Hidaka, K.; Kato, T.; Namba, K.; Sugiyama, H. DNA prism structures constructed by folding of multiple rectangular arms. *J. Am. Chem. Soc.* **2009**, *131*, 15570-15571.
- 46) Jun, H.; Zhang, F.; Shepherd, T.; Ratanalert, S.; Qi, X.; Yan, H.; Bathe, M. Autonomously designed free-form 2D DNA origami. *Sci. Adv.* **2019**, *5*, eaav0655.
- 47) Douglas, S. M.; Dietz, H.; Liedl, T.; Högberg, B.; Graf, F.; Shih, W. M. Self-assembly of DNA into nanoscale three-dimensional shapes. *Nature*. **2009**, *459*, 414-418.
- 48) Han, D.; Pal, S.; Nangreave, J.; Deng, Z.; Liu, Y.; Yan, H. DNA Origami with Complex Curvatures in Three-Dimensional Space. *Science*. **2011**, *332*, 342-346.
- 49) Li, Z.; Wang, L.; Yan, H.; Liu, Y. Effect of DNA Hairpin Loops on the Twist of Planar DNA Origami Tiles. *Langmuir*. **2012**, *28*, 1959-1965.
- 50) Krishnan, Y.; Simmel, F. C. Nucleic Acid Based Molecular Devices. *Angew. Chem. Int. Ed.* **2011**, *50*, 3124-3156.

- 51) Gu, H.; Chao, J.; Xiao, S.-J.; Seeman, N. C. A proximity-based programmable DNA nanoscale assembly line. *Nature*. **2010**, *465*, 202-205.
- 52) He, Y.; Liu, D. R. Autonomous multistep organic synthesis in a single isothermal solution mediated by a DNA walker. *Nat Nanotechnol*. **2010**, *5*, 778-782.
- 53) Liber, M.; Tomov, T. E.; Tsukanov, R.; Berger, Y.; Nir, E. A Bipedal DNA Motor that Travels Back and Forth between Two DNA Origami Tiles. *Small*. **2015**, *11*, 568-575.
- 54) Zhou, C.; Duan, X.; Liu, N. A plasmonic nanorod that walks on DNA origami. *Nat Commun*. **2015**, *6*, 8102.
- 55) Yang, X.; Tang, Y.; Mason, S. D.; Chen, J.; Li, F. Enzyme-Powered Three-Dimensional DNA Nanomachine for DNA Walking, Payload Release, and Biosensing. *ACS Nano*. **2016**, *10*, 2324-2330.
- 56) Shi, J.; Bergstrom, D. E. Assembly of Novel DNA Cycles with Rigid Tetrahedral Linkers. *Angew. Chem. Int. Ed*. **1997**, *36*, 111-113.
- 57) Aldaye, F. A.; Sleiman, H. F. Sequential Self-Assembly of a DNA Hexagon as a Template for the Organization of Gold Nanoparticles. *Angew. Chem. Int. Ed*. **2006**, *45*, 2204-2209.
- 58) Aldaye, F. A.; Sleiman, H. F. Guest-Mediated Access to a Single DNA Nanostructure from a Library of Multiple Assemblies. *J. Am. Chem. Soc*. **2007**, *129*, 10070-10071.
- 59) Serpell, C. J.; Edwardson, T. G. W.; Chidchob, P.; Carneiro, K. M. M.; Sleiman, H. F. Precision Polymers and 3D DNA Nanostructures: Emergent Assemblies from New Parameter Space. *J. Am. Chem. Soc*. **2014**, *136*, 15767-15774.
- 60) Lo, P. K.; Karam, P.; Aldaye, F. A.; McLaughlin, C. K.; Hamblin, G. D.; Cosa, G.; Sleiman, H. F. Loading and selective release of cargo in DNA nanotubes with longitudinal variation. *Nat. Chem*. **2010**, *2*, 319-328.
- 61) Edwardson, T. G. W.; Lau, K. L.; Bousmail, D.; Serpell, C. J.; Sleiman, H. F. Transfer of molecular recognition information from DNA nanostructures to gold nanoparticles. *Nat. Chem*. **2016**, *8*, 162.
- 62) Mitra, D.; Di Cesare, N.; Sleiman, H. F. Self-Assembly of Cyclic Metal-DNA Nanostructures using Ruthenium Tris(bipyridine)-Branched Oligonucleotides. *Angew. Chem. Int. Ed*. **2004**, *43*, 5804-5808.
- 63) Tanaka, K.; Tengeiji, A.; Kato, T.; Toyama, N.; Shionoya, M. A Discrete Self-Assembled Metal Array in Artificial DNA. *Science*. **2003**, *299*, 1212-1213.

-
- 64) Yang, H.; Rys, A. Z.; McLaughlin, C. K.; Sleiman, H. F. Templated Ligand Environments for the Selective Incorporation of Different Metals into DNA. *Angew. Chem. Int. Ed.* **2009**, *48*, 9919-9923.
- 65) Ding, K.; Alemdaroglu, F. E.; Börsch, M.; Berger, R.; Herrmann, A. Engineering the Structural Properties of DNA Block Copolymer Micelles by Molecular Recognition. *Angew. Chem. Int. Ed.* **2007**, *46*, 1172-1175.
- 66) Li, Z.; Zhang, Y.; Fullhart, P.; Mirkin, C. A. Reversible and Chemically Programmable Micelle Assembly with DNA Block-Copolymer Amphiphiles. *Nano Lett.* **2004**, *4*, 1055-1058.
- 67) Alemdaroglu, F. E.; Ding, K.; Berger, R.; Herrmann, A. DNA-templated synthesis in three dimensions: Introducing a micellar scaffold for organic reactions. *Angew. Chem. Int. Ed. Engl.* **2006**, *45*, 4206-4210.
- 68) Albert, S. K.; Thelu, H. V. P.; Golla, M.; Krishnan, N.; Chaudhary, S.; Varghese, R. Self-Assembly of DNA-Oligo(p-phenylene-ethynylene) Hybrid Amphiphiles into Surface-Engineered Vesicles with Enhanced Emission. *Angew. Chem. Int. Ed.* **2014**, *53*, 8352-8357.
- 69) Albert, S. K.; Sivakumar, I.; Golla, M.; Thelu, H. V. P.; Krishnan, N.; K. L, J. L.; Ashish; Varghese, R. DNA-Decorated Two-Dimensional Crystalline Nanosheets. *J. Am. Chem. Soc.* **2017**, *139*, 17799-17802.
- 70) Golla, M.; Albert, S. K.; Atchimaidu, S.; Perumal, D.; Krishnan, N.; Varghese, R. DNA-Decorated, Helically Twisted Nanoribbons: A Scaffold for the Fabrication of One-Dimensional, Chiral, Plasmonic Nanostructures. *Angew. Chem. Int. Ed.* **2019**, *58*, 3865-3869.
- 71) Winiger, C. B.; Li, S.; Kumar, G. R.; Langenegger, S. M.; Häner, R. Long-Distance Electronic Energy Transfer in Light-Harvesting Supramolecular Polymers. *Angew. Chem. Int. Ed.* **2014**, *53*, 13609-13613.
- 72) Ensslen, P.; Brandl, F.; Sezi, S.; Varghese, R.; Kutta, R.-J.; Dick, B.; Wagenknecht, H.-A. DNA-Based Oligochromophores as Light-Harvesting Systems. *Chem. Eur. J.* **2015**, *21*, 9349-9354.
- 73) Kownacki, M.; Langenegger, S. M.; Liu, S.-X.; Häner, R. Integrating DNA Photonic Wires into Light-Harvesting Supramolecular Polymers. *Angew. Chem. Int. Ed.* **2019**, *58*, 751-755.
- 74) Gačanin, J.; Synatschke, C. V.; Weil, T. Biomedical Applications of DNA-Based Hydrogels. *Adv. Funct. Mater.* **2020**, *30*, 1906253.

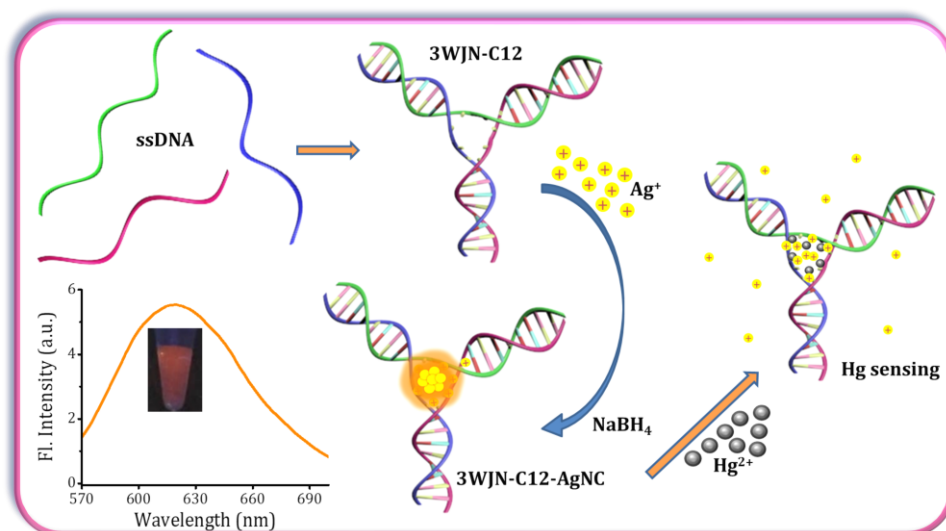
- 75) Li, J.; Mo, L.; Lu, C.-H.; Fu, T.; Yang, H.-H.; Tan, W. Functional nucleic acid-based hydrogels for bioanalytical and biomedical applications. *Chem. Soc. Rev.* **2016**, *45*, 1410-1431.
- 76) Liao, W.-C.; Lilienthal, S.; Kahn, J. S.; Riutin, M.; Sohn, Y. S.; Nechushtai, R.; Willner, I. pH- and ligand-induced release of loads from DNA-acrylamide hydrogel microcapsules. *Chem Sci.* **2017**, *8*, 3362-3373.
- 77) Narayanaswamy, N.; Suresh, G.; Priyakumar, U. D.; Govindaraju, T. Double zipper helical assembly of deoxyoligonucleotides: mutual templating and chiral imprinting to form hybrid DNA ensembles. *Chem. Commun.* **2015**, *51*, 5493-5496.
- 78) Iwaura, R.; Ohnishi-Kameyama, M.; Iizawa, T. Construction of helical J-aggregates self-assembled from a thymidylic acid appended anthracene dye and DNA as a template. *Chemistry (Weinheim an der Bergstrasse, Germany)*. **2009**, *15*, 3729-3735.
- 79) Iwaura, R.; Hoeben, F. J. M.; Masuda, M.; Schenning, A. P. H. J.; Meijer, E. W.; Shimizu, T. Molecular-Level Helical Stack of a Nucleotide-Appended Oligo(p-phenylenevinylene) Directed by Supramolecular Self-Assembly with a Complementary Oligonucleotide as a Template. *J. Am. Chem. Soc.* **2006**, *128*, 13298-13304.
- 80) Surin, M.; Janssen, P. G. A.; Lazzaroni, R.; Leclère, P.; Meijer, E. W.; Schenning, A. P. H. J. Supramolecular Organization of ssDNA-Templated π -Conjugated Oligomers via Hydrogen Bonding. *Adv. Mater.* **2009**, *21*, 1126-1130.
- 81) Yamane, T.; Davidson, N. On the Complexing of Desoxyribonucleic Acid (DNA) by Mercuric Ion¹. *J. Am. Chem. Soc.* **1961**, *83*, 2599-2607.
- 82) New, S. Y.; Lee, S. T.; Su, X. D. DNA-templated silver nanoclusters: structural correlation and fluorescence modulation. *Nanoscale*. **2016**, *8*, 17729-17746.
- 83) Ono, A.; Togashi, H. Highly Selective Oligonucleotide-Based Sensor for Mercury(II) in Aqueous Solutions. *Angew. Chem. Int. Ed.* **2004**, *43*, 4300-4302.
- 84) Xu, H.; Zhu, X.; Ye, H.; Yu, L.; Liu, X.; Chen, G. A simple "molecular beacon"-based fluorescent sensing strategy for sensitive and selective detection of mercury (ii). *Chem. Commun.* **2011**, *47*, 12158-12160.
- 85) Pandeewar, M.; Senanayak, S. P.; Govindaraju, T. Nanoarchitectonics of Small Molecule and DNA for Ultrasensitive Detection of Mercury. *ACS Appl. Mater. Interfaces*. **2016**, *8*, 30362-30371.

-
- 86) Petty, J. T.; Zheng, J.; Hud, N. V.; Dickson, R. M. DNA-Templated Ag Nanocluster Formation. *J. Am. Chem. Soc.* **2004**, *126*, 5207-5212.
- 87) Tao, Y.; Lin, Y. H.; Huang, Z. Z.; Ren, J. S.; Qu, X. G. DNA-templated silver nanoclusters-graphene oxide nanohybrid materials: a platform for label-free and sensitive fluorescence turn-on detection of multiple nucleic acid targets. *Analyst.* **2012**, *137*, 2588-2592.
- 88) Zhu, J.; Zhang, L.; Teng, Y.; Lou, B.; Jia, X.; Gu, X.; Wang, E. G-quadruplex enhanced fluorescence of DNA-silver nanoclusters and their application in bioimaging. *Nanoscale.* **2015**, *7*, 13224-13229.
- 89) Shionoya, M.; Kimura, E.; Shiro, M. A new ternary zinc(II) complex with [12]aneN4 (=1,4,7,10-tetraazacyclododecane) and AZT (=3'-azido-3'-deoxythymidine). Highly selective recognition of thymidine and its related nucleosides by a zinc(II) macrocyclic tetraamine complex with novel complementary associations. *J. Am. Chem. Soc.* **1993**, *115*, 6730-6737.
- 90) Chen, J. Y.; Ji, X. H.; Tinnefeld, P.; He, Z. K. Multifunctional Dumbbell-Shaped DNA-Templated Selective Formation of Fluorescent Silver Nanoclusters or Copper Nanoparticles for Sensitive Detection of Biomolecules. *ACS Appl. Mater. Interfaces.* **2016**, *8*, 1786-1794.
- 91) Schleif, R. DNA binding by proteins. *Science.* **1988**, *241*, 1182-1187.
- 92) Nielsen, P. E. Peptide nucleic acids as therapeutic agents. *Curr. Opin. Struct. Biol.* **1999**, *9*, 353-357.
- 93) Nguyen, T.; Brewer, A.; Stulz, E. Duplex Stabilization and Energy Transfer in Zipper Porphyrin-DNA. *Angew. Chem. Int. Ed.* **2009**, *48*, 1974-1977.
- 94) Mayer-Enthart, E.; Wagner, C.; Barbaric, J.; Wagenknecht, H.-A. Helical self-assembled chromophore clusters based on DNA-like architecture. *Tetrahedron.* **2007**, *63*, 3434-3439.
- 95) Kim, S. K.; Nordén, B. Methyl green. *FEBS Letters.* **1993**, *315*, 61-64.
- 96) Oleksi, A.; Blanco, A. G.; Boer, R.; Usón, I.; Aymamí, J.; Rodger, A.; Hannon, M. J.; Coll, M. Molecular Recognition of a Three-Way DNA Junction by a Metallosupramolecular Helicate. *Angew. Chem. Int. Ed.* **2006**, *45*, 1227-1231.
- 97) Molphy, Z.; Montagner, D.; Bhat, S. S.; Slator, C.; Long, C.; Erxleben, A.; Kellett, A. A phosphate-targeted dinuclear Cu(II) complex combining major groove binding and oxidative DNA cleavage. *Nucleic Acids Res.* **2018**, *46*, 9918-9931.

- 98) Paul, A.; Bhattacharya, S. Chemistry and biology of DNA-binding small molecules. *Curr. Sci.* **2012**, *102*, 212-231.
- 99) Hannah, K. C.; Armitage, B. A. DNA-Templated Assembly of Helical Cyanine Dye Aggregates: A Supramolecular Chain Polymerization. *Acc. Chem. Res.* **2004**, *37*, 845-853.
- 100) Vittala, S. K.; Saraswathi, S. K.; Joseph, J. Fullerene Cluster Assisted Self-Assembly of Short DNA Strands into Semiconducting Nanowires. *Chem. Eur. J.* **2017**, *23*, 15759-15765.
- 101) Vittala, S. K.; Saraswathi, S. K.; Ramesan, A. B.; Joseph, J. Nanosheets and 2-D Networks by Mutually Assisted Self-Assembly of Fullerene Clusters and DNA Three-way Junctions. *Nanoscale Adv.* **2019**, *1*, 4158-4165.
- 102) Ozhalici-Unal, H.; Armitage, B. A. Fluorescent DNA nanotags based on a self-assembled DNA tetrahedron. *ACS Nano.* **2009**, *3*, 425-433.
- 103) Li, H.; Bazan, G. C. Conjugated Oligoelectrolyte/ssDNA Aggregates: Self-Assembled Multicomponent Chromophores for Protein Discrimination. *Adv. Mater.* **2009**, *21*, 964-967.
- 104) Kim, Y.; Li, H.; He, Y.; Chen, X.; Ma, X.; Lee, M. Collective helicity switching of a DNA-coat assembly. *Nat Nanotechnol.* **2017**, *12*, 551-556.
- 105) Kumar, M.; Brocorens, P.; Tonnelé, C.; Beljonne, D.; Surin, M.; George, S. J. A dynamic supramolecular polymer with stimuli-responsive handedness for in situ probing of enzymatic ATP hydrolysis. *Nat Commun.* **2014**, *5*, 5793.
- 106) Kumar, M.; Reddy, M. D.; Mishra, A.; George, S. J. The molecular recognition controlled stereomutation cycle in a dynamic helical assembly. *Org. Biomol. Chem.* **2015**, *13*, 9938-9942.
- 107) Lopez, A.; Liu, J. Self-Assembly of Nucleobase, Nucleoside and Nucleotide Coordination Polymers: From Synthesis to Applications. *ChemNanoMat.* **2017**, *3*, 670-684.
- 108) Liang, H.; Lin, F.; Zhang, Z.; Liu, B.; Jiang, S.; Yuan, Q.; Liu, J. Multicopper Laccase Mimicking Nanozymes with Nucleotides as Ligands. *ACS Appl. Mater. Interfaces.* **2017**, *9*, 1352-1360.
- 109) Peters, G. M.; Davis, J. T. Supramolecular gels made from nucleobase, nucleoside and nucleotide analogs. *Chem. Soc. Rev.* **2016**, *45*, 3188-3206.

-
- 110) Hu, Y.; Xie, D.; Wu, Y.; Lin, N.; Song, A.; Hao, J. Hydrogels Based on Ag⁺-Modulated Assembly of 5'-Adenosine Monophosphate for Enriching Biomolecules. *Chem. Eur. J.* **2017**, *23*, 15721-15728.
- 111) Wang, Y.; Chen, T.; Zhuang, Q.; Ni, Y. One-Pot Aqueous Synthesis of Nucleoside-Templated Fluorescent Copper Nanoclusters and Their Application for Discrimination of Nucleosides. *ACS Appl. Mater. Interfaces.* **2017**, *9*, 32135-32141.
- 112) Angelerou, M. G. F.; Frederix, P. W. J. M.; Wallace, M.; Yang, B.; Rodger, A.; Adams, D. J.; Marlow, M.; Zelzer, M. Supramolecular Nucleoside-Based Gel: Molecular Dynamics Simulation and Characterization of Its Nanoarchitecture and Self-Assembly Mechanism. *Langmuir.* **2018**, *34*, 6912-6921.
- 113) Biswas, A.; Ghosh, T.; Gavel, P. K.; Das, A. K. PEG Functionalized Stimuli Responsive Self-Healable Injectable Dynamic Imino-boronate G-quadruplex Hydrogel for the Delivery of Doxorubicin. *ACS Appl. Bio. Materials.* **2020**, *3*, 1052-1060.
- 114) Deng, M.; Zhang, L.; Jiang, Y.; Liu, M. Role of Achiral Nucleobases in Multicomponent Chiral Self-Assembly: Purine-Triggered Helix and Chirality Transfer. *Angew. Chem. Int. Ed.* **2016**, *55*, 15062-15066.
- 115) Adhikari, B.; Lin, X.; Yamauchi, M.; Ouchi, H.; Aratsu, K.; Yagai, S. Hydrogen-bonded rosettes comprising π -conjugated systems as building blocks for functional one-dimensional assemblies. *Chem. Commun.* **2017**, *53*, 9663-9683.
- 116) Roy, B.; Bairi, P.; Nandi, A. K. Supramolecular assembly of melamine and its derivatives: nanostructures to functional materials. *Rsc Adv.* **2014**, *4*, 1708-1734.
- 117) Wang, D.; Tong, G.; Dong, R.; Zhou, Y.; Shen, J.; Zhu, X. Self-assembly of supramolecularly engineered polymers and their biomedical applications. *Chem. Commun.* **2014**, *50*, 11994-12017.

DESIGN AND SYNTHESIS OF DNA THREE-WAY JUNCTION TEMPLATED FLUORESCENT SILVER NANOCCLUSERS: SEQUENCE PROGRAMMING AND METAL ION SENSING



2.1. ABSTRACT

Fluorescent metal nanoclusters emerged as promising candidates for sensor and imaging applications due to their excellent photostability and tunable optical properties. Among various metal nanoclusters, fluorescent silver nanoclusters (AgNCs) synthesized on DNA templates are particularly attractive due to their inherent bioconjugation onto DNA which opens up immense possibilities for applications in diagnosis and imaging. DNA stabilized, fluorescent silver nanoclusters are reported to exhibit sequence dependent morphological and emission properties and hence the photophysics of these AgNCs could be easily modified by changing the sequence structure of DNA template. Typically, certain nucleic acid sequences such as cytosine rich regions show stabilization of AgNCs and hence are useful as fluorescent tags which

are incorporated in DNA mainframe on the edges as overhangs or as loops on the duplex strands. In this Chapter, we describe a new design strategy for sequence programmed DNA three-way junctions (DNA-3WJs), comprising of unhybridized cytosine nucleobases in the 3WJ-center, capable of binding to silver ions and stabilizing the AgNCs. The formation of AgNCs in these DNA-3WJs were confirmed by various spectroscopic and microscopic techniques. **3WJ20-C12** comprising of 12 cytosine bases in the center of the DNA-3WJ form fluorescent nanoclusters with an emission maximum around 630 nm and 12% fluorescence quantum yield. Control DNA-3WJs with six cytosine bases in the center (**3WJ20-C6**) and ones without cytosine bases (**3WJ20**) failed to form fluorescent AgNCs confirming the requirement of central unhybridized cytosine bases for the stabilization of the nanoclusters. Further, the duplex arms of DNA-3WJs were shown to influence the fluorescent properties of AgNCs by varying the size and stability of the cytosine-loop structure of DNA-3WJs. Metal ion interaction studies show the selectivity of the **3WJ20-C12/AgNCs** towards Hg^{2+} with sensitivity in the nanomolar range.

2.2. INTRODUCTION

Fluorescent metal nanoclusters comprising of 2-20 metal atoms in the sub-nanometer size are emerging competitors for typical fluorophores like organic dyes, quantum dots and fluorescent proteins.^{1,2} The smaller size and better photostability of metal nanoclusters makes them superior over the conventional fluorophores used for biological applications.³ The size of metals is the key factor which governs their optical and electronic properties (Figure 2.1). Bulk metals with higher size in the micro meter range possess high electrical conductivity and reasonable optical reflectance, ascribed to their freely moving electrons in the overlapped valence band

and conduction band. On the other hand, intense color of nanometer sized metal nanoparticles is a result of surface plasmon resonance. Distinct from the aforementioned metals, metal nanoclusters because of its small size in sub-nanometer scale have discrete electronic energy levels like molecules and displays distinct optical spectra, strong fluorescence emission and well separated highest occupied molecular orbital - lowest unoccupied molecular orbital (HOMO-LUMO).⁴

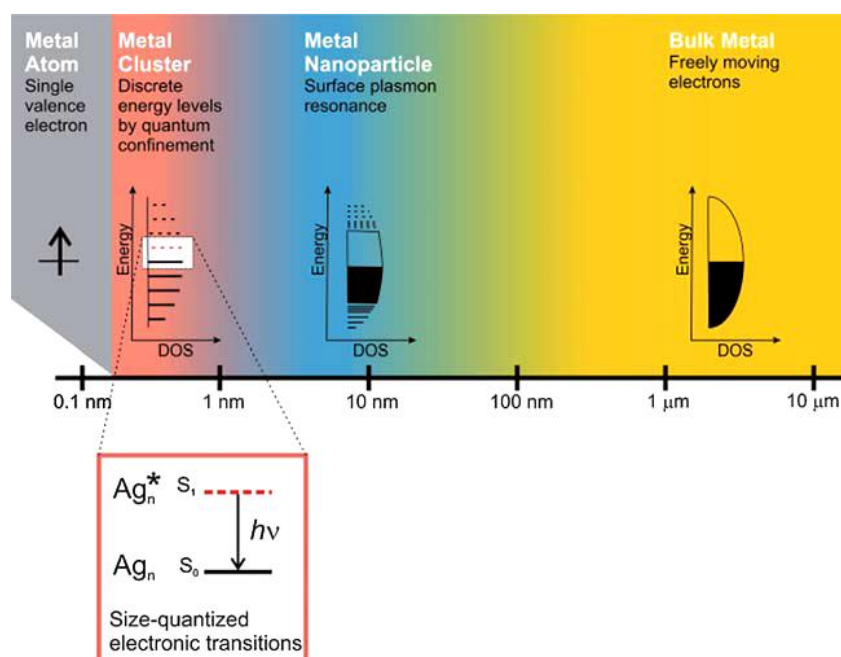


Figure 2.1. Energy level diagrams of metal atom, metal nanocluster, metal nanoparticle and bulk metal (Adapted from reference 4).

Among the various metal nanoclusters (Au, Ag, Pt, Cu etc), silver nanoclusters (AgNCs) possess low toxicity, superior water solubility, easy synthesis and suitable photophysical properties, which make them useful candidates for various applications in optoelectronics, catalysis, bioimaging and biosensing.⁵⁻⁷ However, stabilization of these metal nanoclusters, particularly AgNCs from oxidation and aggregation to larger nanoparticles is a key challenge in this field. The reaction conditions like temperature, stabilizing agent, reducing conditions and the molar ratios of Ag, stabilizer, reducing agent etc play crucial roles in the synthesis of

AgNCs. Previously, various stabilizing agents like small organic molecules, dendrimers, inorganic matrices, synthetic polymers, biopolymers, DNA etc were used in the construction of metal nanoclusters.^{8,9} Even though, there are many reports on the synthesis of AgNCs, it remains difficult to generalize the reaction conditions, since the same reaction conditions could also lead to the formation of nanoparticles or aggregates.

Unique properties of AgNCs, including high fluorescence quantum yields and their cluster stability also depend on the stabilizing agent used during the synthesis of AgNCs. The largest value of fluorescence quantum yield for AgNCs (64%) was reported in presence of DNA as stabilizing agent,¹⁰ whereas, stable AgNCs were formed in presence of polyacrylates.¹¹ Since the pioneering work by Dickson and coworkers on the fluorescence emission of cytosine rich DNA stabilized AgNCs,⁹ numerous DNA stabilized AgNCs with tunable fluorescence emission were developed using single strand oligonucleotides as templates.¹²

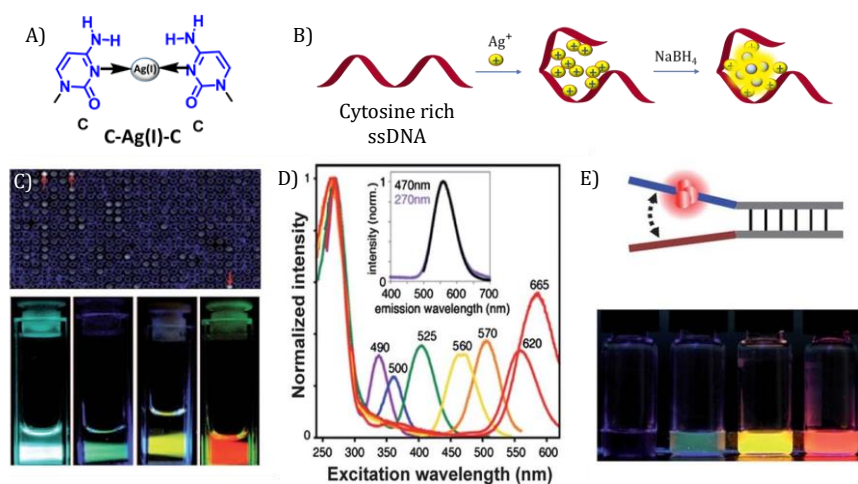


Figure 2.2. A) The specific cytosine-Ag⁺ interaction and B) cartoon representation of the AgNC synthesis using cytosine rich ssDNA sequence. C) Sequence dependent changes in the fluorescence emission of AgNCs, D) a common excitation (270 nm) dependent emission spectra of different ssDNA/AgNCs and E) near-by sequence dependent changes in the fluorescence emission (Adapted from reference 13 and 14).

Here, the specific non-covalent interaction of cytosine nucleobase towards Ag^+ ion is employed to stabilize AgNCs inside the ssDNA sequences upon reduction (Figures 2.2A & 2.2B). Important benefits of using DNA as a template for the synthesis of AgNC are: (i) tunability of fluorescence emission from visible to NIR region by programming the ssDNA sequences,¹³ (ii) single source excitation of all the cluster species present in the sample and (iii) the fluorescence of cluster can be color tuned and turned on or off by changing the nearby DNA sequences (Figures 2.2C-E).^{14,15} These important features and straightforward synthesis of DNA-AgNCs have stimulated the use of silver nanoclusters as fluorophores in bioimaging, sensing of DNA, RNA, proteins, metal ions, small molecules and cancer cells.¹⁶⁻²¹ In addition, several reports have demonstrated the structural and sequence dependence of DNA on the origin and fluorescence modulation of AgNCs.²²⁻²⁷

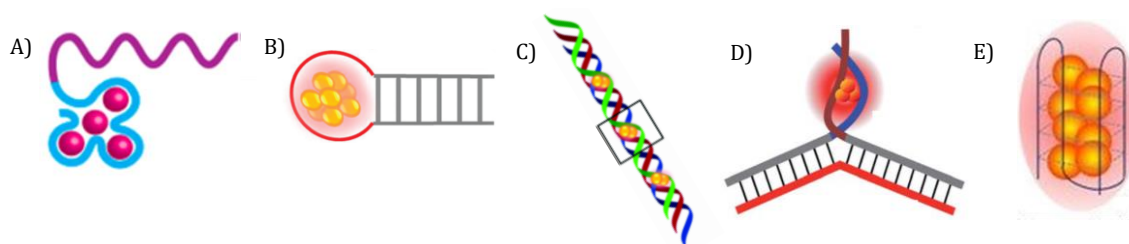


Figure 2.3. AgNCs stabilized inside different DNA nanostructures, A) ssDNA, B) Hairpin loop, C) Triplex, D) overhangs at junctions and E) quadruplex (Adapted from reference 27).

The property of programmable DNA hybridization allows the construction of various AgNCs templated by secondary DNA structures (Figure 2.3) such as duplex,¹⁵ triplex,²⁸ hairpin loop,²⁹ G-quadruplex,³⁰ i-motifs,³¹ branched DNA junctions etc.³² Among these secondary structures, branched DNA junction templated AgNCs have been used for multifunctional applications.^{27,33} For example, Libing Zhang and coworkers developed a target prompted recognition technique for the detection of DNA, thrombin and ATP by engineering the DNA-3WJs with

multifunctional catalytic and fluorescent properties.³² Itamar Willner *et al.* demonstrated the formation of fluorescent DNA hydrogels by the successful incorporation of AgNCs in the sequence-specific hair-pin loops of the Y-shaped DNA units with controlled fluorescence properties (Figure 2.4A).³³

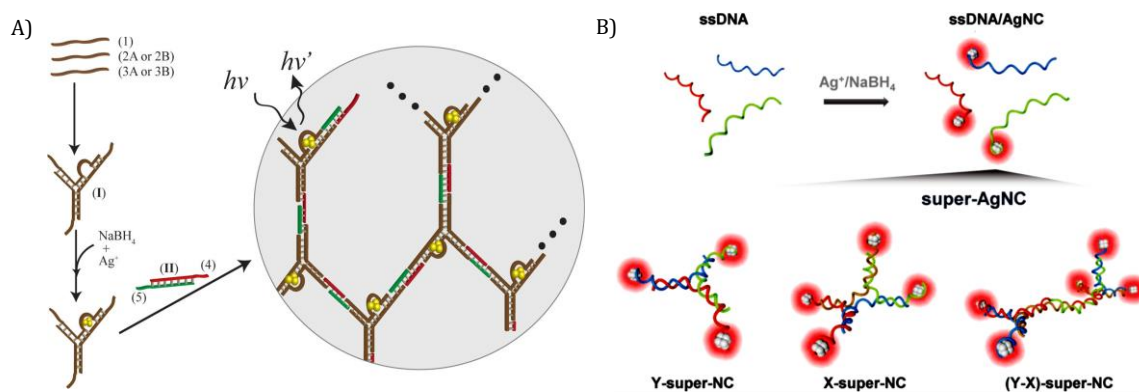


Figure 2.4. AgNCs stabilized inside the A) hairpin loops and B) overhangs of DNA-3WJ structures (Adapted from reference 33 and 34).

Later in 2018, Lu Yang *et al.* reported super AgNCs in the overhangs of X, Y and X-Y type branched DNA structures with higher antibacterial activity and excellent biocompatibility in 293T, SMCs and GLC-82 cells (Figure 2.4B).³⁴ In this line and using the self-assembly tools, recently from our group we have shown the formation of 2D-nanonetworks by the mutually assisted self-assembly of fullerene nanoclusters (**F-An**) and DNA-3WJs with AgNCs stabilized in the cytosine rich overhang (Figure 2.5).³⁵ A 40% enhancement in the fluorescence intensity of AgNC was obtained as a result of the enhanced stability of AgNCs in the DNA-fullerene assemblies.

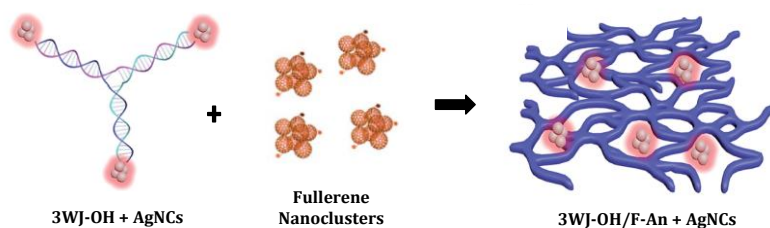


Figure 2.5. Pictorial representation of the formation of AgNCs stabilized in the 2D nanonetworks of 3WJ-OH/F-An assemblies (Adapted from reference 35).

The aforementioned reports highlight the stabilization of AgNCs either on one of the duplex strands of DNA-3WJs with a single strand overhang or by creating hairpin loops on the duplex strand. The overhang or hair pin modifications in the duplex arms, used in these strategies impose structural restrictions in building extended multifunctional sensor conjugates and hence limit their practical applications in biological sensing and imaging. Herein, we describe the construction of a DNA-3WJ for templating AgNCs, without modification at the duplex branches. Instead, a cytosine loop has been inserted at the center of DNA-3WJ using mismatch single strand DNA sequences. The DNA-3WJs with central cytosine loops were shown to act as efficient templates, which stabilize the formation of AgNCs. Multiple DNA-3WJ structures were used to demonstrate the sequence dependence of the central loop region and duplex arms on the formation and stabilization of AgNCs. Further, the fluorescence of the synthesized **3WJ20C12/AgNCs** was used to probe Hg²⁺ ions in aqueous solutions in sub-nanomolar concentrations.

2.3. RESULTS AND DISCUSSION

2.3.1. Synthesis of short ssDNA sequences

Short ssDNA sequences used in this work (Table 2.1 in the experimental section) were synthesized by solid phase oligonucleotide synthesis using an automated DNA synthesizer, which follows the typical phosphoramidite chemistry to synthesize ssDNA sequences. Each addition of single nucleotide follows a cycle of four chemical reactions (Figure 2.6), termed as de-tritylation, coupling, capping and oxidation. After the required ssDNA sequence was synthesized, the white powdered sample was cleaved off from the solid support and deprotected the protecting groups in nucleobases using 30% ammonium hydroxide solution. The samples were

then purified using reverse phase - high performance liquid chromatography (RP-HPLC), desalted and concentrations were calculated using the known ϵ values of nucleobases at 260 nm.

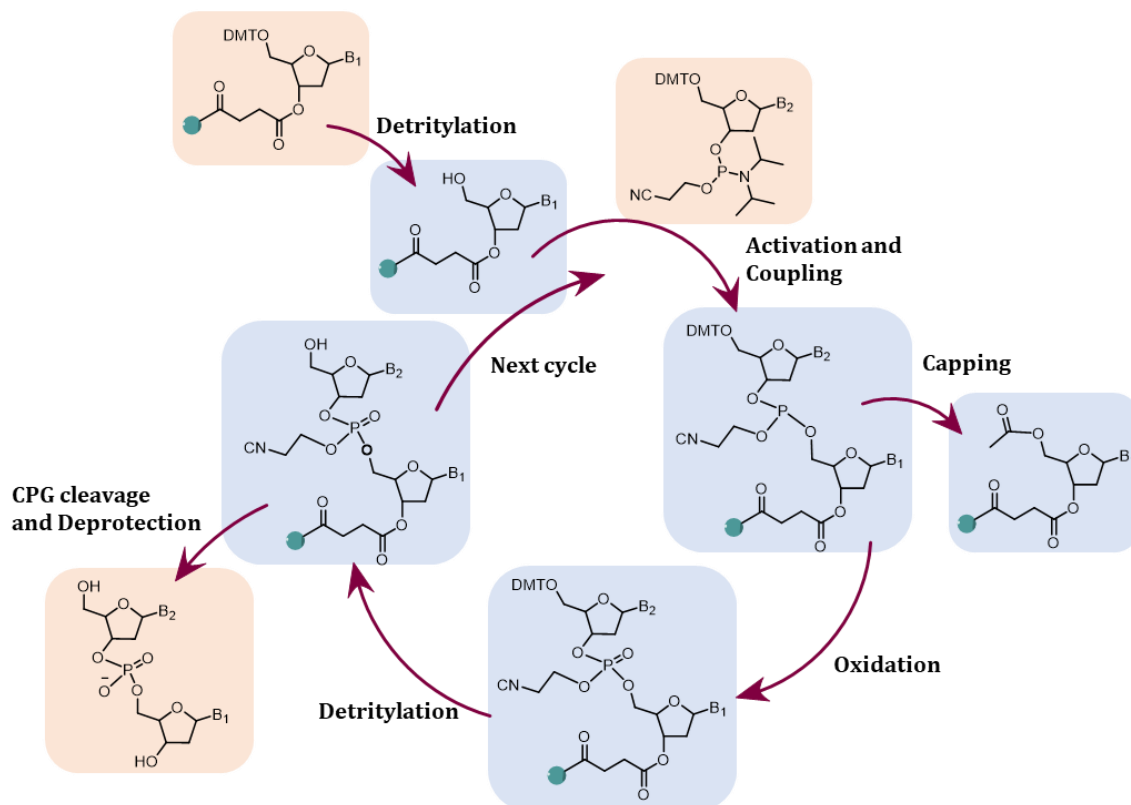


Figure 2.6. Schematic representation of the solid phase oligonucleotide synthesis.

2.3.2. Fluorescent AgNCs templated by ssDNA sequences

To standardize the conditions for AgNC synthesis using DNA templates, we selected two ssDNA sequences (DNA 1 and DNA 2), which were reported earlier to stabilize fluorescent AgNCs³⁶ and followed the synthetic procedures in the literatures reports of Robert M Dickson *et al.*^{9,12}



NaBH₄ was used as the reducing agent for Ag⁺ ions. Synthesis of AgNCs was carried out by introducing AgNO₃ to a solution of ssDNA in PBS (10 mM Phosphate buffer

and 2 mM NaCl), followed by the addition of freshly prepared NaBH_4 (Figure 2.7A). A 1:6:6 ratio of ssDNA to Ag^+ to NaBH_4 was followed for the synthesis and along with this a control experiment without ssDNA was carried out to verify the results.

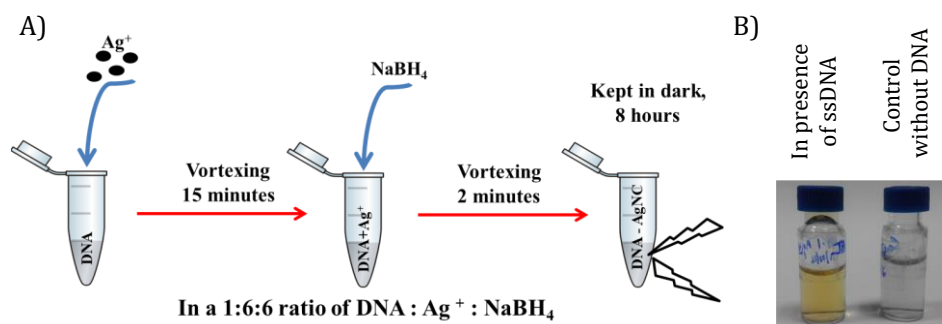


Figure 2.7. A) Schematic representation of the DNA templated AgNC synthesis and B) visible light photographs of samples in the presence and absence of DNA.

After incubation of the reaction mixture in dark for 8 hrs, samples with ssDNA displayed a slight yellow color indicating the presence of Ag nanoparticles or clusters in the samples, whereas, the control experiment was colorless (Figure 2.7B). In agreement with the literature report,³⁶ the UV-visible absorption spectra of AgNC templated by DNA-1 and DNA-2 showed the presence of characteristic absorption band at 714 nm and 744 nm, and emission at 771 nm and 807 nm, respectively (Figures 2.8A and 2.8B). Absorption spectra infers, AgNC stabilization by ssDNA template also accompanies the formation of Ag nanoparticles with 400 nm surface plasmon resonance band.

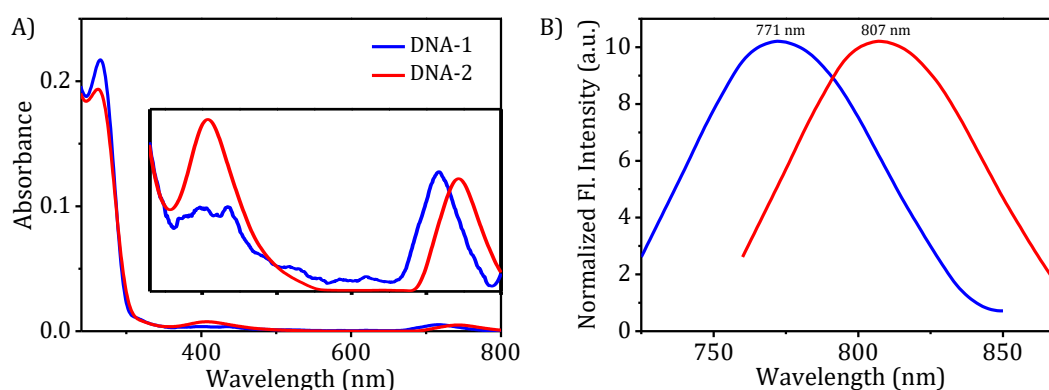


Figure 2.8. A) Absorption and B) emission spectra of AgNCs templated by DNA-1 and DNA-2.

Further, the reaction conditions for DNA/AgNC synthesis like salt concentration, appropriate buffer system and Ag^+ to NaBH_4 ratio required for the synthesis were investigated. With increasing concentrations of NaCl, the fluorescence intensity of **DNA-1/AgNC** was found to decrease (Figure 2.9A). This observation implies the poor interaction of cytosine nucleobases with Ag^+ ions at higher concentrations of Na^+ and hence the formation of fluorescent **DNA-1/AgNC** will be diminished. Among the three buffer systems studied, AgNCs prepared in PBS with $\text{pH} = 7.39$ displayed a relatively higher fluorescence intensity (Figure 2.9B). Similarly, fluorescence emission spectra of **DNA-1/AgNC** synthesis carried out with different ratios of Ag^+ to NaBH_4 (Figure 2.9C) suggested a 1:1 or 1:0.5 ratio are ideal for the synthesis of AgNCs. Above and below these ratios of NaBH_4 concentration, fluorescence intensity of **DNA-1/AgNC** was comparatively weak, which could be due to the enhanced reduction of Ag^+ ions to Ag atoms at higher concentrations of NaBH_4

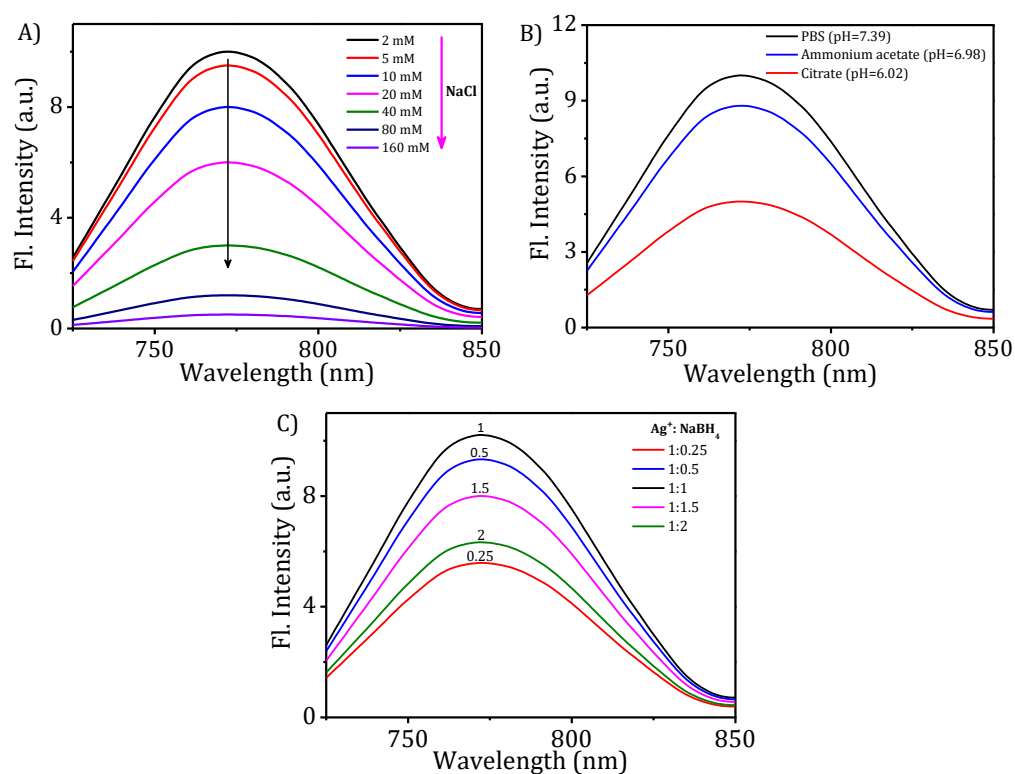


Figure 2.9. Fluorescence emission spectra of DNA-1/AgNCs A) with increasing concentrations of NaCl, B) in different buffer system and C) with different Ag^+ to NaBH_4 ratios.

leading to Ag nanoparticles or Ag aggregates, and the insufficiency of NaBH_4 molecules to reduce Ag^+ ions at lower concentrations. In short, lower concentrations of salt, PBS buffer and 1:1 or 1:0.5 ratios of Ag^+ to NaBH_4 are suitable conditions for the effective synthesis of DNA/AgNCs.

2.3.3. Design, synthesis and characteristics of DNA three-way junctions

Two different types of DNA-3WJs, **3WJN-CX** and **3WJN** described in this work were assembled from corresponding ssDNA sequences (Figure 2.10A), following the typical hybridization protocols. In the initial design, three ssDNA sequences, DNA 1, 2 & 3 (Figure 2.10B and Table 2.1), each containing 20 nucleobases with four cytosines in the center were used, which upon hybridization form a DNA-3WJ with an unpaired, 12-cytosine loop at the center of the 3WJ (hereafter referred as **3WJ20-C12**). On the other hand, DNA 4, 5 & 6 (Figure 2.10B) hybridize to form a 3WJ without a cytosine loop at the center and is used as a control 3WJ (**3WJ20**).³⁷ In general, the DNA-3WJs with and without the central cytosine loops, used in this work are defined as **3WJN-CX** and **3WJN**, respectively, where N represents the total number of nucleobases in one ssDNA and X represents the total number of unpaired, cytosines in the central loop region of the 3WJ.

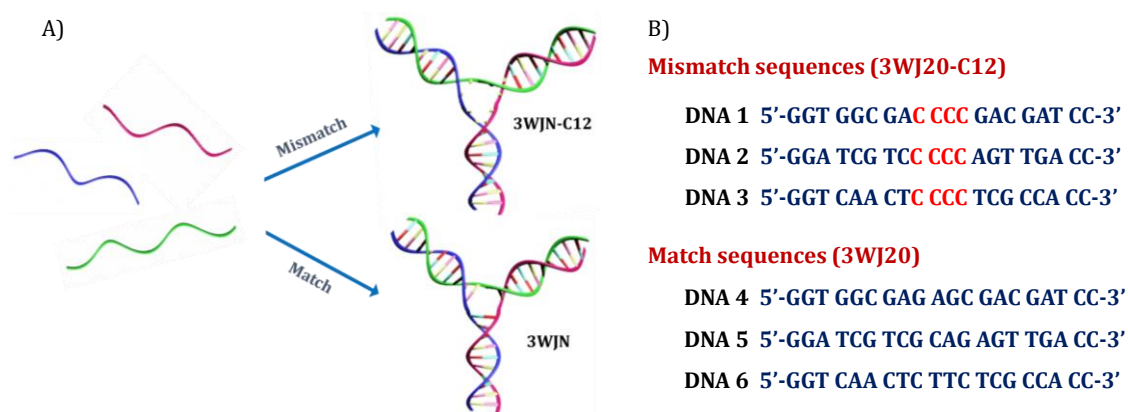


Figure 2.10. A) Schematic illustration of **3WJN-CX** and **3WJN** formations from ssDNA sequences and B) ssDNA sequences used for preparing **3WJ20-C12** and **3WJ20**.

The ssDNA sequences, corresponding DNA-3WJs, HRMS and melting temperature (T_m) values obtained are tabulated in Table 2.1. Thermal denaturation properties of 3WJs were studied by monitoring the absorbance at 260 nm as a function of temperature. **3WJ20-C12** dissociates into ssDNA at 32 °C whereas the fully hybridized **3WJ20** melts at 41 °C. The decrease in the T_m value of **3WJ20-C12** compared to **3WJ20** (Figure 2.11A) is due to the relative destabilization of the 3WJ in the presence of the twelve unpaired cytosine nucleobases in the central loop region. Circular dichroism analysis showed a bisignated CD signal centered at 260 nm, with a positive band at 275 nm and a negative band at 248 nm (Figure 2.11B), which indicates the B-form duplex structure of the arms in the DNA-3WJs.

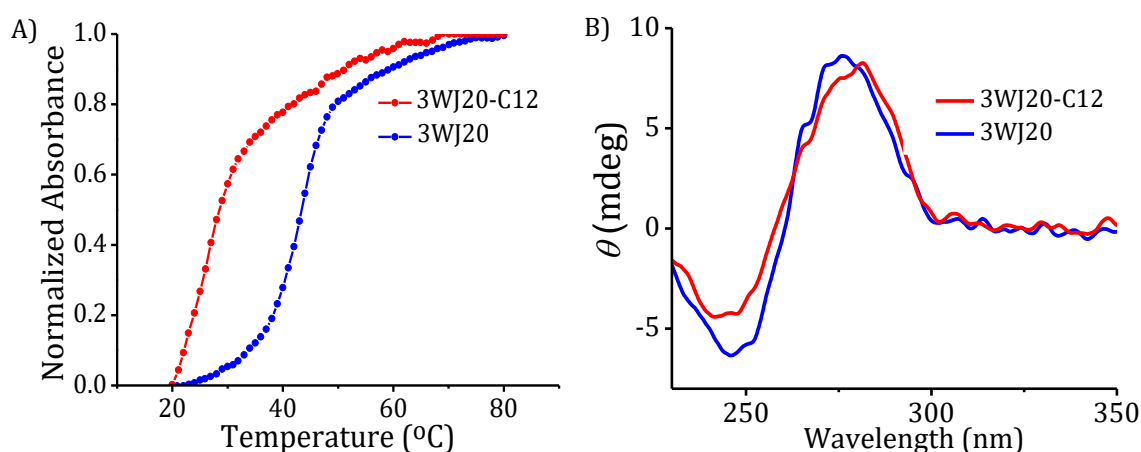


Figure 2.11. A) Thermal denaturation curves and B) circular dichroism spectra of **3WJ20-C12** and **3WJ20**.

The duplex nature of the 3WJ arms and presence of cytosine loop in **3WJ20-C12** were further analyzed by ethidium bromide (EB) intercalation studies (Figures 2.12A & 2.12B for **3WJ20-C12**, inset of B shows the schematic representation of EB intercalation process and Figure 2.13A for **3WJ20**). Upon excitation at 515 nm, an enhancement in the monomeric fluorescence emission of EB with successive addition of DNA-3WJs was observed. A ~30% relative enhancement in the fluorescence emission of EB in presence of fully hybridized **3WJ20** compared to

3WJ20-C12 (Figure 2.13B) indicates the presence of unpaired nucleobases in **3WJ20-C12**. Thus, the DNA melting, CD and EB displacement studies verify the presence of 3WJ branches with duplex structures and cytosine loop in **3WJ20-C12**.

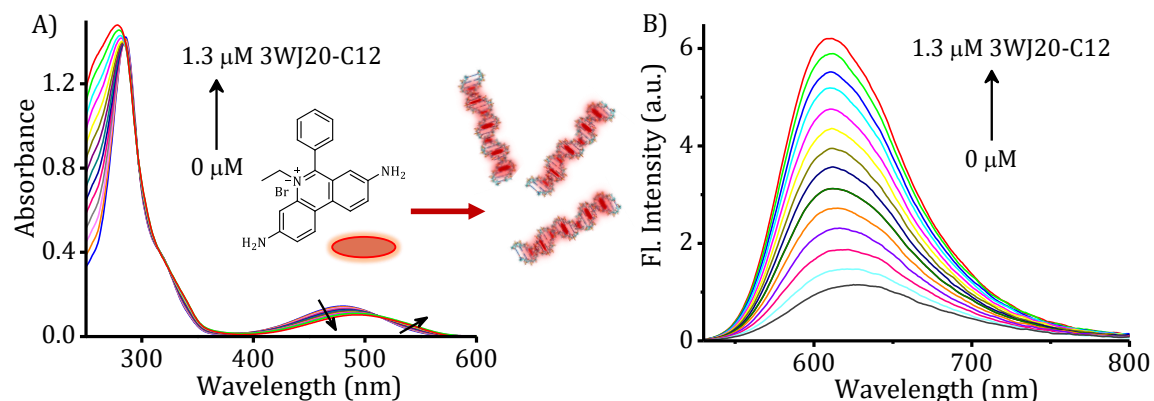


Figure 2.12. Changes in the A) absorption and B) emission spectra of EB with increasing concentrations of **3WJ20-C12**.

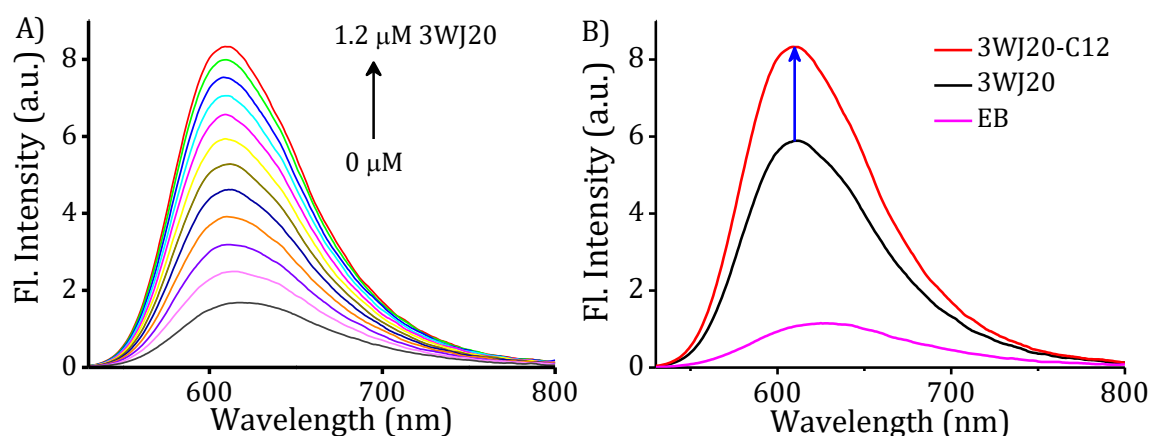


Figure 2.13. Changes in the emission spectra of A) EB with increasing concentrations of **3WJ20** and B) EB, EB with 1.2 μM concentrations of **3WJ20-C12** and **3WJ20**.

2.3.4. Fluorescent AgNCs templated by DNA-3WJs

To demonstrate our strategy of stabilizing AgNCs on cytosine loop inserted at DNA-3WJ center, silver ions were added to DNA-3WJs in buffer solution, followed by reduction using NaBH_4 (Schematic illustration; Figures 2.14A & 2.14B). UV-visible absorption spectra of **3WJ20-C12/AgNC** (AgNC formed in the presence of **3WJ20-C12**) showed a characteristic absorption band at 510 nm along with the surface

plasmonic resonance band of silver nanoparticles (AgNPs) around 400 nm.³⁸ The 510 nm absorption band is characteristic of the DNA templated AgNCs as reported in the literature.³⁹ Control AgNC synthetic experiments in the absence of 3WJs or in the presence of **3WJ20**, showed only the 400 nm surface plasmonic resonance band with no evidence of 510 nm band (Figure 2.14C). These results indicate that only the samples with DNA templates and stabilizes Ag nanoparticles.

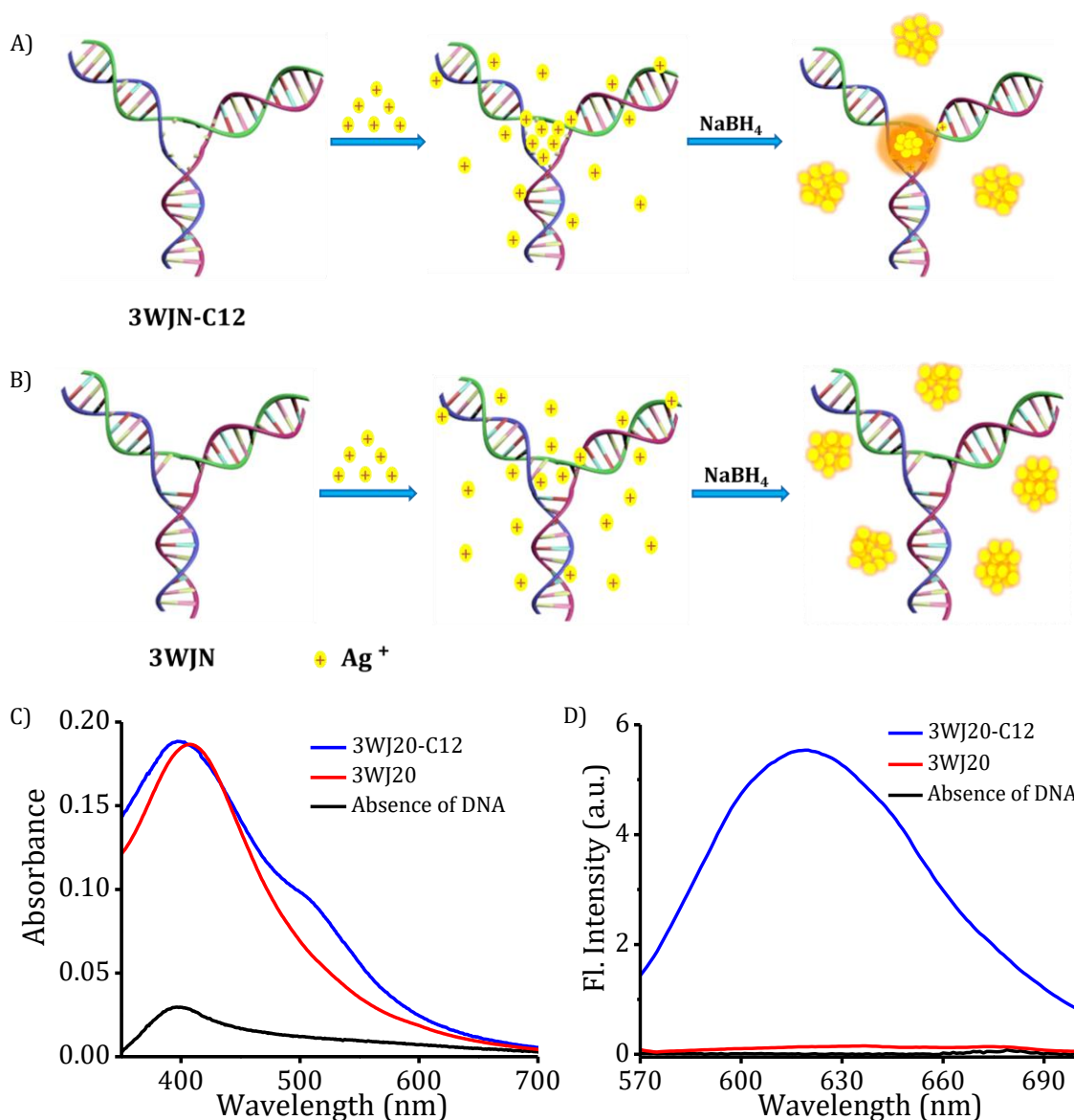


Figure 2.14. Schematic illustration of the strategy for the preparation of fluorescent AgNCs in presence of A) **3WJN-C12** and B) **3WJN**. C) UV-visible absorption spectra and D) corresponding fluorescence emission spectra of AgNCs prepared with **3WJ20-C12**, **3WJ20** and in the absence of DNA ($\lambda_{\text{exc}} = 510 \text{ nm}$).

On the other hand, the one without stabilizing agent results in the formation of more aggregated Ag nanostructures than AgNPs, responsible for the observed surface plasmon band. In addition, fluorescence emission spectra of **3WJ20-C12/AgNC** showed characteristic emission band at 630 nm ($\lambda_{\text{exc}} = 510$ nm), which was not observed in the control experiments (Figure 2.14D). This distinctive absorption and fluorescence behavior of **3WJ20-C12/AgNC** indicates that efficient cytosine-Ag⁺ interaction takes place only in the 3WJs with central cytosine loop leading to the formation and stabilization of fluorescent AgNCs upon reduction, which otherwise results in the formation of aggregated AgNPs.

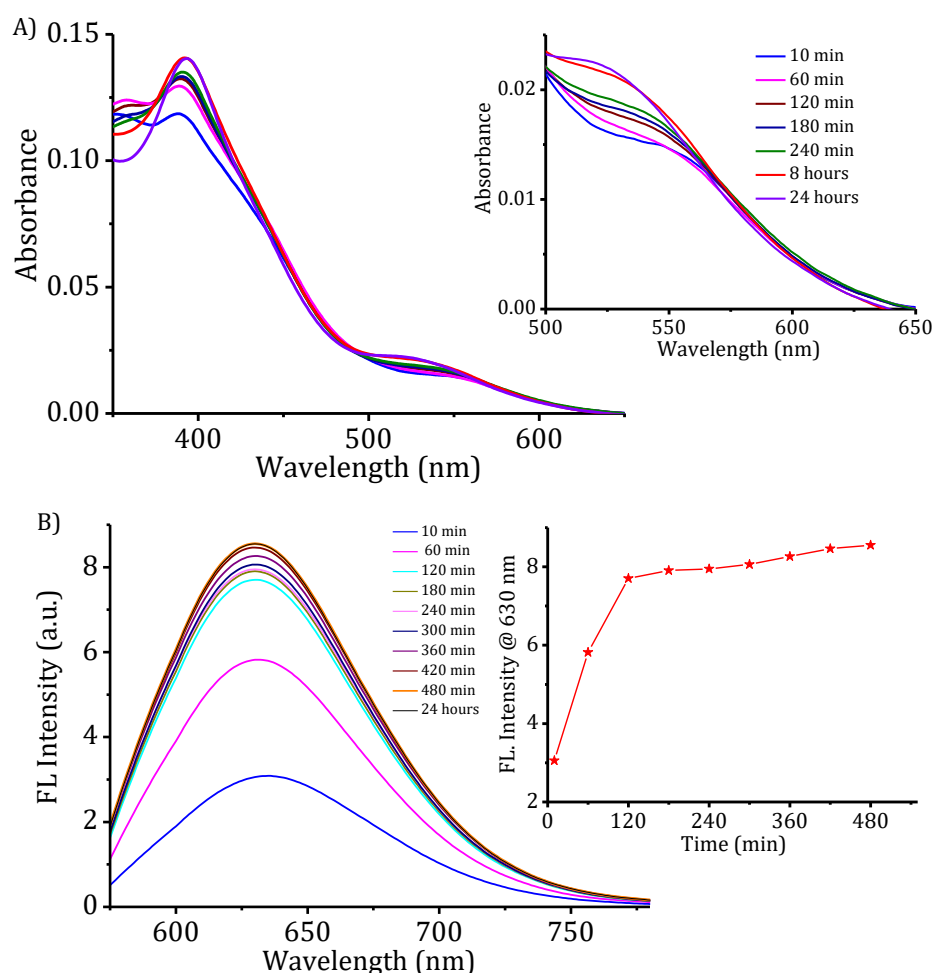


Figure 2.15. Changes in the A) absorption (inset shows the zoomed portion of absorption spectra in 500-650 nm range), and B) emission spectra of **3WJ20-C12/AgNCs** with reaction time (inset shows plot of fluorescence intensity with time obtained by monitoring fluorescence emission at 630 nm, $\lambda_{\text{exc}} = 510$ nm).

The formation of **3WJ20-C12/AgNCs** was monitored by recording the time dependent changes in UV-visible absorption and fluorescence emission spectra. The plasmon absorption of the AgNPs around 400 nm along with a small shoulder band around 510 nm corresponding to the AgNCs started to appear within 10 minutes of the addition of NaBH_4 to a mixture of **3WJ20-C12** and silver ions (Figure 2.15A). The absorption band at 510 nm due to the formation of AgNCs gradually increased up to 8 hours, beyond which it got saturated (inset of Figure 2.15A). Similar to the absorption spectra, a characteristic fluorescence emission band appeared at 630 nm and showed significant emission within 2 hours, with slight enhancement in the fluorescence emission up to 8 hours and gets saturated (Figure 2.15B and inset).

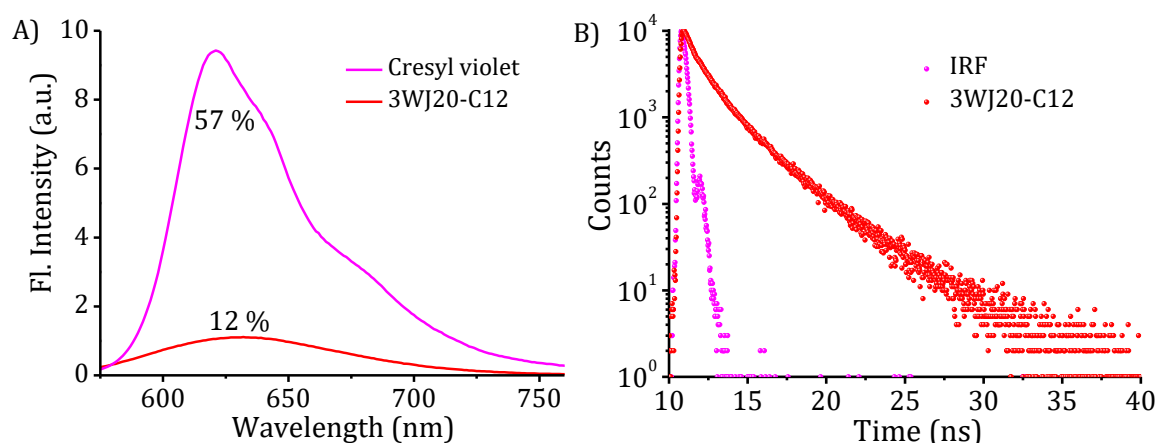


Figure 2.16. A) Fluorescence emission spectra of optically matching solutions of cresyl violet and **3WJ20-C12/AgNCs**, and B) fluorescence life time profile of **3WJ20-C12/AgNCs**

The observed red fluorescence compares well with the fluorescence of AgNCs, reported with 12-cytosine as ssDNA template or as a part of ssDNA/hairpin loop structures.^{27,39,40} The quantum yield (Φ_F) of as synthesized **3WJ20-C12/AgNCs** was found to be 12% in PBS buffer at pH 7.4 (Figure 2.16A). Fluorescence lifetime measurements of these **3WJ20-C12/AgNCs** showed triexponential decay with an average fluorescence lifetime of 1.64 ns (Figure 2.16B). Purification of **3WJ20-C12/AgNCs** from AgNPs was achieved using Ultracel®-10k centrifugal filters by the

continuous washing of sample with buffer solution (Figures 2.17A, 2.17B and inset of Figure 2.17A shows the cartoonic representation of AgNC purification). Purified samples of **3WJ20-C12/AgNCs** showed slight yellow color under day light and intense red emission under 365 nm UV light (inset of Figure 2.17B). Further, the purified **3WJ20-C12/AgNCs** showed higher stability in terms of fluorescence emission compared to the unpurified samples, as evidenced by the fluorescence emission over 72 hours (Figures 2.18A and 2.18B).

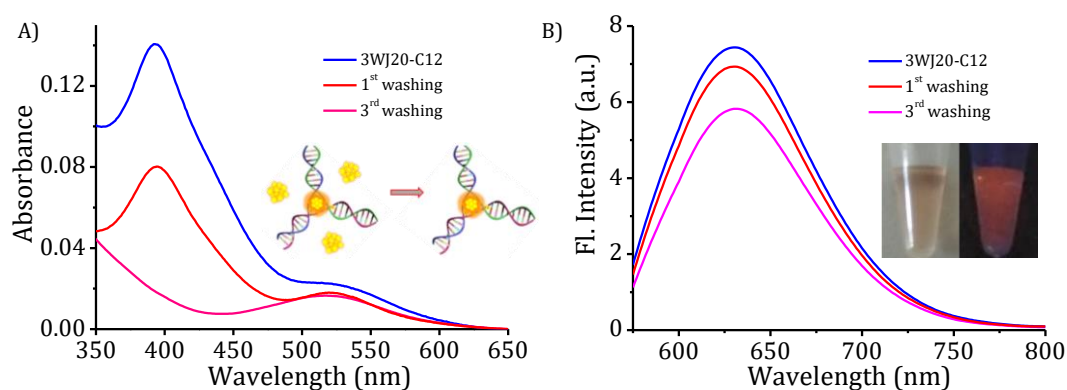


Figure 2.17. A) Absorption and B) emission spectra of **3WJ20-C12/AgNCs** in the purification process using 10k centrifugal filters.

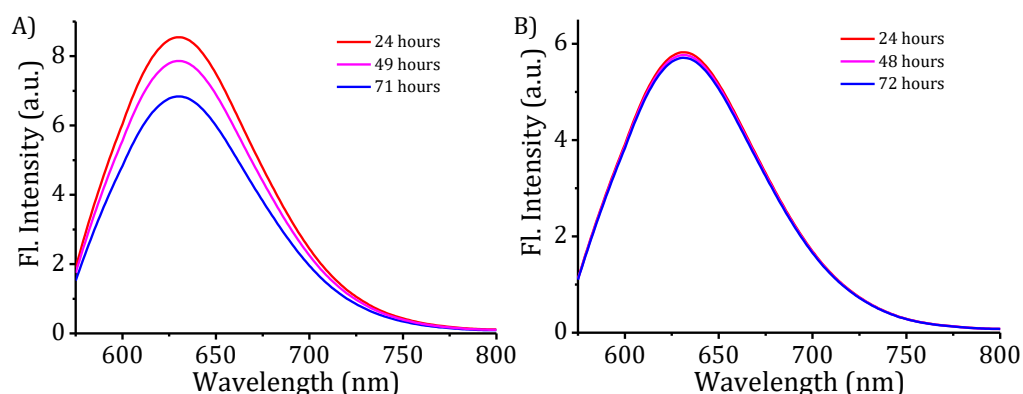


Figure 2.18. Time dependent changes in the emission spectra of **3WJ20-C12/AgNCs** A) before and B) after purification.

2.3.5. Morphology and elemental analysis of **3WJ20-C12/AgNCs**

HR-TEM analysis was used to visualize the size and shape of Ag nanoparticles formed in the presence of different DNA-3WJs. The expected diameter of 3WJ center

is approximately 2.88 nm (calculated using the distance between base pairs and diameter of B-DNA). There can be slight variations expected in this value attributed to the flexibility and helical twist of DNAs. The TEM image of sample drop cast before purification showed a combination of AgNCs, AgNPs and aggregated nanostructures (Figure 2.19A). Whereas, purified samples of **3WJ20-C12/AgNCs** showed 2-3 nm sized clusters, supporting the effective stabilization of AgNCs inside the 3WJ center (Figure 2.19B). Under similar conditions, HR-TEM analysis of the AgNPs formed in the presence of **3WJ20** or in the absence of any DNA, showed 10-12 nm sized AgNPs and aggregated AgNPs (Figures 2.19C & 2.19D).

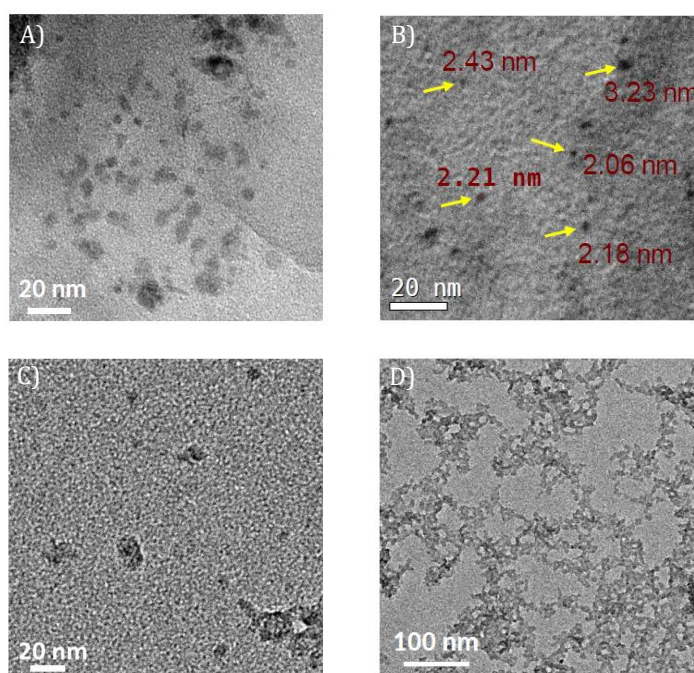


Figure 2.19. TEM images of A) before (presence of different sized Ag nanostructures), B) after purification of **3WJ20-C12/AgNCs** (the presence of 2-3 nm sized **3WJ20-C12/AgNCs** are indicated by yellow arrow mark). C) AgNPs formed in the presence of **3WJ20** and D) Ag aggregates formed in the absence of any DNA sequence.

In addition, EDAX analysis performed with purified **3WJ20-C12/AgNCs**, showed peaks corresponding to Ag and phosphorous validating the presence of AgNCs and DNA (Figure 2.20).⁴¹ The elemental and surface composition of purified

3WJ20-C12/AgNC were further analyzed by XPS. In agreement with the EDAX spectrum, the XPS spectrum (Figure 2.21A) of **3WJ20-C12/AgNC** confirmed the presence of Ag, phosphorous, oxygen and nitrogen. Expanded Ag 3d region of XPS spectrum shows two peaks at 368.29 and 374.3 eV characteristic of the AgNCs (Figure 2.21B).³⁸ Thus, HR-TEM and XPS analysis confirms that emissive AgNCs with 2-3 nm size are formed only in the presence of mismatched **3WJ20-C12** template with cytosine loop and validates our proposed strategy.

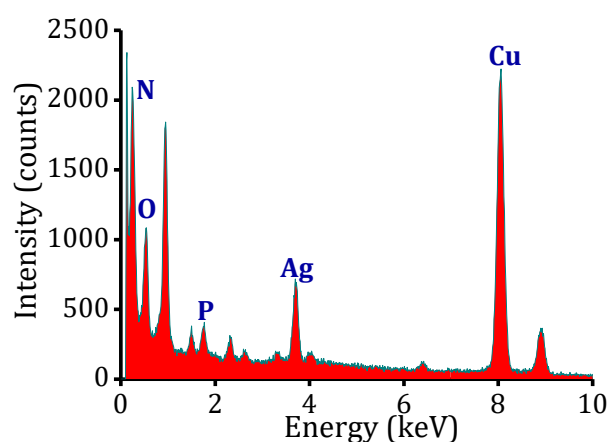


Figure 2.20. EDAX spectrum of purified **3WJ20-C12/AgNCs**.

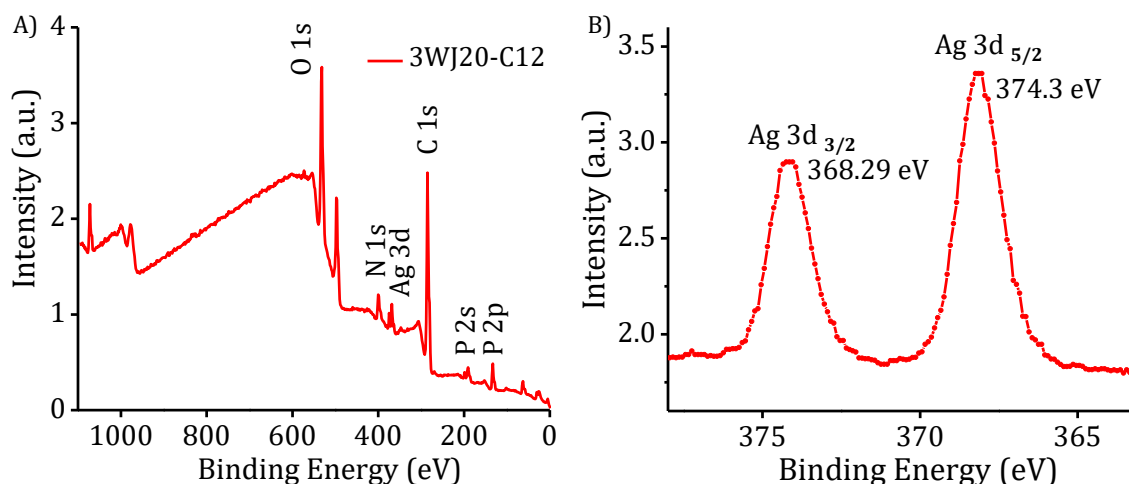


Figure 2.21. A) XPS survey and B) expanded spectrum of purified **3WJ20-C12/AgNCs**.

DLS measurements further confirms the size of nanoparticles formed in presence of different DNA templates (Figure 2.22). DLS hydrodynamic size measurements of a solution of AgNPs formed in the presence of **3WJ20** and in the

absence of DNA, showed the existence of higher sized nanoparticles in comparison with the 3WJ20-C12/AgNC sample.

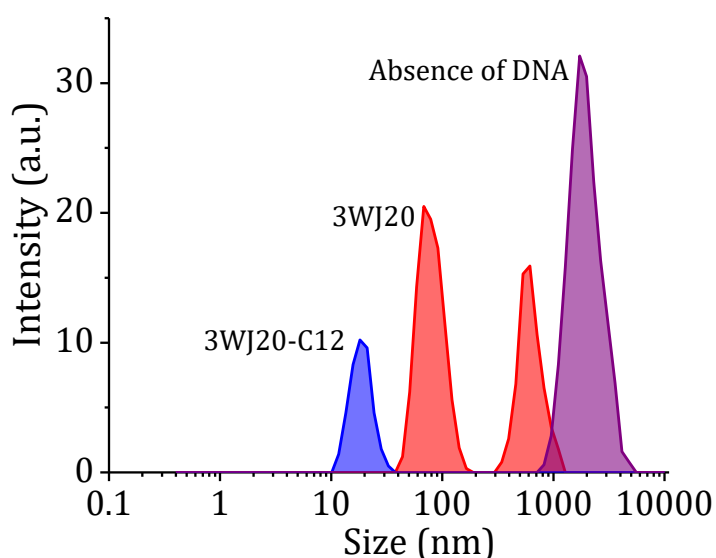


Figure 2.22. DLS size distribution profiles of purified 3WJ20-C12/AgNCs, AgNPs formed in presence of 3WJ20 and in the absence of DNA.

2.3.6. Sequence programming and influence on 3WJN-CX/AgNC formation

Alterations in the formation of AgNCs and corresponding fluorescence emission was inspected by programming the ssDNA sequences as represented in Table 2.1. In the first instance, the duplex branch length of DNA-3WJ was increased from 8 to 13 to obtain 3WJ30-C12 and 3WJ-30, with and without the central cytosine loop, respectively.

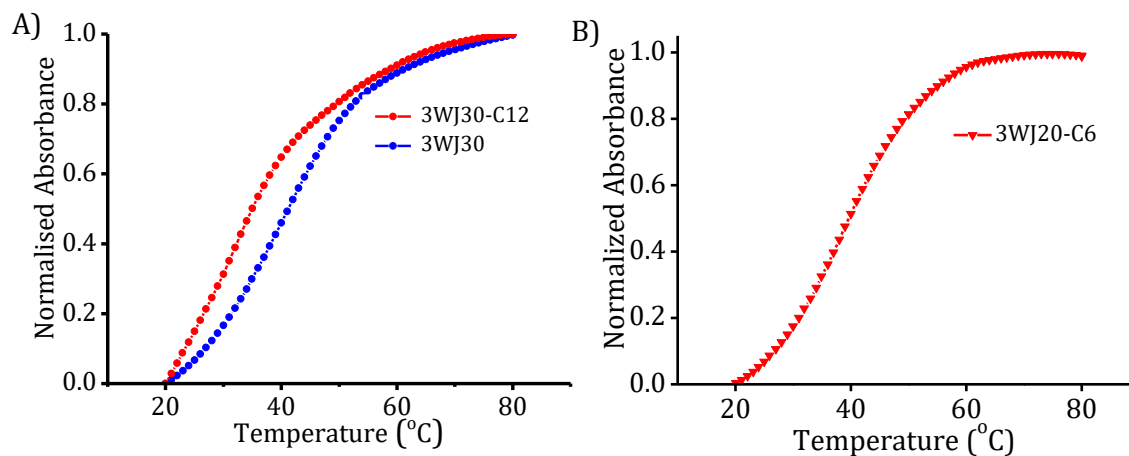


Figure 2.23. Thermal denaturation curves of A) 3WJ30-C12, 3WJ30 and B) 3WJ20-C6.

In the second example, the central cytosine loop size was reduced from 12 to 6 cytosines to obtain **3WJ20-C6**. DNA-3WJs were prepared from the corresponding ssDNAs and T_m values obtained are tabulated (Table 2.1, Figures 2.23A and 2.23B). A comparison of the T_m values of **3WJ30-C12** (51 °C) and **3WJ20-C12** (32 °C) demonstrate the additional stability offered by the extended duplex arms in the case of **3WJ30-C12**.

AgNCs prepared in presence of **3WJ30-C12** showed a characteristic emission at 578 nm ($\lambda_{exc} = 490$ nm), with a blue shift and relatively enhanced emission compared to **3WJ20-C12/AgNCs** (Figure 2.24). This shift in the emission spectrum could be attributed to the presence of higher number of nearby nucleobases and less flexibility of **3WJ30-C12** compared to **3WJ20-C12**.⁴²

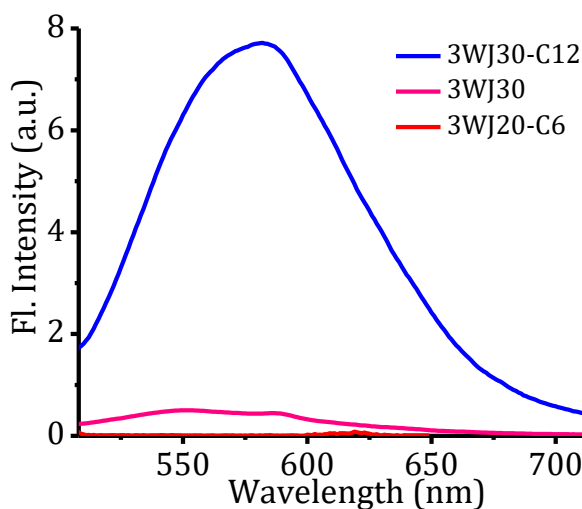


Figure 2.24. Fluorescence emission spectra of AgNCs prepared in the presence of **3WJ30-C12**, **3WJ30** and **3WJ20-C6** ($\lambda_{exc} = 490$ nm).

Control experiments with **3WJ30** doesn't show any characteristic emission as expected, thereby validating the requirement of cytosine loop in the 3WJ center for stabilizing AgNCs. Likewise, attempts to prepare AgNCs with **3WJ20-C6** doesn't show the formation of emissive AgNCs, indicating that a 6-cytosine loop is not enough for stabilization of the emissive AgNCs. These results of fluorescence

emission were further supported with HR-TEM analysis. **3WJ30-C12/AgNCs** showed the presence of 3-4 nm sized AgNCs whereas **3WJ30** and **3WJ20-C6** showed the formation of AgNPs and aggregates (Figures 2.25A-C).

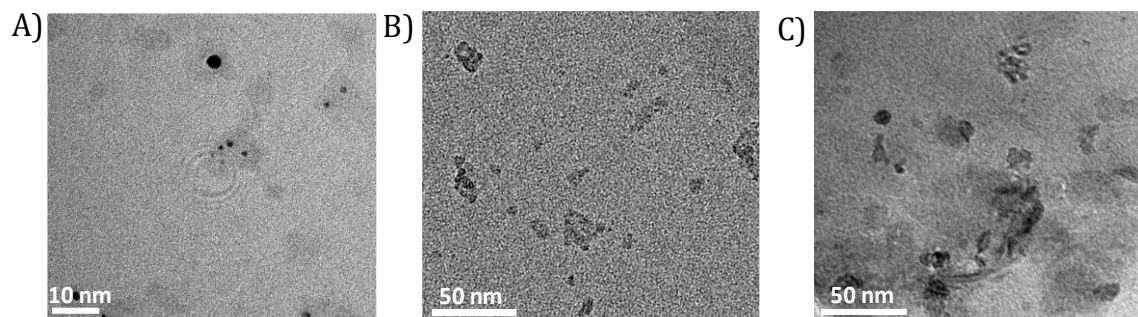


Figure 2.25. TEM images of A) purified **3WJ30-C12/AgNCs** and AgNPs and aggregates formed in presence of B) **3WJ30** and C) **3WJ20-C6**.

2.3.7. Metal ion interaction studies of **3WJ20-C12/AgNCs**

Interestingly, the **3WJN-C12/AgNCs** exhibited highly selective and sensitive interactions with Hg^{2+} ions and hence can be employed in the detection of trace amounts of Hg^{2+} ions in aqueous solutions by a fluorescence turn-off mechanism. For example, the fluorescence of **3WJ20-C12/AgNC**, showed significant quenching in the presence of 1-200 nM Hg^{2+} ions as shown in Figure 2.26A. The sensitive detection is characterized by a significantly low LOD value of 0.7 nM

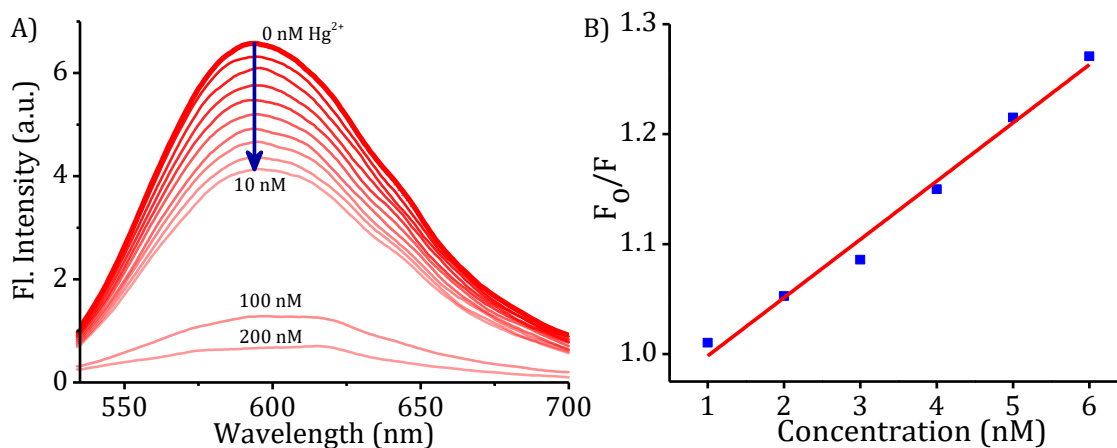


Figure 2.26. A) Quenching in the fluorescence spectra of **3WJ20-C12/AgNC** (6 μM) with increasing concentration of Hg^{2+} (0, 1-10, 100 and 200 nM) and B) F_0/F versus concentration plot of fluorescence quenching of **3WJ20-C12/AgNC** with increasing the Hg^{2+} from 1-6 nM.

calculated by monitoring the changes in fluorescence intensity as a function concentration of Hg^{2+} ions (Figure 2.26B). Similarly, the selectivity of **3WJ20-C12/AgNC** for Hg^{2+} ions was analyzed using various metal ions (K^+ , Li^+ , Ca^{2+} , Mg^{2+} , Cu^{2+} , Zn^{2+} , Cd^{2+} , Al^{3+} , Hg^{2+} and Fe^{3+}) and the results are summarized in Figures 2.27A & 2.27B. Other metal ions, even at 300 times higher concentrations compared to Hg^{2+} , failed to show significant fluorescence quenching.

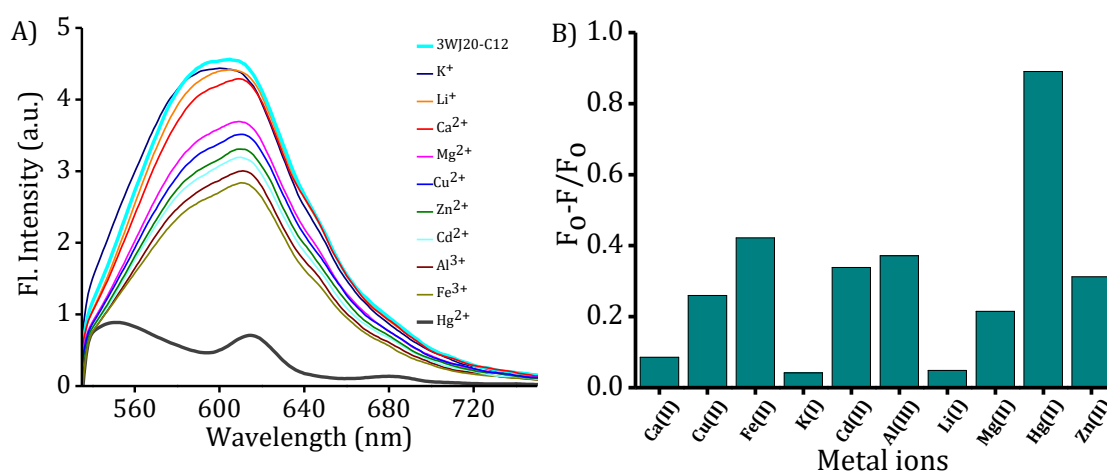


Figure 2.27. A) Fluorescence spectra of **3WJ20-C12/AgNCs** in presence of various metal ions (60 μM) in acetonitrile and B) corresponding bar diagrams of fluorescence quenching, $(F_0 - F)/F_0$ at 630 nm.

A review of existing literature shows that the silver nanoclusters (AgNCs) stabilized by DNA strands and other small molecules are shown to exhibit a highly selective and sensitive interaction with Hg^{2+} , leading to significant fluorescence changes.^{40,43} The leading mechanisms proposed for the selective interaction of AgNCs with Hg^{2+} ions are; (i) d^{10} - d^{10} metallophilic interactions and (ii) redox reactions involving Hg^{2+} and Ag leading to the oxidation of Ag atoms in the cluster to Ag^+ ions, which perturb the fluorescence properties. The highly sensitive fluorescence quenching of **3WJ20-C12/AgNCs** in presence of Hg^{2+} ions could be attributed to the possible oxidation of Ag (0) to Ag^+ ions, which also explains the selectivity of the interactions in this case.

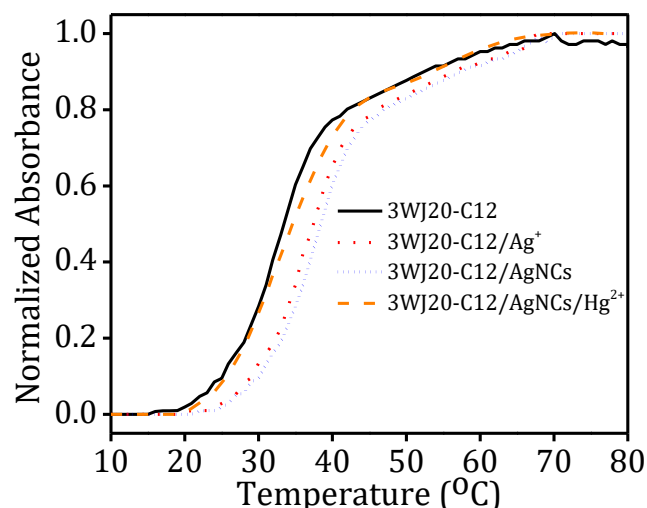


Figure 2.28. Thermal denaturation curves of **3WJ20-C12** in presence of 6 equivalents of Ag^+ , corresponding reduced AgNCs and **3WJ20-C12/AgNCs** with $60 \mu\text{M Hg}^{2+}$.

To get a better insight into the fluorescence quenching mechanism of AgNCs by Hg^{2+} , thermal denaturation studies of **3WJ20-C12** in presence of Ag^+ ions, AgNCs and $\text{AgNC}/\text{Hg}^{2+}$ were conducted (Figure 2.28). The addition of 6 equivalents of Ag^+ to **3WJ20-C12** stabilizes the DNA-3WJ by 3°C and the corresponding AgNCs (obtained by reduction of the same solution using 6 equivalents of NaBH_4) by 4°C . Whereas, subsequent addition of Hg^{2+} to the **3WJ20-C12/AgNC** resulted in the destabilization of **3WJ20-C12/AgNC**. In addition, using a metal/semiconductor/metal planar device with silver electrodes, we monitored the conductivity changes of **3WJ20-AgNP** and **3WJ20-C12/AgNCs** in the absence and presence of Hg^{2+} (Figures 2.29A & 2.29B).

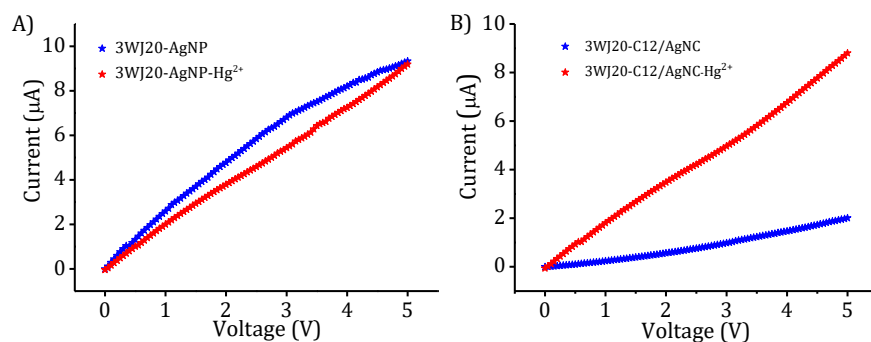


Figure 2.29. The I-V curves of A) **3WJ20/AgNP** and B) **3WJ20-C12/AgNCs** in the absence and presence of Hg^{2+} .

The I-V curve of **3WJ20-C12/AgNCs** showed an enhancement in the conductivity in presence of Hg^{2+} ions,^{44,45} whereas **3WJ20-AgNP** did not display any sensible changes. This implies Hg^{2+} interacts only with **3WJ20-C12/AgNCs** and forms Ag^+ ions and $\text{Hg}(0)$ atoms, as a result the overall conductivity increases. These results further supports the proposed redox mechanism for the fluorescence quenching in **3WJ20-C12/AgNCs** in the presence of Hg^{2+} .¹⁷

2.4. CONCLUSIONS

In summary, we present a novel design of branched **DNA-3WJ** with a cytosine loop at the center for stabilizing AgNCs, which can replace the process of modifying DNA branches for AgNCs used in multifunctional applications. The potential of this strategy to template AgNC is verified using a standard **DNA-3WJ** with a 12-cytosine loop. The formation of AgNCs inside this loop was characterized with photophysical, microscopic and surface analysis techniques. Sequence length and central cytosine loop size dependent changes on the formation and fluorescence properties were also examined. Results suggest that, AgNCs templated by **DNA-3WJ** with a 12-cytosine loop is a reasonably good template with fluorescence properties compared to its 6-cytosine analogue. The length of duplex 3WJ branch shows significant influence on fluorescence properties of AgNCs. The selectivity and sensitivity studies with metal ions demonstrates the ability of **3WJN-C12/AgNCs** to sense Hg^{2+} ions in aqueous solutions with detection limit in nanomolar range. Therefore, this novel design of AgNCs templated by branched DNA structure can be used as a fluorescent nanotag, which offers a better programmability of the duplex branches for multifunctional applications over the normal **DNA-3WJ** templated fluorophores reported.

2.5. EXPERIMENTAL SECTION

2.5.1. Materials and methods

Short oligonucleotide sequences used in this work (Table 2.1) were synthesized using K&A Laboratory H-6/H-8 DNA/RNA/LNA synthesizer. Phosphoramidites used for the solid-phase DNA synthesis were purchased from Glen Research (<http://www.glenresearch.com/index.php>). Anhydrous acetonitrile and all other reagents required for DNA synthesis were purchased from Sigma Aldrich. The synthesized oligonucleotides sequences were purified by LC-6AD Shimadzu Reverse Phase-High Performance Liquid Chromatography (RP-HPLC) with an Inertsil ODS-3, 5 mm, 10 x 250 mm reverse phase column. Deprotection and hybridization of ssDNAs were performed on IKA® dry block heater. Ammonium hydroxide (28% NH₃ in H₂O, 99.99%), ethidium bromide (EB), silver nitrate (AgNO₃, 99.0%), sodium borohydride (NaBH₄, 98.0%), sodium chloride (NaCl, 99%), sodium phosphate dibasic anhydrous (Na₂HPO₄) and sodium phosphate monobasic monohydrate (NaH₂PO₄·H₂O) were purchased from Sigma Aldrich. All the metal salts used in this work are of analytical grade and used as received without further purification. Water used for all the experiments was de-ionized Milli Q (18.2 MΩ·cm). All optical measurements were carried out in buffer solution (10 mM sodium phosphate buffer, pH = 7.39 + 2 mM for initial ssDNA sequences, and 150 mM NaCl for DNA-3WJs) using 1 cm cuvettes at room temperature (25±1 °C), unless otherwise mentioned.

The UV/Vis absorption spectra and melting temperature measurements were performed on Shimadzu UV-2600 Spectrophotometer. Steady state fluorescence emission spectra were recorded on SPEX FLUOROLOG-3 (FL3-221)

Spectrofluorimeter, equipped with 450 W Xenon arc lamp and a slit width of 5 nm. The quantum yield of **3WJ20-C12/AgNCs** was measured by relative comparison method using cresyl violet ($\Phi_F = 57\%$ in methanol) as the fluorescent standard.⁴⁶ The fluorescence life time measurements of **3WJ20-C12/AgNCs** were done using picosecond single photon counting system (Horiba, DeltaFlex) employing 510 nm laser as excitation source using picosecond photon detection module (PPD-850) as a detector. The fluorescence decay profile was deconvoluted using EzTime software and fitted with multi exponential decay of chi-square value 1 ± 0.1 .

CD spectra of DNA-3WJs were obtained at ambient temperatures using JASCO J-810 spectropolarimeter having Peltier controlled thermostatic cell holder with an accumulation of 2 and scan speed of 200 nm/min. The samples for TEM imaging were prepared by drop casting 5 μ L samples on the top of carbon-coated copper grid (400 meshes, Ted Pella). The as-prepared samples were initially dried on copper grid by slow evaporation and subjected to vacuum drying for 2 days before analysis. HR-TEM characterization and Energy Dispersive X-ray spectroscopy (EDAX) were performed with JEOL-JEM0310 microscope with an accelerating voltage of 100 kV and the samples were imaged using Hamamatsu ORCA charge-coupled device (CCD) camera.

Particle size distributions were calculated using Zetasizer (Malvern Nano ZS) operating with a He-Ne laser at a wavelength of 633 nm. Each analysis was performed in triplicate and the mean value is reported. In each run, 10-15 measurements were made. Purified samples of **3WJ20-C12/AgNC**, Ag nanoparticles formed in presence of **3WJ20** (15 μ M) and in the absence of DNA were used for hydrodynamic size measurements. XPS analysis of dried samples were performed

using PHI 5000 Versa Probe II (ULVAC-PHI Inc., USA) equipped with microfocused (200 μm , 15 kV) monochromatic Al-K α X-Ray source ($h\nu = 1486.6$ eV). Survey scans were recorded with X-ray source power of 50 W and pass energy of 187.85 eV. High-resolution spectrum of the Ag was recorded at 46.95 eV pass energy.

2.5.2. Synthesis of sequence specific DNA-3WJs

The short ssDNA sequences (with 20 bases and 30 bases) used in this work are tabulated in Table 2.1. The synthesis was carried out on a 1.0 μmol solid support, CPG (Controlled pore-glass, 1000 \AA pore size) using commercial phosphoramidites. Required oligonucleotide sequences were prepared with automated synthesis, which follows the stepwise addition of nucleoside 3'-phosphoramidite monomers to the 5'-end of resin bound nucleoside. The oligonucleotides were cleaved from the solid support and deprotected using standard conditions (28% NH_4OH , 10 hours at 60 $^\circ\text{C}$ on a dry block heater). The synthesized oligonucleotides were purified by RP-HPLC. A binary gradient system of triethylammonium acetate (TEAA) buffer (0.05 mM, pH = 7) and acetonitrile were used as eluents. The purified oligonucleotide samples were concentrated under vacuum, desalted using Sep-Pak C18 cartridge and concentrations were determined by monitoring the UV absorbance at 260 nm. The samples were then stored at below 4 $^\circ\text{C}$ and used as required to assemble into corresponding DNA-3WJs.

Hybridization of ssDNA sequences into corresponding DNA-3WJs were achieved by following the standard hybridization protocols. Equimolar mixture of three complementary ssDNAs in buffer solution were annealed at 90 $^\circ\text{C}$ for 10 minutes. All of the DNA-3WJs mentioned in this work were assembled by this

procedure and stored at 4 °C. 1 μ M samples of DNA-3WJs were used for thermal denaturation and circular dichroism studies. EB intercalation studies were performed by sequential addition of 10 μ L, 100 μ M samples of DNA-3WJ into 30 μ M, 1 mL EB in buffer solution.

Table 2.1. Table shows the ssDNA sequences, corresponding DNA-3WJ designations, expected and observed mass in HRMS and their melting temperature values.

Sl No.	Oligonucleotide sequence (5'-3')	Expected Mass	Observed Mass	DNA-3WJ	T _m (°C)
A	1 GGTGGCGACCCCACGATCC	6104	6104	3WJ20-C12	32
	2 GGATCGTCCCCAGTTGACC	6054	6053.8		
	3 GGTCAACTCCCCTCGCCACC	5958.9	5959.3		
B	4 GGTGGCGAGAGCGACGATCC	6158	6157.6	3WJ20	41
	5 GGATCGTCGCAGAGTTGACC	6208.1	6208.3		
	6 GGTCAACTCTTCTCGCCACC	5988.9	5989.2		
C	7 ATTACGGTGGCGACCCCACGATCCTGTAT	9183	9183.5	3WJ30-C12	51
	8 ATACAGGATCGTCCCCAGTTGACCATGCT	9127	9127.3		
	9 AGCATGGTCAACTCCCCTCGCCACCGTAAT	9071.9	9072.5		
D	10 ATTACGGTGGCGAGAGCGACGATCCTGTAT	9287.1	9287.8	3WJ30	56
	11 ATACAGGATCGTCGCAGAGTTGACCATGCT	9231.1	9231.5		
	12 AGCATGGTCAACTCTTCTCGCCACCGTAAT	9102	9102.5		
E	13 GGTGGCGAGCCCACGATCC	6144	6144.2	3WJ20-C6	38
	14 GGATCGTCGCCAGTTGACC	6134	6134.79		
	15 GGTCAACTCCCCTCGCCACC	5958.9	5959.3		

2.5.3. Synthesis of 3WJ/AgNCs.

Fluorescent AgNCs were synthesized according to the modified literature reports described by Dickson et al.^{9,12} For the preparation of AgNCs templated by **3WJN-CX** and **3WJN**, 45 μ L, 2 mM AgNO₃ solution was added to a freshly prepared sample of 15 μ M DNA-3WJs in buffer solution to provide a DNA-3WJ to Ag⁺ molar

ratio of 1:6 (final volume of 1 mL solution). After vortexing the sample for 10 minutes at room temperature, the mixture was reduced by quickly adding 45 μL , 2 mM of NaBH_4 (freshly prepared) under vigorously shaking conditions for 2 min. Final concentrations were fixed to 15 μM for the DNA-3WJ template, 90 μM for AgNO_3 , 90 μM for NaBH_4 in a molar ratio 1, 6, 6, respectively. The reaction mixture was kept in the dark at 4 $^\circ\text{C}$ for another 8 hours before optical measurements. The purification of **3WJN-CX/AgNCs** from AgNPs and aggregates was achieved using Amicon[®] Ultra Ultracel[®]-10k centrifugal filters. A similar procedure was followed for all the AgNCs synthesis mentioned in this work.

The **3WJ-AgNCs** concentration is referred to the concentration of DNA-3WJ unless mentioned otherwise. 15 μM samples of **3WJ/AgNCs** in buffer solution was used for UV-visible absorption, fluorescence emission, quantum yield (ϕ) and fluorescence lifetime measurements.

2.5.4. Selectivity and sensitivity measurements of 3WJ20-C12/AgNCs

The selectivity of **3WJ20-C12/AgNC** system for various metal ions were studied by monitoring the changes in fluorescence intensity of this system with the addition of common cations like K^+ , Li^+ , Ca^{2+} , Mg^{2+} , Hg^{2+} , Cu^{2+} , Zn^{2+} , Cd^{2+} , Al^{3+} and Fe^{3+} . For selectivity experiment, 10 μL , 60 μM metal ions in acetonitrile was added to 1mL, 1.5 μM **3WJ20-C12/AgNCs** in buffer solution. The sensitivity of this **3WJ20-C12/AgNCs** system towards Hg^{2+} was studied by adding increasing concentrations of Hg^{2+} (0, 1-10, 100, and 200 nM) to 6 μM **3WJ20-C12/AgNCs**. Fluorescence changes in a range of Hg^{2+} concentrations from 0-5 nM were used for limit of detection (LOD) calculation. LOD is determined from standard deviation of response of the curve (S_y) and slope of calibration curve (S), according to the formula $\text{LOD} =$

3.3 (Sy/S). The standard deviation of response can be determined from the standard deviation of y-intercepts of regression lines.⁴⁷

2.6. REFERENCES

- (1) Tao, Y.; Li, M.; Ren, J.; Qu, X. Metal nanoclusters: novel probes for diagnostic and therapeutic applications. *Chem. Soc. Rev.* **2015**, *44*, 8636-8663.
- (2) Shang, L.; Dong, S.; Nienhaus, G. U. Ultra-small fluorescent metal nanoclusters: Synthesis and biological applications. *Nano Today*. **2011**, *6*, 401-418.
- (3) Lin, C.-A.; Lee, C.-H.; Hsieh, J.-T.; Wang, H.-H.; Li, J.; Shen, J.-L.; Chan, W.-H.; Yeh, H.-I.; Chang, W. Review: Synthesis of Fluorescent Metallic Nanoclusters toward Biomedical Application: Recent Progress and Present Challenges. *J Med Biol Eng.* **2009**, *29*, 276-283.
- (4) Mathew, A.; Pradeep, T. Noble Metal Clusters: Applications in Energy, Environment, and Biology. *Part. Part. Syst. Charact.* **2014**, *31*, 1017-1053.
- (5) Wang, N.; Hu, Y.; Zhang, Z. Sustainable catalytic properties of silver nanoparticles supported montmorillonite for highly efficient recyclable reduction of methylene blue. *Appl. Clay Sci.* **2017**, *150*, 47-55.
- (6) Kondo, J.; Tada, Y.; Dairaku, T.; Hattori, Y.; Saneyoshi, H.; Ono, A.; Tanaka, Y. A metallo-DNA nanowire with uninterrupted one-dimensional silver array. *Nat. Chem.* **2017**, *9*, 956-960.
- (7) Kumar, V.; Gundampati, R. K.; Singh, D. K.; Bano, D.; Jagannadham, M. V.; Hasan, S. H. Photoinduced green synthesis of silver nanoparticles with highly effective antibacterial and hydrogen peroxide sensing properties. *J. Photochem. Photobiol. B.* **2016**, *162*, 374-385.
- (8) Díez, I.; Ras, R. H. A. Fluorescent silver nanoclusters. *Nanoscale.* **2011**, *3*, 1963-1970.
- (9) Petty, J. T.; Zheng, J.; Hud, N. V.; Dickson, R. M. DNA-Templated Ag Nanocluster Formation. *J. Am. Chem. Soc.* **2004**, *126*, 5207-5212.
- (10) Sharma, J.; Yeh, H.-C.; Yoo, H.; Werner, J. H.; Martinez, J. S. A complementary palette of fluorescent silver nanoclusters. *Chem. Commun.* **2010**, *46*, 3280-3282.
- (11) Díez, I.; Pusa, M.; Kulmala, S.; Jiang, H.; Walther, A.; Goldmann, A. S.; Müller, A. H. E.; Ikkala, O.; Ras, R. H. A. Color Tunability and Electrochemiluminescence of Silver Nanoclusters. *Angew. Chem. Int.* **2009**, *48*, 2122-2125.

- (12) Richards, C. I.; Choi, S.; Hsiang, J.-C.; Antoku, Y.; Vosch, T.; Bongiorno, A.; Tzeng, Y.-L.; Dickson, R. M. Oligonucleotide-Stabilized Ag Nanocluster Fluorophores. *J. Am. Chem. Soc.* **2008**, *130*, 5038-5039.
- (13) Guo, W.; Yuan, J.; Dong, Q.; Wang, E. Highly Sequence-Dependent Formation of Fluorescent Silver Nanoclusters in Hybridized DNA Duplexes for Single Nucleotide Mutation Identification. *J. Am. Chem. Soc.* **2010**, *132*, 932-934.
- (14) Obliosca, J. M.; Liu, C.; Yeh, H.-C. Fluorescent silver nanoclusters as DNA probes. *Nanoscale*. **2013**, *5*, 8443-8461.
- (15) Lin, R.; Tao, G.; Chen, Y.; Chen, M.; Liu, F.; Li, N. Constructing a Robust Fluorescent DNA-Stabilized Silver Nanocluster Probe Module by Attaching a Duplex Moiety. *Chem. Eur. J.* **2017**, *23*, 10893-10900.
- (16) Lu, S.; Wang, S.; Zhao, J.; Sun, J.; Yang, X. Fluorescence Light-Up Biosensor for MicroRNA Based on the Distance-Dependent Photoinduced Electron Transfer. *Anal. Chem.* **2017**, *89*, 8429-8436.
- (17) Morishita, K.; MacLean, J. L.; Liu, B.; Jiang, H.; Liu, J. Correlation of photobleaching, oxidation and metal induced fluorescence quenching of DNA-templated silver nanoclusters. *Nanoscale*. **2013**, *5*, 2840-2849.
- (18) Feng, L.; Wu, L.; Xing, F.; Hu, L.; Ren, J.; Qu, X. Novel electrochemiluminescence of silver nanoclusters fabricated on triplex DNA scaffolds for label-free detection of biothiols. *Biosens. Bioelectron.* **2017**, *98*, 378-385.
- (19) Mu, W.-Y.; Yang, R.; Robertson, A.; Chen, Q.-Y. A near-infrared BSA coated DNA-AgNCs for cellular imaging. *Colloids Surf. B: Biointerfaces*. **2018**, *162*, 427-431.
- (20) Cheng, R.; Xu, J.; Zhang, X.; Shi, Z.; Zhang, Q.; Jin, Y. A selective and label-free strategy for rapid screening of telomere-binding Ligands via fluorescence regulation of DNA/silver nanocluster. *Sci. Rep.* **2017**, *7*, 42629.
- (21) Ai, J.; Li, J.; Ga, L.; Yun, G.; Xu, L.; Wang, E. Multifunctional near-infrared fluorescent nanoclusters for simultaneous targeted cancer imaging and photodynamic therapy. *Sens. Actuators B Chem.* **2016**, *222*, 918-922.
- (22) Neidig, M. L.; Sharma, J.; Yeh, H.-C.; Martinez, J. S.; Conradson, S. D.; Shreve, A. P. Ag K-Edge EXAFS Analysis of DNA-Templated Fluorescent Silver Nanoclusters: Insight into the Structural Origins of Emission Tuning by DNA Sequence Variations. *J. Am. Chem. Soc.* **2011**, *133*, 11837-11839.

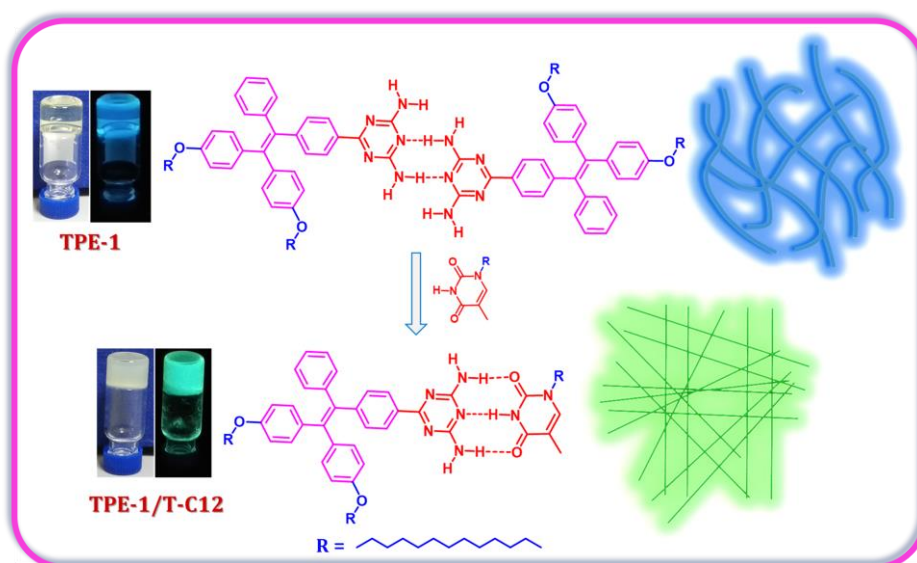
- (23) Gwinn, E. G.; O'Neill, P.; Guerrero, A. J.; Bouwmeester, D.; Fygenson, D. K. Sequence-Dependent Fluorescence of DNA-Hosted Silver Nanoclusters. *Adv. Mater.* **2008**, *20*, 279-283.
- (24) Huard, D. J. E.; Demissie, A.; Kim, D.; Lewis, D.; Dickson, R. M.; Petty, J. T.; Lieberman, R. L. Atomic Structure of a Fluorescent Ag₈ Cluster Templated by a Multistranded DNA Scaffold. *J. Am. Chem. Soc.* **2019**, *141*, 11465-11470.
- (25) Liu, H.; Shen, F.; Haruehanroengra, P.; Yao, Q.; Cheng, Y.; Chen, Y.; Yang, C.; Zhang, J.; Wu, B.; Luo, Q.; Cui, R.; Li, J.; Ma, J.; Sheng, J.; Gan, J. A DNA Structure Containing AgI-Mediated G:G and C:C Base Pairs. *Angew. Chem. Int. Ed.* **2017**, *56*, 9430-9434.
- (26) Chen, Y.; Phipps, M. L.; Werner, J. H.; Chakraborty, S.; Martinez, J. S. DNA Templated Metal Nanoclusters: From Emergent Properties to Unique Applications. *Acc. Chem. Res.* **2018**, *51*, 2756-2763.
- (27) New, S. Y.; Lee, S. T.; Su, X. D. DNA-templated silver nanoclusters: structural correlation and fluorescence modulation. *Nanoscale.* **2016**, *8*, 17729-17746.
- (28) Feng, L.; Huang, Z.; Ren, J.; Qu, X. Toward site-specific, homogeneous and highly stable fluorescent silver nanoclusters fabrication on triplex DNA scaffolds. *Nucleic Acids Res.* **2012**, *40*, e122-e122.
- (29) Chen, J.; Ji, X.; Tinnefeld, P.; He, Z. Multifunctional Dumbbell-Shaped DNA-Templated Selective Formation of Fluorescent Silver Nanoclusters or Copper Nanoparticles for Sensitive Detection of Biomolecules. *ACS Appl. Mater. Interfaces.* **2016**, *8*, 1786-1794.
- (30) Ai, J.; Guo, W.; Li, B.; Li, T.; Li, D.; Wang, E. DNA G-quadruplex-templated formation of the fluorescent silver nanocluster and its application to bioimaging. *Talanta.* **2012**, *88*, 450-455.
- (31) Sengupta, B.; Springer, K.; Buckman, J. G.; Story, S. P.; Abe, O. H.; Hasan, Z. W.; Prudowsky, Z. D.; Rudisill, S. E.; Degtyareva, N. N.; Petty, J. T. DNA Templates for Fluorescent Silver Clusters and I-Motif Folding. *J. Phys. Chem. C.* **2009**, *113*, 19518-19524.
- (32) Zhang, L.; Guo, S.; Zhu, J.; Zhou, Z.; Li, T.; Li, J.; Dong, S.; Wang, E. Engineering DNA Three-Way Junction with Multifunctional Moieties: Sensing Platform for Bioanalysis. *Anal. Chem.* **2015**, *87*, 11295-11300.
- (33) Guo, W.; Orbach, R.; Mironi-Harpaz, I.; Seliktar, D.; Willner, I. Fluorescent DNA Hydrogels Composed of Nucleic Acid-Stabilized Silver Nanoclusters. *Small.* **2013**, *9*, 3748-3752.

- (34) Yang, L.; Yao, C.; Li, F.; Dong, Y.; Zhang, Z.; Yang, D. Synthesis of Branched DNA Scaffolded Super-Nanoclusters with Enhanced Antibacterial Performance. *Small*. **2018**, *14*, 1800185.
- (35) Vittala, S. K.; Saraswathi, S. K.; Ramesan, A. B.; Joseph, J. Nanosheets and 2D-nanonetworks by mutually assisted self-assembly of fullerene clusters and DNA three-way junctions. *Nanoscale Adv.* **2019**, *1*, 4158-4165.
- (36) Yuan, Z.; Chen, Y.-C.; Li, H.-W.; Chang, H.-T. Fluorescent silver nanoclusters stabilized by DNA scaffolds. *Chem. Commun.* **2014**, *50*, 9800-9815.
- (37) Benveniste, A. L.; Creeger, Y.; Fisher, G. W.; Ballou, B.; Waggoner, A. S.; Armitage, B. A. Fluorescent DNA Nanotags: Supramolecular Fluorescent Labels Based on Intercalating Dye Arrays Assembled on Nanostructured DNA Templates. *J. Am. Chem. Soc.* **2007**, *129*, 2025-2034.
- (38) Zhang, X.; Qian, Y.; Ma, X.; Xia, M.; Li, S.; Zhang, Y. Thiolated DNA-templated silver nanoclusters with strong fluorescence emission and a long shelf-life. *Nanoscale*. **2018**, *10*, 76-81.
- (39) Brown, S. L.; Hobbie, E. K.; Tretiak, S.; Kilin, D. S. First-Principles Study of Fluorescence in Silver Nanoclusters. *J. Phys. Chem. C*. **2017**, *121*, 23875-23885.
- (40) O'Neill, P. R.; Velazquez, L. R.; Dunn, D. G.; Gwinn, E. G.; Fygenson, D. K. Hairpins with Poly-C Loops Stabilize Four Types of Fluorescent Ag_n:DNA. *J. Phys. Chem. C*. **2009**, *113*, 4229-4233.
- (41) Vittala, S. K.; Saraswathi, S. K.; Joseph, J. Fullerene Cluster Assisted Self-Assembly of Short DNA Strands into Semiconducting Nanowires. *Chem. Eur. J.* **2017**, *23*, 15759-15765.
- (42) Li, J.; Jia, X.; Li, D.; Ren, J.; Han, Y.; Xia, Y.; Wang, E. Stem-directed growth of highly fluorescent silver nanoclusters for versatile logic devices. *Nanoscale*. **2013**, *5*, 6131-6138.
- (43) Zhou, Y.; Wang, J.; Yang, G.; Ma, S.; Zhang, M.; Yang, J. Cysteine-rich protein-templated silver nanoclusters as a fluorometric probe for mercury(II) detection. *Anal. Methods*. **2019**, *11*, 733-738.
- (44) An, J. H.; Park, S. J.; Kwon, O. S.; Bae, J.; Jang, J. High-Performance Flexible Graphene Aptasensor for Mercury Detection in Mussels. *ACS Nano*. **2013**, *7*, 10563-10571.
- (45) Zhou, G.; Chang, J.; Pu, H.; Shi, K.; Mao, S.; Sui, X.; Ren, R.; Cui, S.; Chen, J. Ultrasensitive Mercury Ion Detection Using DNA-Functionalized Molybdenum

- Disulfide Nanosheet/Gold Nanoparticle Hybrid Field-Effect Transistor Device. *Acs Sensors*. **2016**, *1*, 295-302.
- (46) Brouwer Albert, M.: Standards for photoluminescence quantum yield measurements in solution (IUPAC Technical Report). *In Pure Appl. Chem.*, 2011; Vol. 83; pp 2213.
- (47) Mangalath, S.; Abraham, S.; Joseph, J. pH-Responsive Fluorescence Enhancement in Graphene Oxide–Naphthalimide Nanoconjugates: A Fluorescence Turn-On Sensor for Acetylcholine. *Chem. Eur. J.* **2017**, *23*, 11404-11409.

CHAPTER 3: PART A

1D-ORGANIZATION AND THYMINE INDUCED TRANSITION OF MOLECULAR AGGREGATES IN A DIAMINOTRIAZINE FUNCTIONALIZED TETRAPHENYLETHYLENE DERIVATIVE



3A.1. ABSTRACT

A diaminotriazine functionalized Tetraphenylethylene derivative, **TPE-1** capable of intermolecular hydrogen bonding was synthesized and its self-assembly in dodecane was investigated. **TPE-1** displayed concentration dependent self-assembly in dodecane with characteristic 400 nm monomeric emission for very dilute concentrations and the gradual formation of 307 nm absorption and 430 nm emission band characteristic of aggregation with increase in concentration. Detailed analysis of temperature dependent changes at the aggregate absorption for different concentrations revealed the co-operative/nucleation-elongation pathway for **TPE-1** assembly. Morphology and optical microscopic analysis of these assemblies showed the

presence of blue emissive 1D-fibers with 4-5 nm in height, 70-80 nm in width, and several micrometers in length. Whereas at higher concentrations, these assemblies resulted in transparent supramolecular blue emissive gels with entangled network structure. Further, the self-assembly of **TPE-1** was tuned using a thymine derivative, **T-C12** having a higher association constant for the complementary hydrogen bonding with diaminotriazine (DAT) unit, compared to the self-association constant of DAT. In presence of **T-C12**, green emissive thin 1D-fibrous structures of **TPE-1**≡**T-C12** with 350 nm absorption maxima, 502 nm emission maxima, 2-3 nm height, 35-45 nm width and micrometers in length were formed at lower concentrations and opaque green emissive gels were formed at higher concentrations, instead of the blue emissive **TPE-1** assemblies. FT-IR and XRD studies of xerogels revealed the role of H-bonding, transition of molecular aggregates and molecular packing, responsible for the blue and green emissive assemblies in **TPE-1**. The molecular design and self-assembly strategy put forward here, demonstrate the potential of non-covalent hydrogen bonding interactions of nucleobase and nucleobase analogues in constructing supramolecular assemblies with directional control.

3A.2. INTRODUCTION

Nature practices non-covalent self-assembly as a tool to organize complex biological systems without compromising the control over such living systems. Inspired by this concept, biopolymers like peptides, oligonucleotides and their building blocks were extensively employed in the construction of functional architectures from small π -conjugated organic molecules for applications in chemical sensing, bio-medicine, bio-imaging, optoelectronics and photonics.¹⁻⁴ Among these biological templates, the high programmability and unparalleled

precision offered by DNA and its constituents renders them as promising candidates in organizing chemical systems.^{5,6} It was the invention of DNA objects by Seeman in 1991, which changed the entire identity of DNA from its biological context to material aspect.⁷ Later, the development of DNA nanotechnology using DNA-tiles and DNA-origami structures created a distinct space for DNA based functional assemblies in material science research.⁸ In addition to complex DNA nanostructures as templates, small ssDNA, dsDNA, branched DNA junctions, hairpin loops, nucleotides, nucleosides and nucleobases were also used for the hierarchical organization of nanoparticles, proteins and small organic molecules.^{9,10}

The molecular recognition property of nucleobases is governed primarily by hydrogen bonding interactions, and assisted by other non-covalent interactions like π - π stacking, electrostatic and groove binding interactions to form extended assemblies in most of the DNA based nanomaterials. Other than the aforementioned ideas of using DNA or its constituents directly as templates, the incorporation of nucleobases or nucleobase analogues into chemical systems by the rational molecular engineering, gives the key in our hand to predict and tune the self-assembly properties as required for specific applications. Melamine and cyanuric acid derivatives are the well exploited nucleobase analogues used to construct higher ordered assemblies.^{11,12}

π -Conjugated molecules having the structural capability to form organized supramolecular assemblies, with tunable properties have been extensively investigated for the construction of one-dimensional (1D), two-dimensional (2D) and higher ordered functional materials. Well studied π -conjugated aromatic systems include, perylene bisimide (PBI), phthalocyanine (Pcs), porphyrin (Pp), pyrene, naphthalene, hexabenzocoronene (HBC), tetrathiofulvalene (TTF),

triphenylene derivatives, and oligomers of thiophene (OT), fluorene (OF) and phenylenevinylenes (OPV).^{13,14} As a consequence, a large variety of self-assembled morphologies with ribbon, wire, rod, cylinder, sheet and flower like structures were developed. However, some of these fluorophores suffer from the aggregation caused quenching (ACQ) property upon self-assembly, which affects their optoelectronic performance.¹⁵ In order to overcome this disadvantage of conventional fluorophores, aggregation induced emission (AIE) active fluorophores were introduced as functional materials.^{16,17} Restriction of intramolecular rotation (RIR) is the key factor responsible for the AIE phenomenon in most of the AIE active luminogens.

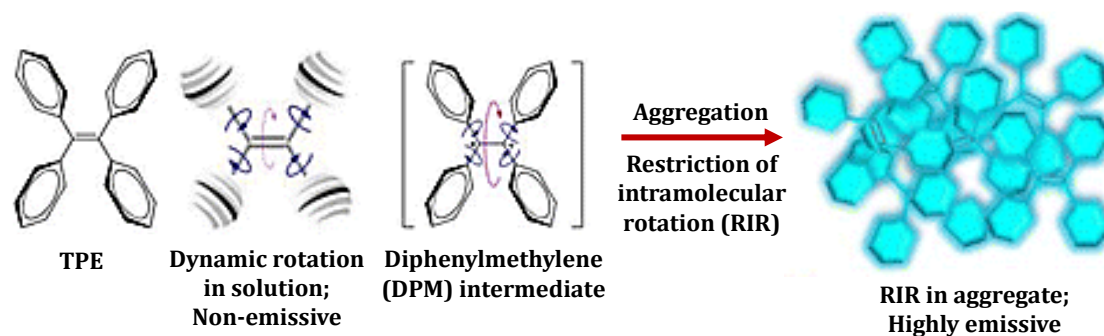


Figure 3A.1. Schematic representation of the AIE process in TPE. (Adapted from reference 16).

Tetraphenylethylene (TPE) and its derivatives are one among this category of promising AIE fluorophores used in chemical and biological sensing, and optoelectronic devices like solar cells, light emitting device and field effect transistors.^{18,19} TPE molecules in solution state are non-emissive, with the phenyl rings in dynamic motion and forms intermediate diphenylmethylene (DPM, two units) upon excitation. As a result of the friction between molecules with each other and with solvent, the excited state relaxes through non-radiative thermal and mechanical decay pathways. Upon aggregation of TPE, dynamic motion of phenyl rings get restricted and so excitons relaxes through the highly preferred radiative

decay pathways (Figure 3A.1).¹⁶ In line with the AIE concepts, there are several reports highlighting the solvent dependent tuning of optical and morphological properties of TPE-derivatives. Consequently, quite a lot morphologies including, globules, tubes, belts, 2D-sheets and flower like structures of TPE-derivatives were developed as required for specific applications.²⁰⁻²²

For example, 3D-flower like structures of amphiphilic TPE-derivatives were reported by S. V. Bhosale and co-workers using solvophobic control over the self-assembly and demonstrated their mechanoresponsive properties upon applying pressure, fuming and thermal conditions.²² Recently in 2020, Myongsoo Lee and Yanqui Wang reported 2D-chiral sheets of TPE-derivatives for selective sensing of enantiomers.²¹ Here, they have synthesized two amphiphilic TPE-derivatives, by functionalizing with tetra- and di- chiral oligoether dendrimers and demonstrated their self-assembly in aqueous methanol. The tetra-substituted molecule self-assembles into nonchiral 2D-sheets and the di-substituted molecule assembles into chiral 2D-sheets with 3.8 nm and 4.6 nm thickness, respectively (Figure 3A.2A).

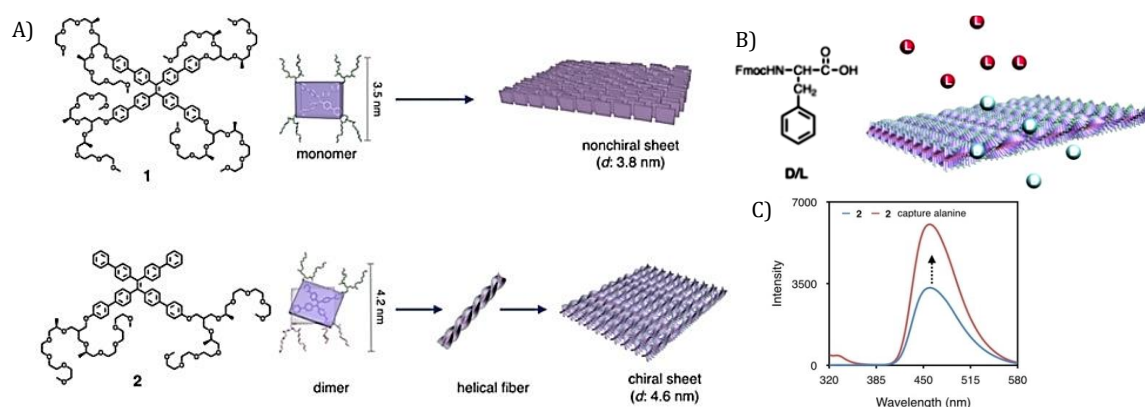


Figure 3A.2. Schematic representation showing the A) self-assembly of tetra- and di- oligoether dendrimer substituted TPE into nonchiral and chiral 2D sheets, respectively, B) selective separation of a single enantiomer from a racemic mixture of protected diphenylalanine and C) corresponding enhancement in the fluorescence of TPE upon separation of enantiomer (Adapted from reference 21).

Further, the chiral sheets were shown to selectively separate a single enantiomer from a racemic solution of phenylalanine (Figure 3A.2B) with an enhancement in the fluorescence emission (Figure 3A.2C), indicative of the increased RIR of TPE in presence of phenylalanine.

Although TPE derivatives with various morphologies were broadly employed in many applications, the directional control over the morphologies of supramolecular assemblies of TPE and tuning of their self-assembly and optical properties are less explored. Due to RIR in the chemical structure upon aggregation under solvophobic conditions, most of the TPE assemblies yet reported are with random aggregates or 2D sheets and 3D flowers like structures, without any order or control over the assembly. There are only very few reports which show the successful organization of TPE derivatives in to 1D nanostructures with directional control over the self-assembly. For example, from the pioneers of AIE: Tang's research group have shown the H-bonding directed self-assembly of fluorescent helical micro/nanofibers from L-leucine, L-valine and bivaline substituted chiral TPE derivatives using intermolecular H-bonding, π -stacking and electrostatic interactions.²³⁻²⁵

In 2017, the same group demonstrated the effect of stereoisomers, Z and E of ureidopyrimidinone substituted TPE derivative (Figure 3A.3A) on the molecular packing and supramolecular self-assembly.²⁶ In this work, they have well explained the synthesis, separation and characterizations of Z and E isomers, and their aggregation properties were studied in chloroform/hexane solvent mixture. In solution state, the isomers displayed similar optical properties. Whereas, in the aggregate state E-isomers were blue emitting with linear fiber like structures and Z-isomers were green emitting with small particle like structures, attributed to the

crystalline and amorphous nature of aggregates, respectively (Figure 3A.3B). In addition, they have exploited these distinct supramolecular assemblies of TPE-isomers: E-isomer to fabricate fluorescent photopatterns and Z-isomers for the selective detection of Hg^{2+} ions inside ureidopyrimidinone cavity.

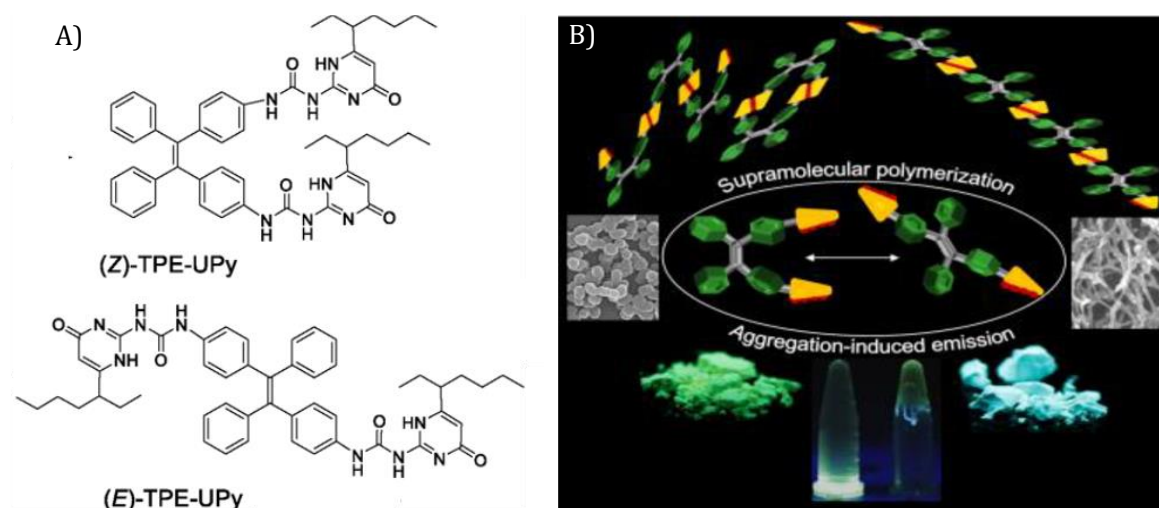


Figure 3A.3. A) Chemical structure of Z and E isomers of ureidopyrimidinone substituted TPE and B) schematic representation of E isomer forming blue emissive supramolecular fibers and Z isomer forming green emissive particle like assemblies (Adapted from reference 26).

If we look in detail in to the aforementioned 1D-assemblies of TPE, all of them possess hydrogen bonding moieties in the chemical structures as a common factor, and yet there is no sufficient clear evidence for role of H-bonding in these assemblies. Therefore, in line with this concept and due to our interest in using DNA or nucleobase and nucleobase analogues in templating the supramolecular functional materials, we set our objective of this present chapter as to investigate the H-bonding directed construction of 1D-assemblies of TPE using a nucleobase analogue, and tune its self-assembly and properties with the addition of complementary hydrogen bonding moieties. A detailed review of literature in this sub-topic revealed few reports of TPE-DNA assemblies used for sensing and catalytic applications.²⁷⁻²⁹

Xiaoding Lou *et al.* in 2014 reported a fluorescence turn on sensor for the selective detection of adenine rich ssDNA from its corresponding dsDNA segment, using the AIE property of a thymine functionalized TPE (TPE-T) derivative (Figure 3A.4A).²⁷ Here, the free adenine units in ssDNA forms complementary H-bonding with the thymine unit of TPE-T and results in the aggregation of TPE molecules. On the other hand, in the case of dsDNA there is no free adenine groups to interact with TPE-T, and fails to display AIE. Other than the external non-covalent interaction of TPE with DNA sequences, covalently modified TPE-DNA conjugates with improved specificity were also used for DNA sensing and construction of self-assembled functional templates for catalytic applications.^{28,29}

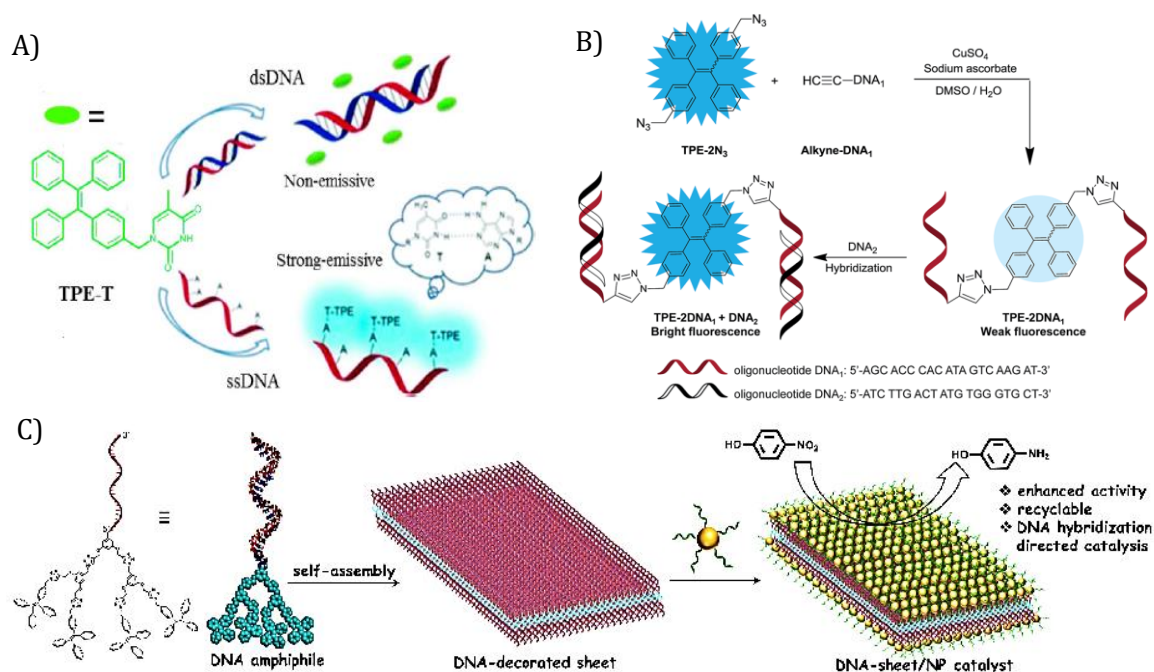


Figure 3A.4. Schematic representation of a fluorescence turn-on sensor for A) adenine rich ssDNA and B) specific ssDNA sequences (Adapted from references 27 and 28). C) Self-assembly of TPE-DNA amphiphiles into nanoparticle decorated 2D-sheets and its recyclable catalytic action (Adapted from references 29).

For example, Ruoyu Zhang and co-workers reported a fluorescence turn-on sensor for the detection of precise ssDNA sequences by using a covalently modified TPE-

ssDNA conjugate (Figure 3A.4B).²⁸ Here, initially the ssDNA sequence complementary to the target sequence is covalently modified on to TPE by click chemistry and upon hybridization with target, TPE aggregates and displays AIE.

N. Krishnan *et al.* reported the amphiphilicity driven self-assembly of covalently modified TPE-DNA conjugates in to 2D nanosheets, which was further decorated with gold nanoparticles and demonstrated its recyclable catalytic activity (Figure 3A.4C).²⁹ Here, the common aggregation tendency of nanoparticles with increase in concentration was avoided by specifically positioning the nanoparticles through complementary hydrogen bonding between ssDNA pointing outward of the 2D sheet and ssDNA functionalized on the nanoparticles. In addition, they have proved that the catalytic activity to convert 4-nitrophenol to 4-aminophenol of 2D-sheet densely decorated with nanoparticle was rationally very high with fifteen times recyclability, compared to the non-assembled single ssDNA modified nanoparticle conjugate.

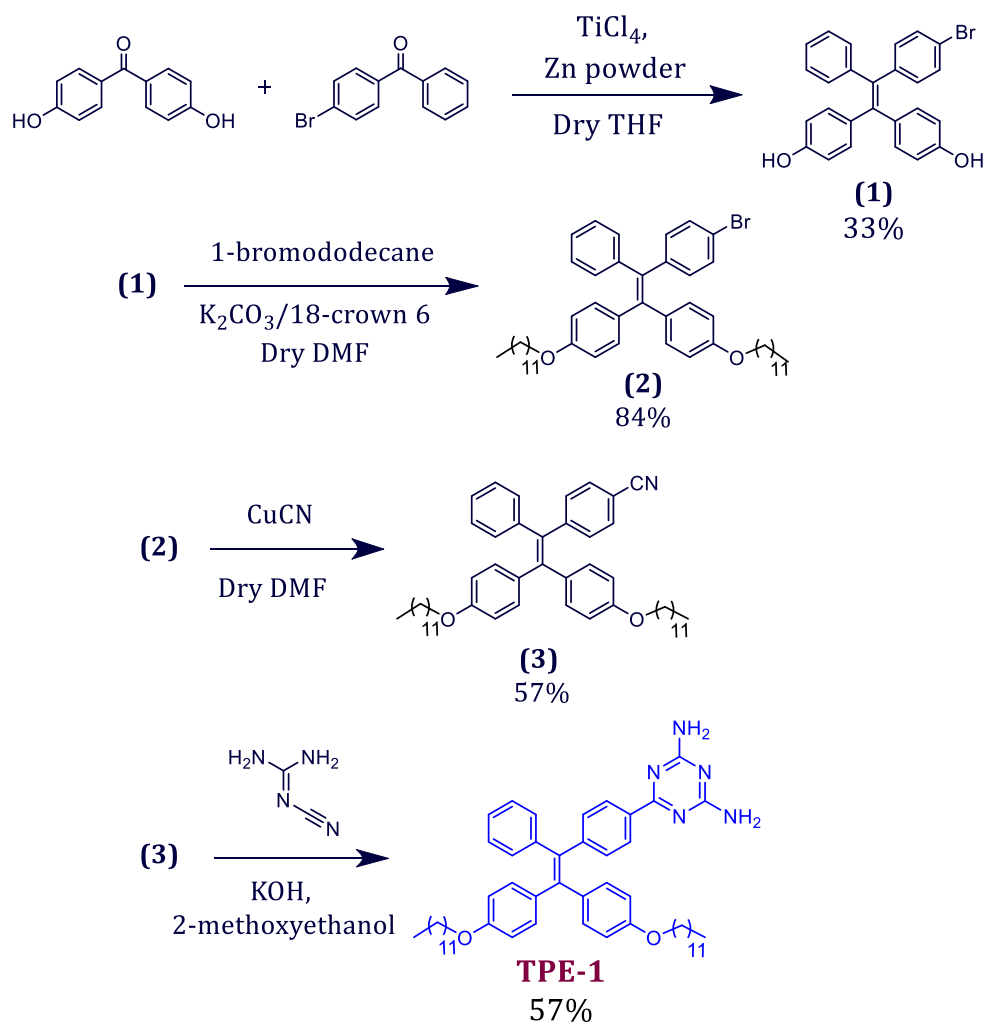
Therefore, with the above understanding of the possible TPE-DNA interactions and assemblies in different solvent systems yet reported, we put forward the strategy of incorporating nucleobase or nucleobase analogues on to TPE chromophore to construct H-bonding directed functional 1D assemblies of TPE. In this chapter, we discuss the design, synthesis and self-assembly studies of a diaminotriazine (DAT) functionalized TPE derivative (**TPE-1**). Random aggregates of **TPE-1** were observed in THF-water solvent system, whereas intensely blue emissive self-assembled 1D-fibers were formed in dodecane solvent. Further, the self-assembly and properties were tuned using a complementary H-bonding thymine derivative (**T-C12**), which changes the self-assembly of **TPE-1** to green emissive thin fibrous structures with a different monomeric repeating unit. At

higher concentrations, these 1D assemblies of **TPE-1** forms supramolecular gels. Detailed photophysical and morphological studies, and gel characterizations were performed to deduce the H-bonding directed self-assembly mechanism of the 1D constructs of the TPE derivative.

3A.3. RESULTS AND DISCUSSION

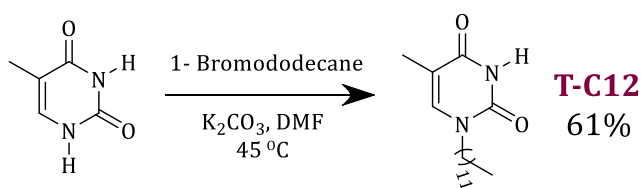
3A.3.1. Synthesis of TPE-1 and T-C12

The molecule **TPE-1** was synthesized by following a four-step synthetic scheme starting with McMurry coupling between 4,4'-Dihydroxybenzophenone and 4-Bromobenzophenone as shown in Scheme 3A.1.



Scheme 3A.1. Synthesis of bis(dodecyloxy) substituted **TPE-DAT** derivative, **TPE-1**.

Initially, the cross product of McMurry coupling 4,4'-(2-(4-bromophenyl)-2-phenylethene-1,1-diyl)diphenol (**1**) was obtained in 33% yield, which upon O-alkylation reaction with 1-bromododecane gave 84% of (**2**). Subsequently, (**2**) was converted into its cyano-derivative using CuCN to give (**3**), followed by the aromatization reaction with dicyandiamide in presence of KOH base to obtain the final product, **TPE-1** in 57% yield. The thymine derivative, **T-C12** was synthesized by the N-alkylation reaction of thymine using 1-Bromododecane as shown in Scheme 3A.2. All the intermediates and final products were characterized using ^1H NMR, ^{13}C NMR and HRMS-ESI analysis techniques. Detailed synthetic procedures and characterization data are provided in the experimental section.



Scheme 3A.2. Synthesis of dodecyl substituted thymine derivative, **T-C12**.

3A.3.2. Aggregation induced emission properties of **TPE-1**

Initially, the UV-visible absorption and emission characteristics of **TPE-1** molecule in soluble solvents like THF, acetonitrile and chloroform were studied. At a $20\ \mu\text{M}$ concentration, **TPE-1** displayed an absorption band around 350 nm corresponding to the $\pi\text{-}\pi^*$ transition of TPE chromophore (Figure 3A.5A) and the corresponding weakly emissive fluorescence maxima in the 400-450 nm range (Figure 3A.5B) in all the prior mentioned solvents with solvatochromic properties. Whereas, the UV-visible absorption and emission studies of **TPE-1** in different THF-water fractions clearly indicated the solvophobic aggregation property with decrease and broadening in the 350 nm absorption band along with gradual shift

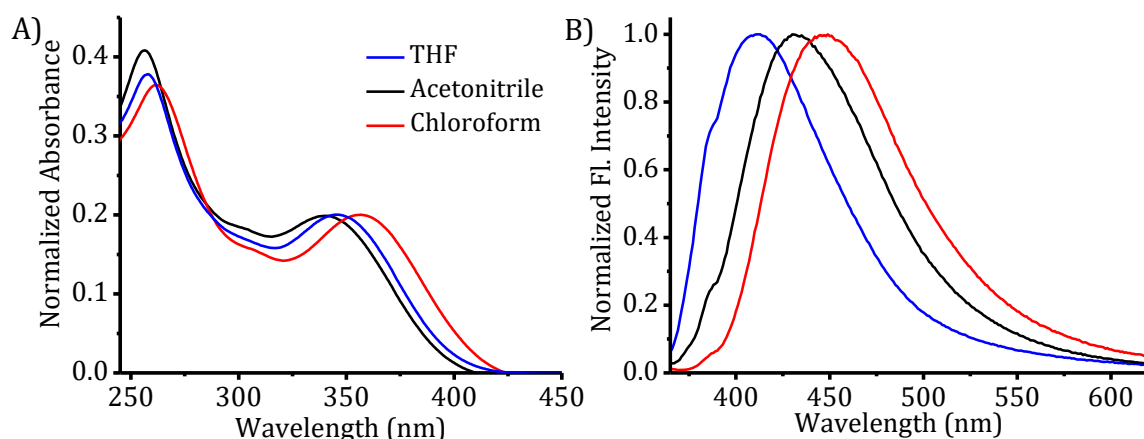


Figure 3A.5. A) Absorption and B) corresponding fluorescence emission spectra of **TPE-1** in THF, acetonitrile and chloroform.

and slight enhancement in fluorescence emission from 400 nm to 450 nm with increasing the water fraction (Figures 3A.6A & 3A.6B). Above 60% water fraction, **TPE-1** started to make larger aggregates and eventually precipitates with a reasonably red shifted yellow emission (around 530 nm) for the resulting suspension. Figure 3A.7A shows the images of fluorescence changes of **TPE-1** in THF-water solvent mixtures with increasing fractions of water, under UV light (365 nm) illumination conditions.

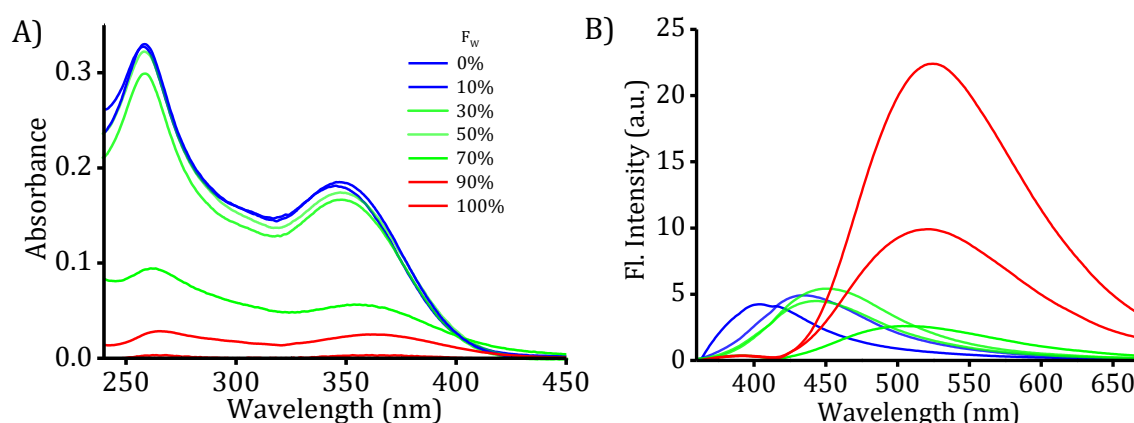


Figure 3A.6. A) Absorption and B) corresponding emission spectra of **TPE-1** (20 μM) in different THF-water mixtures.

The morphological changes associated with the aggregation process was studied using AFM. Random spherical and sheet like structures with nano to

micrometer sized aggregates of **TPE-1** were observed in different fractions of THF-water solvent system (Figures 3A.7B-F). Morphology changes indicate the typical hydrophobicity driven, uncontrolled random aggregation tendency of TPE with increasing fractions of water content, which is responsible for the observed UV-visible absorption and fluorescence changes.

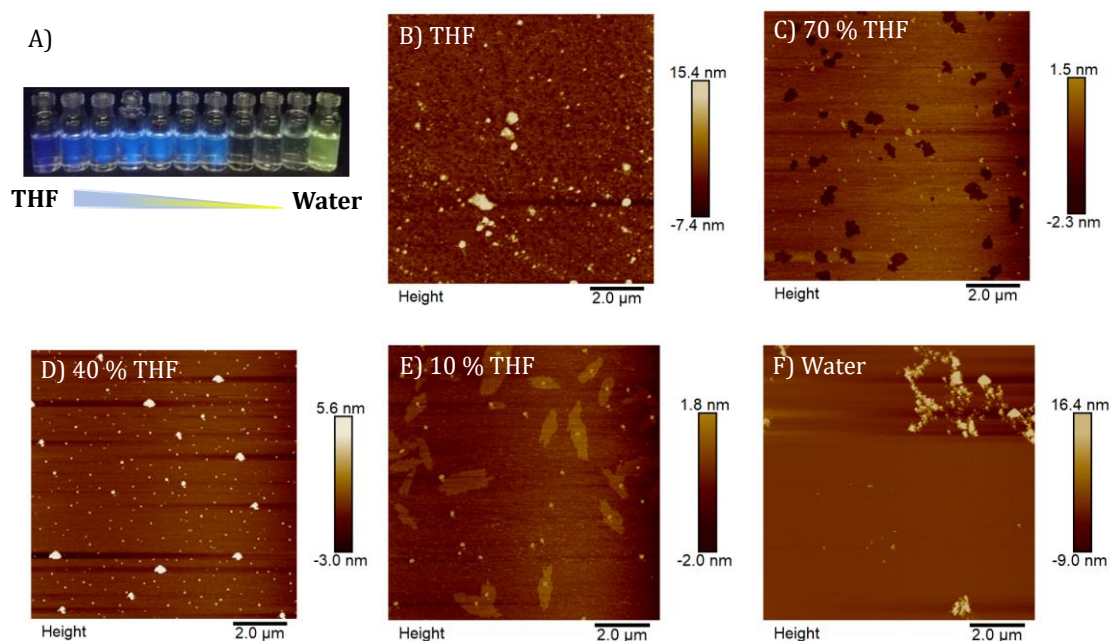


Figure 3A.7. A) Images of fluorescence changes of **TPE-1** under UV-light (365 nm) illumination and B-F) AFM images of **TPE-1** (20 μM) in different THF-water fractions.

3A.3.3. Self-assembly of TPE-1

The photophysical properties of **TPE-1** in a non-polar solvent like dodecane were analyzed to understand the hydrogen bonding directed controlled assembly of TPE molecules. Concentration dependent UV-visible absorption studies in dodecane showed the gradual formation of a new absorption band at 307 nm along with the 352 nm π - π^* absorption band (Figure 3A.8A). At lower concentrations (<10 μM), the fluorescence emission spectra, when excited at 350 nm or 327 nm showed mostly the characteristic monomer emission centered around 400 nm (Figures 3A.8B and 3A.8C). At higher concentrations, the emission spectra of **TPE-1** gradually shift to

lower energy (~ 430 nm) and became broad and featureless with an enhancement in the fluorescence intensity indicating the possibility of AIE. Further, the absorption spectra of $10 \mu\text{M}$ **TPE-1** at 298 K and 363 K revealed the existence of monomeric and assembled states with absorption maxima of 345 nm and 352 nm, respectively, even at very low concentrations (Figure 3A.8D).

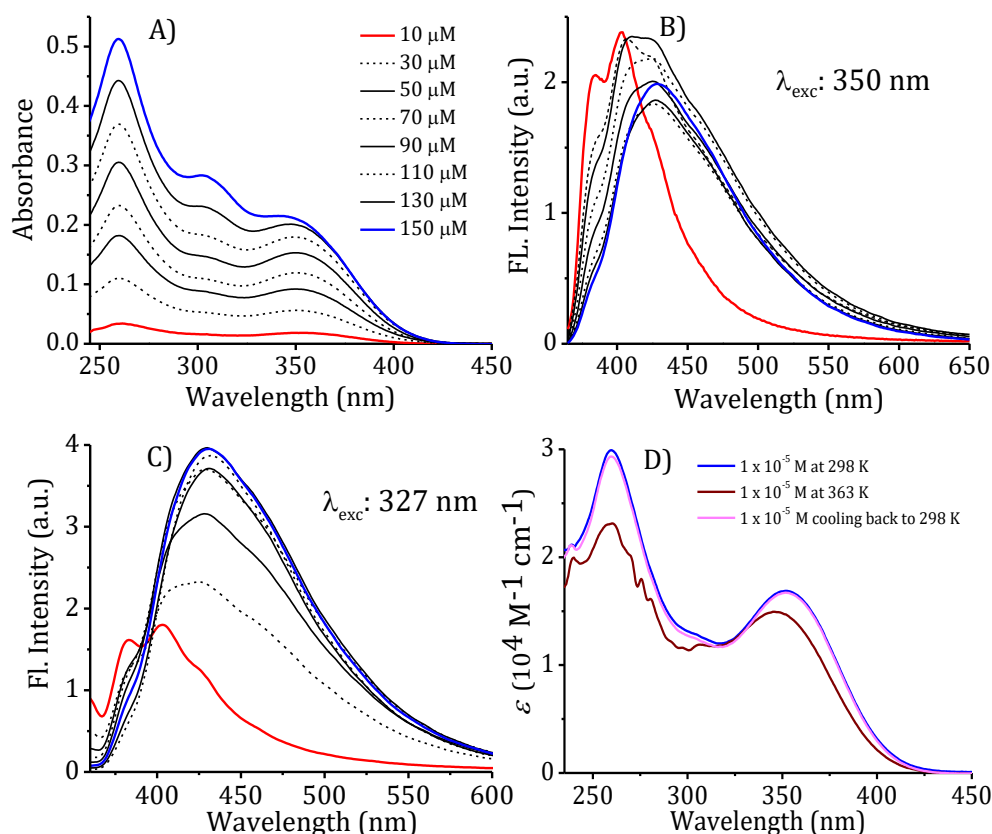


Figure 3A.8. Concentration dependent changes in the A) UV-visible absorption and corresponding fluorescence emission spectra with B) $\lambda_{\text{exc}} = 350$ nm & C) $\lambda_{\text{exc}} = 327$ nm of **TPE-1** in dodecane. D) Temperature dependent absorption spectra of $10 \mu\text{M}$ **TPE-1**.

Based on these preliminary concentration dependent studies of **TPE-1** self-assembly, we choose a fixed **TPE-1** concentration of 3×10^{-4} M for performing detailed self-assembly studies. The UV-visible absorption spectra of chloroform and dodecane solutions of **TPE-1** at 298 K displayed the monomeric absorption band corresponding to molecularly dissolved state at 352 nm and aggregate absorption band at 307 nm, respectively (Figure 3A.9A). As indicated, the 307 nm blue shifted

absorption band implies the aggregation behavior of **TPE-1** in dodecane. Corresponding fluorescence emission spectra (Figure 3A.9B) of **TPE-1** recorded at 298 K displayed the presence of weakly emissive monomeric state in chloroform at 447 nm ($\Phi_F = 0.04\%$) and highly emissive aggregates with an emission maximum of 430 nm in dodecane ($\Phi_F = 32\%$)

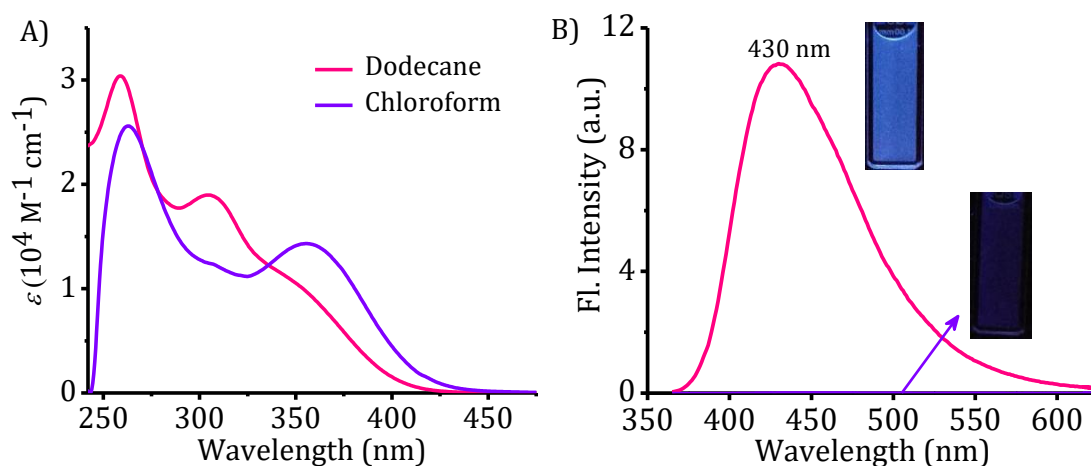


Figure 3A.9. A) UV-visible absorption and B) fluorescence emission spectra of **TPE-1** (3×10^{-4} M) in dodecane and chloroform ($\lambda_{\text{exc}} = 350$ nm and inset of B shows corresponding photographs under 365 nm UV light).

To get further insight into the aggregation behavior, temperature dependent absorption and emission studies of dodecane solutions of **TPE-1** were conducted. Upon heating, a gradual decrease in the aggregate band at 307 nm was observed with a concomitant enhancement of monomeric absorption band at 345 nm, with an isosbestic point at 327 nm, indicating the temperature assisted dissociation of aggregates into monomers (Figure 3A.10A). Similarly, a gradual quenching in the fluorescence emission band at 430 nm upon excitation at the isosbestic point (Figure 3A.10B) supported the dissociation of aggregates upon heating. Further, the self-assembly pathway was monitored by recording the changes in absorption and emission spectra by cooling the corresponding dodecane solutions of **TPE-1** from 363 K to 293 K.

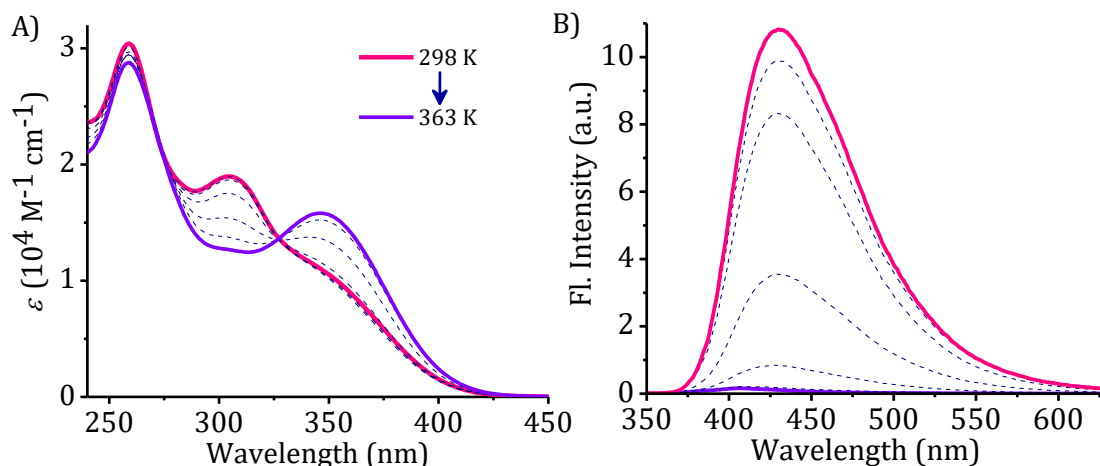


Figure 3A.10. Temperature dependent changes in A) absorption and B) fluorescence emission spectra ($\lambda_{\text{exc}} = 327$ nm) of 3×10^{-4} M **TPE-1** upon heating from 298 K to 363 K.

Upon cooling from 363 K to 303 K, the absorption spectra showed a slight enhancement in the 307 nm band (Figure 3A.11A). The absorption band at 346 nm also showed a slight enhancement and a red shift to 352 nm, upon initial cooling to 303 K. Further cooling to 293 K caused a sudden enhancement in the aggregate absorption at 307 nm and a concomitant decrease in the absorption at 352 nm (inset of Figure 3A.11A). The corresponding fluorescence emission spectra displayed the formation of aggregates with 430 nm emission band at 303 K and a sudden enhancement upon further cooling to 293 K (Figure 3A.11B), indicative of the cooperative pathway for the self-assembly of **TPE-1** in dodecane.

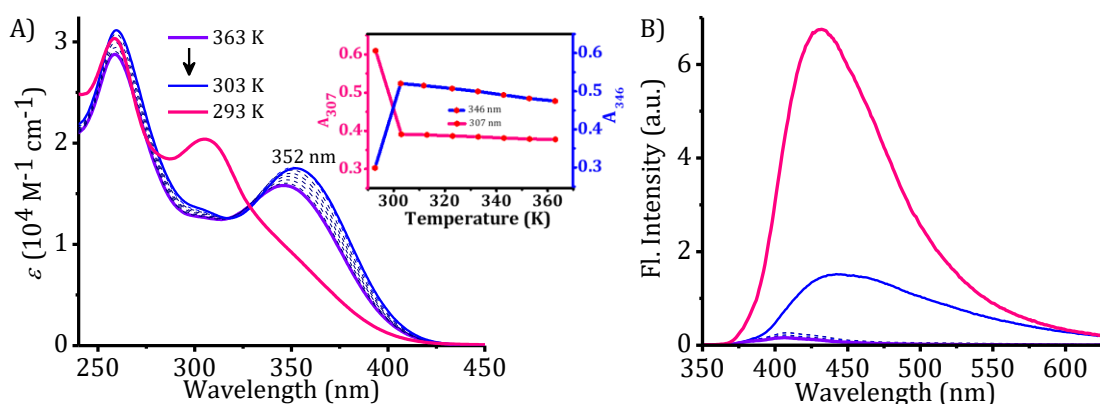


Figure 3A.11. Temperature dependent changes in the A) absorption (inset shows changes in absorption at 307 nm and 346 nm) and B) emission spectra of 3×10^{-4} M **TPE-1** in dodecane upon cooling from 363 K to 293 K.

3A.3.4. Thermodynamic and morphological features of TPE-1 self-assembly

Detailed analysis of **TPE-1** self-assembly pathway was carried out by monitoring the temperature dependent changes at the aggregate absorption band (307 nm) for different concentrations, by keeping a fixed cooling rate of 1 K min⁻¹. Upon cooling, plot of fraction of aggregates (α_{agg}) with respect to temperature for a concentration range of 4×10^{-4} M to 7×10^{-4} M solutions of **TPE-1** resulted in the cooling curves with non-sigmoidal nature (Figures 3A.12). All these cooling curves were well fitted with the cooperative equilibrium model (EQ),³⁰ suggesting the ‘nucleation-elongation’ pathway for the self-assembly of **TPE-1** in dodecane. The elongation temperatures (T_e) for the cooling curves were found to increase with concentration; 294.6 K for 4×10^{-4} M, 295.2 K for 5×10^{-4} M, 299.4 K for 5.9×10^{-4} M and 301.6 K for 7×10^{-4} M. These results further support the low temperature-sudden enhancement observed in the aggregate absorption band of **TPE-1**.

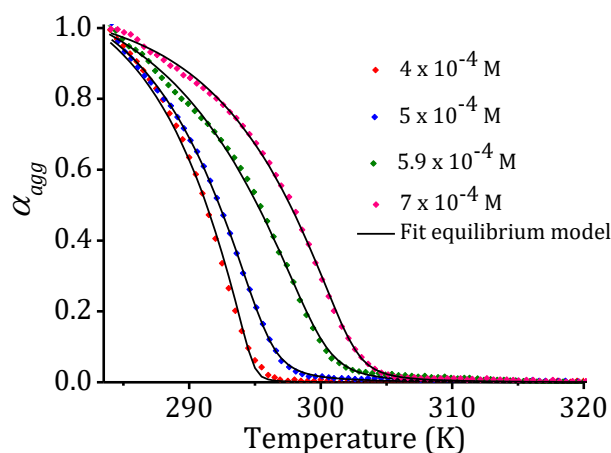


Figure 3A.12. Plots of fraction of aggregates (α_{agg}) against temperature for different concentrations of **TPE-1** in dodecane. The plots were fitted using the individual EQ model of cooperative polymerization.³⁰

Thermodynamic (TD) parameters of this self-assembly were derived using the van't Hoff plot (Figure 3A.13) constructed from the reciprocal of T_e , ($1/T_e$) against logarithm of reciprocal concentration, $\ln(1/C)$. From the linear fits of van't

Hoff plot, standard enthalpy (ΔH°) and standard entropy (ΔS°) for the assembly were obtained as $-55.99 \text{ kJ mol}^{-1}$ and $-125.23 \text{ J mol}^{-1} \text{ K}^{-1}$, respectively. From these parameters, the standard Gibbs free energy (ΔG°) for the self-assembly at 298 K was calculated to be $-18.6 \text{ kJ mol}^{-1}$. The obtained TD values were in line with the reported literatures on H-bonding directed nucleation-elongation supramolecular assemblies, which further confirms the cooperative pathway of **TPE-1** self-assembly.^{31,32}

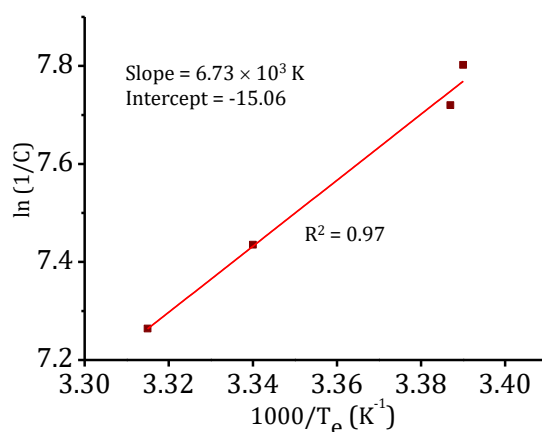


Figure 3A.13. van't Hoff plot constructed from the reciprocal of T_e , ($1/T_e$) versus logarithm of reciprocal concentration ($\ln(1/C)$).

The morphology of **TPE-1** self-assembly were explored using Transmission Electron Microscopy (TEM) and Atomic Force Microscopy (AFM) techniques. TEM images of as-prepared and heat-cooled samples of **TPE-1** assemblies in dodecane revealed the presence of individual and bundled nanofibers, respectively, with 70-80 nm in width and several micrometers in length (Figures 3A.14A & 3A.14B). In agreement with TEM, individual and less bundled fibres were observed in the AFM images of as-prepared **TPE-1** (Figure 3A.14C), while highly bundled fibres with 80-120 nm width and 4-5 nm in height were observed for completely assembled samples drop-casted from the temperature-controlled, heat-cooled **TPE-1** (Figures 3A.14D & 3A.14E). The height profiles for the bundled fibres obtained from the AFM image is given in Figure 3A.14F.

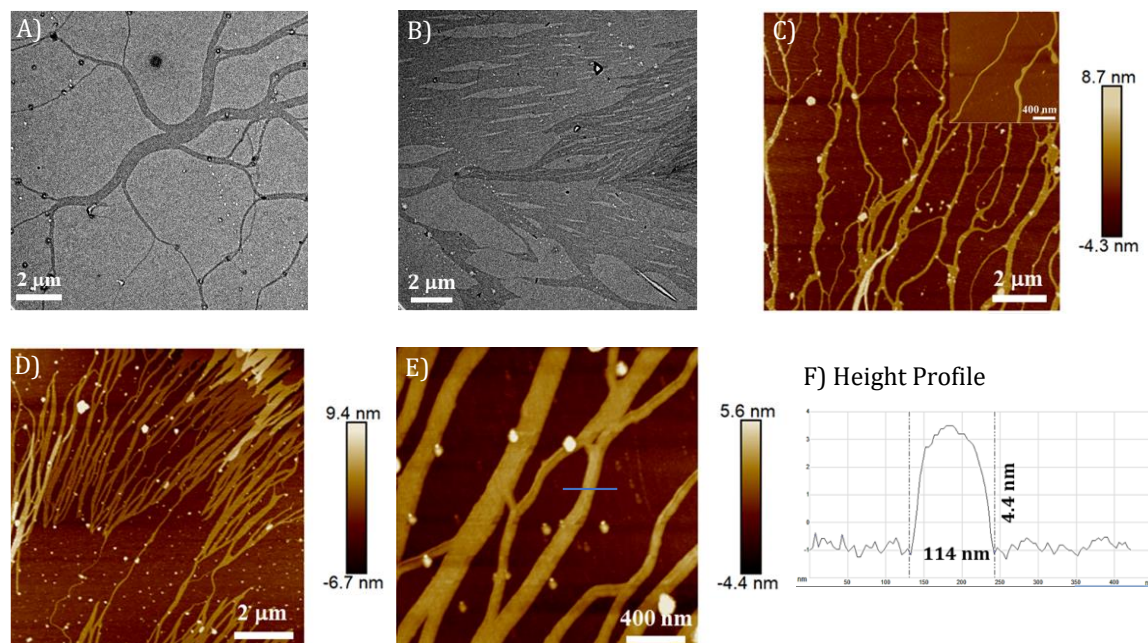


Figure 3A.14. TEM and AFM images of A), C) as such and B), D) heat-cooled samples drop-casted from 3×10^{-4} M **TPE-1** in dodecane. E) zoomed image of D and F) corresponding height profile (blue line in E shows the area of height profile).

3A.3.5. T-C12 directed changes in the TPE-1 self-assembly

Competitive molecular recognition directed tuning of the optical and morphological properties of **TPE-1** 1D-assemblies in dodecane solutions were studied by introducing a thymine derivative, **T-C12**, which can form stronger H-bonds with DAT. Sequential addition of **T-C12** to the self-assembled **TPE-1** (3×10^{-4} M) showed the dissociation of aggregates as indicated by a gradual decrease in the 307 nm aggregate absorption band and increase in the 350 nm monomer absorption band (Figure 3A.15A). Similarly, the emission spectra showed quenching of 430 nm aggregate band with the sequential addition of **T-C12** and the changes follow a 1:1 equivalent ratio of **TPE-1** to **T-C12** (Figure 3A.15B). Above this ratio, negligible changes were observed in the absorption and emission spectra. These results suggest that, the introduction of a competitive complementary H-bonding molecule perturb the homo-assembly of **TPE-1** leading to either monomeric units or H-

bonded **TPE-1**≡**T-C12** assemblies. Further, heating of a solution of **TPE-1** and **T-C12** (1:1) from 298 K to 363 K resulted in the complete disappearance of 307 nm aggregate band with concomitant increase in the 345 nm monomer absorption band (Figure 3A.16A). Correspondingly, the emission spectra showed complete quenching of the 430 nm emission band, supporting the changes in absorption spectrum (Figure 3A.16B).

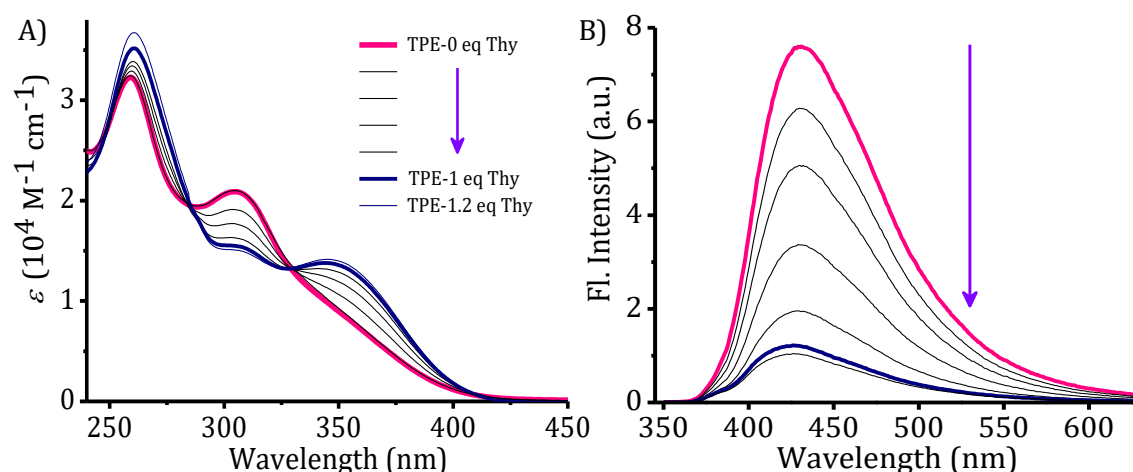


Figure 3A.15. Changes in the A) absorption and B) emission spectra with the sequential addition of **T-C12** (0-1.2 equivalent) into the $3 \times 10^{-4} \text{ M}$ **TPE-1** in dodecane ($\lambda_{\text{exc}} = 327 \text{ nm}$).

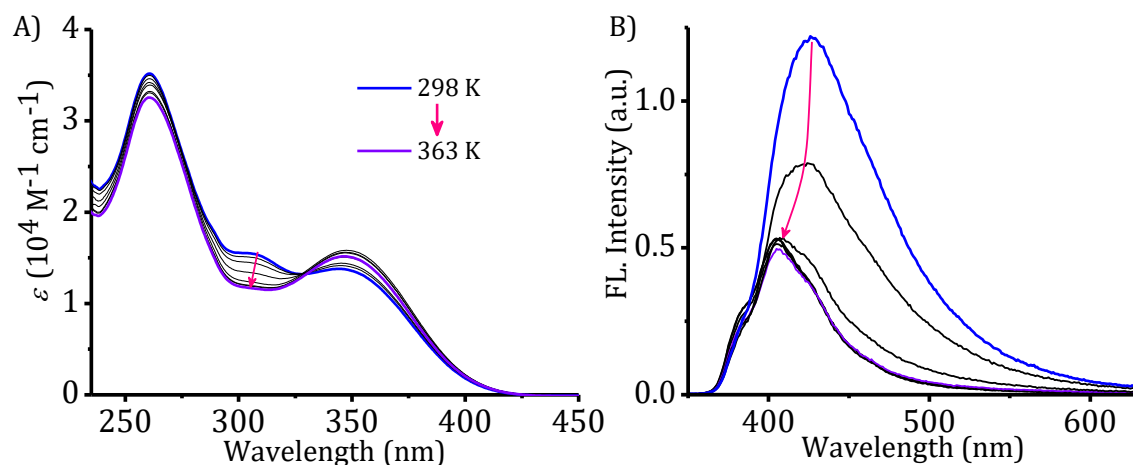


Figure 3A.16. Temperature dependent changes in A) UV-visible absorption and B) fluorescence emission spectra ($\lambda_{\text{exc}} = 327 \text{ nm}$) of a mixture of **TPE-1** and **T-C12** ($3 \times 10^{-4} \text{ M}$, 1:1) in dodecane upon heating from 298 K to 363 K.

Upon controlled cooling of this solution from 363 K to 293 K, an enhancement in the absorption around 346 nm with a 4 nm red shift of the

maximum to 350 nm was observed (Figure 3A.17A). Notably, the absorption around 307 nm remains unchanged, indicating that the heat-cool process didn't lead to the formation of (blue emissive) aggregates of **TPE-1**. Instead, a strongly green emissive aggregate with a 10% fluorescence quantum yield was formed in presence of **T-C12**, as indicated by the corresponding emission spectra (Figure 3A.17B and inset shows the corresponding photograph under UV-light). Thus, the results of the temperature dependent absorption and emission studies of **TPE-1** in presence of **T-C12** suggest that, **T-C12** can effectively perturb the homo-assembly of **TPE-1** (blue emissive aggregates), leading to the formation of **TPE-1**≡**T-C12** hetero-assembly with characteristic green emission.

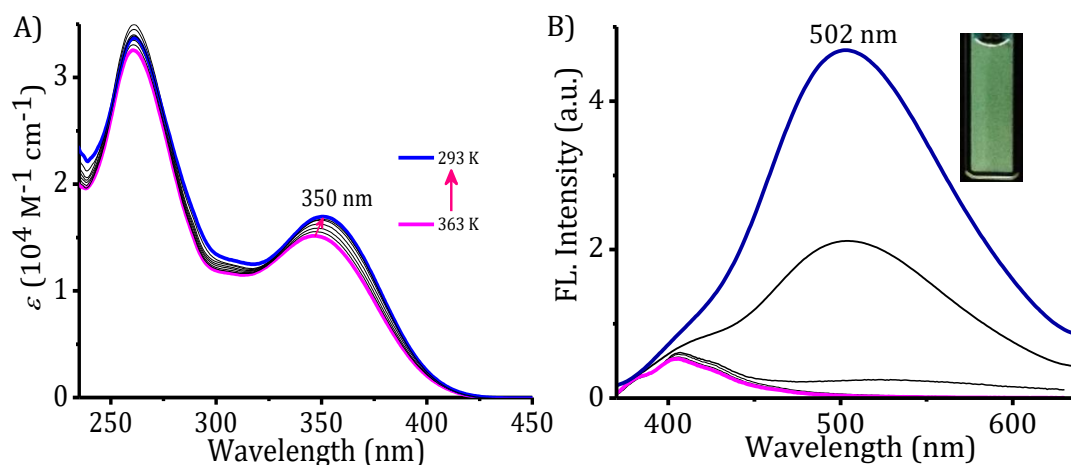


Figure 3A.17. Temperature dependent changes in the A) absorption and B) emission spectra of **TPE-1**≡**T-C12**, upon cooling from 363 K to 293 K ($\lambda_{\text{exc}} = 327 \text{ nm}$). Inset of B shows the corresponding fluorescence image of sample under UV light (365 nm) illumination.

The association constant for the formation of DAT-thymine complex via complementary H-bonding is two order higher compared to self-association constants of DAT.³³ As a result, the formation of complementary H-bonded **TPE-1**≡**T-C12** units in the presence of **T-C12** may dominate the formation of intermolecular H-bonded **TPE-1** molecules. Therefore, detailed investigations of their molecular packing arrangements in these assemblies are required to

understand the distinct blue and green emissive assemblies formed in the absence and presence of **T-C12**, respectively.

3A.3.6. Morphological studies of **TPE-1**≡**T-C12** assembly

Distinct from the bundled fiber like morphology of **TPE-1**, TEM images of **TPE-1**≡**T-C12** assembly displayed thin and stiff fibrillar structures, with 30-40 nm width and few micrometers in length (Figures 3A.18A & 3A.18B). The length and width of nanofibers in **TPE-1**≡**T-C12** assembly was less than that in the blue emissive 1D-assemblies of **TPE-1**. Similarly, in strong agreement with TEM, the AFM morphology of **TPE-1**≡**T-C12** also displayed the presence of thin nano-fibrillar

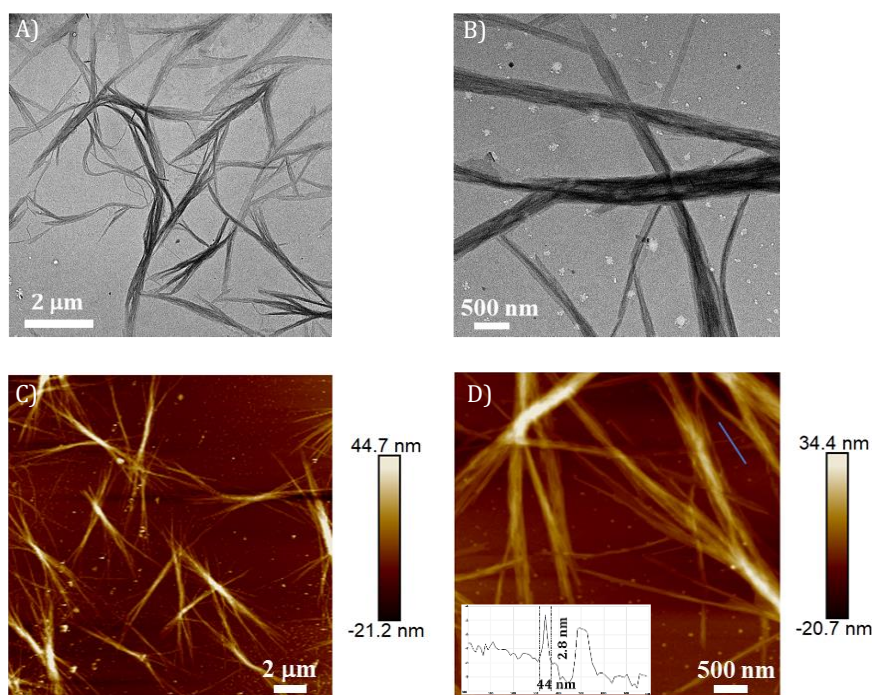


Figure 3A.18. A), B) TEM and C), D) AFM images of **TPE-1**≡**T-C12** (3×10^{-4} M, 1:1) drop-casted from dodecane and inset of D shows the height profile of a single fiber in D (below the blue line).

structures with 2-3 nm height and 35-45 nm width (Figures 3A.18C & 3A.18D, inset shows the height profile of a very thin fiber observed in Figure 3A.18D). Thus, the TEM and AFM morphologies of **TPE-1** and **TPE-1**≡**T-C12** clearly show the structural transition from bundled nanofibers to thin nano-fibrillar structures. This reduced

length and entirely different fibrous morphologies observed for **TPE-1** in the presence of **T-C12**, further suggest the possibility of having different molecular arrangements in these two types of assemblies.

3A.3.7. Fluorescence lifetime and optical microscopic analysis

The fluorescence decay profiles of **TPE-1** in the absence and presence of **T-C12** were analyzed using picosecond, time correlated single photon counting (TCSPC) techniques to understand the perturbations in the photophysical properties, accompanying the molecular self-assembly. The monomer emission of **TPE-1** in chloroform displayed mono-exponential decay ($\lambda_{em} = 447$ nm) with a lifetime of 3.52 ns, whereas 1D-assemblies in dodecane ($\lambda_{em} = 430$ nm) displayed biexponential decay with lifetimes of 2.45 ns (90%) and 0.76 ns (10%) (Figure 3A.19A).

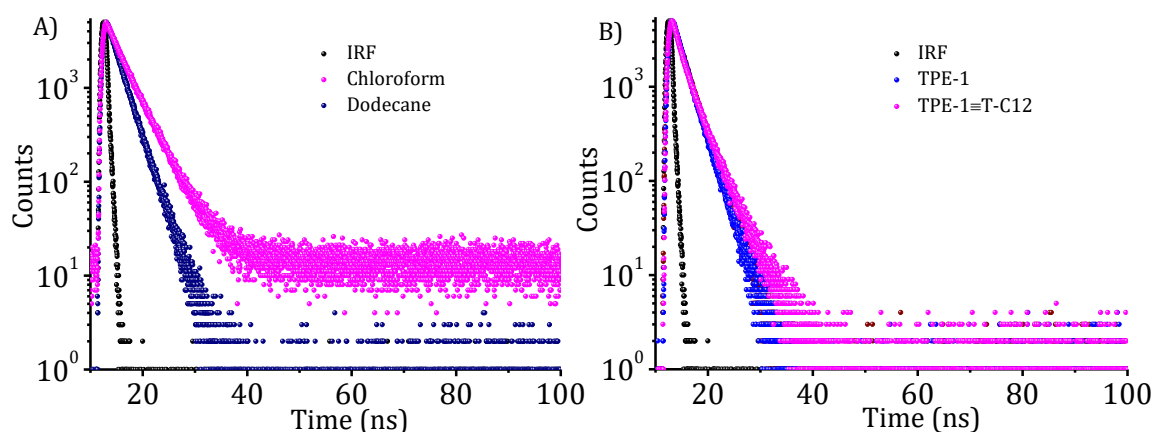


Figure 3A.19. Fluorescence decay profiles of A) **TPE-1** in chloroform and dodecane (3×10^{-4} M), and B) heat-cooled samples of **TPE-1** and **TPE-1** \equiv **T-C12** (3×10^{-4} M, 1:1) samples in dodecane.

Similar to the **TPE-1** 1D assemblies in dodecane, the heat-cooled solutions of **TPE-1** \equiv **T-C12** also fits to a biexponential decay with slightly enhanced lifetimes 2.86 ns (77%) and 0.86 ns (22%) (Figure 3A.19B). This difference in the lifetime values could be attributed to the formation of complementary H-bonded **TPE-1** \equiv **T-C12**

hetero-molecular assemblies in presence of **T-C12**, instead of the homo-molecular assemblies of **TPE-1**.

To get more insight into the self-assembly process, we also recorded the concentration dependent changes in fluorescence decay profiles of **TPE-1** and time resolved emission spectra (TRES) of **TPE-1** and **TPE-1**≡**T-C12** assemblies. At relatively lower concentrations of **TPE-1** (10 μM) in dodecane, a biexponential decay with lifetimes of 3.6 ns (74%) and 1.02 ns (26%) was observed and the longer fluorescence lifetime of 3.6 ns was closer to the lifetime value of **TPE-1** monomer in chloroform (Figure 3A.20). Yet there is evidence for aggregation even at this concentration, which justifies the biexponential behaviour. At higher concentrations of 1×10^{-4} M (2.45 ns; 74% and 0.15 ns; 14%) and 5×10^{-4} M (2.4 ns; 91% and 0.7 ns; 9%), fluorescence decay profiles were similar to that obtained for 3×10^{-4} M solutions in dodecane, which infers the concentration dependent self-assembly of **TPE-1**, as observed in UV-visible absorption and fluorescence emission studies.

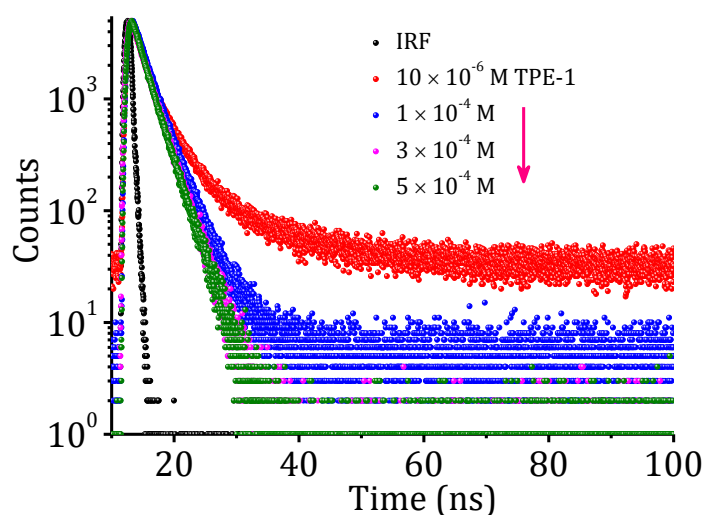


Figure 3A.20. Concentration dependent changes in the fluorescence decay profiles of **TPE-1** in dodecane.

TRES analysis of **TPE-1** and **TPE-1**≡**T-C12** dodecane solutions using a 375 nm laser excitation (<200 ps pulse width) are shown in Figures 3A.21A and 3A.21B,

which shows the spectral evolution during the 200 ps – 9.5 ns window. The TRES spectra show independent emission spectral evolution for the two assemblies and there is no evidence for exciton migration or excimer formation in both cases. Moreover, in the case of heat-cooled samples of **TPE-1**≡**T-C12** assemblies, there is no contribution observed from the blue emitting component of **TPE-1** homo-assembly indicating a complete transition to a competitive hetero-assembly (**TPE-1**≡**T-C12**).

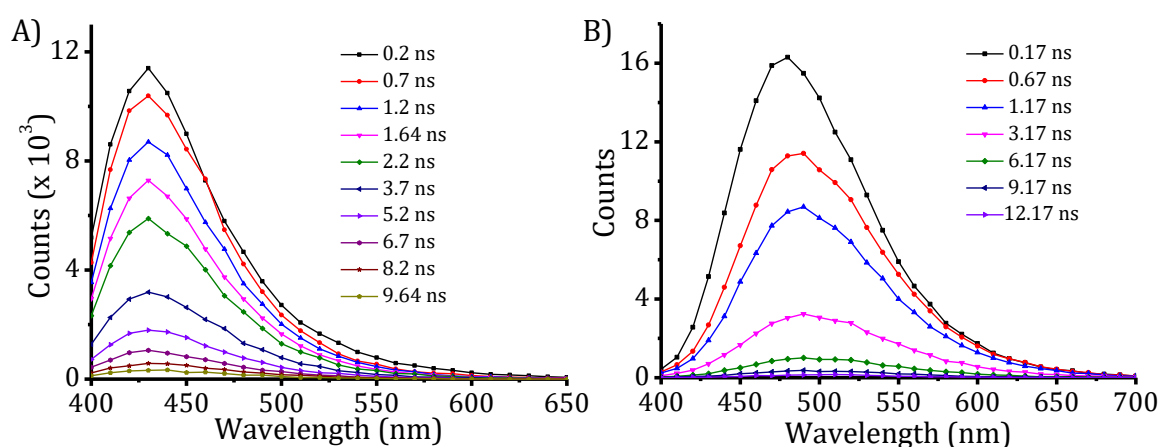


Figure 3A.21. Time resolved emission spectra of A) **TPE-1** and B) **TPE-1**≡**T-C12** in dodecane obtained by excitation at 375 nm laser source shown for a spectral delay time from 0.2 to 9.64 ns for A and 0.17 ns to 12.17 ns for B.

Optical fluorescence microscopic studies of solid samples prepared by drop-casting solutions over glass plates, followed by air drying revealed the presence of blue emissive bundled fiber like structures in **TPE-1** (Figure 3A.22A) and green emissive thin fibrous structures in **TPE-1**≡**T-C12** (Figure 3A.22B). Moreover, the morphologies observed in both fluorescence and polarization microscopic images of **TPE-1** and **TPE-1**≡**T-C12** (Figures 3A.22C & 3A.22D) were similar to the structures visualized in TEM and AFM analysis. These solid-state visual fluorescence changes of 1D-fibers further support the **T-C12** induced transition of blue to green emissive molecular assemblies, as observed in the photophysical studies.

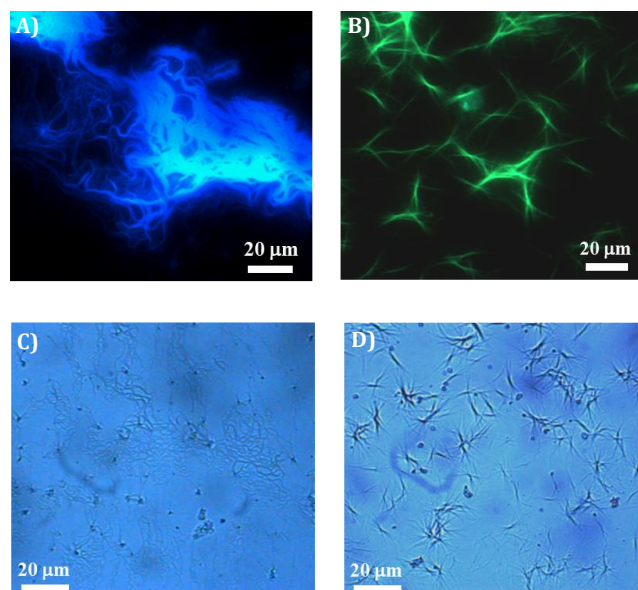


Figure 3A.22. Optical fluorescence and polarization microscopic images of A) and C) **TPE-1** (3×10^{-4} M) and B) and D) **TPE-1**≡**T-C12** (3×10^{-4} M, 1:1), respectively.

3A.3.8. Organogels of **TPE-1** and **TPE-1**≡**T-C12**

As discussed in previous sections, dodecane solutions of **TPE-1** show the formation of bundled nanofibres at lower concentrations. Very remarkably, higher concentrations of **TPE-1** in dodecane upon heat-cool conditions showed the formation of transparent gels with characteristic blue emission (Figure 3A.23A). We investigated the gelation behavior of **TPE-1** in various organic solvents and the results are tabulated (Table 3A.1). The critical gelator concentration (CGC) of **TPE-1** in dodecane is 10 mM, which was comparatively lower than the CGC values in other solvents examined. In addition, a lower CGC value of 3.8 mM for **TPE-1** was obtained by controlled cooling of the samples.

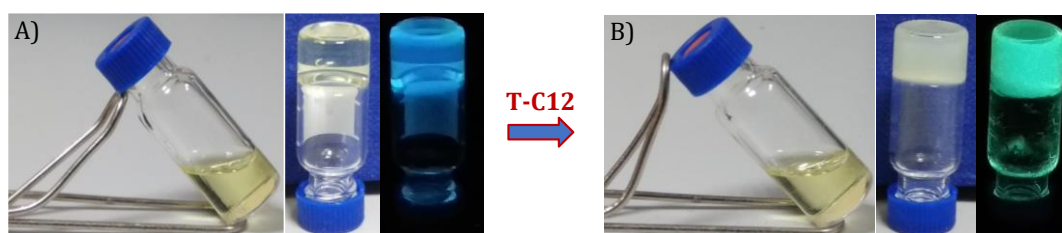


Figure 3A.23. Photographs of A) **TPE-1** and B) **TPE-1**≡**T-C12** (10 mM in dodecane) hot solution and cooled gel under normal and UV light.

On the other hand, the hetero-assemblies of 1:1 **TPE-1**≡**T-C12** in dodecane at higher concentrations (10 mM each) resulted in opaque gels with characteristic green emission (Figure 3A.23B) with a CGC of 2 mM under temperature-controlled cooling conditions.

Table 3A.1. Critical gelator concentration (CGC) of **TPE-1** in different solvents. Tr-transparent, Th-thixotropic, PG-partial gel and S-soluble.

Dodecane	n-decane	Cyclohexane	n-hexane	Toluene	Chloroform
8.12 mg (10 mM, Tr, stable)	10.06 mg (12.4 mM, Tr, stable)	19.23 mg (23.7 mM, Tr, Th)	7.84 mg (9.68 mM, PG)	16 mg (S)	20 mg (S)

These observations of blue to green emissive transition of the supramolecular gels in presence of **T-C12** is in agreement with the results obtained at lower concentrations of **TPE-1**. We have carried out further characterization of the photophysical and morphological properties of the **TPE-1** and **TPE-1**≡**T-C12** gels, using solid state UV-visible absorption, fluorescence emission and Scanning Electron Microscopic (SEM) analysis to understand the hierarchical evolution of the supramolecular assemblies with concentration.

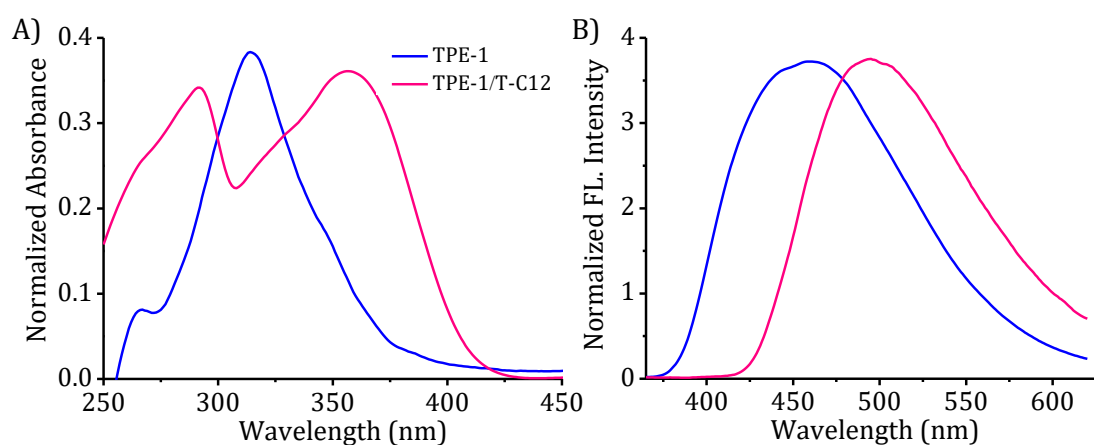


Figure 3A.24. Solid state A) absorption and B) emission spectra of the dried xerogel samples prepared by drop-casting the hot solutions of **TPE-1** (4 mM) and **TPE-1**≡**T-C12** (4 mM each, 1:1) in dodecane.

Solid-state absorption and emission studies of dried xerogels of **TPE-1** displayed an absorption maximum of 314 nm and broad emission band around 456 nm (Figures 3A.24A and 3A.24B, blue spectra). On the other hand, xerogels of **TPE-1≡T-C12** showed an absorption maximum of 356 nm and slightly broad emission band with maxima around 495 nm (Figures 3A.24A and 3A.24B, pink spectra). These results of solid-state absorption and emission spectra of both the xerogel samples agree well with the low concentration (3×10^{-4} M) solution state UV-visible absorption and emission spectra of **TPE-1** and **TPE-1≡T-C12**, indicating an intact primary self-assembly in these gels.

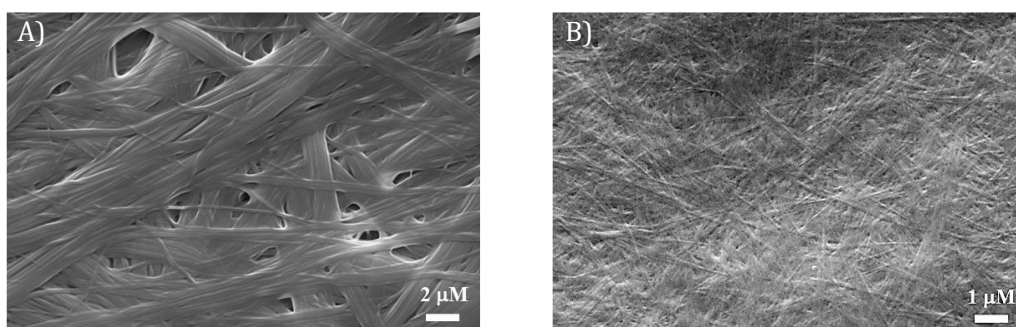


Figure 3A.25. SEM images of A) **TPE-1** and B) **TPE-1≡T-C12** dried xerogel samples.

In order to understand the morphological features of the higher order assemblies in these gels, the morphologies of **TPE-1** and **TPE-1≡T-C12** gels were inspected using SEM. The SEM image of dried xerogels of **TPE-1** displayed the presence of individual as well as bundled fibers (Figure 3A.25A), while **TPE-1≡T-C12** displayed stiff and thin fibrous structures (Figure 3A.25B). This result is also consistent with the observations from AFM, TEM and optical microscopic studies at lower concentrations, which further confirms that the basic molecular assembly process in these two systems (**TPE-1** alone and **TPE-1≡T-C12**) and the blue to green emissive transition are the same at different concentrations. With this general understanding about the photophysics and morphology, we went ahead with

additional gel characterizations like FT-IR, rheology and XRD to find out the self-assembly mechanism of **TPE-1** in the absence and presence of **T-C12**.

3A.3.9. Gel characterizations: FT-IR and rheology

FT-IR measurements of xerogels were performed to understand the involvement of H-bonding in the self-assembly of **TPE-1** and **TPE-1**≡**T-C12**, and the results were analyzed in comparison with FT-IR values reported in literatures for similar studies.³⁴⁻³⁶ Solution state FT-IR studies of **TPE-1** and **T-C12** in chloroform-d showed two characteristic IR peaks of NH₂ at 3538 cm⁻¹(non-bonded, asymmetric stretching), 3422 cm⁻¹ (non-bonded, symmetric stretching) and characteristic stretching peak of NH at 3394 cm⁻¹, respectively (black and violet lines in Figure 3A.26A and expanded FT-IR in 3100-3600 cm⁻¹, Figure 3A.26B).³⁴

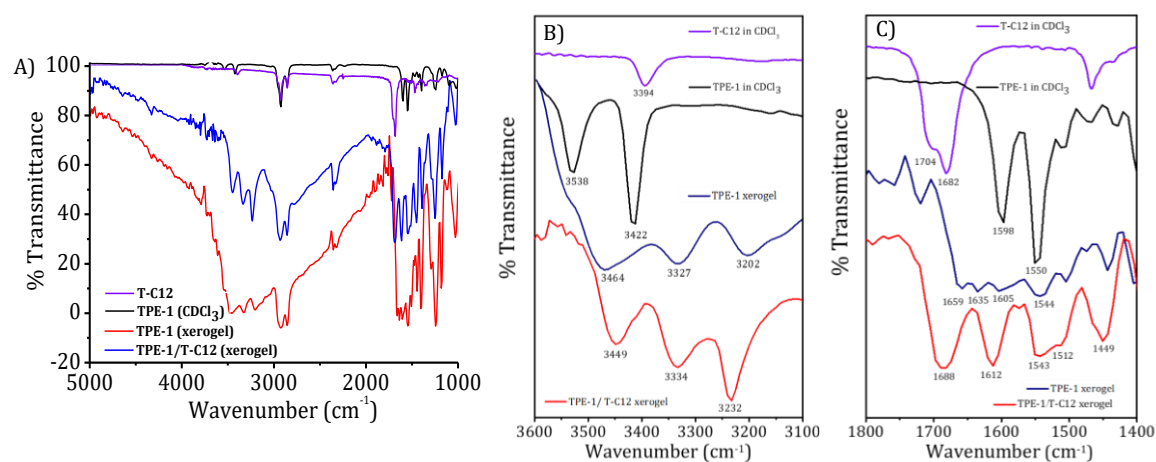


Figure 3A.26. A) FT-IR spectrum and expanded spectra in the B) 3100-3600 cm⁻¹ and C) 1400-1800 cm⁻¹ regions of **T-C12** and **TPE-1** in chloroform-d and xerogels of **TPE-1** and **TPE-1**≡**T-C12**.

Whereas, FT-IR spectrum of xerogel of **TPE-1** displayed two representative bands of bonded NH₂ at 3464 and 3327 cm⁻¹, accompanied by 3202 cm⁻¹ band (overtone band of the N-H bending at 1598). Similarly, in xerogels of **TPE-1**≡**T-C12**, these vibrational bands were observed at 3449, 3334 and 3232 cm⁻¹ (blue and red lines in

Figures 3A.26A and 3A.26B). In both cases, the vibrational bands were broadened and shifted towards lower wavenumber/frequency compared to the monomeric FT-IR spectra recorded in chloroform-d. The broadening and shift in frequencies imply the presence of intermolecular H-bonding in the self-assembly pathways of **TPE-1** and **TPE-1≡T-C12**.³⁶ In addition, the difference observed in the vibrational frequency values of **TPE-1** (3464 and 3327 and 3202 cm⁻¹) and **TPE-1≡T-C12** (3449, 3334 and 3232 cm⁻¹) xerogels in the 3100-3600 cm⁻¹ region indicate that the hydrogen bonding units involved in these assemblies are of different nature.

Further, analysis of FT-IR spectra in the 1400-1800 cm⁻¹ region gives more information about changes in C=O stretching, N-H bending and ring stretching vibrations (Figure 3A.26C). The characteristic non-bonded C=O stretching vibrations, 1704 and 1682 cm⁻¹ in the monomeric **T-C12** was found to be shifted to 1688 cm⁻¹ in xerogels of **TPE-1≡T-C12**.³⁴ Similarly, the N-H bending and ring strain stretching vibrations of **TPE-1** in monomeric state was observed at 1598 and 1550 cm⁻¹. In xerogels of **TPE-1** these bands were shifted to 1605, 1544 cm⁻¹, accompanied by 1659, 1635 cm⁻¹ bands associated with the H-bonded amino groups).³⁴ Thus the FT-IR studies confirm the role of complementary H-bonding in the 1D-assemblies of **TPE-1** and **TPE-1≡T-C12** and highlight the differential H-bonding in these two systems.

Rheology studies were carried out to understand the mechanical strength of gels. Dynamic frequency sweep measurements of **TPE-1** and **TPE-1≡T-C12** gels showed a higher value of storage modulus (G') than that of its corresponding loss modulus (G''), confirming the soft solid like elastic behavior of gels (Figure 3A.27). Nearly parallel values obtained for storage and loss modulus in the linear viscoelastic region (LVR) of transparent **TPE-1** and opaque **TPE-1≡T-C12** gels

indicate, the capacity to store and dissipate energy are almost similar for these bundled and thin fibrous assemblies.

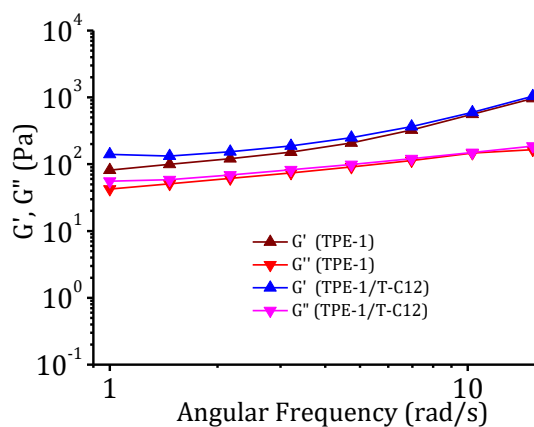


Figure 3A.27. Plot of storage modulus and loss modulus against angular frequency of **TPE-1** (4 mM) and **TPE-1≡T-C12** (4 mM each, 1:1) dodecane gels at 298 K.

3A.3.10. Mechanism of self-assembly

Wide angle X-ray scattering (WAXS) analysis was performed to understand the molecular packing in **TPE-1** and **TPE-1≡T-C12** assemblies. Figure 3A.28 shows the WAXS pattern of **TPE-1** xerogel films with characteristic long-range ordering of molecules. The reflections (2θ) observed in the WAXS pattern were at 2.43, 4.23 and 4.81 corresponding to the d-spacings of 36.32, 20.53 and 18.39 Å, which follows a reciprocal ratio of $1: \sqrt{3} : 2$. This ratio represents the (100), (110) and (200) planes of hexagonal columnar packing with inter-columnar distance (a) of 41.93 Å.^{37,38} The broad reflections in the WAXS pattern corresponding to the d-spacing of 4.5 Å and 3.86 Å indicate the ordered arrangement of dodecyl side chains and π - π stacking of aromatic units in columnar packing.³⁹ On the other hand, the WAXS pattern of **TPE-1≡T-C12** xerogel displayed reflections at 3.68, 5.27 and 7.57 corresponding to d-spacings of 23.99, 16.76 and 11.66 Å (Figure 3A.29). These d-spacing values at lower reflection regions represent the (100), (110) and (200) planes in $1: \sqrt{2} : 2$ ratio, characteristic of tetragonal columnar packing with 23.06 Å intercolumnar

distance.^{40,41} Similar to **TPE-1**, broad reflections characteristic of alkyl chains and π - π stacking of aromatic units were observed at d spacings of 4.42 Å and 3.91 Å.

Based on the experimental results of FT-IR, XRD and energy optimized structures of **TPE-1** and **TPE-1**≡**T-C12**, we propose a self-assembly mechanism for the formation of long range ordered 1D-assemblies of **TPE-1** as shown schematically in Figure 3A.28. The monomers of **TPE-1** initially assemble into dimers through hydrogen bonding interactions between DAT units, which further packs into hexagonal columnar structure by the π - π stacking of TPE units with an intercolumnar distance perpendicular to the molecular axis of **TPE-1** dimer. The TPE chromophores in these long range hexagonal columnar assemblies shows characteristic blue emission, and at higher concentrations this orderly packed 1D-assemblies gives rise to the formation of transparent supramolecular gels with blue emission.

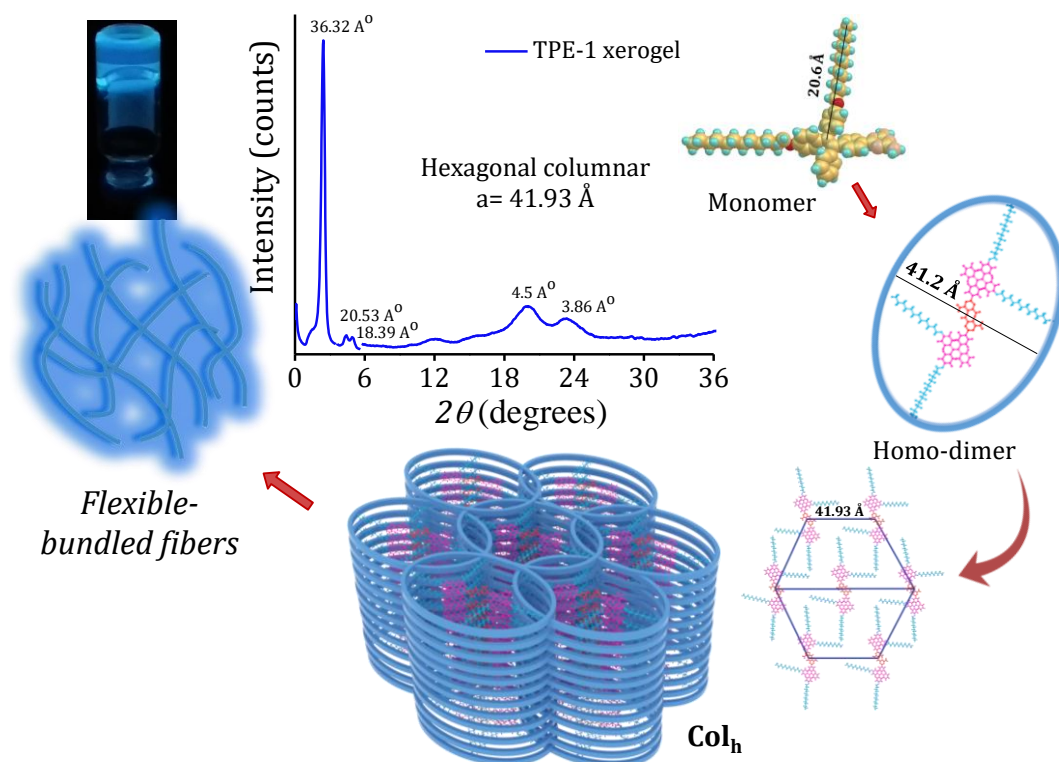


Figure 3A.28. WAXS pattern of **TPE-1** xerogel and the schematic representation of the proposed **TPE-1** self-assembly in the absence of **T-C12**.

While in presence of **T-C12**, instead of forming the homo-dimers of **TPE-1**, hetero-dimers of **TPE-1**≡**T-C12** will be formed upon a complete heat-cool cycle. The **TPE-1**≡**T-C12** dimers further pack through π - π stacking interactions into tetragonal columnar arrangement with an intercolumnar distance of 23.06 Å, as shown schematically in Figure 3A.29. This intercolumnar distance is obtained only when **TPE-1**≡**T-C12** dimers are arranged as in Figure 3A.29. The fluorescence emission transition from blue to green could be attributed to the change in monomeric units of assembly and could originate from the changes in relative planarity of the monomeric units and intermolecular distance between the TPE chromophores.⁴²

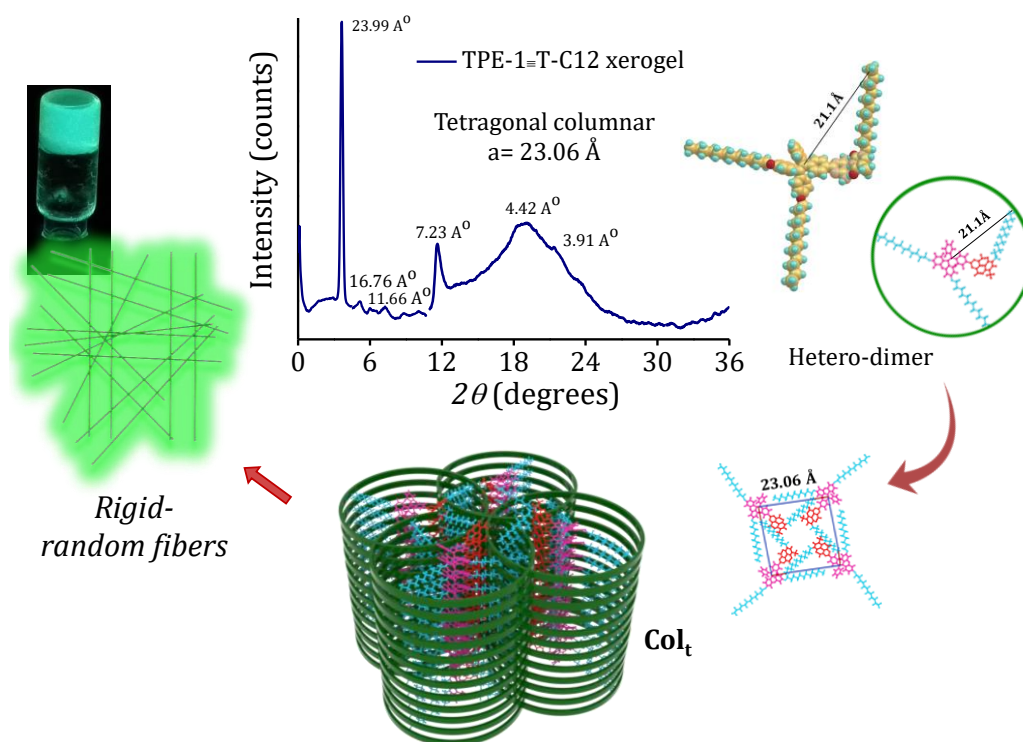


Figure 3A.29. WAXS pattern of **TPE-1**≡**T-C12** xerogel and the schematic representation of proposed **TPE-1** self-assembly in the presence of **T-C12**.

The hetero-dimer **TPE-1**≡**T-C12** with higher association constant may prefer to be more planar compared to **TPE-1** dimers, which results in better π - π stacking and a corresponding shift in the fluorescence emission to lower energy. Additionally, in such a tetragonal packing mode, the alkyl substituents are randomly distributed

compared to the ordered hexagonal columnar assemblies of **TPE-1**. As a result, **TPE-1**≡**T-C12** tetragonal columns will no longer undergo bundling to achieve long-range order and the random arrangement of initially formed fibers could lead to opaque gels.^{43,44}

3A.4. CONCLUSIONS

In summary, to achieve control over self-assembly and the random aggregation tendency of tetraphenylethylene derivatives, we employed the non-covalent hydrogen bonding ability of a nucleobase analogue, diaminotriazine (DAT) for imparting directionality and order to the self-assembly. A diaminotriazine functionalized tetraphenylethylene derivative, **TPE-1** was successfully synthesized and its detailed photophysical properties and hydrogen bonding directed self-assembly in dodecane were investigated. **TPE-1** self-assembles into blue emissive (430 nm) 1D-fibers at low concentration and entangled supramolecular transparent supramolecular gels at higher concentration, with homo-dimers of **TPE-1** as the basic self-assembly units. Further, using a complementary thymine derivative **T-C12**, the basic monomeric units of assembly was transformed to **TPE-1**≡**T-C12** hetero-dimer, which forms green emissive (502 nm) 1D fibrous structures at low concentration and supramolecular opaque gels at higher concentration (Figure 3A.30 shows the schematic representation of overall process). Detailed photophysical and morphological studies, gel and xerogel characterizations and the corresponding self-assembly mechanisms of **TPE-1** in the absence and presence of **T-C12** are described in this chapter. Moreover, to verify the proposed strategy and mechanism to construct 1D self-assemblies of TPE by functionalizing with nucleobase analogues, three more TPE-DAT derivatives, vary in their chemical

structure by different alkoxy-substitutions were synthesized and the results of which are described in the next part, Chapter 3B.

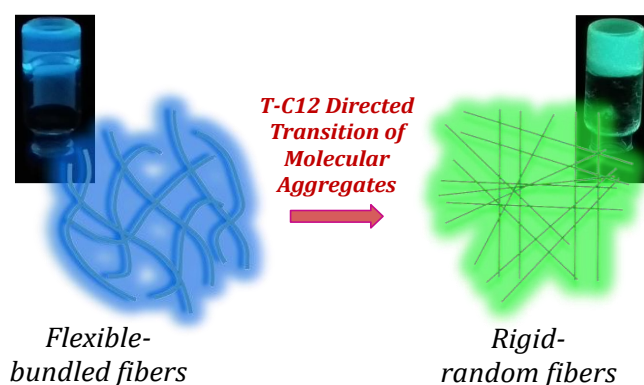


Figure 3A.30. Cartoonic representation of the overall **T-C12** directed transition of blue (**TPE-1**) to green (**TPE-1**≡**T-C12**) emissive supramolecular assemblies explained in this chapter.

3A.5. EXPERIMENTAL SECTION

3A.5.1. Materials and methods

All reagents and chemicals used for synthesis were purchased from Sigma-Aldrich, TCI chemicals and used without any additional purification. Moisture and oxygen sensitive reactions were carried out under argon atmosphere in dried solvents purchased from Merck and Sigma-Aldrich chemical suppliers. Thin Layer Chromatography (TLC) analysis was performed using aluminum plates coated with silica gel, purchased from Merck. 100-200 and 230-400 mesh silica gels were used for column chromatography. ^1H NMR (500 MHz) and ^{13}C NMR (125 MHz) analysis were achieved using Bruker Avance DPX spectrometer, with TMS as the internal standard ($\delta_{\text{H}} = 0$ ppm and $\delta_{\text{C}} = 77$ ppm). Dimethyl sulphoxide- d_6 and Chloroform- d were used as solvents for NMR analysis. High resolution mass spectra (HRMS) were obtained from Thermo Scientific Q Exactive Hybrid Quadrupole-Orbitrap electrospray ionization mass spectrometer (ESI-MS). Stuart melting point apparatus SMP30 was used for melting point measurements. Molecular size measurements

were performed on the energy minimized molecular structures obtained from GaussView 6.0.16.

Shimadzu UV-2600 UV-vis spectrophotometer equipped with Peltier controlled thermostatic cell holder was used for ambient and temperature dependent absorption spectral measurements. SPEX Fluorolog-3 (FL3-221) and FluoroMax-4 (Fluoromax-4c) spectrofluorometers were used for ambient temperature fluorescence emission, solution state absolute quantum yield (QY) and temperature dependent fluorescence emission spectral measurements, respectively. Solution state optical measurements were carried out in 1 and 0.1 cm quartz cuvettes. Solid state absorption spectra were recorded using PerkinElmer UV/VIS/NIR spectrophotometer (Lambda 950). Clean Quartz plate was used as reference and absorption spectra were deconvoluted from % transmittance spectra. Fluorescence lifetime measurements were performed using picosecond single photon counting system (Horiba, Delta Flex) employing 330 nm laser as excitation source and picosecond photon detection module (PPD-850) as a detector. The lifetime decay profiles were deconvoluted using EzTime software and fitted with chi-square value 1 ± 0.1 .

3A.5.2. AFM/TEM/OFM sample preparations

HR-TEM analysis was performed with JEOL-JEM0310 microscope with an accelerating voltage of 100 kV and the samples were imaged using Hamamatsu ORCA charge-coupled device (CCD) camera. Samples for TEM studies were prepared by drop-casting 10-30 μ L samples over carbon-coated copper grid (400 meshes, Ted Pella) and dried by slow evaporation at room temperature followed by vacuum drying for 24 hours before imaging. AFM images under ambient conditions were

recorded using Bruker multimode AFM Nano Scope instrument operating under tapping mode. Micro-fabricated TiN cantilever tips (Model: TESP) with a resonance frequency of 320 kHz and a spring constant of 42 Nm⁻¹ was used. AFM samples were prepared by drop-casting (5 µL) samples over silicon wafer and then air dried overnight before measurements. Fluorescence microscopic images of samples were obtained from Leica DM2500P Optical Microscope equipped with UV excitation (330-380 nm), violet excitation source (379-420 nm) and DFC 490 camera. Samples for fluorescence microscopic studies were prepared by drop casting 10-20 µL samples over cover slips followed by air drying.

3A.5.3. Gelation studies and xerogel sample preparations

Weighed amount of **TPE-1** was taken in different glass vials and solvents of known volume was added to check the gelation properties. Afterwards, these solutions were heated to dissolve the solute and the hot solutions were allowed to cool to room temperature. The formation of gel was confirmed by inverted vial experiment. In which the sample will not flow down when the sample vial is in inverted position. Following this procedure, the gelation behaviour of **TPE-1** in non-polar solvents like dodecane, n-decane, n-hexane, cyclohexane and toluene were tested and CGC values were tabulated. Depending upon the nature of solvent, gelation, clear solution and precipitation were observed. Similarly, gelation behaviour of self-assembled **TPE-1**≡**T-C12** was studied by dissolving equimolar ratios of **TPE-1** and **T-C12** in dodecane under heating and cooling. Rheology characteristics of gels were obtained using Anton Paar modular compact (MCR 102) rheometer, fitted with a parallel plate geometry of 20 mm diameter.

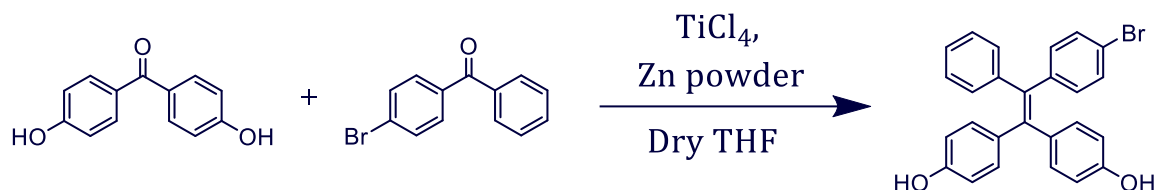
FT-IR spectra was recorded on Shimadzu IR Prestige-21 FT-IR spectrophotometer using demountable plates for solution and KBr plates for film state studies. Measurements were performed at room temperature and dry air environment. Solution state IR studies of **TPE-1** was carried out in chloroform-d and film state studies of xerogel samples were performed by drop casting hot solutions of gel on aluminium foil, followed by air drying. Xerogel samples for SEM were prepared by drop casting hot solutions of sample over aluminium foil and then air dried. The SEM images were recorded after sputtering with gold using Zeiss EVO 18cryo SEM Special Edn., operating with an accelerating voltage of 20 kV. WAXS analysis of xerogels were performed on XEUSS SAXS/WAXS system using a Genix micro source from Xenocs and the generator was operated at 0.6 mA and 50 kV. FOX2D mirror and two pairs of scatter-less slits from Xenocs were used to collimate the Cu K α radiation with $\lambda = 1.54 \text{ \AA}$. A mar345dtb image plate detector and Fit2D software were used to obtain the 2D-WAXS patterns. Samples for WAXS analysis were prepared by vacuum drying of solvents followed by air drying of the gels for 3 days.

3A.5.4. Synthetic procedures and characterizations

3A.5.4.1. Synthesis of 4,4'-(2-(4-bromophenyl)-2-phenylethene-1,1-diyl) di phenol, (1)⁴⁵

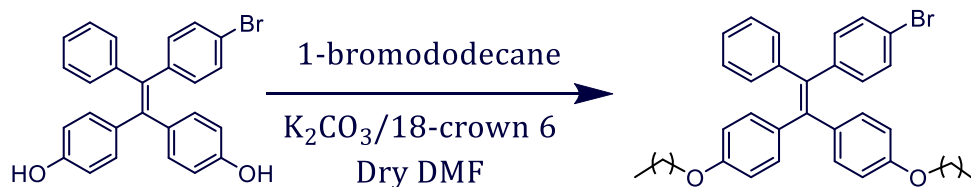
McMurry Coupling: Into a 250 mL two-necked RB flask 4,4'-dihydroxybenzophenone (2.0388 g, 9.336 mmol), 4-Bromobenzophenone (2.4427 g, 9.336 mmol) and zinc dust (5.5821 g, 84.024 mmol) were added. The flask was vacuumed and purged with Argon for three times. Afterwards, 120 mL of dry THF was injected into the flask, followed by cooling down to lower temperature. TiCl₄ (4.6 mL, 42.012 mmol) was

added. Then reaction was refluxed overnight under Argon conditions. After cooling to rT, the reaction mixture was extracted with ethyl acetate and dried with anhydrous sodium sulphate. The crude product was purified by silica column chromatography using 20% ethyl acetate-hexane as the eluent to give a pale-yellow solid. Yield = 33% (1.4 g).



^1H NMR (500 MHz, DMSO-d_6), δ (ppm): 9.412 (s, 1H), 9.368 (s, 1H), 7.324 (d, $J = 8.5$ Hz, 2H), 7.153-7.123 (m, 2H), 7.099-7.085 (m, 1H), 6.937 (d, $J = 7$ Hz, 2H), 6.864-6.847 (d, $J = 8.5$ Hz, 2H), 6.758-6.720 (m, 4H), 6.540-6.477 (m, 4H). ^{13}C NMR (125 MHz, DMSO-d_6), δ (ppm): 155.76, 144.06, 143.71, 141.57, 136.88, 134.90, 132.62, 131.35, 129.68, 127.69, 126.01, 119.59, 114.84. HRMS (ESI): m/z calcd., for $\text{C}_{26}\text{H}_{19}\text{BrO}_2$, 442.06 [M]; found, 442.05 [M] $^+$.

3A.5.4.2. 4,4'-(2-(4-bromophenyl)-2-phenylethene-1,1-diyl)bis((dodecyloxy)benzene), (2)

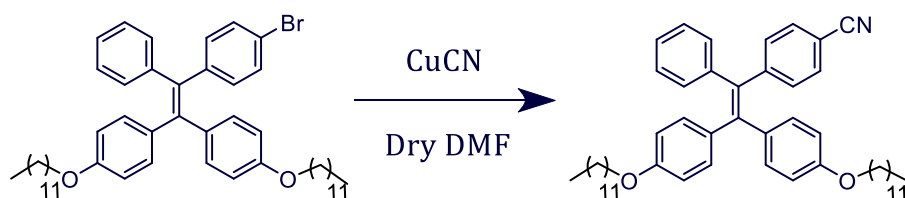


1 (0.9934 g, 2.262 mmol) and K_2CO_3 (1.6461 g, 11.31 mmol) were taken in a 250 mL two-necked RB flask. The flask was vacuumed and purged with Argon for three times. To this mixture, 1-bromododecane (2.172 mL, 9.048 mmol) and DMF (10 mL) were added. The reaction was stirred at 70 °C overnight under Argon

condition. After the mixture cooled to rT, it was extracted with ethyl acetate and washed with distilled water several times. The organic part was separated and dried with anhydrous sodium sulphate. The crude product was purified by silica column chromatography using 1% ethyl acetate-hexane as the elution solution to give a pale-yellow viscous oil. Yield = 84% (1.5 g).

^1H NMR (500 MHz, CDCl_3), δ (ppm): 7.217 (d, $J = 8$ Hz, 2H), 7.105-7.058 (m, 3H), 7.000 (d, $J = 7$ Hz, 2H), 6.914-6.870 (m, 6H), 6.634-6.598 (m, 4H), 3.899-3.846 (m, 4H), 1.736-1.709 (m, 4H), 1.426-1.412 (m, 4H), 1.260 (m, 32H), 0.893 (t, $J = 6.5$ Hz, 6H). ^{13}C NMR (125 MHz, CDCl_3), δ (ppm): 157.86, 143.89, 143.41, 140.95, 137.64, 135.81, 133.07, 132.56, 130.83, 127.80, 126.24, 119.93, 113.69, 67.87, 31.94, 29.62, 26.08, 22.71, 14.15. HRMS (ESI): m/z calcd., for $\text{C}_{50}\text{H}_{67}\text{BrO}_2$, 778.43 [M]; found, 779.15 [M+1] $^+$.

3A.5.4.3. 4-(2,2-bis(4-(dodecyloxy)phenyl)-1-phenylvinyl)benzonitrile, (3)

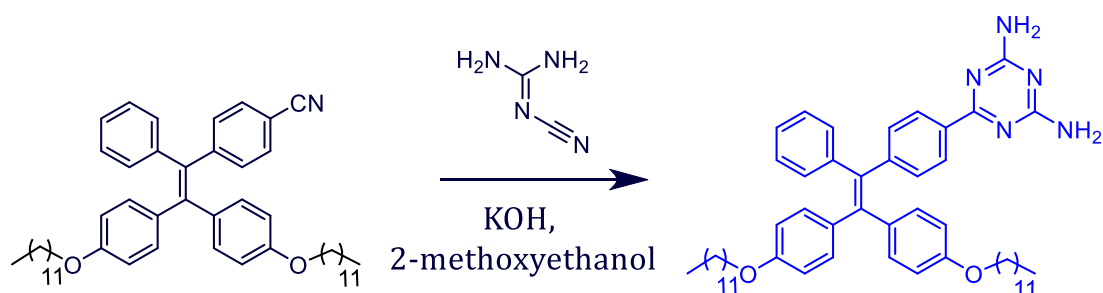


Into a 100 mL two-necked RB flask containing **2** (1.4924 g, 1.917 mmol), CuCN (0.5152 g, 5.751 mmol) was added. The flask was vacuumed and purged with Argon for three times. The mixture was heated to reflux with dry DMF (15 mL) for 60 hrs under Argon atmosphere. Afterwards, the reaction mixture was suspended into 68 mL water. Ethylenediamine (2.2 mL) was added, and the resulting mixture was stirred at 100 °C for 1 h and filtered. The filtrate was extracted with ethyl acetate, washed with distilled water several times and dried with anhydrous sodium

sulphate. The crude product was purified by silica column chromatography using hexane as the eluent to give a pale-yellow viscous oil. Yield = 57% (0.8 g).

^1H NMR (500 MHz, CDCl_3), δ (ppm): 7.357 (d, 2H), 7.115-7.091 (m, 5H), 6.985 (d, J = 6.5 Hz, 2H), 6.906-6.873 (m, 4H), 6.648-6.606 (m, 4H), 3.898-3.852 (m, 4H), 1.731-1.565 (m, 4H), 1.426-1.414 (m, 4H), 1.262 (s, 32H), 0.892 (t, J = 6.5 Hz, 6H). ^{13}C NMR (125 MHz, CDCl_3), δ (ppm): 158.12, 140.95, 135.81, 133.65, 132.55, 132.03, 131.49, 131.34, 128.03, 126.57, 119.83, 113.59, 109.45, 67.87, 31.92, 29.60, 29.35, 26.06, 22.69, 14.12. HRMS (ESI): m/z calcd., for $\text{C}_{51}\text{H}_{67}\text{NO}_2$, 726.08 [M]; found, 749.50 [M+Na $^+$] $^+$.

3A.5.4.4. 6-(4-(2,2-bis(4-(dodecyloxy)phenyl)-1-phenylvinyl)phenyl)-1,3,5-triazine-2,4-diamine, (TPE-1)

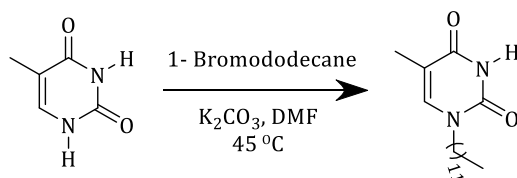


Into a 100 mL two-necked RB flask containing **3** (1.106 g, 1.531 mmol) and dicyandiamide (0.2571 g, 3.062 mmol), KOH (0.3150 g, 4.593 mmol) was added. The flask was vacuumed and purged with Argon for three times. 2-methoxy ethanol (11 mL) was added into the mixture and heated at reflux for 60 hrs under Argon atmosphere. It was then extracted with ethyl acetate, washed with distilled water several times and dried over anhydrous sodium sulphate. The crude product was purified by silica column chromatography using 20% ethyl acetate-hexane as the eluent to give **TPE-1** as a pale yellow solid. Yield = 57% (0.7 g).

Melting point: 115-120 °C. ¹H NMR (500 MHz, CDCl₃), δ (ppm): 8.035-8.020 (d, *J* = 7.5 Hz, 2H), 7.262-7.085 (m, 4H), 7.013-7.000 (d, *J* = 6.5 Hz, 2H), 6.928-6.916 (m, 4H), 6.626-6.588 (m, 4H), 5.098 (s, 4H), 3.878-3.835 (m, 4H), 1.724-1.617 (m, 4H), 1.412-1.400 (m, 4H), 1.258 (s, 32H), 0.877 (t, *J* = 6.5 Hz, 6H). ¹³C NMR (125 MHz, CDCl₃), δ (ppm): 172.31, 167.55, 157.90, 157.81, 141.29, 140.95, 135.94, 132.63, 131.56, 131.48, 127.71, 126.17, 113.62, 113.52, 67.83, 31.93, 29.58, 29.36, 26.07, 22.70, 14.14. HRMS (ESI): *m/z* calcd., for C₅₃H₇₁N₅O₂, 809.56 [M]; found, 810.59 [M+1]⁺.

3A.5.4.5. 1-dodecyl-5-methylpyrimidine-2,4(1H, 3H)-dione, (T-C12)

T-C12 was synthesized by following a modified literature procedure.⁴⁶ To a mixture of thymine (2 g, 15.8 mmol) and activated K₂CO₃ (2.4 g, 17.4 mmol) in 100 mL RB flask, DMF (40 mL) was added. The mixture was stirred at rT for 10 minutes and 1-bromododecane (4 mL, 17.4 mmol) was slowly added to this suspension. The mixture was heated at 45 °C for 48 hrs. Afterwards, water was introduced into this reaction mixture and extracted with diethyl ether (2 × 100 mL). Organic layer was separated and washed with brine solution and dried over sodium sulphate. The crude product was purified using silica column chromatography with 15 % ethyl acetate-hexane as eluent to yield **T-C12** as white powder. Yield = 61% (2.3 g).



¹H NMR (500 MHz, CDCl₃), δ (ppm): 8.149 (s, 1H), 6.974 (s, 1H), 3.694-3.664 (m, 2H), 1.926 (s, 3H), 1.668-1.656 (m, 2H), 1.316-1.257 (m, 18H), 0.894 (m, *J* = 7 Hz, 3H). ¹³C NMR (125 MHz, CDCl₃), δ (ppm): 163.7, 150.8, 139.2, 110.9, 50.5, 31.9, 30.3,

29.6, 29.3, 26.7, 22.7, 14.1, 12.4. HRMS (ESI): m/z calcd., for C₁₇H₃₀N₂O₂, 294.30 [M]; found, 295.23 [M+1]⁺.

3A.6. REFERENCES

- 1) Liu, K.; Zhang, R.; Li, Y.; Jiao, T.; Ding, D.; Yan, X. Tunable Aggregation-Induced Emission of Tetraphenylethylene via Short Peptide-Directed Self-Assembly. *Adv. Mater. Interfaces*. **2017**, *4*, 1600183.
- 2) Janssen, P. G. A.; Ruiz-Carretero, A.; González-Rodríguez, D.; Meijer, E. W.; Schenning, A. P. H. J. pH-Switchable Helicity of DNA-Templated Assemblies. *Angew. Chem. Int. Ed.* **2009**, *48*, 8103-8106.
- 3) Trinh, T.; Chidchob, P.; Bazzi, H. S.; Sleiman, H. F. DNA micelles as nanoreactors: efficient DNA functionalization with hydrophobic organic molecules. *Chem. Commun.* **2016**, *52*, 10914-10917.
- 4) Lopez, A.; Liu, J. W. Self-Assembly of Nucleobase, Nucleoside and Nucleotide Coordination Polymers: From Synthesis to Applications. *Chemnanomat*. **2017**, *3*, 670-684.
- 5) Surin, M. From nucleobase to DNA templates for precision supramolecular assemblies and synthetic polymers. *Polym Chem-Uk*. **2016**, *7*, 4137-4150.
- 6) Pu, F.; Ren, J.; Qu, X. Nucleobases, nucleosides, and nucleotides: versatile biomolecules for generating functional nanomaterials. *Chem. Soc. Rev.* **2018**, *47*, 1285-1306.
- 7) Chen, J.; Seeman, N. C. Synthesis from DNA of a molecule with the connectivity of a cube. *Nature*. **1991**, *350*, 631-633.
- 8) Seeman, N. C.; Sleiman, H. F. DNA nanotechnology. *Nat. Rev. Mater.* **2017**, *3*, 17068.
- 9) Wijnands, S. P. W.; Meijer, E. W.; Merckx, M. DNA-Functionalized Supramolecular Polymers: Dynamic Multicomponent Assemblies with Emergent Properties. *Bioconjugate Chem.* **2019**, *30*, 1905-1914.
- 10) Chen, Y.; Phipps, M. L.; Werner, J. H.; Chakraborty, S.; Martinez, J. S. DNA Templated Metal Nanoclusters: From Emergent Properties to Unique Applications. *Acc. Chem. Res.* **2018**, *51*, 2756-2763.
- 11) Roy, B.; Bairi, P.; Nandi, A. K. Supramolecular assembly of melamine and its derivatives: nanostructures to functional materials. *Rsc Adv.* **2014**, *4*, 1708-1734.

- 12) Adhikari, B.; Lin, X.; Yamauchi, M.; Ouchi, H.; Aratsu, K.; Yagai, S. Hydrogen-bonded rosettes comprising π -conjugated systems as building blocks for functional one-dimensional assemblies. *Chem. Commun.* **2017**, *53*, 9663-9683.
- 13) Hoeben, F. J. M.; Jonkheijm, P.; Meijer, E. W.; Schenning, A. P. H. J. About Supramolecular Assemblies of π -Conjugated Systems. *Chem. Rev.* **2005**, *105*, 1491-1546.
- 14) Yagai, S. Supramolecularly Engineered Functional π -Assemblies Based on Complementary Hydrogen-Bonding Interactions. *Bull. Chem. Soc. Jpn.* **2015**, *88*, 28-58.
- 15) v. Bünau, G. J. B. Birks: Photophysics of Aromatic Molecules. *Wiley-Interscience, London 1970. 704 Seiten. Preis: 210s.* **1970**, *74*, 1294-1295.
- 16) Mei, J.; Leung, N. L. C.; Kwok, R. T. K.; Lam, J. W. Y.; Tang, B. Z. Aggregation-Induced Emission: Together We Shine, United We Soar! *Chem. Rev.* **2015**, *115*, 11718-11940.
- 17) Mei, J.; Hong, Y.; Lam, J. W. Y.; Qin, A.; Tang, Y.; Tang, B. Z. Aggregation-Induced Emission: The Whole Is More Brilliant than the Parts. *Adv. Mater.* **2014**, *26*, 5429-5479.
- 18) La, D. D.; Bhosale, S. V.; Jones, L. A.; Bhosale, S. V. Tetraphenylethylene-Based AIE-Active Probes for Sensing Applications. *ACS Appl. Mater. Interfaces.* **2018**, *10*, 12189-12216.
- 19) Yu, M.; Huang, R.; Guo, J.; Zhao, Z.; Tang, B. Z. Promising applications of aggregation-induced emission luminogens in organic optoelectronic devices. *Photonix.* **2020**, *1*, 11.
- 20) La, D. D.; Malegaonkar, J. N.; Kobaisi, M. A.; Bhosale, R. S.; Bhosale, S. V.; Bhosale, S. V. Spermine-directed supramolecular self-assembly of water-soluble AIE-active tetraphenylethylene: nanobelt, nanosheet, globular and nanotubular structures. *New J. Chem.* **2018**, *42*, 15379-15386.
- 21) Wang, Y.; Lee, M. Self-Assembly of Tetraphenylethylene-Based Amphiphiles in Aqueous Methanol Solution into Two-Dimensional Chiral Sheets for Enantioselective Sorption. *ChemPlusChem.* **2020**, *85*, 711-714.
- 22) Salimimarand, M.; La, D. D.; Kobaisi, M. A.; Bhosale, S. V. Flower-like superstructures of AIE-active tetraphenylethylene through solvophobic controlled self-assembly. *Sci. Rep.* **2017**, *7*, 42898.

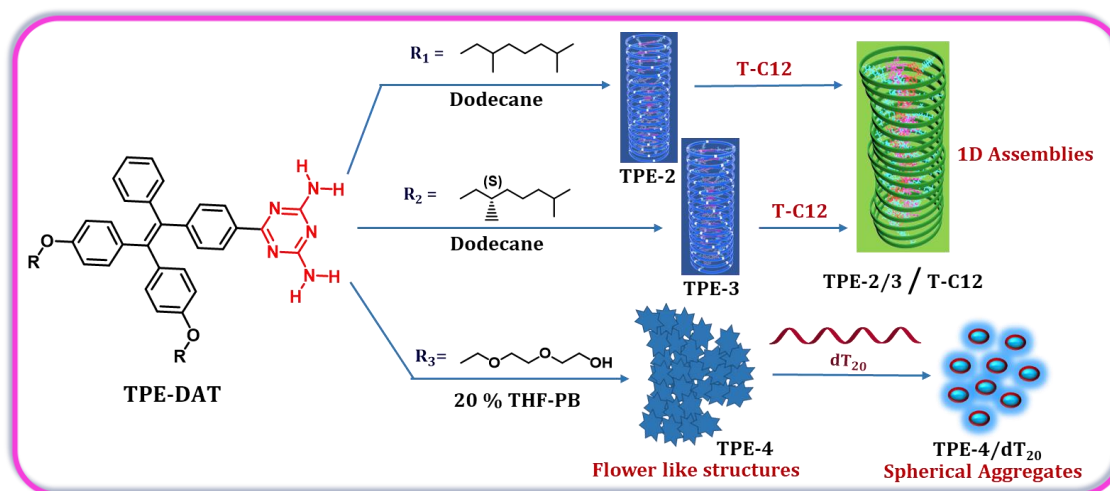
-
- 23) Li, H.; Cheng, J.; Zhao, Y.; Lam, J. W. Y.; Wong, K. S.; Wu, H.; Li, B. S.; Tang, B. Z. L-Valine methyl ester-containing tetraphenylethene: aggregation-induced emission, aggregation-induced circular dichroism, circularly polarized luminescence, and helical self-assembly. *Mater. Horiz.* **2014**, *1*, 518-521.
- 24) Li, H.; Cheng, J.; Deng, H.; Zhao, E.; Shen, B.; Lam, J. W. Y.; Wong, K. S.; Wu, H.; Li, B. S.; Tang, B. Z. Aggregation-induced chirality, circularly polarized luminescence, and helical self-assembly of a leucine-containing AIE luminogen. *J Mater Chem C.* **2015**, *3*, 2399-2404.
- 25) Li, H.; Zheng, X.; Su, H.; Lam, J. W. Y.; Sing Wong, K.; Xue, S.; Huang, X.; Huang, X.; Li, B. S.; Tang, B. Z. Synthesis, optical properties and helical self-assembly of a bivaline-containing tetraphenylethene. *Sci. Rep.* **2016**, *6*, 19277.
- 26) Peng, H.-Q.; Zheng, X.; Han, T.; Kwok, R. T. K.; Lam, J. W. Y.; Huang, X.; Tang, B. Z. Dramatic Differences in Aggregation-Induced Emission and Supramolecular Polymerizability of Tetraphenylethene-Based Stereoisomers. *J. Am. Chem. Soc.* **2017**, *139*, 10150-10156.
- 27) Lou, X.; Leung, C. W. T.; Dong, C.; Hong, Y.; Chen, S.; Zhao, E.; Lam, J. W. Y.; Tang, B. Z. Detection of adenine-rich ssDNA based on thymine-substituted tetraphenylethene with aggregation-induced emission characteristics. *Rsc Adv.* **2014**, *4*, 33307-33311.
- 28) Zhang, R.; Kwok, R. T. K.; Tang, B. Z.; Liu, B. Hybridization induced fluorescence turn-on of AIEgen-oligonucleotide conjugates for specific DNA detection. *Rsc Adv.* **2015**, *5*, 28332-28337.
- 29) Krishnan, N.; Golla, M.; Thelu, H. V. P.; Albert, S. K.; Atchimaidu, S.; Perumal, D.; Varghese, R. Self-assembly of DNA-tetraphenylethylene amphiphiles into DNA-grafted nanosheets as a support for the immobilization of gold nanoparticles: a recyclable catalyst with enhanced activity. *Nanoscale.* **2018**, *10*, 17174-17181.
- 30) ten Eikelder, H. M. M.; Markvoort, A. J.; de Greef, T. F. A.; Hilbers, P. A. J. An Equilibrium Model for Chiral Amplification in Supramolecular Polymers. *J. Phys. Chem. B.* **2012**, *116*, 5291-5301.
- 31) Ogi, S.; Stepanenko, V.; Sugiyasu, K.; Takeuchi, M.; Würthner, F. Mechanism of Self-Assembly Process and Seeded Supramolecular Polymerization of Perylene Bisimide Organogelator. *J. Am. Chem. Soc.* **2015**, *137*, 3300-3307.
- 32) Hifsudheen, M.; Mishra, R. K.; Vedhanarayanan, B.; Praveen, V. K.; Ajayaghosh, A. The Helix to Super-Helix Transition in the Self-Assembly of π -Systems:

- Superseding of Molecular Chirality at Hierarchical Level. *Angew. Chem. Int. Ed.* **2017**, *56*, 12634-12638.
- 33) Krakovský, I.; Lokaj, J.; Sedláková, Z.; Ikeda, Y.; Nishida, K. Hydrogen bonding interactions of styrene-maleimide copolymers with diaminotriazine derivatives. *J. Appl. Polym. Sci.* **2006**, *101*, 2338-2346.
- 34) Kyogoku, Y.; Lord, R. C.; Rich, A. An Infrared Study of Hydrogen Bonding between Adenine and Uracil Derivatives in Chloroform Solution. *J. Am. Chem. Soc.* **1967**, *89*, 496-504.
- 35) Bohanon, T. M.; Denzinger, S.; Fink, R.; Paulus, W.; Ringsdorf, H.; Weck, M. Barbituric Acid/2,4,6-Triaminopyrimidine Aggregates in Water and Their Competitive Interaction with a Monolayer of Barbituric Acid Lipids at the Gas-Water Interface. *Angew. Chem. Int. Ed.* **1995**, *34*, 58-60.
- 36) Das, G.; Thirumalai, R.; Vedhanarayanan, B.; Praveen, V. K.; Ajayaghosh, A. Enhanced Emission in Self-Assembled Phenyleneethynylene Derived π -Gelators. *Adv. Optical Mater.* **2020**, *8*, 2000173.
- 37) Yagai, S.; Usui, M.; Seki, T.; Murayama, H.; Kikkawa, Y.; Uemura, S.; Karatsu, T.; Kitamura, A.; Asano, A.; Seki, S. Supramolecularly Engineered Perylene Bisimide Assemblies Exhibiting Thermal Transition from Columnar to Multilamellar Structures. *J. Am. Chem. Soc.* **2012**, *134*, 7983-7994.
- 38) Yagai, S.; Goto, Y.; Lin, X.; Karatsu, T.; Kitamura, A.; Kuzuhara, D.; Yamada, H.; Kikkawa, Y.; Saeki, A.; Seki, S. Self-Organization of Hydrogen-Bonding Naphthalene Chromophores into J-type Nanorings and H-type Nanorods: Impact of Regioisomerism. *Angew. Chem. Int. Ed.* **2012**, *51*, 6643-6647.
- 39) Lu, L.; Sun, H.-J.; Zeng, Y.-T.; Shao, Y.; Bermeshev, M. V.; Zhao, Y.; Sun, B.; Chen, Z.-J.; Ren, X.-K.; Zhu, M. Perylene diimide derivative via ionic self-assembly: helical supramolecular structure and selective detection of ATP. *J Mater Chem C.* **2020**, *8*, 10422-10430.
- 40) Kartha, K. K.; Allampally, N. K.; Politi, A. T.; Prabhu, D. D.; Ouchi, H.; Albuquerque, R. Q.; Yagai, S.; Fernández, G. Influence of metal coordination and light irradiation on hierarchical self-assembly processes. *Chem Sci.* **2019**, *10*, 752-760.
- 41) Bando, Y.; Sakamoto, S.; Yamada, I.; Haketa, Y.; Maeda, H. Charge-based and charge-free molecular assemblies comprising π -extended derivatives of anion-responsive acyclic oligopyrroles. *Chem. Commun.* **2012**, *48*, 2301-2303.

-
- 42) Wang, Y.; Zhang, G.; Zhang, W.; Wang, X.; Wu, Y.; Liang, T.; Hao, X.; Fu, H.; Zhao, Y.; Zhang, D. Tuning the Solid State Emission of the Carbazole and Cyano-Substituted Tetraphenylethylene by Co-Crystallization with Solvents. *Small*. **2016**, *12*, 6554-6561.
- 43) Sutar, P.; Suresh, V. M.; Jayaramulu, K.; Hazra, A.; Maji, T. K. Binder driven self-assembly of metal-organic cubes towards functional hydrogels. *Nat Commun*. **2018**, *9*, 3587.
- 44) Mahesh, S.; Thirumalai, R.; Yagai, S.; Kitamura, A.; Ajayaghosh, A. Role of complementary H-bonding interaction of a cyanurate in the self-assembly and gelation of melamine linked tri(p-phenyleneethynylene)s. *Chem. Commun*. **2009**, 5984-5986.
- 45) Zhao, E.; Chen, Y.; Wang, H.; Chen, S.; Lam, J. W. Y.; Leung, C. W. T.; Hong, Y.; Tang, B. Z. Light-Enhanced Bacterial Killing and Wash-Free Imaging Based on AIE Fluorogen. *ACS Appl. Mater. Interfaces*. **2015**, *7*, 7180-7188.
- 46) Tao, Y.; Satoh, K.; Kamigaito, M. Nucleobase-Mediated Stereospecific Radical Polymerization and Combination with RAFT Polymerization for Simultaneous Control of Molecular Weight and Tacticity. *Macromol Rapid Commun*. **2011**, *32*, 226-232.

CHAPTER 3: PART B

EFFECT OF DIFFERENT ALKOXY SUBSTITUTIONS ON THE SELF-ASSEMBLY PROPERTIES OF TETRAPHENYLETHYLENE-DIAMINOTRIAZINE DERIVATIVES: PHOTOPHYSICAL AND MORPHOLOGICAL STUDIES



3B.1. ABSTRACT

Three TPE-DAT derivatives analogous to **TPE-1** were synthesized by changing the alkoxy substitutions and the mechanism of intermolecular hydrogen bonding directed self-assembly of **TPE-1** put forward in chapter 3A was verified. The three TPE-DAT derivatives include, (i) **TPE-2** with racemic, (ii) **TPE-3** with chiral and (iii) **TPE-4** with triethylene glycol, alkoxy substitutions. In dodecane, **TPE-2** and **TPE-3** self-assembles via cooperative pathway and forms 1D fibers, with characteristic 307 nm absorption maxima and 430 nm emission maxima, as observed in the case of **TPE-1** at lower concentrations. On the other hand, at higher concentration, this assembly results in the formation of opaque supramolecular gels, which is distinct

from the transparent gelation behaviour of **TPE-1**. The chiral derivative, **TPE-3** showed an induced CD signal upon self-assembly, yet failed to show any chiral morphology indicating a primary chiral organization of the monomeric units with secondary molecular packing assisted masking of the structural chirality. Moreover, the **T-C12** assisted transition of molecular aggregates in the **TPE-2** and **TPE-3** self-assembly, to green emissive 1D-fibrous structures at lower concentration and opaque gel formation at higher concentrations were studied, and the detailed mechanism of self-assembly in the absence and presence of **T-C12** were deduced using the FT-IR and XRD features of xerogels. The triethylene glycol substituted derivative, **TPE-4** was designed to study the self-assembly properties in aqueous solvent systems, and the reported self-assembly properties are different from **TPE-1/2/3** due to the changes in the amphiphilic nature of the molecule. The nucleic acid interaction studies of **TPE-4** with *dT*₂₀ in 20% THF-water system revealed the formation of uniformly distributed TPE-DNA condensates with 40-50 nm in size, instead of the expected 1D assemblies. As demonstrated, molecular engineering of the TPE amphiphiles having a H-bonding recognition unit such as DAT could be useful for the construction of functional materials with directional control over morphologies and hence can be used as required for specific applications.

3B.2. INTRODUCTION

Hierarchical and programmable self-assembly of small π -conjugated organic molecules in to one, two or higher dimensions with precise control over the morphology offers the construction of smart functional materials, which finds potential applications in bio-medical field and, electronic and photonic devices.¹⁻⁵ Molecular design plays key role in supramolecular self-assembly and tuning of their

optical and morphological properties.⁶⁻⁸ Changes in the chemical structure such as position of atoms, cis-trans isomers or differences in substituent groups etc., has significant impact on the molecular packing and self-assembly.⁹⁻¹⁵ The impact includes, either a complete change in the mechanism of self-assembly resulting in entirely different properties from the former or a validation for the existing self-assembly with similar results. Supramolecular chemists are using these tools wisely to explore the potential of non-covalent interactions in constructing ordered functional assemblies of small organic chromophores.¹⁶⁻¹⁸

It has been demonstrated that a change in the side-chain substitution can change the entire morphology of perylene bisimide (PBI) self-assembly from zero-dimensional nanoparticle to one dimensional nanobelt.¹⁹ Similarly, Shiki Yagai and coworkers reported the formation of 1D assemblies of numerous PBI dyads in THF by varying the alkyl substitution and the morphology tuning by varying the water fraction in THF-water solvent system.²⁰⁻²² For example, they have shown the formation of various morphologies from an amphiphilic PBI-3 dyad, having both hydrophobic alkyl and hydrophilic polyethylene glycol chains as substituents in to

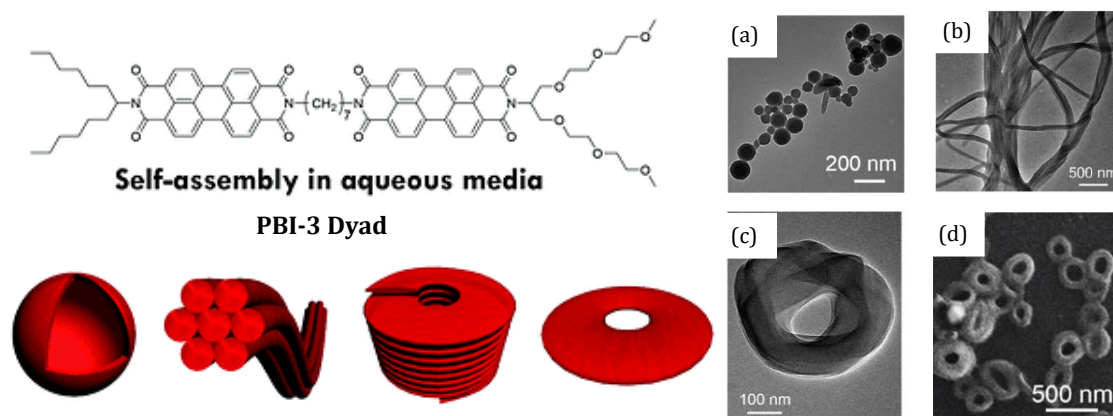


Figure 3B.1. Chemical structure of PBI-3 dyad, schematic representation of different morphologies obtained by varying temperature and water fraction, and the corresponding TEM images of (a) hollow vesicles, (b) nanofibers, (c) nanocoils and SEM image of (d) nanorings self-assembled from PBI-3 (Adapted from reference 20).

1D nanofibers in THF, hollow vesicular structures in 50% THF-water solvent mixture, and formation of nanoring like structures in the same solvent system using a micro-flow device.²⁰ Under temperature and entropy control, the vesicular structures formed in 50% THF-water further transforms to thermodynamically stable hexagonally packed nanofibers and kinetically trapped nanocoils (Figure 3B.1).

The H-bonding directed supramolecular assemblies of many organic chromophores by changing the alkyl substitution with chiral isomers were established.²³⁻²⁶ Subi J. George *et al.* demonstrated the formation of supramolecular gels from oligo(p-phenylenevinylene)s (OPVs) with coiled helical structures by a chiral substitution on the chemical structure, which otherwise will result in the formation of achiral lamellar 1D assemblies.^{25,26} Here, upon gelation, the initially formed chiral aggregates stacks to form left-handed helical assemblies, which further undergoes twisting by itself to form rope like 1D fibers (Figure 3B.2A).²⁵ From the same group, they have reported a chiral guest induced helical assembly of an achiral OPV derivative, functionalized with ureidotriazine unit (OPVUT).²⁷

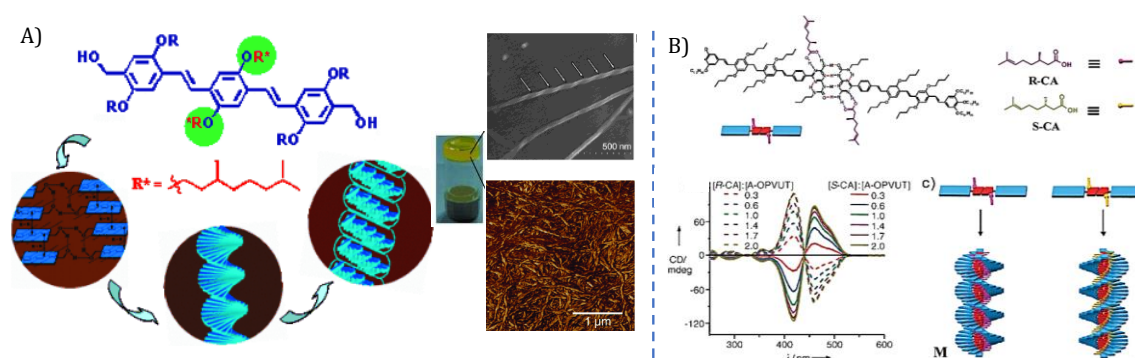


Figure 3B.2. A) Chemical structure of OPV, schematic representation of the self-assembly, and corresponding TEM and AFM images of the coiled helical fibers (Adapted from reference 25). B) Chemical structures of OPVUT and guest molecules, chiroptical properties and schematic representation of the chirality induction and amplification process (Adapted from reference 27).

R and S isomers of citronelic acid (CA) was used as the chiral regulators, which can interact with OPVUT dimer through complementary H-bonding interaction. Cooling a mixture of OPVUT and R/S-CA gives rise to the formation of corresponding M and P helical assemblies of OPVUT decorated with CA, having characteristic chiroptical and morphological features (Figure 3B.2B). Moreover, they have also investigated the co-operative self-assembly pathway in detail, and verified the role of elongation temperature and concentration of chiral regulators in the chirality induction and amplification.

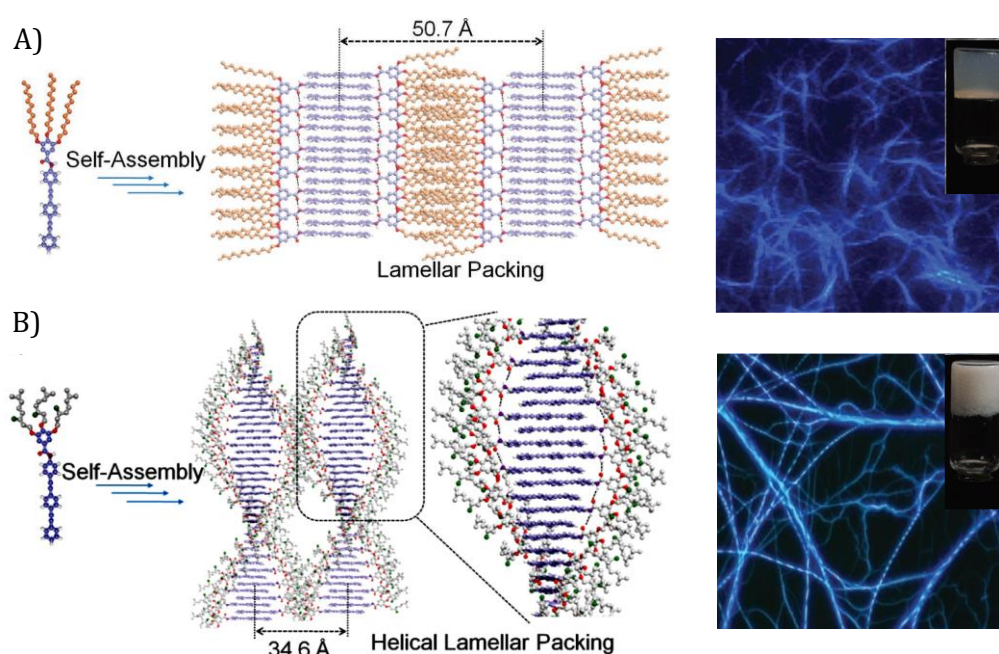


Figure 3B.3. Schematic representation of the self-assembly, optical fluorescence microscopic images and corresponding gel photographs of A) achiral linear alkyl and B) chiral branched alkyl substituted PE (Adapted from reference 28).

Recently, G. Das *et al.* reported the effect of alkyl substitutions in the terminal position of phenyleneethynylene (PE) derivatives on their fluorescence properties.²⁸ A linear achiral alkyl and a branched chiral alkyl substituted, amide functionalized PE molecules were self-assembled into 1D fibers through H-bonding and their supramolecular gelation properties at higher concentrations were

established in detail. Using the characteristics of gels, they have deduced a suitable mechanism for self-assembly. Here, as a consequence of the chiral substitution, the ordered lamellar packing (Figure 3B.3A) in achiral PE changes to helical lamellar packing (Figure 3B.3B), and the chirality of assembly was proven by using optical and morphological studies.

Distinct from the above reports, there are few works demonstrating the effect of chiral substituents on self-assembly without displaying any visible chirality in the morphologies.^{29,30} For instance, Takuho Saito and Shiki Yagai showed the ordered self-assembly of two scissor shaped, chiral azobenzene derivatives (varying in their structure by position of NH and CO in amide group), 1 and 2 into toroids and nanotubes.²⁹ In methylcyclohexane, the molecular structure undergoes folding through π - π stacking and the folded structures further assemble into toroid through inter or intra molecular H-bonding. These toroids upon aging results in the formation of 1D-nanotubes with fibrous morphologies (Figure 3B.4A). Though assembled toroids and nanotubes were CD active (Figures 3B.4B & 3B.4C), as a consequence of the secondary molecular packing they didn't display any structural chirality.

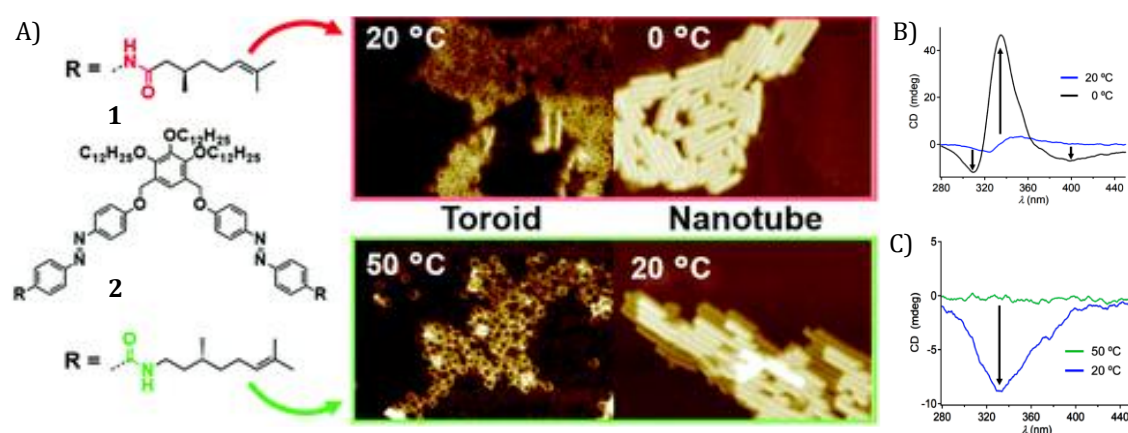


Figure 3B.4. A) Chemical structure of the azobenzene derivatives, assembled morphologies at different temperatures and B) & C) corresponding CD spectra (Adapted from reference 29).

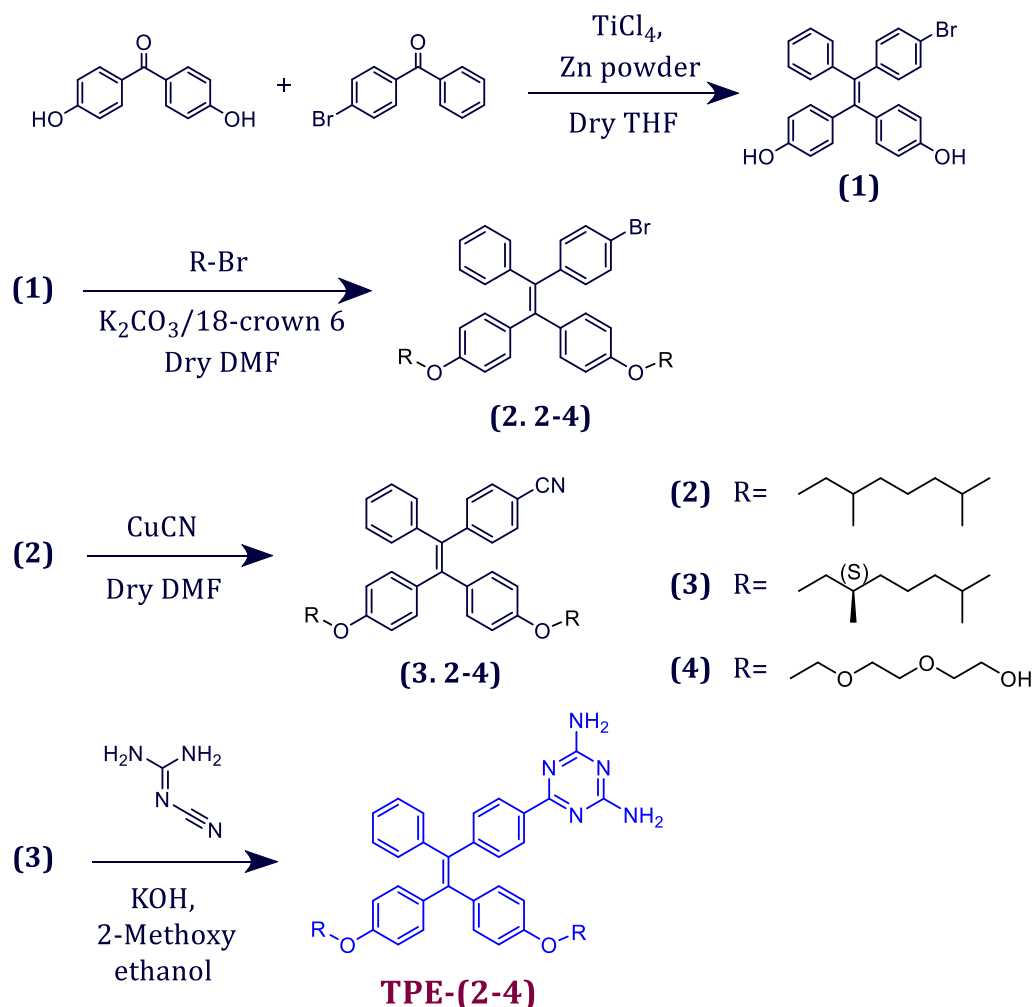
We have demonstrated the self-assembly and supramolecular gel formation of a Tetraphenylethylene-Diaminotriazine (TPE-DAT) derivative, **TPE-1** in Chapter 3A and proposed a mechanism for the hierarchical supramolecular assembly. In order to understand the effect of alkoxy substitution in TPE-DAT self-assembly and to verify the proposed mechanism in chapter 3A, we have synthesized three TPE-DAT molecules by changing the dodecyloxy substituent in **TPE-1** with 3,7-dimethyloctane (**TPE-2**), (S)-3,7-dimethyloctane (**TPE-3**) and triethylene glycol (**TPE-4**), alkoxy substitutions. In this chapter, we describe the optical and morphological characteristics of AIE and self-assembly studies of **TPE-2/3/4** in detail. Using the properties of self-assembly, a suitable mechanism was deduced and the results were correlated with mechanism of **TPE-1** assemblies.

3B.3. RESULTS AND DISCUSSION

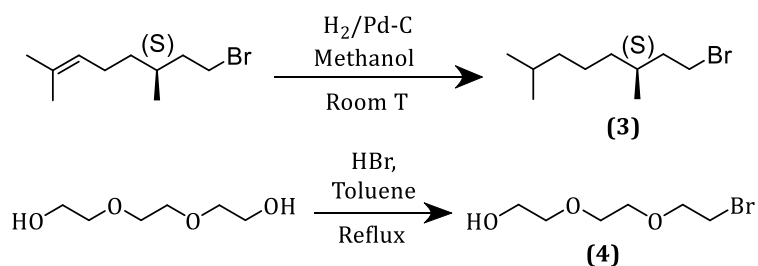
3B.3.1. Design and synthesis of TPE-DAT derivatives

To verify our proposed mechanism of **TPE-DAT** and **TPE-DAT \equiv T-C12** self-assembly described in chapter 3A, we designed three novel **TPE-DAT** molecules, **TPE-2** (racemic), **TPE-3** (chiral) and **TPE-4** (triethylene glycol), varying their chemical structure by different alkoxy substitutions. The molecules were synthesized by following similar synthetic procedures detailed in Chapter 3A and as shown below in Scheme 3B.1. The final molecules **TPE-2**, **TPE-3** and **TPE-4** were obtained in 71%, 64% and 34% yields, respectively. The mono-bromo alkyl derivatives, **(3)** and **(4)** used in the second step of **TPE-3** and **TPE-4** synthesis, respectively were prepared separately from the corresponding commercially available parent molecules as shown in Scheme 3B.2. (S)-Citronellyl bromide was

reduced in presence of Pd-C to give (S)-1-bromo-3,7-dimethyloctane (**3**) in 97% yield and triethylene glycol was brominated with 48% HBr in toluene to give 2-(2-(2-bromoethoxy)ethoxy)ethan-1-ol, (**4**) in 50% yield. Synthetic procedures and characterization data for all the intermediates and final molecules are noted in the experimental section.



Scheme 3B.1. Synthetic scheme for different alkoxy-substituted TPE-DAT derivatives, TPE-2, TPE-3 and TPE-4.



Scheme 3B.2. Synthetic scheme of mono-bromo alkyl derivatives, (3) and (4).

3B.3.2. Photophysical properties

Basic photophysical properties like UV-visible absorption and fluorescence emission of **TPE-DAT** derivatives, **TPE-2**, **TPE-3** and **TPE-4** were initially analyzed in soluble organic solvents. **TPE-2** and **TPE-3** displayed similar characteristics to that of **TPE-1** in THF, acetonitrile and chloroform, with weakly emissive monomeric emission maxima at 408 nm, 431 nm and 447 nm, respectively (Figures 3B.5A & 3B.5B, the chiral derivative **TPE-3** also displayed similar properties). On the other hand, the triethylene glycol derivative **TPE-4** was soluble in polar solvent like methanol with similar absorption maxima as that in THF (Figure 3B.6A).

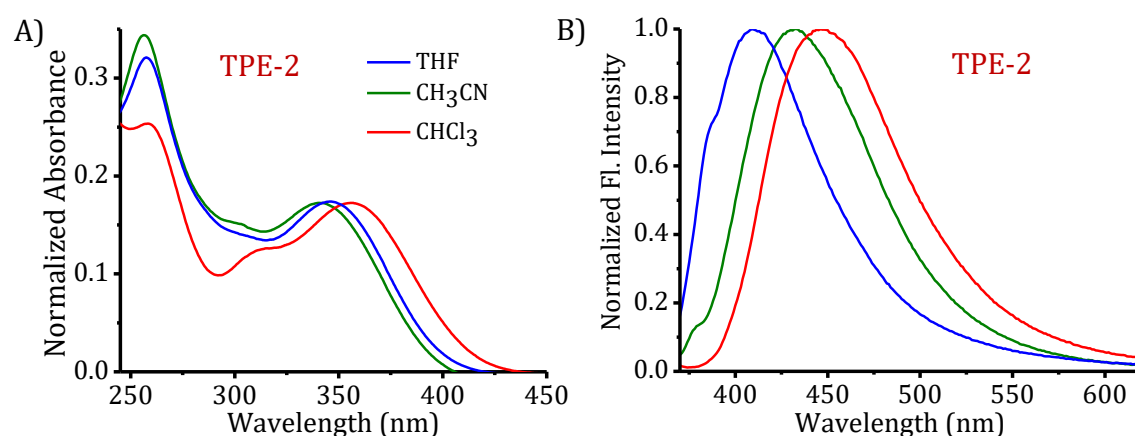


Figure 3B.5. A) UV-visible absorption and B) emission spectra of **TPE-2** in THF, acetonitrile and chloroform.

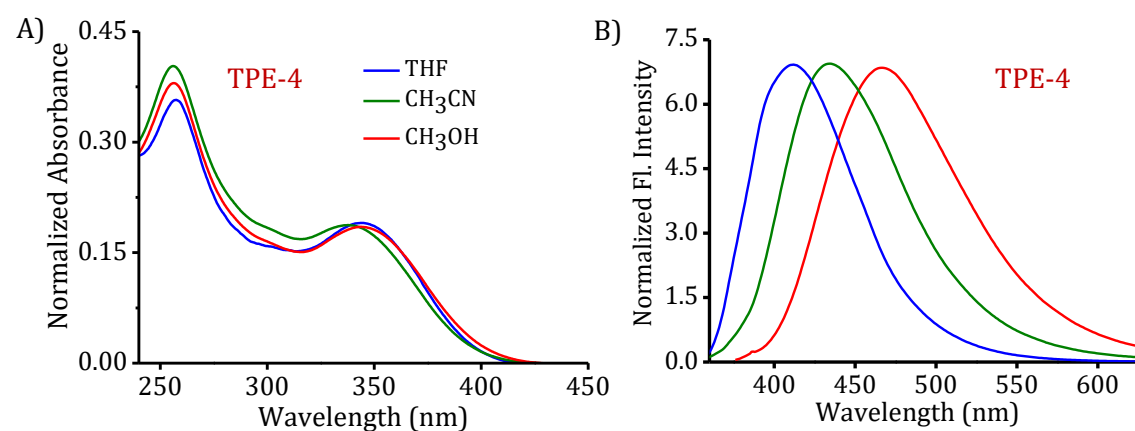


Figure 3B.6. A) UV-visible absorption and B) emission spectra of **TPE-4** in THF, acetonitrile and methanol.

Notably, TPE-4 displayed considerable solvatochromism with a distinct red shifted, weakly emissive 466 nm fluorescence emission band in methanol (Figure 3B.6B), which implies the stabilization of the excited state in polar solvents. The triethylene glycol derivative, **TPE-4** was comparatively more soluble in polar solvents than **TPE-2/3** and hence it could be useful for studying the interaction with nucleic acid derivatives via complementary H-bonding in aqueous solvents.

3B.3.3. Aggregation: optical and morphological properties

The aggregation features of **TPE-2** and **TPE-4** molecules were studied in THF-water solvent system using UV-visible absorption, fluorescence emission and AFM analysis.

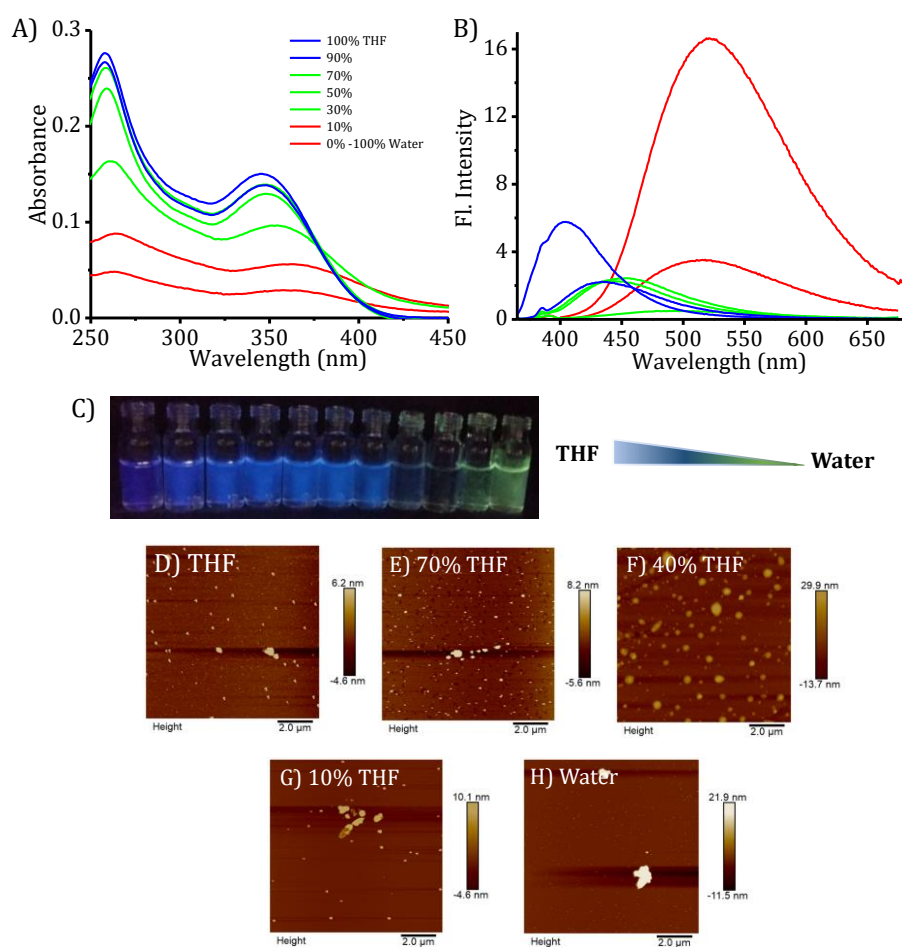


Figure 3B.7. A) UV-visible absorption and B) emission spectra, C) photographs of solution under UV light and D-H) AFM images of **TPE-2** (20 μM) in different THF-water fractions.

TPE-2 molecule displayed a gradual decrease and broadening in the absorption around 345 nm (Figure 3B.7A) and red shift in the fluorescence emission (Figure 3B.7B) from 400 nm to 450 nm, up to 70% of water in solvent system. Afterwards, with increasing water fraction, the samples started to form agglomerates and precipitated out (Figure 3B.7C, photographs of 20 μ M **TPE-2** samples in different THF-water fractions under UV-light). An enhanced emission band corresponding to the solid suspensions was observed at 540 nm, as seen in the case of **TPE-1** in Chapter 3A. These results were further supported by the presence of random spherical aggregates in the AFM images of samples drop-casted from different THF-water solvent fractions (Figures 3B.7D-H).

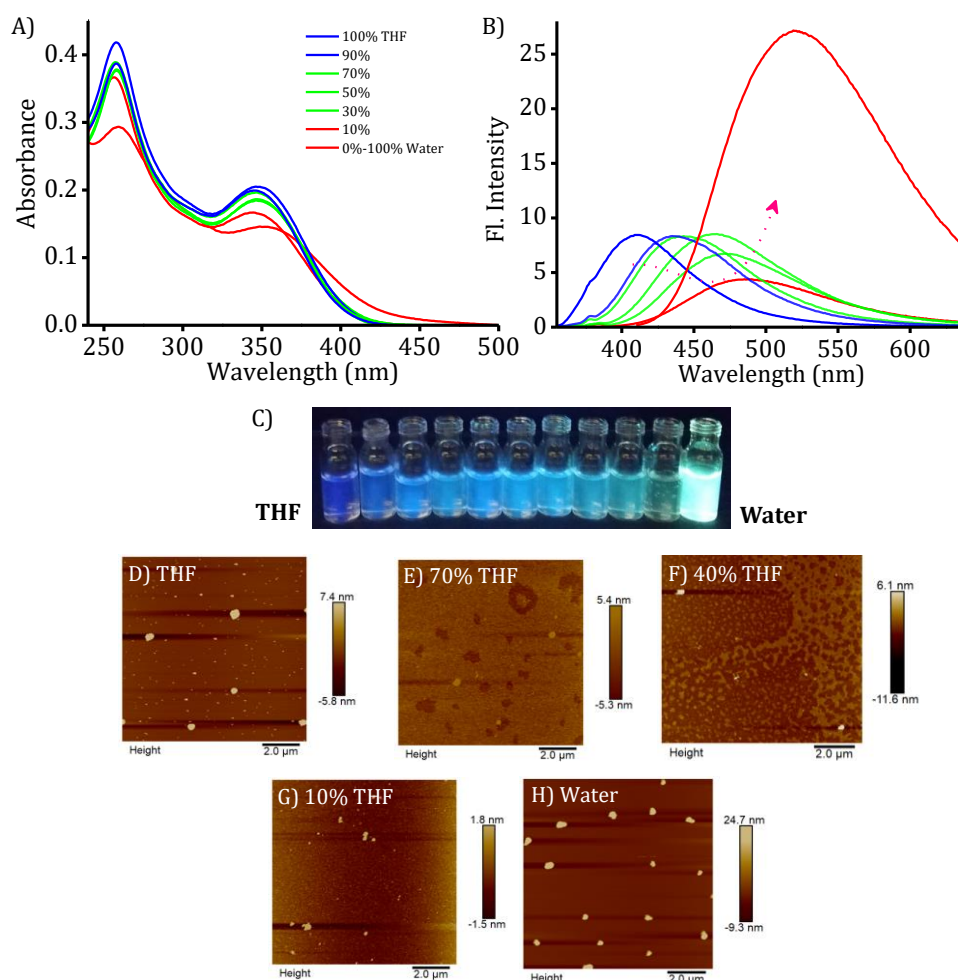


Figure 3B.8. A) UV-visible absorption and B) emission spectra, C) photographs of solution under UV light and D-H) AFM images of **TPE-4** (20 μ M) in different THF-water fractions.

In contrast to **TPE-2/3** and in agreement with the typical AIE property of TPE, **TPE-4** with higher polarity displayed clear changes in the UV-visible absorption and fluorescence emission with increasing fractions of water (Figure 3B.8A-C). The samples were miscible in all solvent fractions and didn't display any tendency to precipitate as observed in case of **TPE-1/2/3** even at higher fractions of water, and random aggregates were observed in the AFM images of **TPE-4** in THF-water mixtures (Figures 3B.8D-G). However, different from **TPE-1/2/3**, **TPE-4** displayed the formation of uniformly distributed spherical aggregates in water (Figure 3B.8H), which further suggests the enhanced solvophobic interaction directed aggregation of **TPE-4** in water.

3B.3.4. Self-assembly of TPE-2 and TPE-3

Based on the concentration dependence of the self-assembly of **TPE-1** established and detailed in Chapter 3A, we choose an appropriate concentration of 4×10^{-4} M and 6×10^{-4} M for **TPE-2** and **TPE-3**, respectively to analyze the self-assembly process in dodecane. **TPE-2** in chloroform displayed the presence of weakly emissive monomers with 452 nm absorption band (blue spectrum in Figures 3B.9A & 3B.9B). Whereas, the absorption spectra in dodecane exhibited 307 nm absorption maxima along with 452 nm shoulder band, and a strong fluorescence emission band at 430 nm corresponding to the assembled state (pink spectrum in Figures 3B.9A & 3B.9B). Further, temperature dependent cooling of **TPE-2** in dodecane from 363 K to 283 K displayed the gradual formation of 307 nm absorption band up to a temperature of 293 K, followed by a sudden enhancement upon cooling to 283 K (Figure 3B.10A). Similarly, the corresponding fluorescence spectra displayed the formation of assembled state with an intense blue (430 nm)

emission band, intensity of which is significantly enhanced below 298 K (Figure 3B.10B). These results suggest the cooperative pathway for **TPE-2** self-assembly in dodecane.

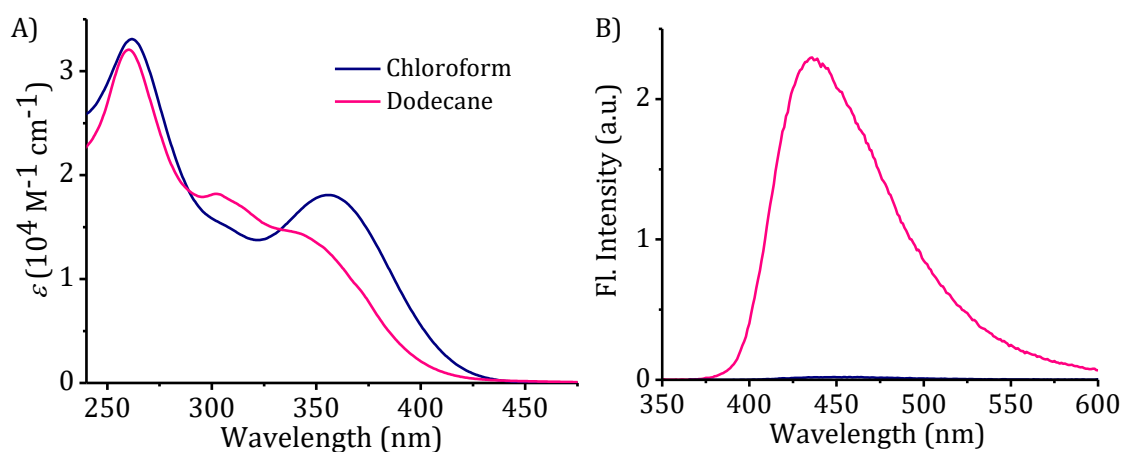


Figure 3B.9. A) UV-visible absorption and B) fluorescence emission spectra of **TPE-2** (4×10^{-4} M) in chloroform and dodecane at 298 K ($\lambda_{\text{exc}} = 350$ nm).

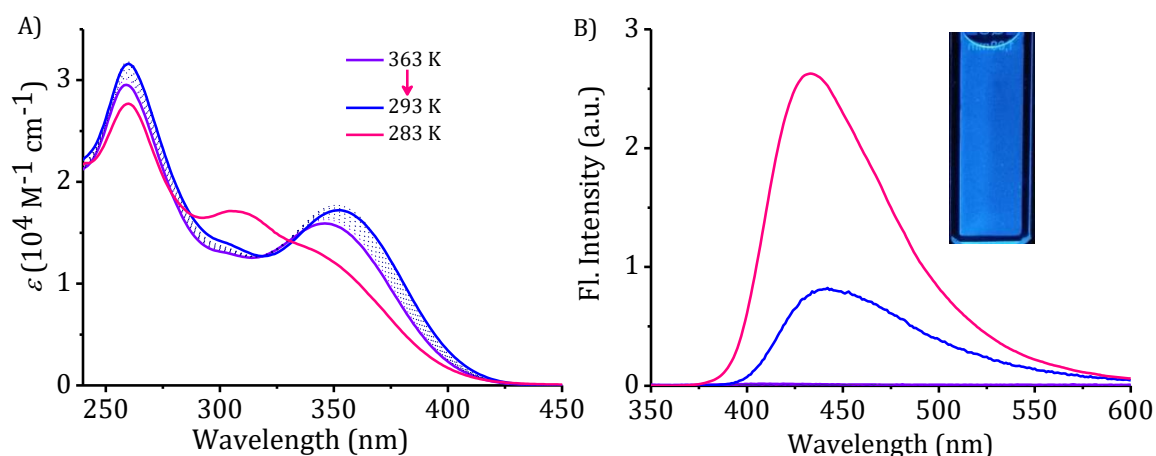


Figure 3B.10. Temperature dependent changes in the A) absorption and B) emission spectra of 4×10^{-4} M **TPE-2** in dodecane upon cooling from 363 K to 293 K, and inset of B shows the photograph of **TPE-2** in dodecane at 298 K under 365 nm UV light.

We investigated the changes in the self-assembly in detail and the photophysical properties of **TPE-2** in presence of a competitive H-bonding derivative, **T-C12**. With the sequential addition of **T-C12** to the assembled **TPE-2**, a decrease in the 307 nm absorption band along with gradual formation of 350 nm band was observed in the absorption spectra (Figure 3B.11A). These changes

indicate the perturbation of **TPE-2** homo-assembly in presence of **T-C12**, and is additionally supported by the observed quenching of the fluorescence emission band at 430 nm (Figure 3B.11B). Further, controlled cooling of a hot dodecane solution of **TPE-2** in presence of **T-C12** (1:1 equivalent) from 363 K to 283 K showed significant enhancement in the 350 nm absorption band and formation of a broad emission band at 460 nm (Figures 3B.12A & 3B.12B).

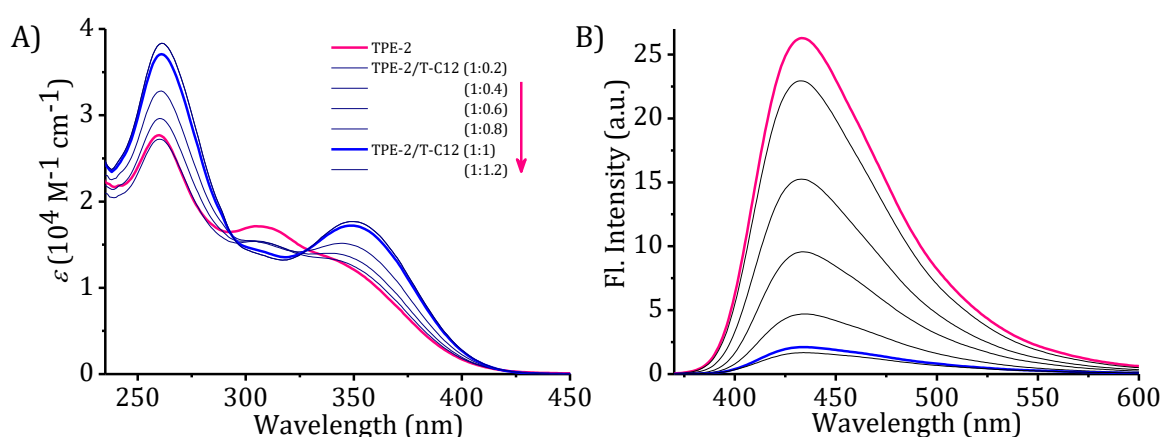


Figure 3B.11. Changes in the A) absorption and B) emission spectra with the sequential addition of **T-C12** (0-1.2 equivalent) into $4 \times 10^{-4} \text{ M}$ **TPE-2** in dodecane ($\lambda_{\text{exc}} = 327 \text{ nm}$).

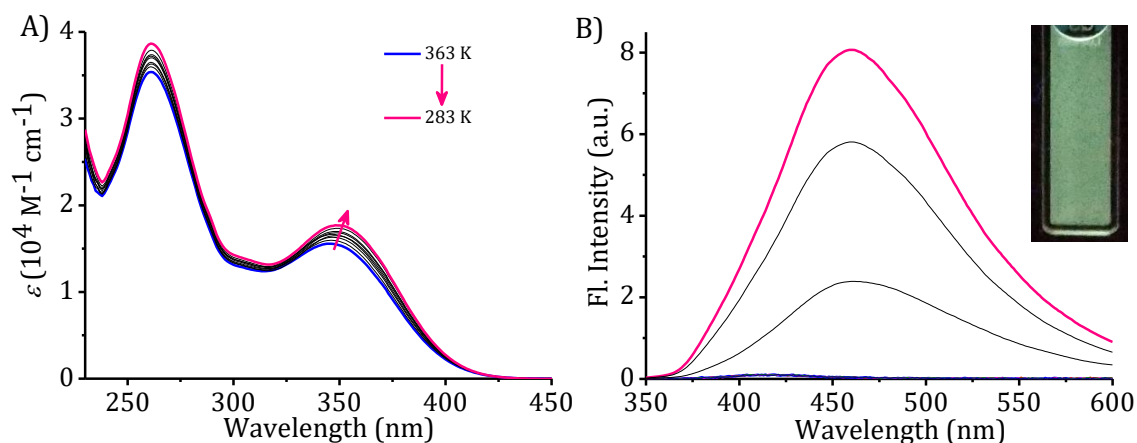


Figure 3B.12. Temperature dependent changes in the A) absorption and B) emission spectra of **TPE-2**/**T-C12**, upon cooling from 363 K to 293 K ($\lambda_{\text{exc}} = 327 \text{ nm}$ and inset of B shows the photograph of **TPE-2**/**T-C12** at 298 K under UV-light).

This newly formed, green emissive assembly of **TPE-2** in presence of **T-C12**, suggest the presence of a different monomeric unit in the assembly, which is

distinct from the blue emissive **TPE-2** homo-assembly in the absence of **T-C12**. These results of photophysical properties of **TPE-2** self-assembly were in agreement with the properties of dodecyloxy-substituted **TPE-1** self-assembly described in chapter 3A. Except the 40 nm blue shift observed in the fluorescence emission of **TPE-2**≡**T-C12** (460 nm) from 502 nm of **TPE-1**≡**T-C12** assembly. This blue shift in **TPE-2**≡**T-C12** emission was also noticeable from the whitish green color of UV-light images of sample at 298 K (inset of Figure 3B.12B), in place of the pure green color observed for **TPE-1**≡**T-C12**.

The self-assembly of chiral alkoxy substituted TPE-DAT derivative, **TPE-3** were also initially analyzed in dodecane and chloroform solvents. Unlike **TPE-1** and **TPE-2**, and even with a higher concentration of 6×10^{-4} M **TPE-3** in dodecane, the characteristic 307 nm absorption band of assembly was not prominent at 298 K with a comparatively weak fluorescence emission band at 430 nm (pink spectra in Figures 3B.13A & 3B.13B). Whereas, **TPE-3** was completely soluble in chloroform with 352 nm absorption and a weak 450 nm emission band, as expected (blue spectra in Figures 3B.13A & 3B.13B).

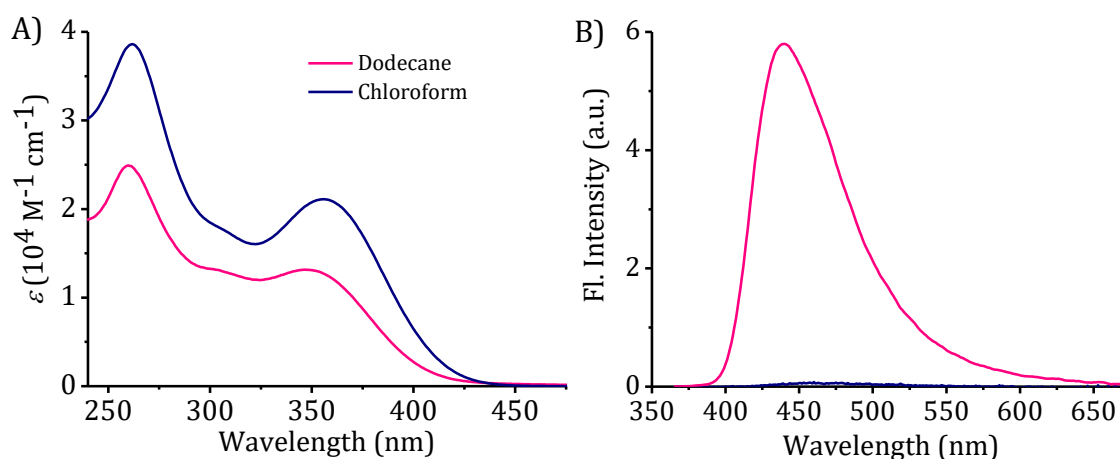


Figure 3B.13. A) UV-visible absorption and B) fluorescence emission spectra of **TPE-3** (6×10^{-4} M) in chloroform and dodecane at 298 K ($\lambda_{\text{exc}} = 350$ nm).

The temperature-controlled cooling of 6×10^{-4} M **TPE-3** in dodecane from 363 K to 283 K showed an initial slow formation of the 307 nm aggregate absorption band up to 293 K, followed by a fast formation below 293 K along with corresponding enhancement in the 430 nm emission band. These observations are indicative of the cooperative pathway for **TPE-3** self-assembly (Figures 3B.14A & 3B.14B).

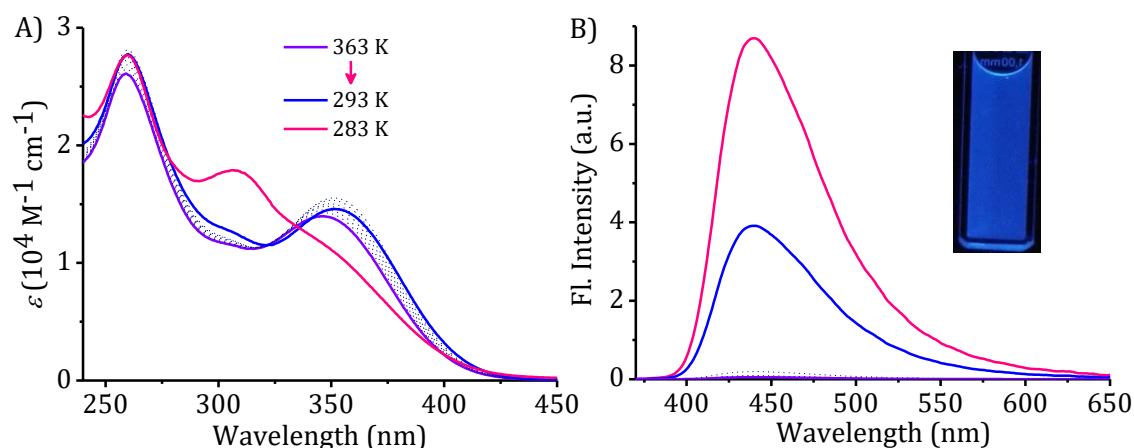


Figure 3B.14. Temperature dependent changes in the A) absorption and B) emission spectra of 6×10^{-4} M **TPE-3** in dodecane upon cooling from 363 K to 283 K. Inset of B shows the photograph of **TPE-3** in dodecane at 298 K under 365 nm UV light.

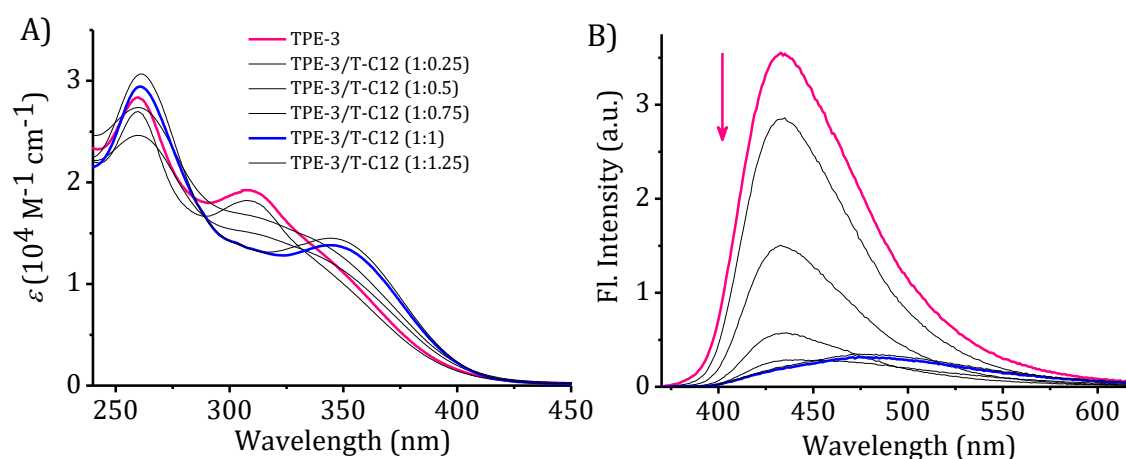


Figure 3B.15. Changes in the A) absorption and B) emission spectra with the sequential addition of **T-C12** (0-1.2 equivalent) into the 6×10^{-4} M **TPE-3** in dodecane ($\lambda_{exc} = 327$ nm).

Similar to **TPE-2**, the UV-visible absorption and emission studies indicate the dissociation of **TPE-3** self-assembly in presence of **T-C12** (Figures 3B.15A & 3B.15B) and formation of green emissive assemblies with 350 nm absorption and

480 nm fluorescence emission maxima upon cooling from 363 K to 283 K (Figures 3B.16A & 3B.16B). In addition, the UV-light images of **TPE-3**≡**T-C12** samples displayed whitish green emission (inset of Figure 3B.16B) with characteristic 22 nm blue shift from the green emissive assemblies of **TPE-1**≡**T-C12**. These similarities in the photophysical properties of **TPE-2** and **TPE-3** assemblies with the results observed in the case of **TPE-1**, partially verifies our proposed mechanism of self-assembly in chapter 3A.

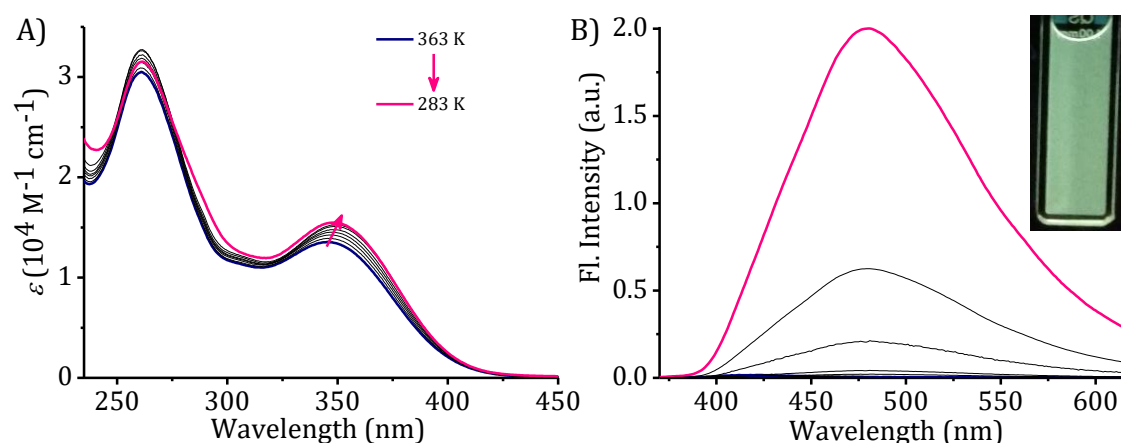


Figure 3B.16. Temperature dependent changes in the A) absorption and B) emission spectra of **TPE-3**≡**T-C12**, upon cooling from 363 K to 283 K ($\lambda_{\text{exc}} = 327$ nm and inset of B shows the photograph of **TPE-3**≡**T-C12** at 298 K under UV-light).

3B.3.5. Thermodynamic and chiroptical properties of self-assembly

Detailed investigation of the TPE-DAT self-assembly pathway of **TPE-2** and **TPE-3** were conducted by monitoring the temperature dependent changes in the 307 nm absorption band, characteristic of the assembly as a function of different concentrations. Figures 3B.17 and 3B.18 show the plot of fraction of aggregates versus temperature for **TPE-2** and **TPE-3**, respectively. The non-sigmoidal nature of cooling curves well fitted with the co-operative equilibrium model reported in the literature,³¹ which implies the nucleation-elongation self-assembly pathway for

both **TPE-2** and **TPE-3** self-assembly. Elongation temperatures (T_e) of self-assembly for different concentrations were obtained from the cooling curves and van't Hoff plot was constructed for **TPE-2** and **TPE-3**, separately as shown in Figures 3B.19A & 3B.19B. From the linear fits of van't Hoff plot, thermodynamic parameters (TD) of self-assembly like standard enthalpy (ΔH°), standard entropy ΔS° and standard Gibbs free energy ΔG° at 298 K for **TPE-2** and **TPE-3** were calculated.

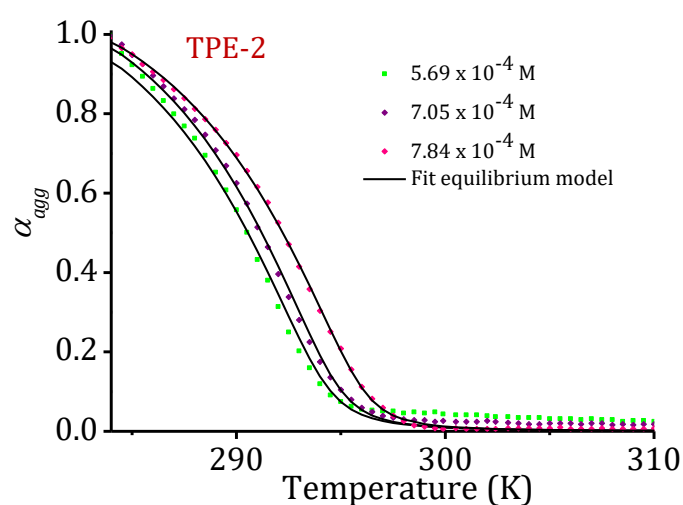


Figure 3B.17. Plots of fraction of aggregates (α_{agg}) against temperature for different concentrations of **TPE-2** in dodecane; 294.9 K for 5.69×10^{-4} M, 295.5 K for 7.05×10^{-4} M and 296.8 K for 7.84×10^{-4} M.

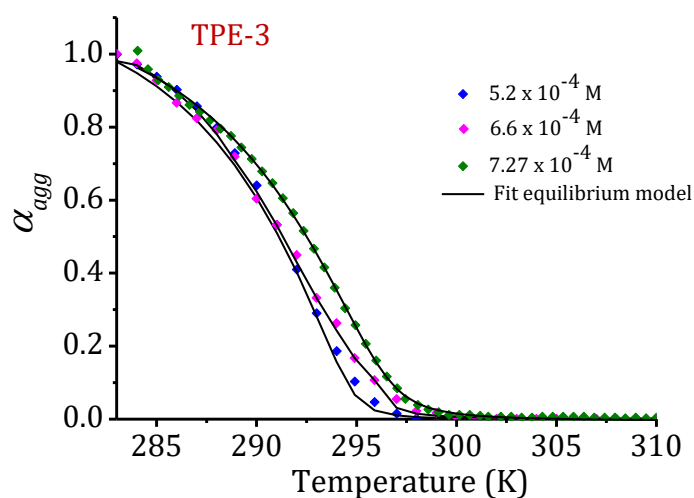


Figure 3B.18. Plots of fraction of aggregates (α_{agg}) against temperature for different concentrations of **TPE-3** in dodecane; 295.3 K for 5.2×10^{-4} M, 296.2 K for 6.6×10^{-4} M and 299.8 K for 7.27×10^{-4} M.

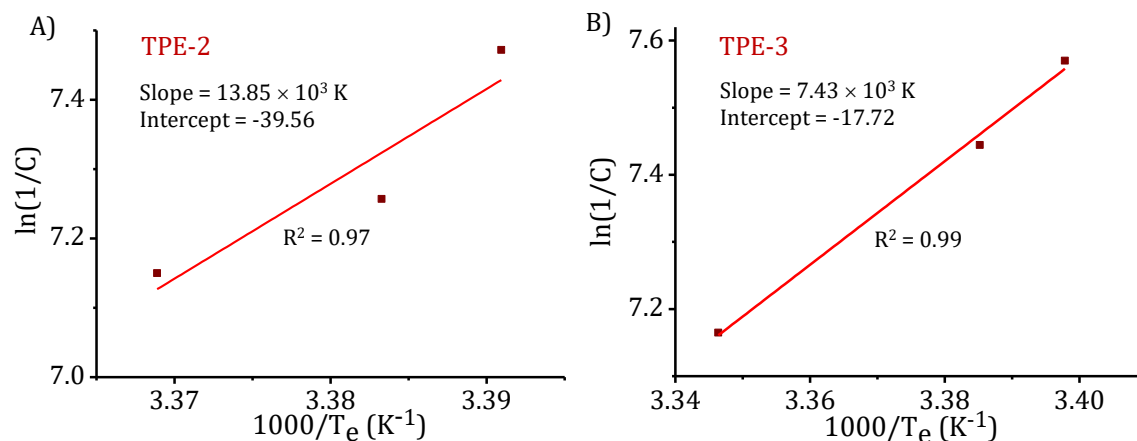


Figure 3B.19. van't Hoff plot constructed from the reciprocal of T_e , ($1/T_e$) versus logarithm of reciprocal concentration ($\ln(1/C)$) for A) **TPE-2** and B) **TPE-3**.

The values of ΔH° , ΔS° and ΔG° obtained for **TPE-2** self-assembly are -115.21 kJ mol^{-1} , -328.82 J $\text{mol}^{-1} \text{K}^{-1}$ and -17.22 kJ mol^{-1} , respectively, and for **TPE-3** self-assembly are -61.8 kJ mol^{-1} , -147.33 J $\text{mol}^{-1} \text{K}^{-1}$ and -17.89 kJ mol^{-1} , respectively. The obtained ΔG° values of **TPE-2** and **TPE-3** self-assembly were almost near to the ΔG° (-18.6 kJ mol^{-1}) value of **TPE-1** self-assembly with H-bonding assisted cooperative nucleation-elongation pathway as explained in chapter 3A.

To check the role of chiral substituent in the **TPE-3** self-assembly and to verify the proposed general self-assembly mechanism of TPE-DAT in dodecane, the chiroptical properties of **TPE-2** and **TPE-3** were analyzed by CD studies. Interestingly, the CD spectrum of **TPE-3** in dodecane exhibited Cotton effect with a bisignated CD signal having a zero crossing at 307 nm (Figure 3B.20). Whereas, the dodecane solution of **TPE-2** and chloroform solutions of **TPE-2** and **TPE-3** didn't showed any characteristic CD signal. To get more insight in to the chirality transfer from individual **TPE-3** molecule to the self-assembled state, temperature dependent changes in the CD spectrum were analyzed by cooling a hot solution of **TPE-3** from 343 K to 283 K. Upon cooling, the formation of a bisignated CD signal in the characteristic absorption range of self-assembly was observed below 300 K,

which was additionally verified by recording the corresponding CD intensity variations at 266 nm (Figures 3B.21A & 3B.21B). On the other hand, similar experiment performed with **TPE-3**≡**T-C12** didn't display any characteristic changes (red spectrum in Figures 3B.21B). These results suggest the initial ordered chiral assembly of the monomeric units in the molecular packing of **TPE-3** and loss of chirality in the presence of **T-C12**.

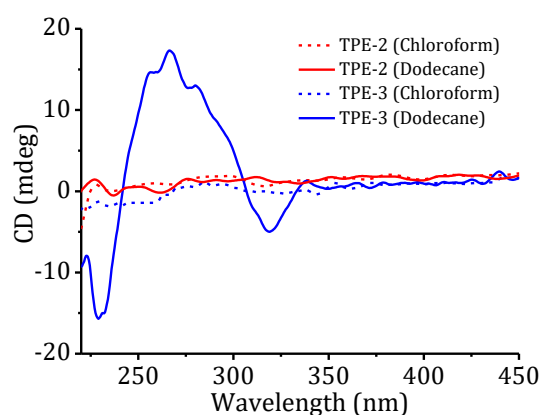


Figure 3B.20. CD spectra of 4×10^{-4} M **TPE-2** and 6×10^{-4} M **TPE-3** in dodecane and chloroform.

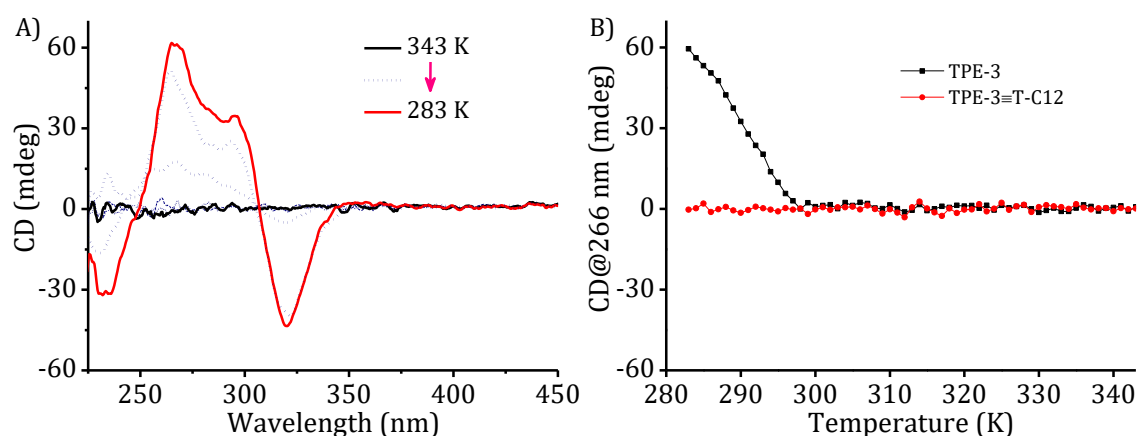


Figure 3B.21. A) CD spectra of 6×10^{-4} M **TPE-3** in dodecane recorded by cooling from 343 K to 283 K, with 10 K difference between each spectral measurement and B) CD spectral intensity variations at $\lambda = 266$ nm for **TPE-3** and **TPE-3**≡**T-C12**.

3B.3.6. Microscopic studies

The morphology changes associated with the above-mentioned racemic **TPE-2** and chiral **TPE-3** assemblies, in the absence and presence of **T-C12** were

studied using AFM, TEM and optical fluorescence microscopic (OFM) techniques. AFM images of **TPE-2** and **TPE-3** displayed individual and bundled fiber like structures (Figures 3B.22A & 3B.22D) with ~ 11 nm height and 120-150 nm width (Figure 3B.22C, height profile of **TPE-2**). Whereas in the presence of **T-C12**, the assembly changes to fibrous structures with a reduced height of 2-3 nm, as observed for **TPE-1** (Figures 3B.23B, 3B.23E & 3B.23F).

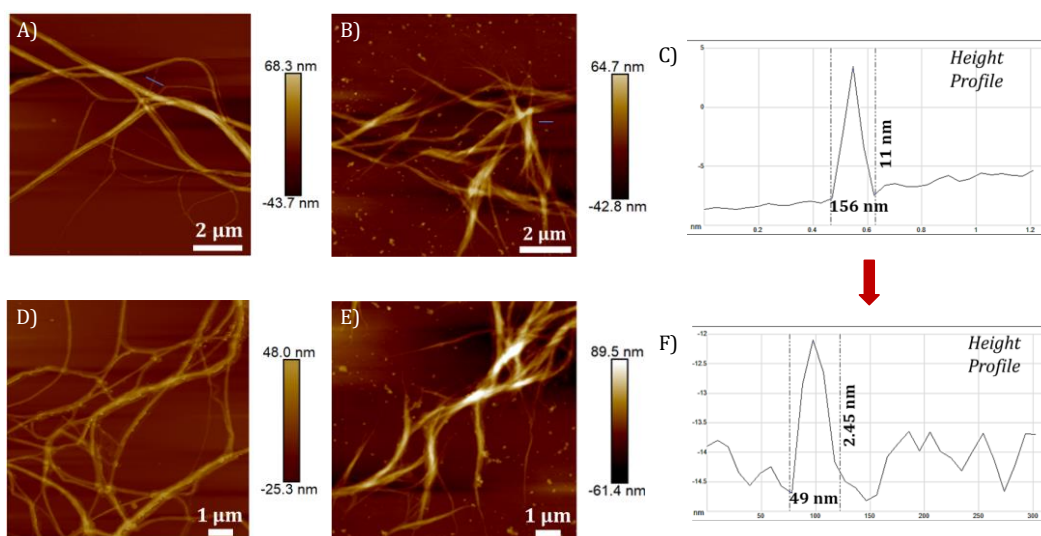


Figure 3B.22. AFM images of A) **TPE-2** (4×10^{-4} M), B) **TPE-2** \equiv **T-C12** (4×10^{-4} M, 1:1), D) **TPE-3** (6×10^{-4} M) and E) **TPE-3** \equiv **T-C12** (6×10^{-4} M, 1:1). C) & F) Height profiles of a very thin fiber in A & B, respectively. (The area of height profiles is marked as blue line in A and B).

In agreement with AFM morphologies, the TEM images of respective samples also displayed individual and bundled 1D-fiber like structures in the absence of **T-C12** (Figures 3B.23A & 3B.23C, left panel) and thin fibrous structures in the presence of **T-C12** (Figures 3B.23B & 3B.23D, left panel). Even though **TPE-3** assemblies were CD active with Cotton effect, the corresponding AFM and TEM morphologies didn't display any visible structural features of supramolecular chirality in the 1D-bundled or individual fibers. These conflicting results of CD and morphology studies suggests the secondary molecular packing directed masking of structural chirality in **TPE-3** assemblies.^{29,30}

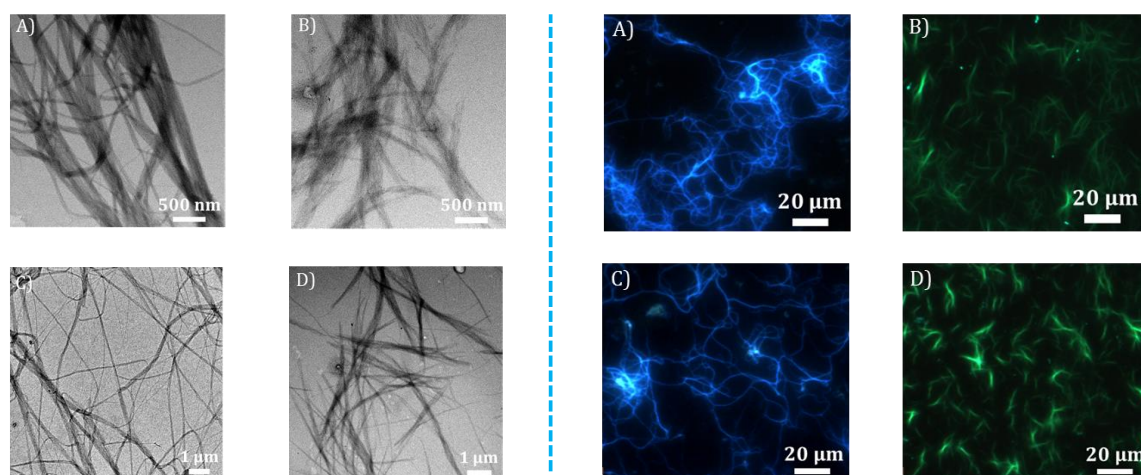


Figure 3B.23. TEM (left panel) and OFM (right panel) images of samples drop-casted from A) **TPE-2** (4×10^{-4} M), B) **TPE-2** \equiv **T-C12** (4×10^{-4} M, 1:1), C) **TPE-3** (6×10^{-4} M) and D) **TPE-3** \equiv **T-C12** (6×10^{-4} M, 1:1).

The solid-state fluorescence properties of the 1D assemblies of **TPE-2** and **TPE-3** inspected using optical fluorescence microscope showed the presence of long coiled blue emissive fibers of TPE in the absence of **T-C12** (Figures 3B.23A & 3B.23C, right panel) and green emissive short fibrous structures in the presence of **T-C12** (Figures 3B.23B & 3B.23D, right panel). These results of morphology and fluorescence changes from blue to green emissive assemblies, similar to the 1D-supramolecular assembly of **TPE-1** demonstrated in chapter 3A, suggest the possibility of similar mechanism and gelation behaviour for **TPE-2** and **TPE-3**.

3B.3.7. Self-assembly of TPE-4 with dT₂₀ template

Due to the insolubility of triethylene glycol substituted **TPE-4** in dodecane, the self-assembly properties were investigated in 20% THF-PBS solvent system. The template, **T-C12** used for tuning the self-assembly properties of other derivatives was insoluble in 20% THF-PBS. Therefore, we choose a better template, dT₂₀ (polydeoxythymidine with 20 thymine nucleobases) with enhanced solubility in 20% THF-PBS to study the interactions with **TPE-4**. The UV-visible absorption

and emission spectra of 5×10^{-4} M **TPE-4** in 20% THF-PBS exhibited a 350 nm absorption band and a 468 nm broad emission band, respectively (blue spectra in Figures 3B.24A & 3B.24B). This reasonably high fluorescence intensity implies that **TPE-4** exist as aggregates in 20% THF-PBS and they are different from the assemblies formed in the case of other TPE-DAT derivatives in dodecane with 307 nm absorption and 430 nm fluorescence emission.

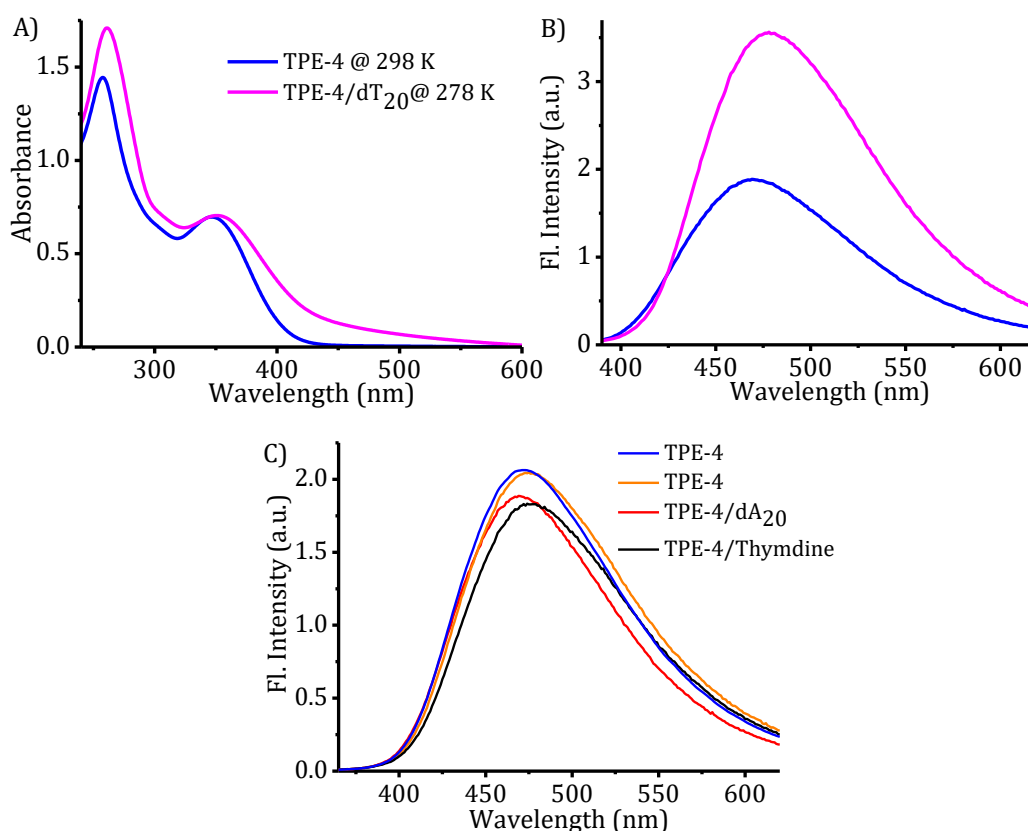


Figure 3B.24. A) Absorption and B) corresponding emission spectra of 5×10^{-4} M **TPE-4** at 298 K and the heat-cooled samples of **TPE-4/dT₂₀** (5×10^{-4} M, 20:1) at 278 K. C) Fluorescence emission spectra of **TPE-4** at 298 K, the annealed samples of **TPE-4**, **TPE-4/dA₂₀** (20:1) and **TPE-4/thymidine** (1:1) at 278 K. All these experiments were carried out in 20% THF-PBS.

To check the complementary H-bonding abilities of the **TPE-4** aggregates, a 1:20 ratio of dT₂₀ to **TPE-4** mixture was heated to 363 K, followed by cooling back to 278 K. Upon cooling to 278 K, a broadening of the absorption spectra with a tail end absorption extending up to 600 nm and a fluorescence enhancement with 10

nm red shift in the fluorescence emission maxima (from 468 nm to 478 nm) were observed (pink spectra in Figures 3B.24A & 3B.24B). To verify these observations, control experiments were carried out under similar conditions with **TPE-4** alone and **TPE-4** in presence of dA₂₀ (1:20 ratio) and thymidine (1:1 ratio), which failed to show any significant changes in the fluorescence emission (Figure 3B.24C). These results suggest that **TPE-4** interacts with dT₂₀ primarily through complementary H-bonding interaction, and the resultant assembly/aggregate is responsible for the spectral changes.

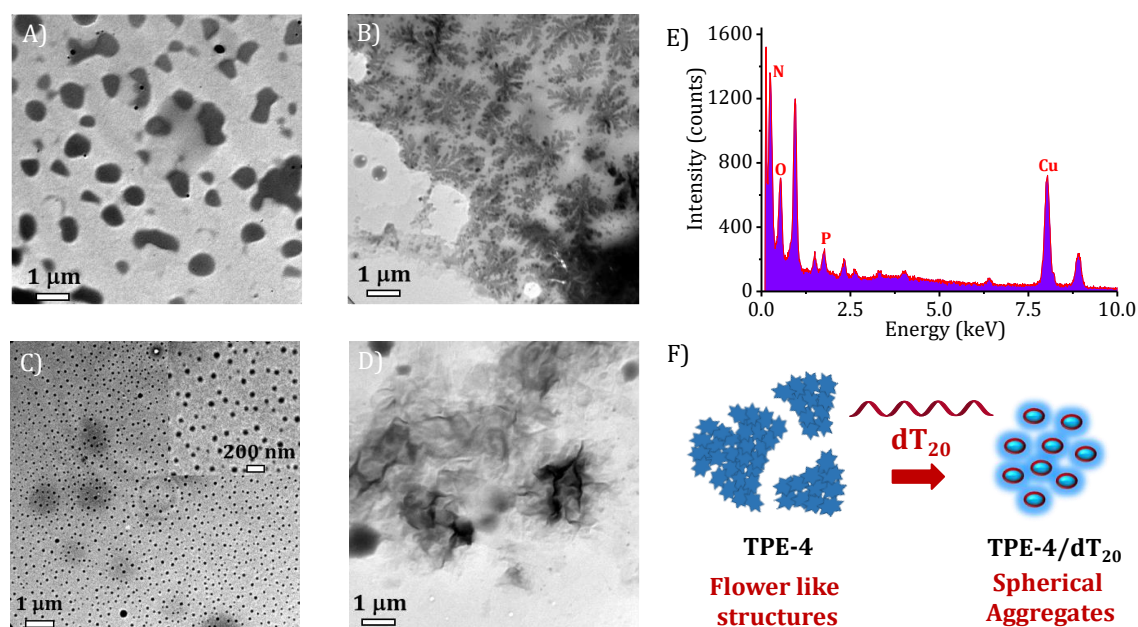


Figure 3B.25. TEM images of A) **TPE-4** (5×10^{-4} M) in THF and B) in 20% THF-PBS, and annealed samples of C) **TPE-4/dT₂₀** & D) **TPE-4** in 20% THF-PBS. E) EDAX spectrum of **TPE-4/dT₂₀** recorded with D and F) schematic representation of the mechanism of assembly.

Morphology changes accompanying the absorption and fluorescence spectral changes of **TPE-4** in presence of dT₂₀ was monitored by drop-casting the samples for TEM analysis. TEM images of **TPE-4** displayed random aggregates in THF and growing flower like morphology in 20% THF-PBS (Figures 3B.25A & 3B.25B). Whereas, the heat-cooled samples of **TPE-4/dT₂₀** (20:1) displayed uniformly distributed spherical nanostructures with 40-50 nm in size (Figure

3B.25C). This distinct observation was further checked by examining the TEM images of heat-cooled samples of **TPE-4** alone, which displayed fused flower like structures (Figure 3B.25D) with resemblances to the TEM images in Figure 3B.25B of **TPE-4** without heat treatment. Further, the occurrence of phosphorous atom in the EDAX spectrum recorded over the TEM samples of **TPE-4/dT₂₀** confirms the presence of **dT₂₀** in the uniformly distributed spherical nanostructures (Figure 3B.25E). In short, as a result of the poor H-bonding possibility of **TPE-4** in the solvophobic environment of 20% THF-PBS, **TPE-4**≡**dT₂₀** interactions result in condensation of **dT₂₀** strands (Figure 3B.25F shows the cartoonic illustration of morphology changes), instead of forming 1D-assemblies as observed in the case of other TPE-DAT molecules.

3B.3.8. Supramolecular gels of TPE-2 and TPE-3

As the important results helped to understand the mechanism of TPE-DAT self-assembly proposed in Chapter 3A was obtained from the gel characterizations, we have investigated the gelation properties of **TPE-2** and **TPE-3** in dodecane to verify the proposed mechanism. As expected, higher concentration of **TPE-2** and **TPE-3** in dodecane upon annealing lead to the formation of blue emissive gels, which transformed to green emissive gels in the presence of an equivalent amount of **T-C12** (Figures 3B.26A & 3B.26B).

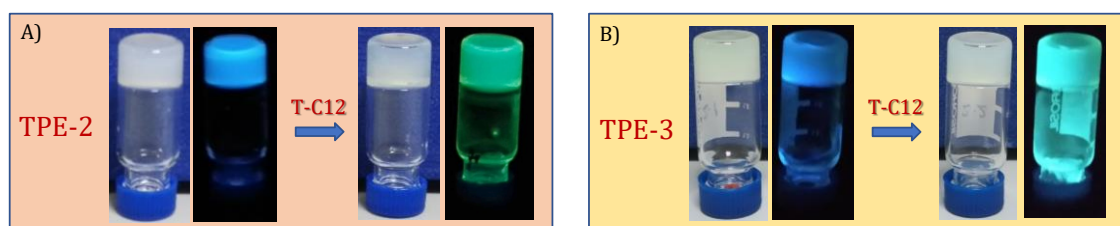


Figure 3B.26. Photographs of A) **TPE-2** and B) **TPE-3** gels in the absence and presence of **T-C12** under normal and UV light (6 mM, 1:0 and 1:1 ratio of **TPE-2/3** to **T-C12** in dodecane).

Both racemic **TPE-2** and chiral **TPE-3** derivatives formed opaque gels in contrast to the transparent gels formed by **TPE-1**. The CGC values for both **TPE-2** and **TPE-3** was ~ 6.1 mM, which can be reduced to 2.5 mM by the addition of an equivalent amount of **T-C12**.

SEM and solid-state absorption and emission measurements of xerogels were performed to verify the resemblances of supramolecular gels with low concentration solution state studies. The absorption spectra of the xerogels of **TPE-2** and **TPE-3** displayed a broad spectrum with absorption maxima around 300 nm in the absence of **T-C12** and 355 nm in the presence of **T-C12** (Figure 3B.27A), as observed in solution state photophysical studies. Whereas, the emission spectrum of **TPE-2** and **TPE-3** displayed slightly red shifted 445 nm emission maxima (Figure 3B.27B) in the absence of **T-C12** and almost similar emission maxima of 500 nm in the presence of **T-C12** compared to the solution state studies. This red shift of 15 nm from 430 to 445 nm in the solution and solid-state studies can be attributed to the formation of opaque gels, as a consequence of the changes in molecular arrangement of **TPE-2/3** assemblies. These results further validate the observation of blue and green emissive fibers in the solid-state optical fluorescence microscopic studies.

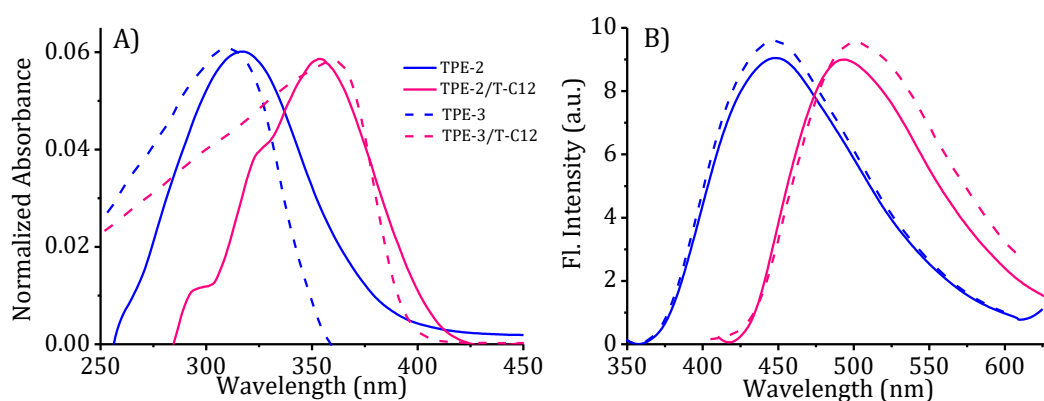


Figure 3B.27. Solid state A) absorption and B) emission spectra of the xerogel samples of **TPE-2**, **TPE-3**, **TPE-2** \equiv **T-C12** and **TPE-3** \equiv **T-C12** prepared from dodecane.

SEM images of **TPE-2** and **TPE-3** xerogel samples displayed the presence of highly cross-linked bundled fiber like structures (Figures 3B.28A & 3B.28C), On the other hand, **TPE-2 \equiv T-C12** and **TPE-3 \equiv T-C12** xerogels displayed randomly distributed stiff and thin fibrous structures (Figures 3B.28B & 3B.28D). These results of SEM analysis are in agreement with morphologies observed in AFM and TEM studies performed at lower concentrations, and therefore suggests a similar mechanism for assemblies in both solution and gel state.

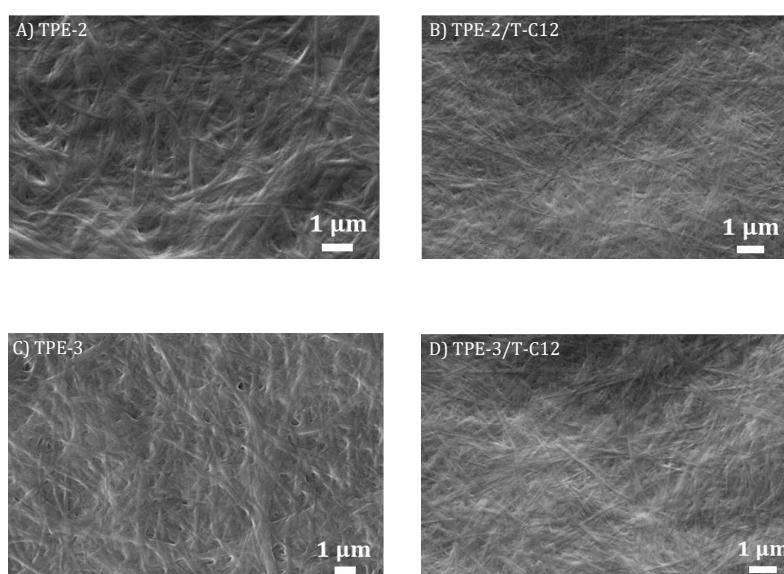


Figure 3B.28. SEM images of the xerogel samples prepared from A) **TPE-2**, B) **TPE-2 \equiv T-C12**, C) **TPE-3** and D) **TPE-3 \equiv T-C12** gels in dodecane.

3B.3.9. FT-IR and rheology studies of xerogels

The bonding nature and strength of **TPE-2**, **TPE-2 \equiv T-C12**, **TPE-3** and **TPE-3 \equiv T-C12** gels were analyzed using FT-IR and rheology measurements. The FT-IR spectrum of **TPE-2**, **TPE-3** and **T-C12** monomers in chloroform-d displayed the presence of free -NH₂ vibrational bands at 3535 & 3423 cm⁻¹, and N-H stretching band at 3394 cm⁻¹, respectively.^{28,32,33} These bands were shifted to 3488, 3318 and 3203 cm⁻¹ for **TPE-2** and **TPE-3** xerogels and 3449, 3329 and 3233 cm⁻¹ for **TPE-2 \equiv T-C12** and **TPE-3 \equiv T-C12** xerogels, characteristic of bonded -NH₂ (Figure

3B.29A). This shift of vibrational peaks towards lower frequency and broadening with respect to monomers indicate intermolecular H-bonding in xerogel samples. In addition, the difference in the vibrational peak values implies existence of different type H-bonded units in **TPE-2/ TPE-3** xerogel and **TPE-2≡T-C12/TPE-3≡T-C12** xerogels.

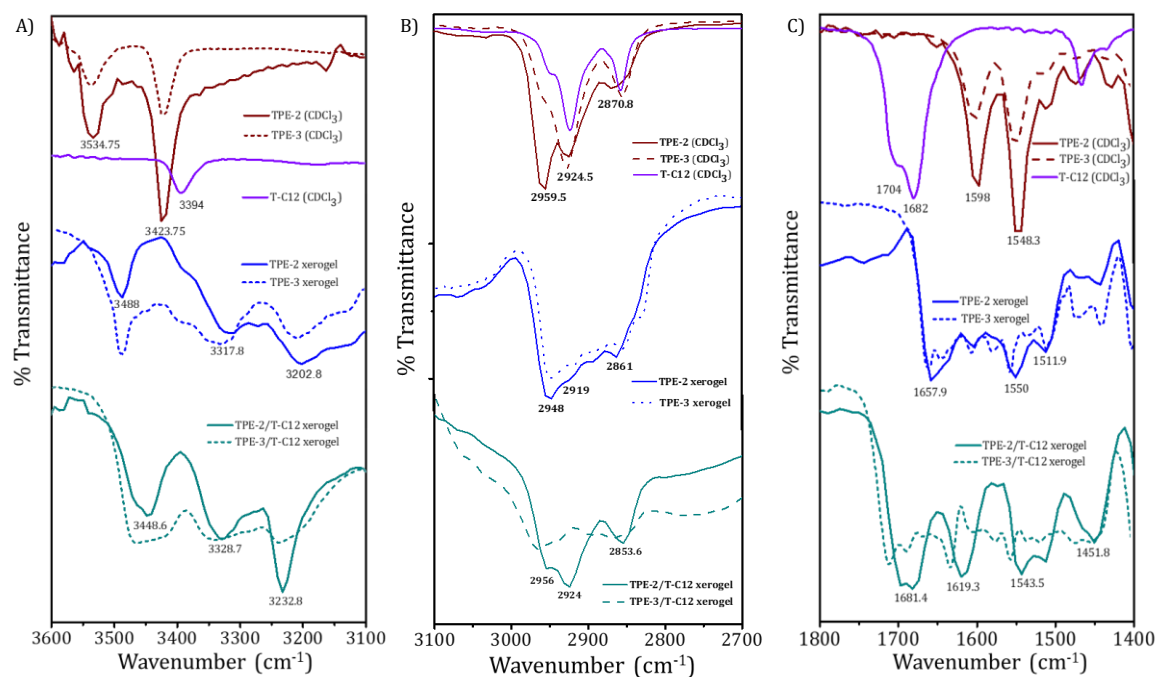


Figure 3B.29. FT-IR spectrum of **TPE-2** and **TPE-3** (monomer and xerogel), **T-C12** (monomer), **TPE-2≡T-C12** (xerogel), and **TPE-3≡T-C12** (xerogel) samples in the A) 3100-3600 cm⁻¹, B) 3100-2700 cm⁻¹ and C) 1400-1800 cm⁻¹ regions.

Similarly, the FT-IR spectrum in the 2700-3100 cm⁻¹ region of monomers displayed vibrational bands at 2960 cm⁻¹ (asymmetric -CH₃ stretching), 2925 cm⁻¹ (asymmetric -CH₂- stretching) and 2871 cm⁻¹ (symmetric -CH₃ stretching). These vibrational frequency values were found to be shifted to lower frequency in the case of **TPE-2** and **TPE-3** xerogels, and remained unaltered for **TPE-2≡T-C12** and **TPE-3≡T-C12** xerogels, with respect to monomeric spectra (Figure 3B.29B). This shift in the stretching vibrational frequency implies the presence of interdigitated alkyl chains in the molecular packing of **TPE-2** and **TPE-3** xerogel samples.

Moreover, the C=O stretching, N-H bending and ring stretching vibrations in the 1400 to 1800 cm^{-1} region of all the xerogel samples were complex with additional peaks compared to the monomeric spectrum (Figure 3B.29C). These spectral differences could be attributed to the changes in vibrational frequencies of aforementioned vibrations upon gelation, which further confirms the presence of H-bonding in the TPE-DAT self-assembly.

Dynamic frequency sweep measurements of all the gel samples performed using rheometer showed higher values of storage modulus (G') than loss modulus (G'') with a linear viscoelastic region (LVR) indicative of the viscoelastic nature of gels, as observed in the case of **TPE-1** gels in Chapter 3A. Lower values of G' and G'' for **TPE-2** and **TPE-3** compared to corresponding **TPE-2 \equiv T-C12** and **TPE-3 \equiv T-C12** suggests the improved capacity of the latter to store and disperse energy (Figures 3B.30A & 3B.30B). This implies, the gel strength of **TPE-2 \equiv T-C12** and **TPE-3 \equiv T-C12** are relatively high compared to gels in the absence of **T-C12**. In addition, the lower values of G' and G'' for **TPE-2** and **TPE-3** gels (1-10 range) compared to transparent **TPE-1** gel (10-100 range in Figure 3A.27 of Chapter 3A) could be ascribed to the dis-ordered molecular packing leading to gels.

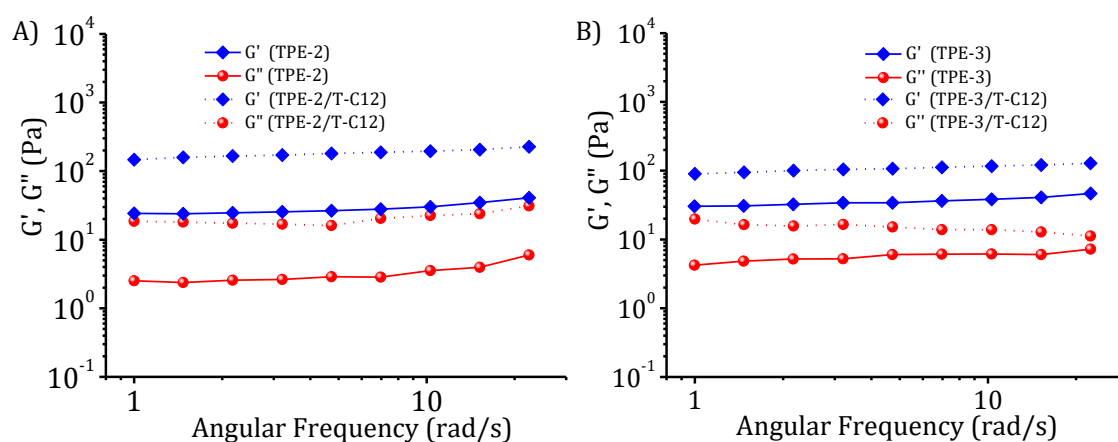


Figure 3B.30. Plot of G' and G'' against angular frequency of A) **TPE-2** and **TPE-2 \equiv T-C12**, and B) **TPE-3** and **TPE-3 \equiv T-C12** dodecane gels at 298 K (2.5 mM and 1:1 ratio).

3B.3.10. XRD and mechanism of self-assembly

To verify the mechanism of 1D-assemblies of **TPE-1** proposed in Chapter 3A of TPE-DAT molecules in dodecane, and to summarize the above experimental results of **TPE-2** (racemic) and **TPE-3** (chiral), WAXS analysis of the four xerogel samples were carried out. WAXS patterns of the xerogel films displayed reflections with d spacing of 34.75, 19.7 & 17.45 Å for **TPE-2** and 34.61, 19.88 & 17.78 Å for **TPE-3** (Figure 3B.31A). These d values with 1: $\sqrt{3}$: 2 ratio represents the (100), (110) and (200) planes of hexagonal columnar packing, giving rise to an intercolumnar distance of 39.96 Å for **TPE-2** and 40.12 Å for **TPE-3**.

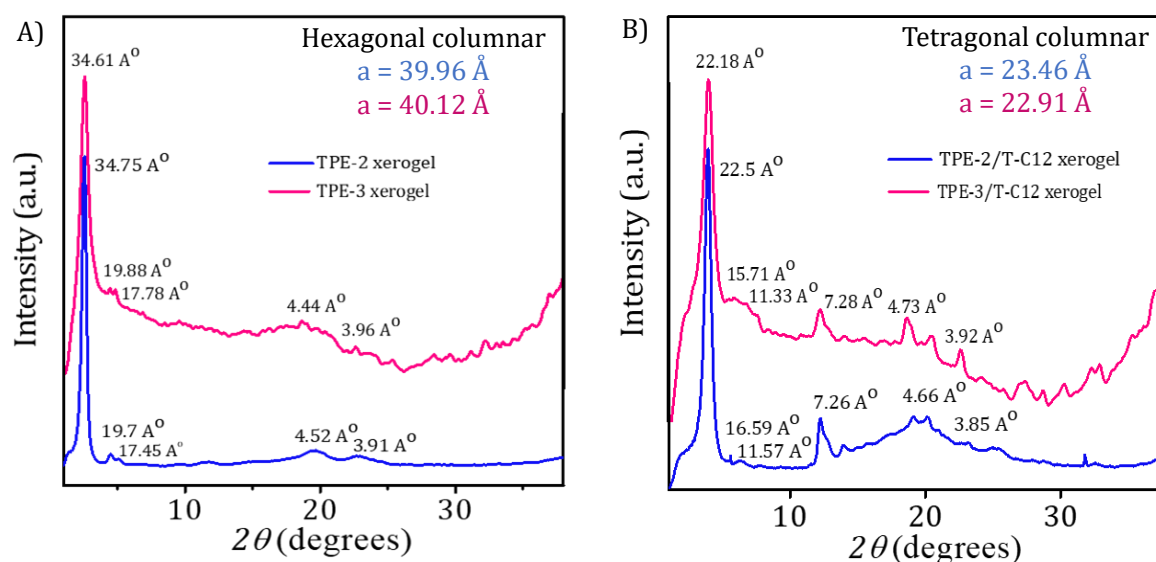


Figure 3B.31. WAXS patterns of A) **TPE-2** and **TPE-3**, and B) **TPE-2**≡**T-C12** and **TPE-3**≡**T-C12** xerogel samples.

Similarly, significant reflections with d spacing of 22.5, 16.59 and 11.57 Å for **TPE-2**≡**T-C12** and 22.18, 15.71 and 11.33 Å for **TPE-3**≡**T-C12** were observed in the WAXS patterns. These d spacings in 1: $\sqrt{2}$: 2 represents (100), (110) and (200) planes of tetragonal columnar packing with intercolumnar distance of 23.46 Å for **TPE-2**≡**T-C12** and 22.91 Å for **TPE-3**≡**T-C12** (Figure 3B.31B). In addition, reflections with d spacing around 4.42 Å and 3.91 Å were observed in all the cases,

which represents the arrangement of alkyl chains and π - π stacking of aromatic units in the self-assemblies.

Further, the structural details obtained from the energy minimized structures of **TPE-2/3** dimer and **TPE-2/3** \equiv **T-C12** were correlated with XRD, FT-IR and CD results to propose a possible mechanism of self-assembly. An intercolumnar distance of 39.96 Å or 40.12 Å for a hexagonal molecular packing is obtained only when, dimers of **TPE-2/3** molecules are arranged in a hexagonal manner with interdigitated alkyl chains (Figure 3B.32A). This type of molecular arrangement is also supported by the alkyl chain interdigitation observed in FT-IR studies of **TPE-2/3** xerogels. As a result, the theoretical intercolumnar distance of 48.4 Å (molecular size of a dimer) can be reduced to 39.96 Å or 40.12 Å in hexagonal columnar packing.

In addition, from the literature knowledge,^{34,35} we can envisage that in the case of the **TPE-3** with a single isomer (S), the molecular stacking will take place in a specific direction and impart chirality to the columnar packing, displaying CD signal with Cotton effect in the **TPE-3** assemblies (Figure 3B.32B). Whereas, the racemic **TPE-2** dimer stacks in random directions and result in a CD inactive molecular packing. With the above inferred mechanism of self-assembly, many of the discrepancies observed in the experimental studies can be clarified. For example, the absence of helicity in the morphology studies of **TPE-3** could be ascribed to the masking of structural chirality by the secondary molecular packing of the hexagonal columnar structures to form 1D-fibers. Similarly, compared to the orderly packed hexagonal columnar **TPE-1** assemblies described in Chapter 3A, **TPE-2/3** assemblies are structurally crowded due to presence of interdigitated alkyl chain in the columnar packing. As a result, increase in concentration of the

sample leads to the random arrangement of 1D assemblies resulting in opaque supramolecular blue emissive **TPE-2/3** gels (Figure 3B.32C).

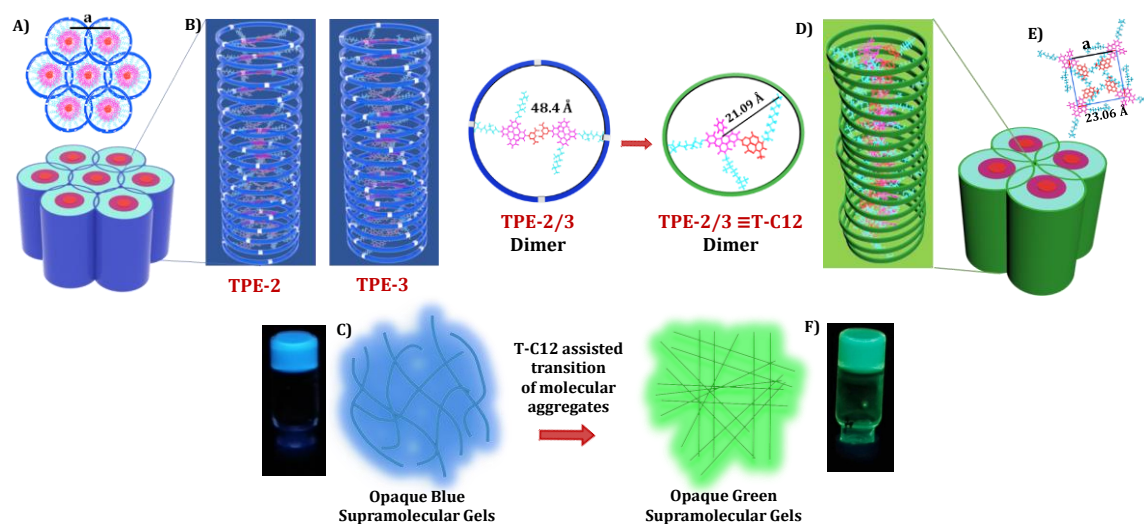


Figure 3B.32. Schematic representation of the **TPE-2** and **TPE-3** self-assembly in the A), B) & C) absence (left side) and D), E) & F) presence of **T-C12** (right side).

In case the of **TPE-2/3≡T-C12** assemblies, XRD, molecular size of monomeric unit in the assembly and FT-IR results were analogues to that observed in **TPE-1**. Which suggests similar mechanism for TPE-DAT self-assembly in the presence of **T-C12**, without much variations in the molecular packing. From the FT-IR results, it is clear that the monomeric unit in **TPE-2/3≡T-C12** assemblies are different from **TPE-2/3** assemblies, leading to the transition of blue to green emissive assemblies. And the theoretical tetragonal intercolumnar distance of 23.06 Å is obtained only when H-bonded **TPE-2≡T-C12** unit or **TPE-3≡T-C12** are tetragonally arranged as shown in Figure 3B.32E. In addition, due to the structural asymmetry of this monomeric unit, we can also expect randomness in the direction of chiral substituent upon π - π stacking Figure 3B.32D. Further, at higher concentrations, the structurally stressed tetragonal columnar packs of **TPE-2/3≡T-C12** tends to be randomly arranged, which results in opaque green emissive supramolecular gels (Figure 3B.32F).

3B.4. CONCLUSIONS

In summary, to achieve directional control over the morphologies of tetraphenylethylene derivatives and to prove the proposed mechanism of H-bonding directed self-assembly in **TPE-1**, three more TPE-DAT derivatives with varying alkoxy substitution were synthesized and their self-assembly properties were investigated. **TPE-2** and **TPE-3** in dodecane displayed the formation of 1D fibers at lower concentrations and supramolecular gels with entangled network structure at higher concentrations. The tuning of self-assembly from blue to green emissive assemblies was demonstrated using a complementary H-bonding **T-C12**, thymine derivative. Mechanism of self-assembly for both these assemblies were deduced using gel characteristics, mainly FT-IR & XRD results, and confirmed the proposed mechanism of **TPE-1** self-assembly for TPE-DAT type molecules in dodecane. Whereas, **TPE-4** with triethylene glycol substituent was insoluble in dodecane and so we tested the H-bonding directed self-assembly with dT₂₀ in 20% THF-water. Distinct from the **TPE-2/3** and the expected 1D assemblies, interaction of **TPE-4** with DNA resulted in TPE-DNA condensates with 40-50 nm spherical nanoparticles. In short, these results verify the role of alkoxy substitutions and solvent system in directing H-bonded self-assemblies, and put forward a facile strategy of using nucleobase and nucleobase analogues to construct supramolecular functional materials of small organic chromophores with control over the morphology.

3B.5. EXPERIMENTAL SECTION

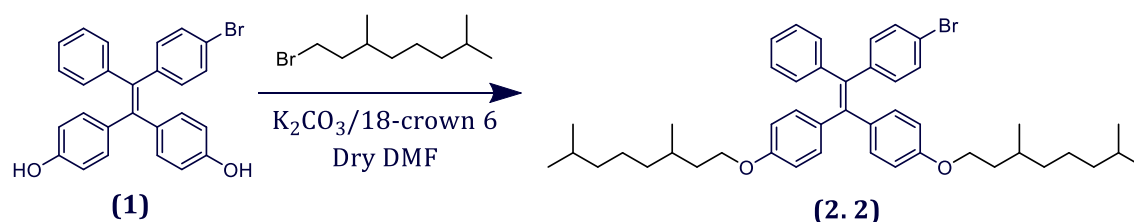
3B.5.1. Materials and methods

The poly(dT) sequence; dT₂₀, poly(dA) sequence; dA₂₀ and thymidine used as template in the **TPE-4** self-assembly studies were purchased from Sigma Aldrich. DNA samples were diluted with milli Q deionized water (18.2 MΩ) and, concentrations were calculated by measuring the absorption and using the known ϵ values of nucleobases at 260 nm. HPLC grade THF was purchased from Merck and used as received for spectroscopic studies. All the experiments involving dT₂₀ were carried out in 20% THF-PBS solvent system. Circular dichroism studies were performed in 0.1 cm quartz cuvette using JASCO J-810 spectropolarimeter equipped with Peltier controlled thermostatic cell holder. All other materials and methods applied in this chapter are same as that described in Chapter 3A.

3B.5.2. Synthetic procedures and characterizations

Synthesis of **1**,³⁶ **2.(2-4)**,³⁷ **3.(2-4)**³⁸ and **TPE-(2-4)**³⁹ follows similar synthetic procedures as detailed in experimental section, page 128 of chapter 3A.

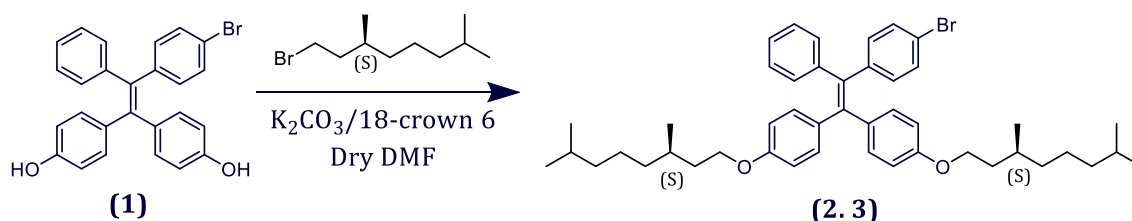
3B.5.2.1. Synthesis of 4,4'-(2-(4-bromophenyl)-2-phenylethene-1,1-diyl)bis(((3,7-dimethyloctyl)oxy)benzene), (**2.2**)



1 (1.0045 g, 2.262 mmol), K₂CO₃ (1.5883 g, 11.310 mmol), 1-bromo-3,7-dimethyloctane (1.87 mL, 9.048 mmol) and DMF (10 mL) were used to synthesize **2.2**. Yield = 63% (1.04 g, pale-yellow viscous oil).

^1H NMR (500 MHz, CDCl_3), δ (ppm): 7.200 (d, 2H), 7.104-7.075 (m, 3H), 7.001-6.987 (m, 2H), 6.916-6.872 (m, 6H), 6.654-6.602 (m, 4H), 3.933-3.892 (m, 4H), 1.802-1.764 (m, 2H), 1.633-1.573 (m, 2H), 1.531-1.522 (m, 4H), 1.306 (d, 6H), 1.256 (m, 6H), 1.146-1.135 (m, 6H), 0.973-0.917 (m, 12H). ^{13}C NMR (125 MHz, CDCl_3), δ (ppm): 157.85, 143.88, 143.40, 140.94, 135.81, 132.51, 131.36, 130.82, 129.68, 127.78, 126.22, 119.93, 113.53, 66.18, 39.23, 35.49, 37.32, 29.82, 27.97, 24.65, 22.66, 21.06. HRMS (ESI): m/z calcd., for $\text{C}_{46}\text{H}_{59}\text{BrO}_2$, 722.39 [M]; found, 761.33 [M+K] $^+$.

3B.5.2.2. Synthesis of 1-bromo-4-((E)-2-(4-(((S)-3,7-dimethyloctyl)oxy)phenyl)-2-(4-(((S)-3,7-dimethyloctyl)oxy)phenyl)-1-phenylvinyl)benzene, (2.3)

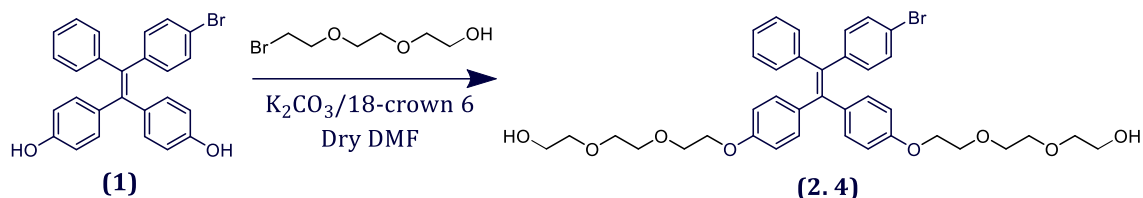


1 (0.3815 g, 0.86 mmol), K_2CO_3 (0.477 g, 3.45 mmol), (S)-1-bromo-3,7-dimethyloctane (0.477 mL, 2.16 mmol) and DMF (10 mL) were used to synthesize **2.3**. Yield = 77% (0.47 g, pale-yellow viscous oil).

^1H NMR (500 MHz, CDCl_3), δ (ppm): 7.216-7.201 (d, $J = 5.5$ Hz, 2H), 7.105-7.075 (m, 3H), 7.002-6.987 (d, $J = 7.5$ Hz, 2H), 6.917-6.872 (m, 6H), 6.654-6.602 (m, 4H), 3.934-3.892 (m, 4H), 1.777-1.612 (m, 4H), 1.532-1.334 (m, 4H), 1.329-1.32 (m, 6H), 1.319-1.134 (m, 6H), 0.933-0.902 (m, 6H), 0.875-0.857 (m, 12H). ^{13}C NMR (125 MHz, CDCl_3), δ (ppm): 157.88, 143.90, 143.41, 140.98, 137.68, 135.83, 133.05, 132.53, 130.83, 127.78, 126.23, 119.94, 113.74, 66.17, 39.24, 37.31, 36.26, 29.85,

27.97, 24.64, 22.70, 19.71. HRMS (ESI): m/z calcd for $C_{46}H_{59}BrO_2$: 722.39 [M]; found, 722.37 [M]⁺.

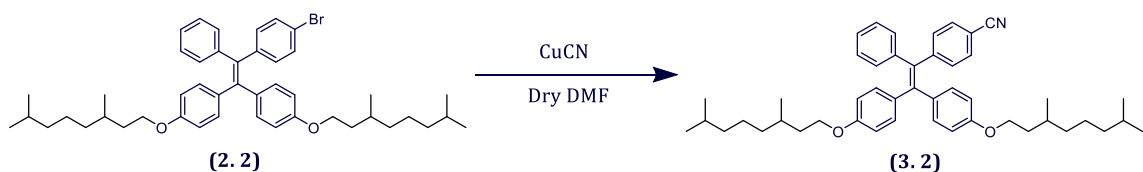
3B.5.2.3. Synthesis of 2. 4.



1 (0.3534 g, 7.99 mmol), K_2CO_3 (0.5524 g, 3.99 mmol), 2-(2-(2-bromoethoxy)ethoxy)ethan-1-ol (0.5084 g, 2.39 mmol) and DMF (15 mL) were used to synthesize **2.4**. Yield = 21% (0.12 g, pale yellow viscous oil).

1H NMR (500 MHz, $CDCl_3$), δ (ppm): 7.219 (d, $J = 8.5$ Hz, 2H), 7.202-6.993 (m, 3H), 6.915 (m, 2H), 6.901-6.880 (m, 5H), 6.863 (s, 1H), 6.680-6.627 (m, 4H), 4.092-4.045 (m, 4H), 3.849-3.809 (m, 4H), 3.742-3.687 (m, 12H), 3.683-3.601 (m, 4H). HRMS (ESI): m/z calcd., for $C_{38}H_{43}BrO_8$, 706.21 [M]; found, 729.20 [M+Na]⁺.

3B.5.2.4. Synthesis of 4-(2,2-bis(4-((3,7-dimethyloctyl)oxy)phenyl)-1-phenyl vinyl)benzotrile, (3. 2)



2.2 (1.0418 g, 1.442 mmol), CuCN (0.388 g, 4.326 mmol), dry DMF (15 mL), water (30 mL) and Ethylenediamine (1.6 mL) were used to synthesize **3.2**. Yield = 50% (0.49 g, pale-yellow viscous oil).

1H NMR (500 MHz, $CDCl_3$), δ (ppm): 7.39 (d, 2H), 7.094 (m, 5H), 6.988 (d, $J = 6$ Hz, 2H), 6.910-6.878 (m, 4H), 6.654-6.613 (m, 4H), 3.933-3.885 (m, 4H), 1.793-1.769

(m, 4H), 1.636 (m, 2H), 1.578-1.786 (m, 4H), 1.539-1.527 (m, 6H), 1.310-1.257 (m, 6H), 1.149 (m, 6H), 0.935-0.875 (m, 12H). ^{13}C NMR (125 MHz, CDCl_3), δ (ppm): 158.28, 149.66, 143.32, 142.83, 137.12, 135.22, 132.56, 132.04, 131.49, 128.03, 126.58, 119.21, 113.83, 109.25, 66.25, 39.24, 37.32, 36.21, 29.85, 27.98, 24.66, 22.72, 19.69. HRMS (ESI): m/z calcd., for $\text{C}_{47}\text{H}_{59}\text{NO}_2$, 669.45 [M]; found, 670.46 [M+1] $^+$.

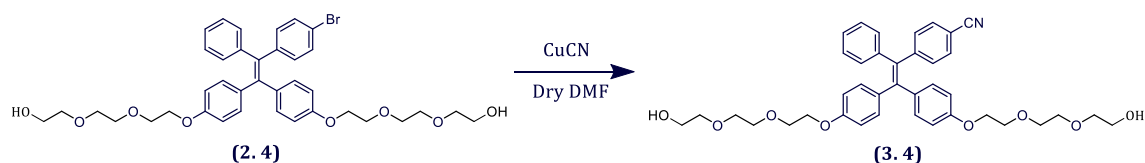
3B.5.2.5. Synthesis of 4-((E)-2-(4-(((S)-3,7-dimethyloctyl)oxy)phenyl)-2-(4-(((S)-3,7-dimethyloctyl)oxy)phenyl)-1-phenylvinyl)benzonitrile, (3. 3)



2. 3 (0.4757 g, 0.658 mmol), CuCN (0.236 g, 2.6 mmol), dry DMF (10 mL), water (20 mL) and Ethylenediamine (1 mL) were used to synthesize **3. 3**. Yield = 61% (0.25 g, pale-yellow viscous oil).

^1H NMR (500 MHz, CDCl_3), δ (ppm): 7.373 (d, $J = 8$ Hz, 2H), 7.094 (m, 5H), 7.130-7.093 (m, 2H), 6.989-6.876 (m, 4H), 6.653-6.612 (m, 4H), 3.933-3.899 (m, 4H), 1.793-1.769 (m, 2H), 1.636 (m, 2H), 1.578-1.786 (m, 4H), 1.539-1.527 (m, 6H), 1.310-1.257 (m, 6H), 1.149 (m, 6H), 0.935-0.875 (m, 12H). ^{13}C NMR (125 MHz, CDCl_3), δ (ppm): 158.12, 149.65, 143.32, 142.85, 137.14, 135.10, 132.54, 132.02, 131.48, 128.02, 126.57, 119.17, 113.86, 109.29, 66.28, 39.24, 37.32, 36.22, 29.87, 27.97, 24.64, 22.64, 19.68. HRMS (ESI): m/z calcd., for $\text{C}_{47}\text{H}_{59}\text{NO}_2$, 669.45 [M]; found, 692.44 [M+Na] $^+$.

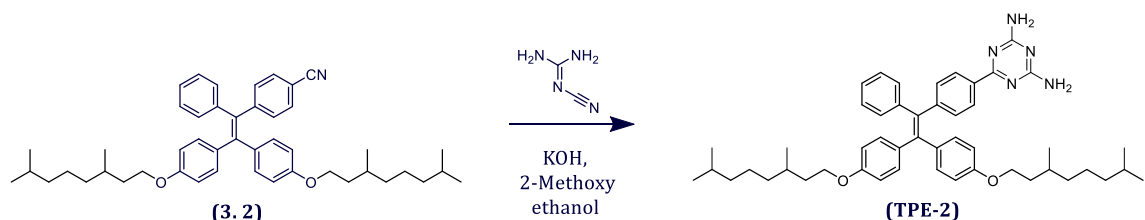
3B.5.2.6. Synthesis of 4-(2,2-bis(4-(2-(2-(2-hydroxyethoxy)ethoxy)ethoxy)phenyl)-1-phenylvinyl)benzonitrile, (3. 4)



2. 4 (0.449 g, 0.635 mmol), CuCN (0.1139 g, 1.27 mmol), dry DMF (10 mL), water (15 mL) and Ethylenediamine (1 mL) were used to synthesize **3. 4**. Yield = 73% (0.3 g, pale-yellow viscous oil).

The product **3. 4** was not stable, so could not able to characterize by NMR techniques. HRMS (ESI): m/z calcd., for $\text{C}_{39}\text{H}_{43}\text{NO}_8$, 653.30 [M]; found, 676.27 [M+Na]⁺.

3B.5.2.7. Synthesis of 6-(4-(2,2-bis(4-((3,7-dimethyloctyl)oxy)phenyl)-1-phenylvinyl)phenyl)-1,3,5-triazine-2,4-diamine, (TPE-2)



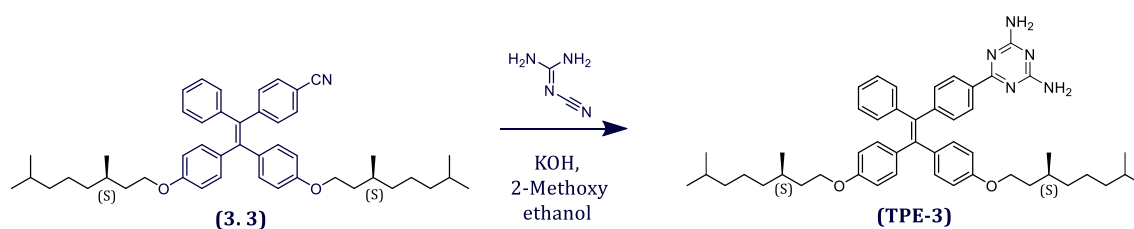
3. 2 (0.51 g, 0.76 mmol), dicyandiamide (0.1285 g, 1.519 mmol), KOH (0.1488 g, 2.277 mmol) and 2-methoxyethanol (6 mL) were used to synthesize **TPE-2**. Yield = 71% (0.41 g, yellow powder).

Melting point: 95-100 °C. ¹H NMR (500 MHz, CDCl_3), δ (ppm): 8.037 (d, J = 8 Hz, 2H), 7.26-7.09 (m, 5H), 7.014 (d, J = 6.5 Hz, 2H), 6.924 (d, J = 4 Hz, 4H), 6.632-6.593 (m, 4H), 5.098 (s, 4H), 3.914-3.883 (m, 4H), 1.795-1.756 (m, 2H), 1.613 (m, 4H), 1.566-1.510 (m, 8H), 1.32-1.26 (m, 6H), 1.15-1.14 (m, 6H), 0.92 (m, 12H). ¹³C NMR (125 MHz, CDCl_3), δ (ppm): 172.31, 167.53, 157.88, 148.39, 144.04, 141.29, 138.37,

135.94, 135.81, 133.82, 132.65, 131.56, 127.72, 126.18, 113.63, 66.14, 39.24, 37.32, 36.26, 29.82, 27.98, 24.66, 22.73, 19.70 ppm; HRMS (ESI): m/z calcd., for $C_{49}H_{63}N_5O_2$, 753.50 [M]; found, 754.50 [M+1]⁺.

3B.5.2.8. Synthesis of 6-(4-((E)-2-(4-(((R)-3,7-dimethyloctyl)oxy)phenyl)-2-(4-(((S)-3,7-dimethyloctyl)oxy)phenyl)-1-phenylvinyl)phenyl)-1,3,5-triazine-2,4-diamine, (TPE-3)

3. 3 (0.25 g, 0.37 mmol), dicyandiamide (0.078 g, 0.933 mmol), KOH (0.073 g, 1.3 mmol) and 2-methoxyethanol (6 mL) were used to synthesize **TPE-3**. Yield = 64% (0.17 g, yellow powder).

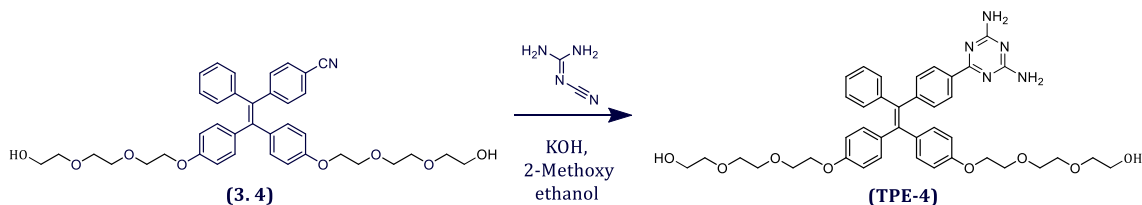


Melting point: 95-100 °C. ¹H NMR (500 MHz, CDCl₃), δ (ppm): 8.039 (d, J = 8 Hz, 2H), 7.113-7.084 (m, 5H), 7.014 (d, J = 6.5 Hz, 2H), 6.939-6.914 (m, 4H), 6.631-6.592 (m, 4H), 5.103 (s, 4H), 3.915-3.883 (m, 4H), 1.795-1.624 (m, 2H), 1.537-1.510 (m, 4H), 1.324-1.245 (m, 8H), 1.161-1.136 (m, 6H), 0.919-0.906 (m, 6H), 0.873-0.853 (m, 12H). ¹³C NMR (125 MHz, CDCl₃), δ (ppm): 172.32, 167.60, 157.82, 148.36, 144.05, 141.3, 138.41, 135.96, 135.83, 133.85, 132.62, 131.52, 127.71, 126.15, 113.67, 66.11, 39.24, 37.32, 36.25, 29.85, 27.96, 24.64, 22.69, 19.69. HRMS (ESI): m/z calcd., for $C_{49}H_{63}N_5O_2$, 753.50 [M]; found, 754.50 [M+1]⁺.

3B.5.2.9. Synthesis of TPE-4

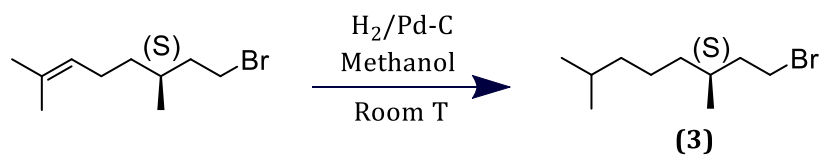
3. 4 (0.3 g, 0.459 mmol), dicyandiamide (0.115 g, 1.377 mmol), KOH (0.0773 g, 1.377 mmol) and 2-methoxyethanol (6 mL) were used to synthesize **TPE-4**. The

crude product was purified by silica column chromatography using 3% methanol-chloroform as the eluent to give **TPE-4** as a pale-yellow solid. The product was further purified by dissolving in chloroform and re-precipitation using pentane. Yield = 34% (0.115 g yellow powder).



Melting point: 130-135 °C. ^1H NMR (500 MHz, DMSO- d_6), δ (ppm): 7.911 (d, J = 8.5 Hz, 2H), 7.092-7.077 (m, 2H), 7.055-7.040 (m, 1H), 6.962-6.907 (m, 4H), 6.801 (d, J = 8.5 Hz, 4H), 6.644 (d, J = 8 Hz, 8H), 4.528-4.498 (m, 2H), 3.927 (s, 4H), 3.631-3.604 (m, 4H), 3.497-3.478 (m, 4H), 3.462-3.445 (m, 4H), 3.417-3.400 (m, 4H), 3.353-3.325 (m, 4H). ^{13}C NMR (125 MHz, DMSO- d_6), δ (ppm): 170.38, 167.83, 157.61, 147.16, 143.91, 141.11, 138.85, 135.99, 132.53, 131.25, 128.42, 127.65, 126.89, 114.17, 72.81, 70.39, 69.37, 67.43, 60.68. HRMS (ESI): m/z calcd., for $\text{C}_{41}\text{H}_{47}\text{N}_5\text{O}_8$, 737.34 [M]; found, 738.35 [M+1] $^+$.

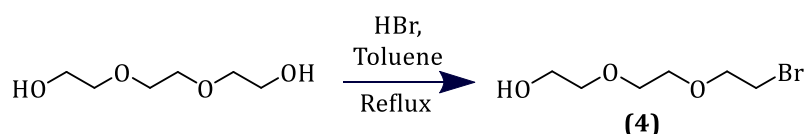
3B.5.2.10. Synthesis of (S)-1-bromo-3,7-dimethyloctane, (3)⁴⁰



A mixture of (S)-8-bromo-2,6-dimethyloct-2-ene (3.0187 g, 13.84 mmol) and Pd-C (0.327 g) in methanol (35 mL) was stirred under H_2 atmosphere for 24 hrs. Afterwards, the mixture was filtered through celite and the filtrate was concentrated under reduced pressure to give the product as pale-yellow oil. Yield = 97% (2.96 g).

^1H NMR (500 MHz, CDCl_3), δ (ppm): 3.417-3.308 (m, 2H), 1.828-1.791 (m, 1H), 1.618-1.538 (m, 2H), 1.484-1.431 (m, 1H), 1.232-1.204 (m, 3H), 1.195-1.178 (m, 3H), 0.915-0.861 (m, 9H). ^{13}C NMR (125 MHz, CDCl_3), δ (ppm): 39.10, 38.18, 35.73, 31.11, 30.68, 26.94, 23.53, 21.66, 17.96. HRMS (ESI): m/z calcd., for $\text{C}_{10}\text{H}_{21}\text{Br}$, 220.08 [M]; found, 221.09 [M+1]⁺.

3B.5.2.11. Synthesis 2-(2-(2-bromoethoxy)ethoxy)ethan-1-ol, (4)⁴¹



To a solution of 2,2'-(ethane-1,2-diylbis(oxy))bis(ethan-1-ol) (5 g, 33.3 mmol) in toluene (80 mL), concentrated HBr (4 mL of 48% aqueous solution, 41.7 mmol) was added. The mixture was refluxed for 72 hrs and cooled to room temperature. After phase separation, the aqueous layer was removed and organic layer was diluted with 100 mL of DCM; then extracted with 1M NaOH, dried over with MgSO_4 and concentrated. The crude product was purified by silica column chromatography using 50% ethyl acetate- hexane as eluent to give a pale-yellow oil. Yield = 50% (3.54 g).

^1H NMR (500 MHz, CDCl_3), δ (ppm): 3.840-3.815 (m, 2H), 3.756-3.738 (m, 2H), 3.693 (s, 4H), 3.634-3.616 (m, 2H), 3.502-3.478 (m, 2H). ^{13}C NMR (125 MHz, CDCl_3), δ (ppm): 72.72, 71.13, 70.49, 70.26, 61.84, 30.58. HRMS (ESI): m/z calcd., for $\text{C}_6\text{H}_{13}\text{BrO}_3$, 212 [M]; found, 234.99 [M+Na]⁺.

3B.6. REFERENCES

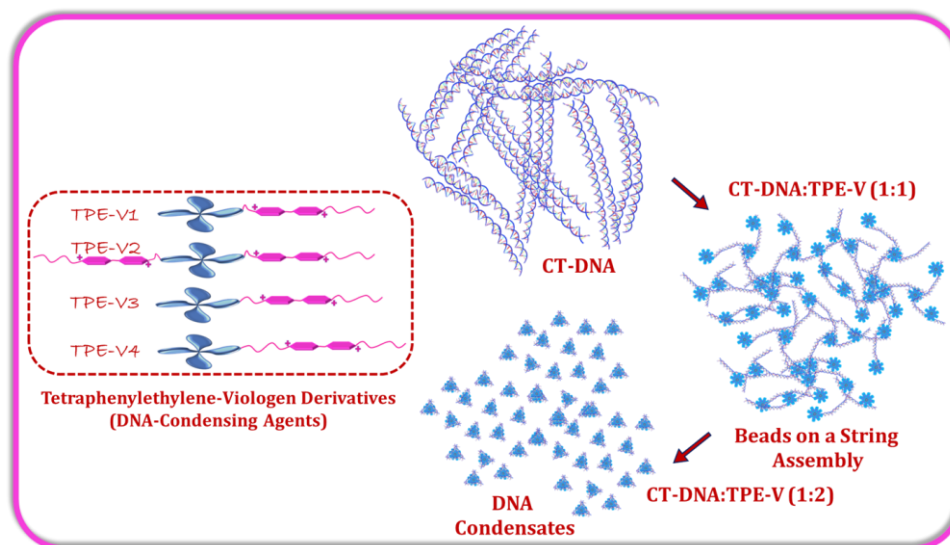
- (1) Schill, J.; Schenning, A. P. H. J.; Brunsveld, L. Self-Assembled Fluorescent Nanoparticles from π -Conjugated Small Molecules: En Route to Biological Applications. *Macromol. Rapid Commun.* **2015**, *36*, 1306-1321.
- (2) Schenning, A. P. H. J.; Meijer, E. W. Supramolecular electronics; nanowires from self-assembled π -conjugated systems. *Chem. Commun.* **2005**, 3245-3258.
- (3) Wong, K.-T.; Bassani, D. M. Energy transfer in supramolecular materials for new applications in photonics and electronics. *NPG Asia Materials* **2014**, *6*, e116-e116.
- (4) Praveen, V. K.; Vedhanarayanan, B.; Mal, A.; Mishra, R. K.; Ajayaghosh, A. Self-Assembled Extended π -Systems for Sensing and Security Applications. *Acc. Chem. Res.* **2020**, *53*, 496-507.
- (5) Zhang, Y.; Fang, F.; Li, L.; Zhang, J. Self-Assembled Organic Nanomaterials for Drug Delivery, Bioimaging, and Cancer Therapy. *Acs Biomater. Sci. Eng.* **2020**, *6*, 4816-4833.
- (6) Ishiwari, F.; Shoji, Y.; Fukushima, T. Supramolecular scaffolds enabling the controlled assembly of functional molecular units. *Chem Sci* **2018**, *9*, 2028-2041.
- (7) Stupp, S. I.; Palmer, L. C. Supramolecular Chemistry and Self-Assembly in Organic Materials Design. *Chem. Mater.* **2014**, *26*, 507-518.
- (8) Würthner, F.; Saha-Möller, C. R.; Fimmel, B.; Ogi, S.; Leowanawat, P.; Schmidt, D. Perylene Bisimide Dye Assemblies as Archetype Functional Supramolecular Materials. *Chem. Rev.* **2016**, *116*, 962-1052.
- (9) Psutka, K. M.; LeDrew, J.; Taing, H.; Eichhorn, S. H.; Maly, K. E. Synthesis and Self-Assembly of Liquid Crystalline Triphenylenedicarboxythioimides. *J. Org. Chem.* **2019**, *84*, 10796-10804.
- (10) Xu, F.; Pfeifer, L.; Stuart, M. C. A.; Leung, F. K.-C.; Feringa, B. L. Multi-modal control over the assembly of a molecular motor bola-amphiphile in water. *Chem. Commun.* **2020**, *56*, 7451-7454.
- (11) Bujosa, S.; Castellanos, E.; Frontera, A.; Rotger, C.; Costa, A.; Soberats, B. Self-assembly of amphiphilic aryl-squaramides in water driven by dipolar π - π interactions. *Org. Biomol. Chem.* **2020**, *18*, 888-894.

-
- (12) Chen, S.; Costil, R.; Leung, F. K.-C.; Feringa, B. L. Self-Assembly of Photoresponsive Molecular Amphiphiles in Aqueous Media. *Angew. Chem.* **2021**, *133*, 2-26.
- (13) Herbst, S.; Soberats, B.; Leowanawat, P.; Stolte, M.; Lehmann, M.; Würthner, F. Self-assembly of multi-stranded perylene dye J-aggregates in columnar liquid-crystalline phases. *Nat Commun.* **2018**, *9*, 2646.
- (14) Zhu, X.-y.; Tu, B.; Hu, G.-j.; Fang, Q.-j.; Qi, J.-j.; Xiao, X.-w.; Geng, Y.-f.; Zeng, Q.-d. Self-assemblies of TTF derivatives programmed by alkyl chains and functional groups. *PCCP.* **2018**, *20*, 6383-6389.
- (15) Lu, J.; Yu, S.; Li, Z.; Lee, M.; Yang, Y.; Jin, L. Y. The relationship between molecular structure and supramolecular morphology in the self-assembly of rod-coil molecules with oligoether chains. *Soft Matter.* **2020**, *16*, 2224-2229.
- (16) Aida, T.; Meijer, E. W. Supramolecular Polymers – we've Come Full Circle. *Isr. J. Chem.* **2020**, *60*, 33-47.
- (17) Mishra, A.; Dhiman, S.; George, S. J. ATP-Driven Synthetic Supramolecular Assemblies: From ATP as a Template to Fuel. *Angew. Chem. Int.* **2021**, *60*, 2740-2756.
- (18) Hashim, P. K.; Bergueiro, J.; Meijer, E. W.; Aida, T. Supramolecular Polymerization: A Conceptual Expansion for Innovative Materials. *Prog. Polym. Sci.* **2020**, *105*, 101250.
- (19) Balakrishnan, K.; Datar, A.; Naddo, T.; Huang, J.; Oitker, R.; Yen, M.; Zhao, J.; Zang, L. Effect of side-chain substituents on self-assembly of perylene diimide molecules: morphology control. *J. Am. Chem. Soc.* **2006**, *128*, 7390-7398.
- (20) Ogasawara, M.; Lin, X.; Kurata, H.; Ouchi, H.; Yamauchi, M.; Ohba, T.; Kajitani, T.; Fukushima, T.; Numata, M.; Nogami, R.; Adhikari, B.; Yagai, S. Water-induced self-assembly of an amphiphilic perylene bisimide dyad into vesicles, fibers, coils, and rings. *Mater. Chem. Front.* **2018**, *2*, 171-179.
- (21) Lin, X.; Hirono, M.; Seki, T.; Kurata, H.; Karatsu, T.; Kitamura, A.; Kuzuhara, D.; Yamada, H.; Ohba, T.; Saeki, A.; Seki, S.; Yagai, S. Covalent Modular Approach for Dimension-Controlled Self-Organization of Perylene Bisimide Dyes. *Chem. Eur. J.* **2013**, *19*, 6561-6565.
- (22) Lin, X.; Kurata, H.; Prabhu, D. D.; Yamauchi, M.; Ohba, T.; Yagai, S. Water-induced helical supramolecular polymerization and gel formation of an alkylene-tethered perylene bisimide dyad. *Chem. Commun.* **2017**, *53*, 168-171.

- (23) Kartha, K. K.; Nair, V. S.; Praveen, V. K.; Takeuchi, M.; Ajayaghosh, A. A self-recovering mechanochromic chiral π -gelator. *J Mater Chem C* **2019**, *7*, 1292-1297.
- (24) García, F.; Sánchez, L. Structural Rules for the Chiral Supramolecular Organization of OPE-based Discotics: Induction of Helicity and Amplification of Chirality. *J. Am. Chem. Soc.* **2012**, *134*, 734-742.
- (25) George, S. J.; Ajayaghosh, A.; Jonkheijm, P.; Schenning, A. P. H. J.; Meijer, E. W. Coiled-Coil Gel Nanostructures of Oligo(p-phenylenevinylene)s: Gelation-Induced Helix Transition in a Higher-Order Supramolecular Self-Assembly of a Rigid π -Conjugated System. *Angew. Chem. Int.* **2004**, *43*, 3422-3425.
- (26) Ajayaghosh, A.; George, S. J.; Praveen, V. K. Gelation-Assisted Light Harvesting by Selective Energy Transfer from an Oligo(p-phenylenevinylene)-Based Self-Assembly to an Organic Dye. *Angew. Chem. Int.* **2003**, *42*, 332-335.
- (27) George, S. J.; Tomović, Ž.; Smulders, M. M. J.; de Greef, T. F. A.; Leclère, P. E. L. G.; Meijer, E. W.; Schenning, A. P. H. J. Helicity Induction and Amplification in an Oligo(p-phenylenevinylene) Assembly through Hydrogen-Bonded Chiral Acids. *Angew. Chem. Int.* **2007**, *46*, 8206-8211.
- (28) Das, G.; Thirumalai, R.; Vedhanarayanan, B.; Praveen, V. K.; Ajayaghosh, A. Enhanced Emission in Self-Assembled Phenyleneethynylene Derived π -Gelators. *Adv. Opt. Mater.* **2020**, *8*, 2000173.
- (29) Saito, T.; Yagai, S. Hierarchical self-assembly of an azobenzene dyad with inverted amide connection into toroidal and tubular nanostructures. *Org. Biomol. Chem.* **2020**, *18*, 3996-3999.
- (30) Kato, T.; Matsuoka, T.; Nishii, M.; Kamikawa, Y.; Kanie, K.; Nishimura, T.; Yashima, E.; Ujiie, S. Supramolecular Chirality of Thermotropic Liquid-Crystalline Folic Acid Derivatives. *Angew. Chem. Int.* **2004**, *43*, 1969-1972.
- (31) ten Eikelder, H. M. M.; Markvoort, A. J.; de Greef, T. F. A.; Hilbers, P. A. J. An Equilibrium Model for Chiral Amplification in Supramolecular Polymers. *J. Phys. Chem. B.* **2012**, *116*, 5291-5301.
- (32) Bohanon, T. M.; Denzinger, S.; Fink, R.; Paulus, W.; Ringsdorf, H.; Weck, M. Barbituric Acid/2,4,6-Triaminopyrimidine Aggregates in Water and Their Competitive Interaction with a Monolayer of Barbituric Acid Lipids at the Gas-Water Interface. *Angew. Chem. Int. Ed.* **1995**, *34*, 58-60.

-
- (33) Kyogoku, Y.; Lord, R. C.; Rich, A. An Infrared Study of Hydrogen Bonding between Adenine and Uracil Derivatives in Chloroform Solution. *J. Am. Chem. Soc.* **1967**, *89*, 496-504.
- (34) Hifsudheen, M.; Mishra, R. K.; Vedhanarayanan, B.; Praveen, V. K.; Ajayaghosh, A. The Helix to Super-Helix Transition in the Self-Assembly of π -Systems: Superseding of Molecular Chirality at Hierarchical Level. *Angew. Chem. Int. Ed.* **2017**, *56*, 12634-12638.
- (35) Korevaar, P. A.; George, S. J.; Markvoort, A. J.; Smulders, M. M. J.; Hilbers, P. A. J.; Schenning, A. P. H. J.; De Greef, T. F. A.; Meijer, E. W. Pathway complexity in supramolecular polymerization. *Nature*. **2012**, *481*, 492-496.
- (36) Zhao, E.; Chen, Y.; Wang, H.; Chen, S.; Lam, J. W. Y.; Leung, C. W. T.; Hong, Y.; Tang, B. Z. Light-Enhanced Bacterial Killing and Wash-Free Imaging Based on AIE Fluorogen. *ACS Appl. Mater. Interfaces*. **2015**, *7*, 7180-7188.
- (37) Wang, K.; Li, J.; Ji, S.; Li, L.; Qiu, Z.; Pan, C.; Zhang, J.; Huo, Y. Fluorescence probes based on AIE luminogen: application for sensing Hg²⁺ in aqueous media and cellular imaging. *New J. Chem.* **2018**, *42*, 13836-13846.
- (38) Hurlock, M. J.; Kan, Y.; Lécivain, T.; Lapka, J.; Nash, K. L.; Zhang, Q. Molecular Association-Induced Emission Shifts for E/Z Isomers and Selective Sensing of Nitroaromatic Explosives. *Cryst. Growth Des.* **2018**, *18*, 6197-6203.
- (39) Wolffs, M.; George, S. J.; Tomović, Ž.; Meskers, S. C. J.; Schenning, A. P. H. J.; Meijer, E. W. Macroscopic Origin of Circular Dichroism Effects by Alignment of Self-Assembled Fibers in Solution. *Angew. Chem. Int. Ed.* **2007**, *46*, 8203-8205.
- (40) Mikami, K.; Yokozawa, T. Helical folding of poly(naphthalenecarboxamide) in apolar solvent. *J. Polym. Sci., Part A-1: Polym. Chem.* **2013**, *51*, 739-742.
- (41) Zhu, J.; Waengler, C.; Lennox, R. B.; Schirrmacher, R. Preparation of Water-Soluble Maleimide-Functionalized 3 nm Gold Nanoparticles: A New Bioconjugation Template. *Langmuir*. **2012**, *28*, 5508-5512.

**TETRAPHENYLETHYLENE-VIOLOGEN
DERIVATIVES: SYNTHESIS AND STUDY OF THEIR
DNA INTERACTION AND CONDENSATION PROPERTIES**



4.1. ABSTRACT

Gene Transfection is a method of delivering nucleic acids into cell and is the key step in gene therapy. Usually, gene transfection is achieved by condensing DNA into neutral compact structures with the aid of positively charged condensing agents. In this chapter, we synthesized four novel viologen functionalized tetraphenylethylene (TPE-V) derivatives; differing in the number of viologen units or spacer length between TPE and viologen units, as condensing agents for DNA. Their binding interactions with calf-thymus DNA (CT-DNA) and subsequent concentration dependent condensation process were investigated using photophysical and morphological techniques. Preliminary photophysical and morphological studies revealed the existence of TPE-V derivatives as random aggregates in Tris buffer. With the addition of CT-DNA to these

random aggregates of **TPE-V** derivatives, a characteristic decrease in the 315 nm absorption band and weak enhancement in the 260 nm absorption band was observed, indicative of the interaction of **TPE-V** with CT-DNA. Corresponding morphology change analyzed by reverse titration, displayed the transformation of CT-DNA from its fibrous network structure to partially condensed “beads on a string” like arrangement. Upon further increasing the concentration of **TPE-V**, the “beads on a string” type assembly of **TPE-V/CT-DNA** complex changes to completely condensed compact structures with 40-50 nm in diameter. In addition, compared to the other **TPE-V** derivatives, the presence of di-viologen units in **TPE-V2** reduces the concentration of sample required to initiate the interaction with CT-DNA, which suggests the electrostatic mode of binding between **TPE-V** derivatives and CT-DNA. Enhancement in the melting temperature of CT-DNA, quenching in the fluorescence emission of ethidium bromide/CT-DNA complex and the formation of induced CD signal in the presence of **TPE-V** derivatives agrees with the observed morphological changes and thereby verifies the DNA-condensation abilities of **TPE-V** derivatives. Further, decrease in the hydrodynamic size and increase in the zeta-potential value with the addition of **TPE-V** derivatives to CT-DNA, and the failure of **TPE-V/Cucurbit[8]uril** complex to condense CT-DNA confirmed the importance of positively charged viologen units in DNA condensation process. The practical applicability of our DNA condensing agents was tested by performing the initial cytotoxicity studies on A549 cancer and WI-38 normal cells, which revealed the non-toxic nature of **TPE-V1**, **TPE-V2** and **TPE-V3** derivatives. Moreover, these results imply the potential of **TPE-V** derivatives as non-viral vectors for gene transfection and development of such smaller fluorophores with DNA condensation abilities via non-covalent interactions can replace the clinically unsafe conventional condensing agents like viral vectors.

4.2. INTRODUCTION

DNA condensation is the process of converting elongated, negatively charged double helical random coils of DNA into smaller, charge neutralized micro- or nano-sized compact structures with the help of condensing or compaction agents.^{1,2} The general strategies for inducing DNA condensation include, developing attraction between individual DNA double strands by charge neutralization process or by creating unfavorable interaction between DNA strands and the solvent.^{3,4} Common DNA condensing agents are multivalent counter-ions of metals, polyamines, peptides, cationic polymers, dendrimers, surfactants, nanoparticles, carbon nanotubes and small molecules (Figure 4.1A).⁵⁻¹⁴ There are mainly three important pathways for *in vitro* DNA condensation (Figure 4.1B). The first type is all-or-none DNA compaction, usually takes places in the presence of small multi-valent counter ions or as a result of the unfavorable interaction between the solvent and DNA. Second type involves the progressive transition from long-coiled structure to compact DNA structure, which usually occurs in presence of poly-cations and the third type is the adsorption of DNA on condensing agents, followed by wrapping around it to form compact structures similar to the compaction of DNA to chromatin in eukaryotic cells.^{3,15,16}

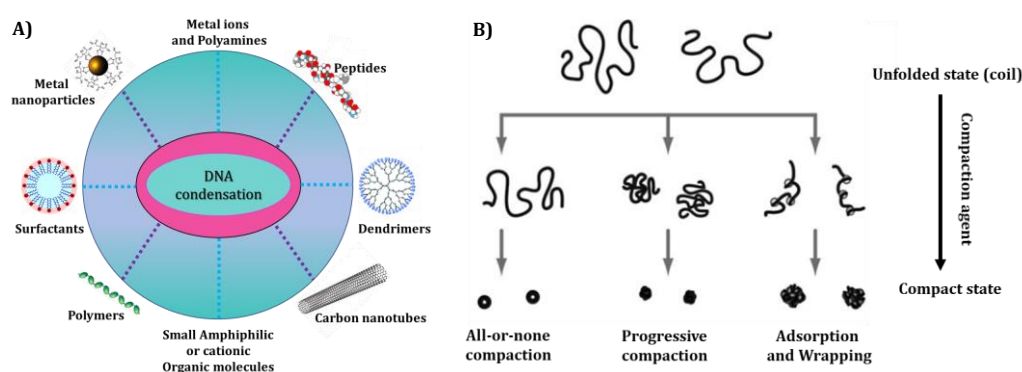


Figure 4.1. A) Different DNA condensing agents and B) three important pathways of DNA condensation process (Adapted from reference 3).

Among the above-mentioned different DNA condensing agents, cationic surfactants are the most commonly employed non-viral gene delivery vectors, because of their highly cooperative binding behavior with DNA.¹⁷⁻¹⁹ In 2017, Yaxun Fan and coworkers demonstrated the calf-thymus DNA condensation induced by a star-shaped hexameric cationic surfactant, PAHB.¹⁰ With the addition of PAHB in to CT-DNA, conformational changes in the DNA structure from long coil to partially condensed cluster aggregates, globules on a string structure and subsequent formation of completely condensed globule like structures were reported (Figure 4.2). Here, the electrostatic interaction between multiple positively charged PAHB and negatively charged phosphate back-bone of CT-DNA is the key factor, which promotes the DNA condensation process. In general, in the case of surfactants the condensation abilities were found to increase with increase in the size of hydrophobic apolar tails or in the presence of a co-solute which promotes the surfactant aggregation.^{20,21}

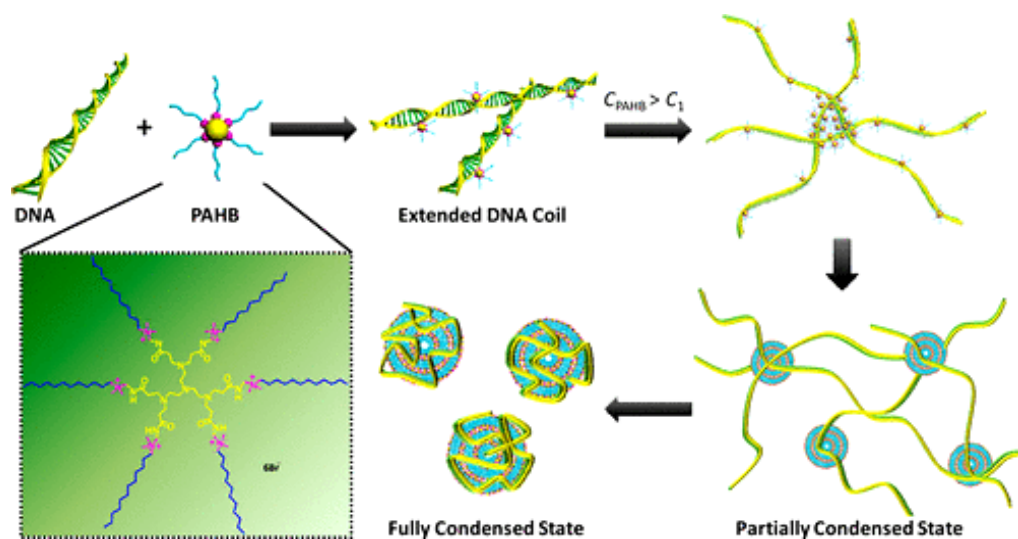


Figure 4.2. A cationic surfactant, PAHB induced DNA condensation process (Adapted from reference 10).

Small cationic or amphiphilic organic molecules and their self-assembled supramolecular structures also got significant attention because of their unique

interactions with nucleic acids via groove binding, π - π stacking and/or electrostatic interactions and subsequent condensation capabilities.²²⁻²⁷ Functionalized fullerene derivatives are one among this category, which is well explored for *in vivo* gene delivery applications. Nakamura and coworkers are pioneers in this field, who developed several fullerene derivatives and demonstrated their applicability in *in vitro* DNA condensation and *in vivo* gene delivery process.^{28,29}

Inspired from these works and due to our interest in the area of developing DNA templated functional materials, recently we have demonstrated a fullerene cluster assisted self-assembly of short DNA double strands into nanowires, DNA three-way junction structures into nanosheets and 2-dimensional nanonetworks, and the chiral organization of fullerene clusters on CT-DNA templates followed by concentration dependent DNA condensation process.³⁰⁻³²

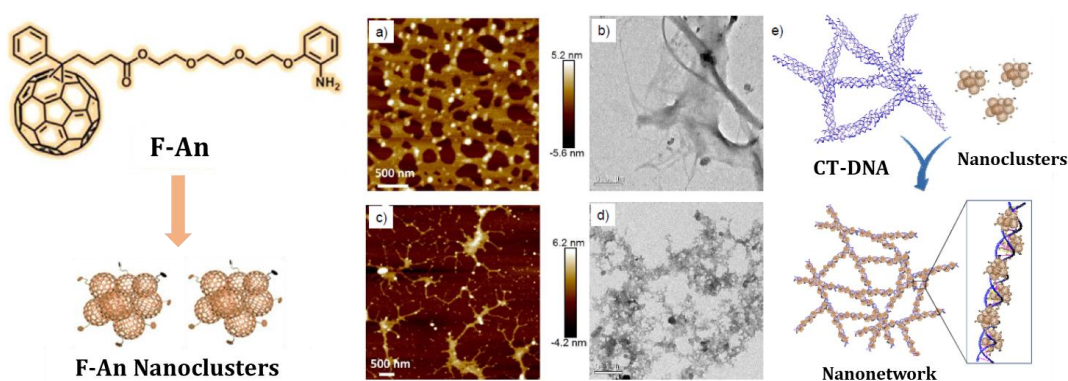


Figure 4.3. Chemical structure of **F-An**, formation of **F-An** nanoclusters in 10% DMSO-PBS and the AFM and TEM morphologies of CT-DNA: (a) and (b) in the absence and (c) and (d) in presence of **F-An** nanoclusters (Adapted from reference 32).

Here, we employed the unique hydrophilic-hydrophobic balance in the molecular structure of an aniline functionalized fullerene derivative, **F-An** in 10% DMSO-PBS solvent system to prepare 3-5 nm sized fullerene nanoclusters and their interactions with different DNA structures were demonstrated.³² In the case of CT-DNA, the highly fibrous networked structure with ~ 250 nm width breaks down into 50-100

nm sized small fibrous structures and subsequently into compact structures as a result of the **F-An** - DNA groove binding directed condensation process (Figure 4.3).

As mentioned earlier, carbon-based nanostructures like fullerenes and carbon nanotubes are well exploited candidates in non-viral gene delivery applications. On the other hand, organic chromophores with unique photophysical and self-assembling properties are not much explored for DNA condensation studies because of their poor aqueous solubility, and hence lesser biocompatibility for gene delivery applications. Recently, J. H. Mondal *et al.* demonstrated the use of a water-soluble ethyl viologen functionalized tetra-cationic Perylenediimide derivative (PDEV) for effective CT-DNA condensation process using spectroscopic, morphological and imaging techniques (Figure 4.4).²⁴ Here, the fluorescence changes in the PDEV chromophore as a result of the conformational changes in PDEV/CT-DNA complex were well probed to study the DNA condensation process. As in this example, development of organic chromophores with improved water solubility, and significant changes in the absorption and fluorescence properties upon interaction with DNA can be utilized for absorption/fluorescence-based monitoring of the DNA condensation process and turns out to be promising compaction agents in non-viral gene delivery.

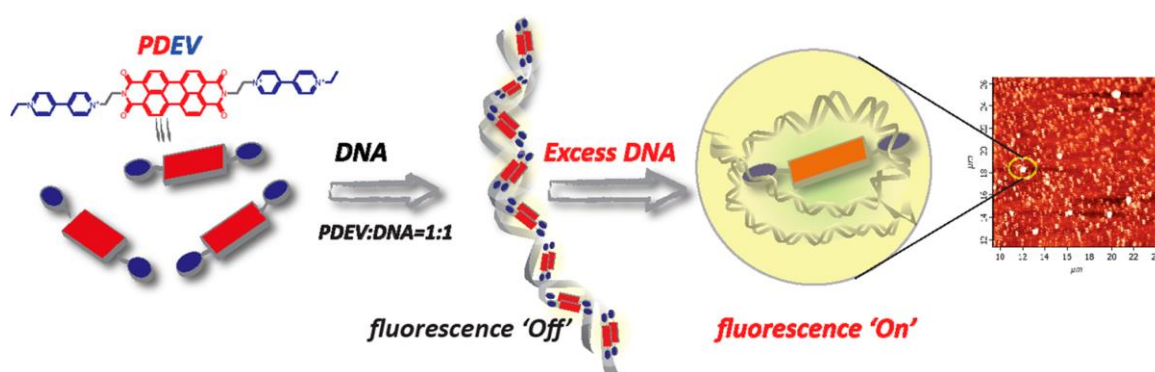


Figure 4.4. Chemical structure of PDEV and the proposed mechanism of CT-DNA interaction and condensation process (Adapted from reference 24).

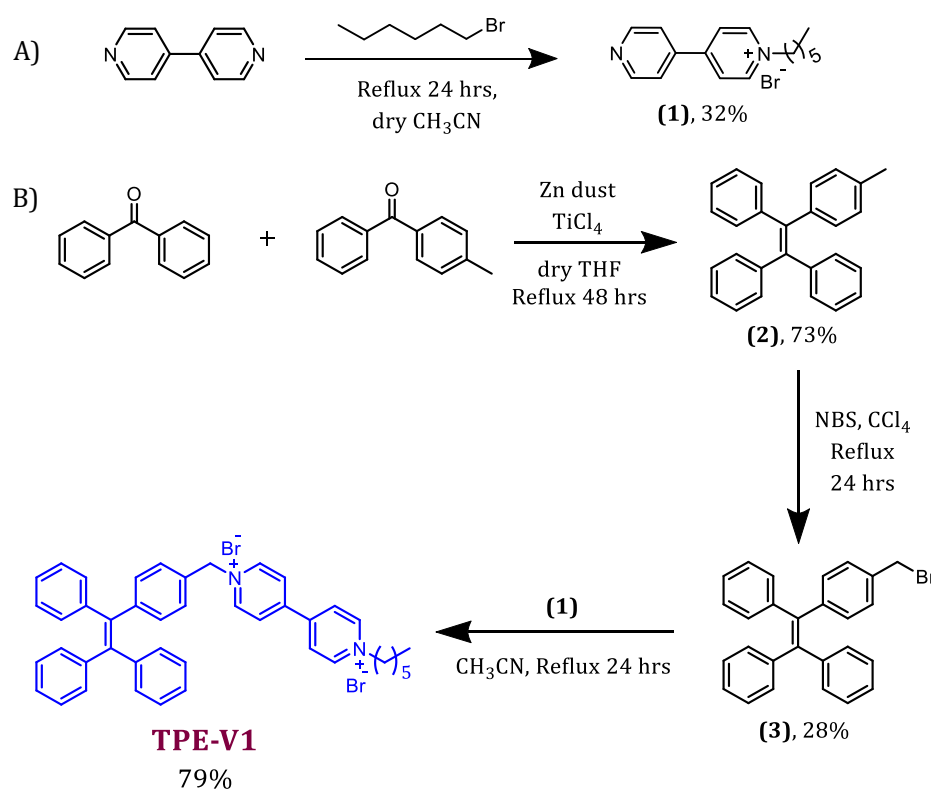
Tetraphenylethylene (TPE) chromophores are well known for its aggregation induced emission (AIE) property and there are few reports on TPE-DNA conjugates for sensing and catalytic applications.³³⁻³⁷ In this chapter, we describe the design, synthesis, CT-DNA interaction and condensation properties of four novel viologen functionalized TPE derivatives. Random aggregates of these molecules in Tris buffer interacts with CT-DNA through electrostatic modes and forms “beads on a string” type assembly, which further transforms into completely charge neutralized compact DNA structures at higher concentration of TPE derivatives. The process of DNA condensation was probed with photophysical and morphological analysis techniques. Further, we also demonstrate the applicability of these small organic chromophores by performing cytotoxicity studies on A546 cancer and WI-38 normal cells using MTT assay.

4.3. RESULTS AND DISCUSSION

4.3.1. Molecular design and synthesis

Tetraphenylethylene derivatives possess unique aggregation properties in solvent mixtures characterized by significant changes in their photophysical properties. In order to study the DNA interactions and induced DNA condensation properties with TPE chromophores, we have designed four viologen appended TPE derivatives, named as **TPE-V** derivatives (**TPE-V1**, **TPE-V2**, **TPE-V3** and **TPE-V4**; Scheme 4.1-4.3), varying the number of viologen units or the spacer group between the TPE and viologen units. For example, **TPE-V1** has one viologen group separated by a methylene spacer, whereas **TPE-V2** has two viologen units separated by methylene spacers from the TPE chromophore. **TPE-V3** and **TPE-V4** have one

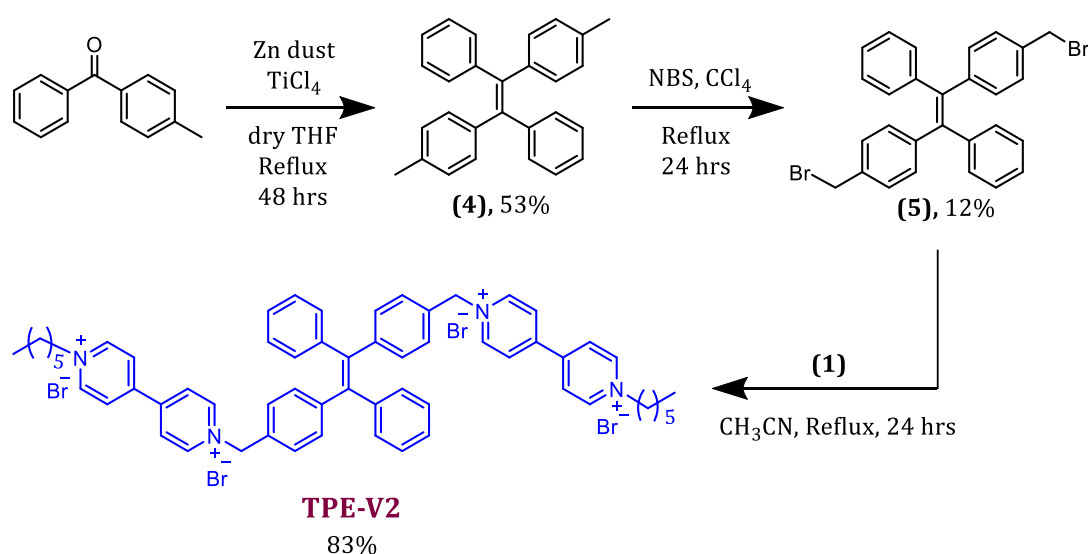
viologen unit each, separated from TPE chromophore via spacer groups of different length. The quaternary amine groups in viologen moiety impart moderate aqueous solubility to the hydrophobic TPE core and are known to bind strongly with DNA via groove binding and electrostatic interactions with negatively charged sugar-phosphate backbone of DNA.³⁸⁻⁴⁰ Further, the interaction of the viologen moiety with DNA could alter the aggregation properties of the hydrophobic TPE core leading to perturbations in the morphology of the complex.



Scheme 4.1. Synthesis of 1-hexyl-([4, 4'-bipyridine]-1-ium)bromide, (**1**) and **TPE-V1**.

The **TPE-V** derivatives were synthesized by following multistep synthetic procedures (Scheme 4.1, 4.2, and 4.3), starting from McMurry coupling reaction between appropriately substituted benzophenone derivatives. The free nitrogen in 1-hexyl-([4, 4'-bipyridine]-1-ium)bromide, (**1**) is linked to TPE core via different alkyl and alkoxy spacers to synthesize the TPE-viologen D-A molecular systems developed in this work. (**1**) was synthesized by following Scheme 4.1A (N-alkylation

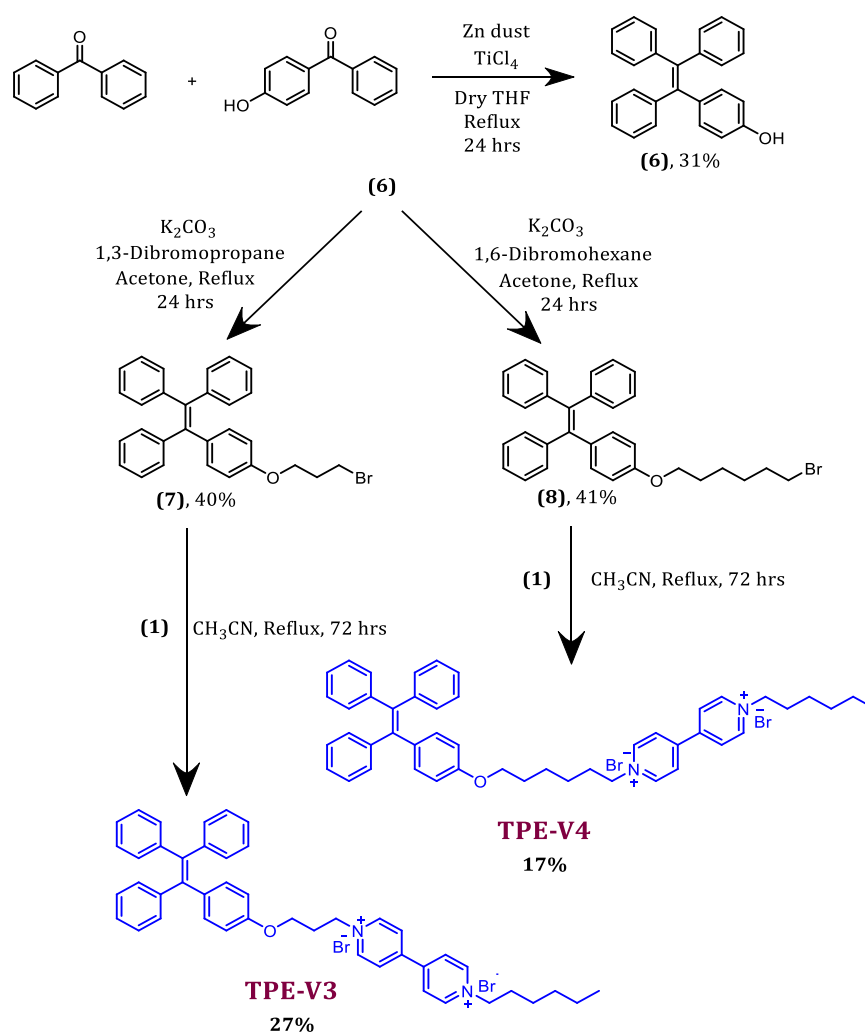
reaction of 4,4'-bipyridine) and selectively separated from a mixture of **(1)** and di-alkylated product formed in the reaction by dissolving in hot DMF. The synthesis of mono-viologen functionalized TPE derivative, **TPE-V1** was achieved by following Scheme 4.1B. McMurry coupling reaction between Benzophenone and 4-Methylbenzophenone afforded the cross product **(2)** in 73% yield, followed by bromination with N-bromosuccinimide (NBS) gave (2-(4-(bromomethyl)phenyl) ethene-1,1,2-triyl)tribenzene, **(3)** in 28% yield. Further, quaternization of the remaining nitrogen in **(1)** using **(3)** resulted in **TPE-V1** with 79% yield. The di-viologen functionalized TPE molecule, **TPE-V2** was obtained by following a similar synthetic protocol as shown in Scheme 4.2. In this case, 4-Methylbenzophenone undergoes self-coupling McMurry reaction to give **(4)**, followed by bromination, and quaternizes the free nitrogen in **(1)** to give **TPE-V2**.



Scheme 4.2. Synthesis of di-viologen functionalized **TPE-V2**.

The synthesis of molecules, **TPE-V3** and **TPE-V4** with $-\text{O}(\text{CH}_2)_3-$ and $-\text{O}(\text{CH}_2)_6-$ spacer units, respectively between TPE and **(1)** were obtained by following Scheme 4.3. Here, Benzophenone and 4-Hydroxybenzophenone were taken as ketones to undergo McMurry coupling reaction, which afforded a mixture of

homo and cross-coupled products. From this mixture, the cross-product **(6)** was separated out with 31% yield, and upon O-alkylation reaction with 1-bromopropane and 1-bromohexane, in presence of base resulted in **(7)** and **(8)**, respectively. And in the last step quaternization of **(1)** with **(7)** and **(8)**, afforded **TPE-V3** and **TPE-V4**, respectively in quantitative yields. Chemical structure characterization data of all the compounds are provided in the experimental section.



Scheme 4.3. Synthesis of **TPE-V3** and **TPE-V4**, with -O(CH₂)₃- and -O(CH₂)₆- spacers, respectively.

4.3.2. Photophysical and morphological properties

In order to understand the interaction and condensation abilities of **TPE-V** derivatives with DNA templates, we have initially investigated the photophysical

properties of these derivatives in water and organic solvents such as methanol and THF. The UV-visible absorption and corresponding fluorescence emission spectra of **TPE-V** derivatives at a concentration of 20 μM are shown in Figures 4.5 & 4.6. **TPE-V1** in methanol showed absorption maxima at 246 nm and 315 nm ($\epsilon_{\text{max}} = 1.04 \times 10^4 \text{ M}^{-1} \text{ cm}^{-1}$), with a tail end absorption extending up to 380 nm (Figure 4.5A). With a similar profile to earlier, absorption spectra of **TPE-V1** in water displayed a slight decrease in the characteristic absorption maxima at 315 nm ($\epsilon_{\text{max}} = 8.17 \times 10^3 \text{ M}^{-1} \text{ cm}^{-1}$). In contrast to the absorption spectra in methanol and water, **TPE-V1** in THF showed a 5 nm redshift and enhancement in the absorption maxima around 315 nm with considerable absorption extending up to 500 nm, indicating the aggregation behavior. Fluorescence analysis of corresponding sample displayed a broad emission in water and methanol centered at 421 nm and 467 nm, respectively (Figure 4.5B). Whereas, in agreement with changes in absorption spectra; **TPE-V1** in THF displaced a sharp, red shifted and enhanced fluorescence emission at 551 nm.

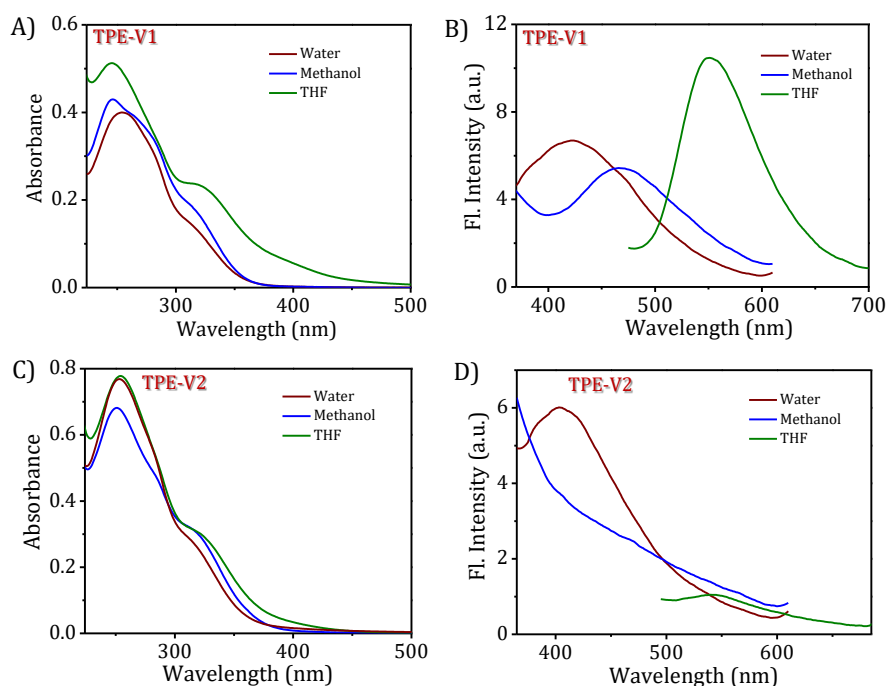


Figure 4.5. Absorption and corresponding fluorescence emission spectra of A) & B) **TPE-V1**, C) & D) **TPE-V2**.

Absorption profiles of **TPE-V2** displayed similar trends as observed in the case of **TPE-V1** in water ($\epsilon_{\max} = 1.16 \times 10^4 \text{ M}^{-1} \text{ cm}^{-1}$) and methanol ($\epsilon_{\max} = 1.37 \times 10^4 \text{ M}^{-1} \text{ cm}^{-1}$) (Figure 4.5C). Whereas in THF, the absorption maxima were similar to that in methanol with a slight broadening up to 450 nm. Corresponding fluorescence spectra of **TPE-V2** in water showed a broad emission centered around 404 nm and non-emissive and weakly emissive profiles in methanol and THF, respectively (Figure 4.5D). The absorption and fluorescence properties of **TPE-V3** (Figures 4.6A & 4.6B) and **TPE-V4** (Figures 4.6C & 4.6D) showed similar results as in the case of **TPE-V1**.

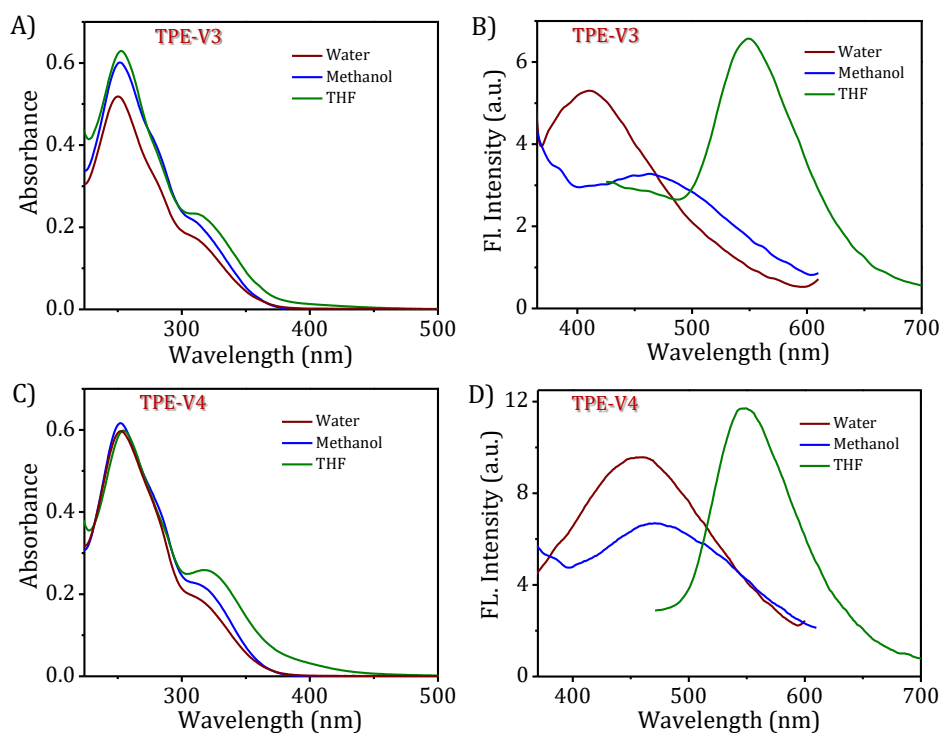


Figure 4.6. Absorption and corresponding fluorescence emission spectra of A) & B) **TPE-V3**, C) & D) **TPE-V4**.

For example, **TPE-V3** in water ($\epsilon_{\max} = 8.56 \times 10^3 \text{ M}^{-1} \text{ cm}^{-1}$), methanol ($\epsilon_{\max} = 1.04 \times 10^4 \text{ M}^{-1} \text{ cm}^{-1}$) and THF exhibited 411 nm (broad), 462 nm (broad) and 549 nm (sharp) fluorescence emission, respectively. Similarly, **TPE-V4** in water ($\epsilon_{\max} = 8.12 \times 10^3 \text{ M}^{-1} \text{ cm}^{-1}$), methanol ($\epsilon_{\max} = 1.03 \times 10^4 \text{ M}^{-1} \text{ cm}^{-1}$) and THF exhibited 455 nm

(broad), 470 nm (broad) and 546 nm (sharp) fluorescence emission, respectively. In short, **TPE-V** derivatives are reasonably soluble in methanol with the weakly emissive monomeric property and exist as dissimilar aggregates in water and THF, with characteristics of the AIE property.

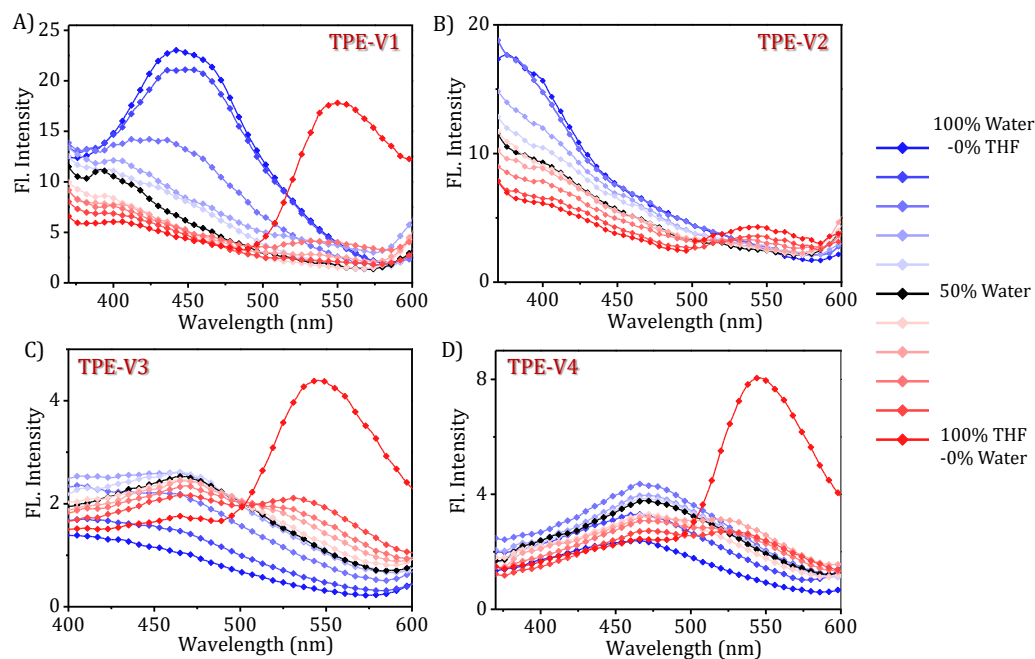


Figure 4.7. Changes in the fluorescence emission spectra of A) **TPE-V1**, B) **TPE-V2**, C) **TPE-V3** and D) **TPE-V4** (10 μ M) in different THF-water solvent compositions.

Aggregation features of **TPE-V** derivatives (10 μ M) were further studied by monitoring the changes in the fluorescence emission and AFM morphologies in different THF-water solvent mixtures. Figures 4.7A-D clearly shows the changes in fluorescence emission maxima of **TPE-V** derivatives with increasing the THF fraction in water, indicating the transition of molecular aggregates. AFM analysis of these samples (Figure 4.8) displayed the presence of random aggregates (with spherical and sheet like structures) in water and lower fractions of THF in water (< 50%), responsible for the emission band around 400 nm for **TPE-V2** and 450 nm for **TPE-V1**, **TPE-V3** and **TPE-V4**. Whereas in THF and higher fractions of THF in water (> 50%), molecularly dissolved states for **TPE-V2** and roughly spherical shape

aggregates for and **TPE-V1**, **TPE-V3** and **TPE-V4** were observed. Therefore, these smaller aggregates are responsible for the distinct fluorescence emission around 550 nm for **TPE-V** derivatives in THF.

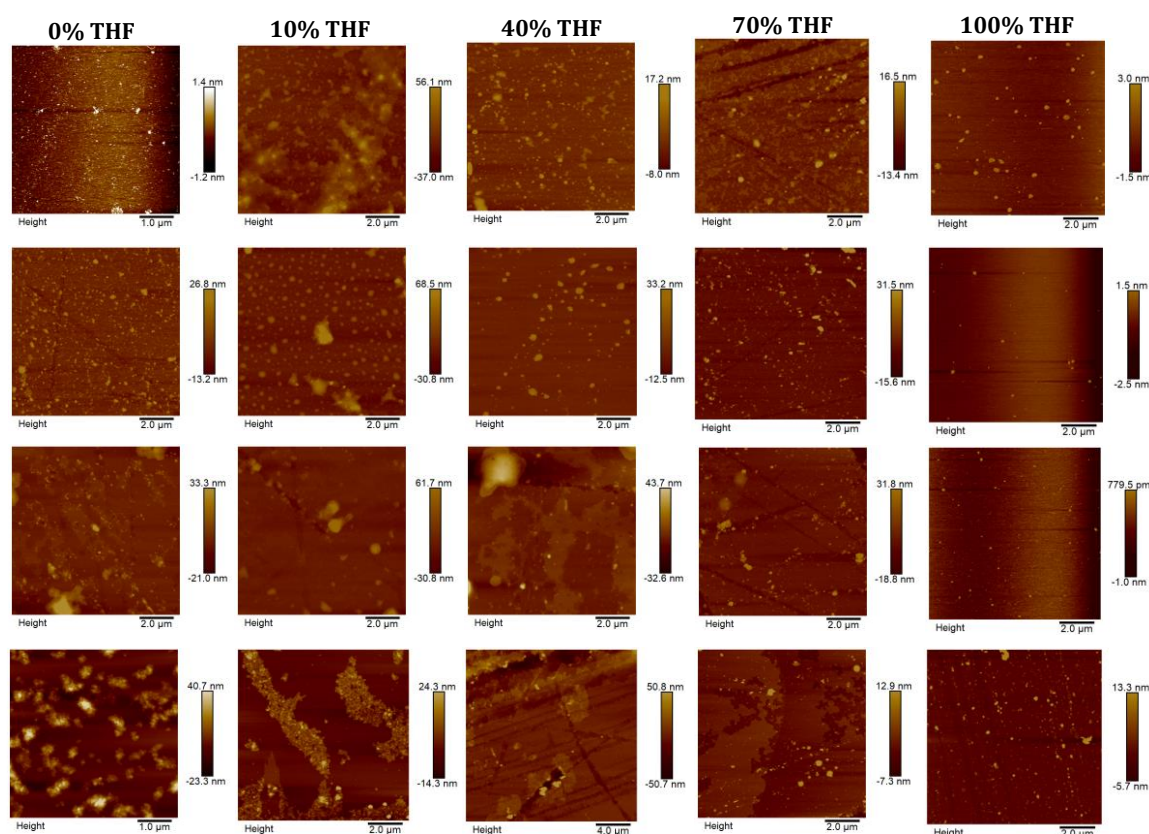


Figure 4.8. AFM morphologies of **TPE-V1** (1st row), **TPE-V2** (2nd row), **TPE-V3** (3rd row) and **TPE-V4** (4th row) in different THF-water solvent compositions.

4.3.3. Interactions of TPE-V derivatives with CT-DNA

As mentioned in the previous section, **TPE-V** derivatives exist as random aggregates in water due to the aggregation tendency of hydrophobic TPE core. We have studied the DNA-interaction and consequent DNA condensation abilities of these aggregates with long double stranded genomic CT-DNA. Primarily, UV-visible absorption and fluorescence emission spectroscopic techniques were used to understand the interactions of **TPE-V** derivatives with CT-DNA. The absorption spectra of all these derivatives in Tris buffer (10 mM Tris buffer with 2 mM NaCl)

displayed an attenuated absorbance than in water, indicating the enhanced aggregation tendency in Tris buffer. Upon sequential addition of CT-DNA to **TPE-V1** (15 μM) in Tris buffer, the characteristic absorption band at 315 nm showed a consistent hypochromic shift up to one equivalent addition of CT-DNA (Figure 4.9A, CT-DNA concentration is per single nucleotide with unit negative charge), suggesting further aggregation of **TPE-V1/CT-DNA** complex. Above this 1:1 ratio, negligible decrease was observed in the 315 nm absorbance band.

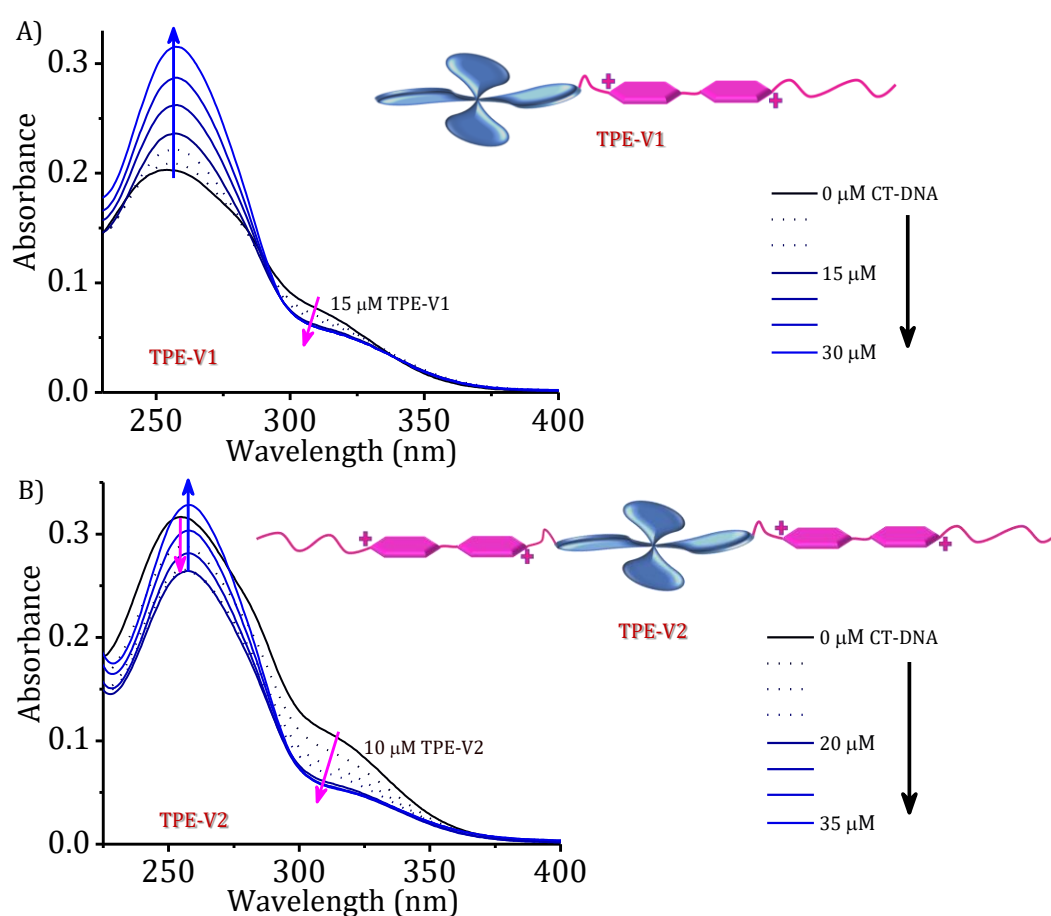


Figure 4.9. Changes in the absorption spectra of A) **TPE-V1** (15 μM), B) **TPE-V2** (10 μM) in Tris buffer with sequential addition of CT-DNA (each single addition makes 5 μM in the final volume) and cartoonic representation of the molecular structures of **TPE-V1** and **TPE-V2**.

On the other hand, the absorption band at 260 nm where the contributions from both **TPE-V1** and CT-DNA occur displayed very slight enhancement up to 1:1 ratio of CT-DNA to **TPE-V1**, above which a comparatively enhanced absorbance was

observed. These results suggest the charge neutralization process accomplished by the interaction of one of the two positive charges on viologen head group in **TPE-V1** with negatively charged phosphate back bone of CT-DNA leading to aggregation of **TPE-V1/CT-DNA** complex, indicated by the decrease in 315 nm absorbance band. In addition, negligible changes in the UV-visible absorption spectra above this 1:1 ratio implies that, only one positive charge on the **TPE-V1** derivative is primarily interacting with CT-DNA. As a result, further addition of CT-DNA doesn't offer additional interactions with **TPE-V1** and hence the absorbance at 260 nm showed a continuous enhancement beyond 1:1 ratio of **TPE-V1/CT-DNA** complex.

Similarly, sequential addition of CT-DNA in to **TPE-V2** in Tris buffer showed the aggregation of **TPE-V2/CT-DNA** complex (Figure 4.9B) with a consistent hypochromicity in the 260 nm and 315 nm absorption bands, up to a 1:2 equivalent ratio of **TPE-V2** to CT-DNA. Above this 1:2 equivalent ratio, negligible decrease in the 315 nm absorption band and considerable enhancement in the 260 nm absorption band was observed, indicating the charge neutralization process through electrostatic interactions. In this case, the **TPE-V2** molecule with positively charged di-viologen head groups can interact with a quantitatively higher amount of negatively charged CT-DNA backbone compared to **TPE-V1**. As a result, the DNA-interaction characteristics were observed up to two equivalent addition of CT-DNA. Similar to **TPE-V1**, mono-viologen functionalized **TPE-V3** (Figures 4.10A & 4.10B) and **TPE-V4** (Figures 4.10A & 4.10C) also showed interactions within 1:1 equivalent ratio of **TPE-V** to CT-DNA, further confirming the electrostatic mode of binding between **TPE-V** derivatives and CT-DNA. In contrast to first three, **TPE-V4** doesn't show a consistent decrease with the initial sequential addition of CT-DNA. Though it follows the similar mode of interactions by charge neutralization process until the

1:1 binding ratio, the irregularity observed in this case could be attributed to the higher aggregation tendency of **TPE-V4** molecule in Tris buffer system compared to other **TPE-V** derivatives.

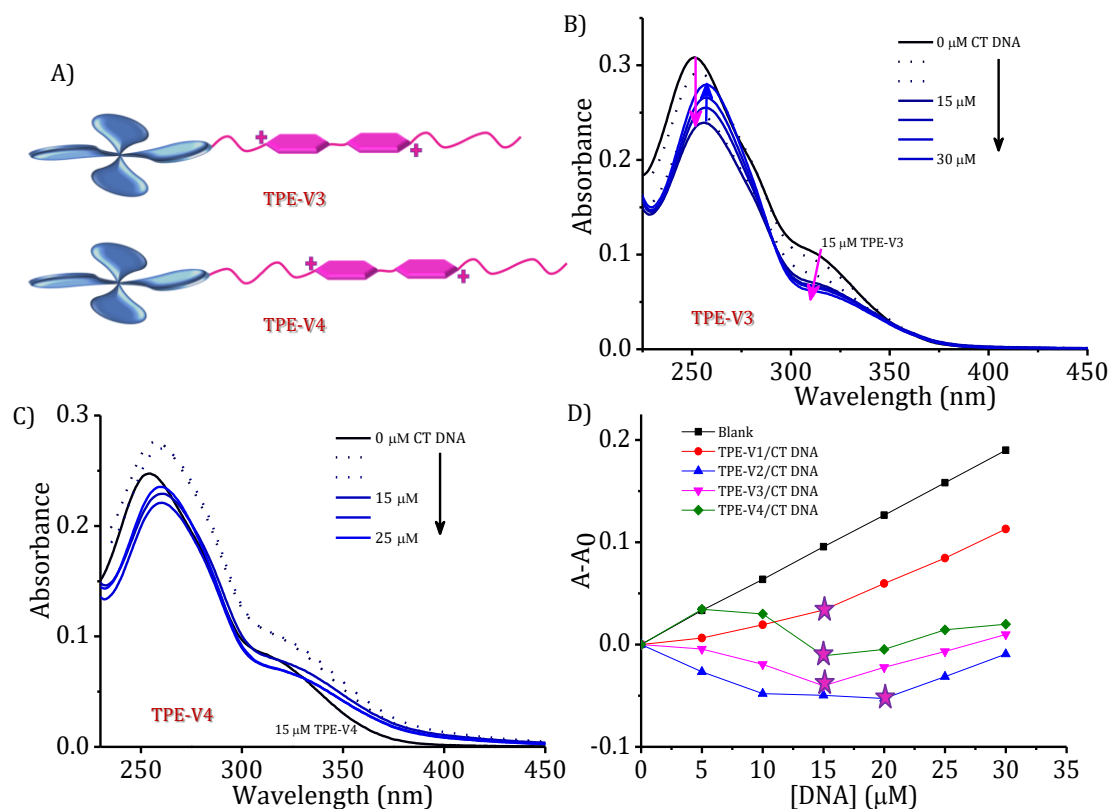


Figure 4.10. A) Cartoonic representation of the molecular structures of **TPE-V3** and **TPE-V4**, changes in the absorption spectra of B) **TPE-V3** and C) **TPE-V4** in Tris buffer with sequential addition of CT-DNA (15 μM **TPE-V** and 5 μM addition of CT-DNA). D) Changes in the absorption spectra of **TPE-V** derivatives in buffer system and blank (Buffer system alone, 10 mM Tris buffer and 2 mM NaCl) at 260 nm with as a function of CT-DNA concentration.

A comparison of changes in the absorption spectra of **TPE-V** derivatives and a blank solution (buffer alone), at 260 nm with sequential addition of CT-DNA (Figure 4.10D) showed a very weak change for **TPE-V** derivatives up to an equivalent ratio of 1:1 for **TPE-V1**, **TPE-V3**, **TPE-V4** and 1:2 for **TPE-V2** with CT-DNA. While, above this ratio a gradual enhancement was observed similar to the blank experiment. The observed differences during the initial CT-DNA addition could be due to the interaction of **TPE-V** derivatives with CT-DNA through

electrostatic binding, leading to a decrease in the absorption at 260 nm. This hypochromism at 260 nm can be ascribed to the combined effect of decrease in the TPE absorption due to aggregation of **TPE-V** derivatives and rise in the DNA absorption due to increase in the DNA concentration. As a result, negligible change in the 260 nm absorption was observed during the initial additions of CT-DNA to **TPE-V** derivatives. Whereas, a gradual upsurge completely due to the increase in free CT-DNA, which is no longer interacting with the **TPE-V** derivatives was observed at higher concentrations of CT-DNA.

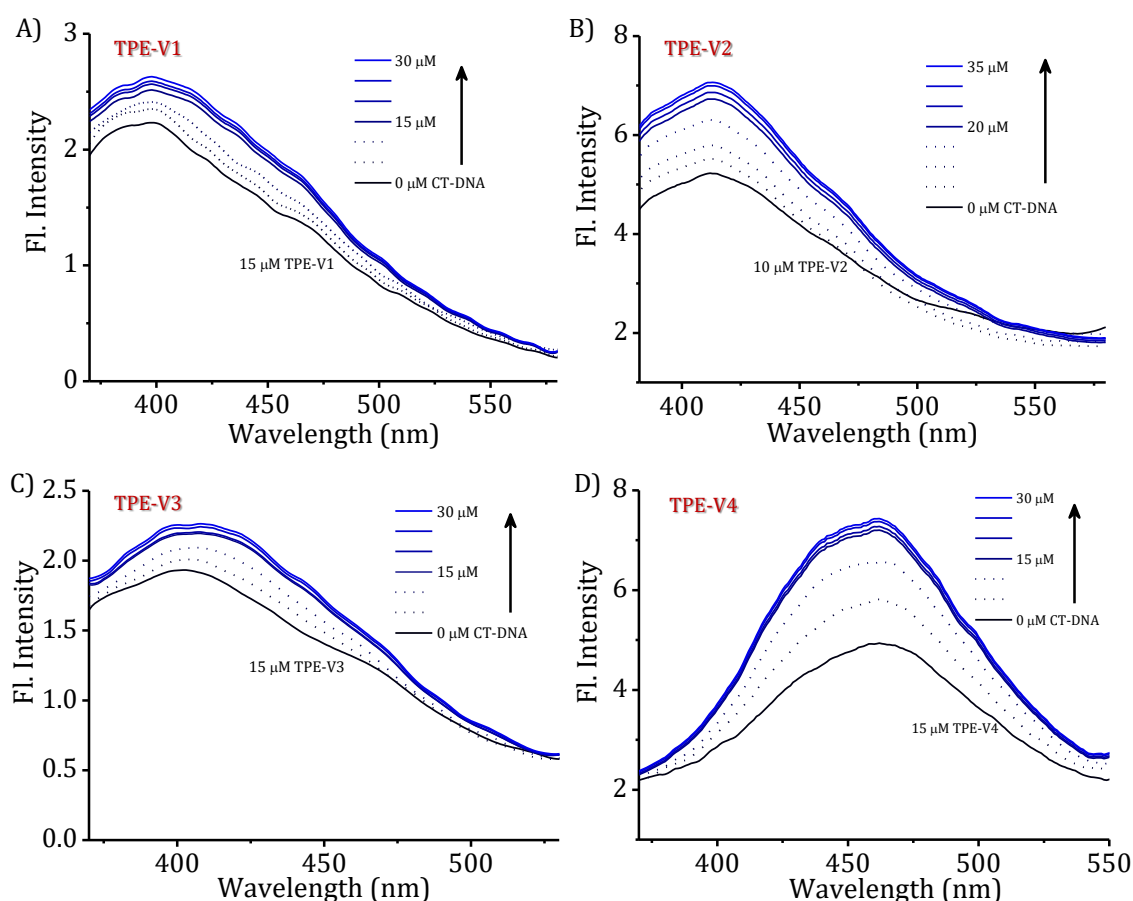


Figure 4.11. Changes in the emission spectra of A) **TPE-V1**, B) **TPE-V2**, C) **TPE-V3** and D) **TPE-V4** in Tris buffer with sequential addition of CT-DNA.

The fluorescence emission profiles of **TPE-V** derivatives corresponding to the above experiment shows a slight enhancement with the sequential addition of CT-DNA, up to a concentration equivalent ratio of 1:1 for **TPE-V1**, **TPE-V3**, **TPE-V4** and

1:2 for **TPE-V2** with CT-DNA (Figures 4.11A-D). Above this ratio, a comparatively negligible enhancement was observed. These differences could be attributed to the initial interaction and subsequent aggregation tendency of the random aggregated structures of **TPE-V** derivatives with the added CT-DNA template. At higher concentrations of CT-DNA, there will not be any free available positive charge on **TPE-V** aggregates to interact with the CT-DNA template, and hence no further changes were observed in the fluorescence emission spectra of **TPE-V** derivatives. Among the **TPE-V** derivatives, **TPE-V2** and **TPE-V4** displayed a relatively higher enhancement in the fluorescence emission upon interaction with CT-DNA. In the case of **TPE-V2**, the enhancement could be attributed to the possibility of interaction between soluble **TPE-V2** molecules with CT-DNA, in addition to the interaction of random aggregates. Whereas in **TPE-V4**, initial enhancement could be ascribed as a collective result of the in-solubility directed aggregation of **TPE-V4** molecule and interaction with CT-DNA.

4.3.4. Thermal denaturation and circular dichroism studies

Thermal denaturation studies of CT-DNA and **TPE-V/CT-DNA** complexes (in a ratio, 1:1 for **TPE-V1**, **TPE-V3**, **TPE-V4** and 0.5:1 for **TPE-V2** with CT-DNA) were performed to understand the changes in the thermal stability of the duplex structure of CT-DNA, upon interaction with **TPE-V** derivatives. Figure 4.12 shows the melting curves constructed by recording the changes in absorption at 260 nm with increase in the temperature from 20 °C to 100 °C with a heating rate of 1 °C per minute. The melting temperature of CT-DNA increases from 68 °C to 78 °C in presence of **TPE-V1** (1:1 complex), and to 88 °C in the presence of **TPE-V2** (0.5:1 complex). Whereas, the **TPE-V3/CT-DNA** and **TPE-V4/CT-DNA** complexes did not melt in this temperature

range, which implies a higher thermal stability for these complexes. These results suggest the cationic molecule directed DNA compaction gives rise to a condensed structure with enhanced thermal stability for DNA.²⁴ Here, the enhanced thermal stability of **TPE-V/CT-DNA** complexes indicate that **TPE-V** derivatives interact reasonably well with CT-DNA, but with differential strengths. The higher thermal stability of **TPE-V2/CT-DNA** compared to **TPE-V1/CT-DNA** could be attributed to the presence of di-viologen units in the former, which gives rise to a quantitative enhancement in DNA binding. On the other hand, the cationic viologen part in **TPE-V3** and **TPE-V4** molecules are freely movable in comparison with the other two derivatives. As a result, they can interact more freely with CT-DNA, thereby resulting in more stable complexes with CT-DNA compared to **TPE-V1** and **TPE-V2**.

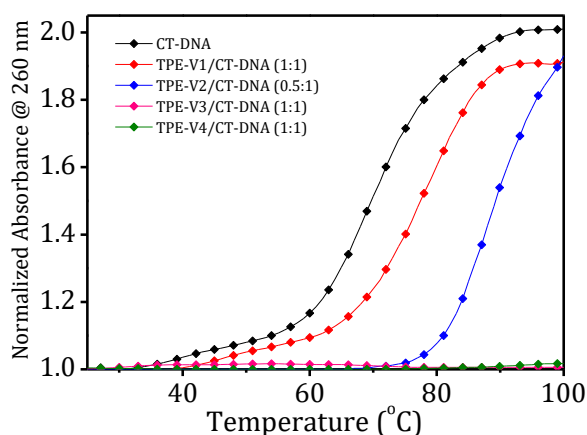


Figure 4.12. Thermal denaturation curves of CT-DNA in the absence and presence of **TPE-V** derivatives.

Structural changes in the CT-DNA, upon interaction with **TPE-V** derivatives were investigated by measuring the changes in circular dichroism (CD). To the solution of CT-DNA in buffer system, varying concentrations of **TPE-V** derivatives were added and the spectral changes observed are shown in Figures 4.13A-D. The CD spectrum of CT-DNA displayed a typical B-form duplex DNA signature with characteristic 247 nm negative band corresponding to polynucleotide helicity and

277 nm positive band originating from base stacking. However, CD spectra of CT-DNA in presence of increasing concentrations of **TPE-V** derivatives (0 to 1.2 molar equivalent) showed a gradual decrease in the 247 nm band and the formation of a slightly red shifted and broadened band at 305 nm from the initial 277 nm band, extending up to 350 nm.

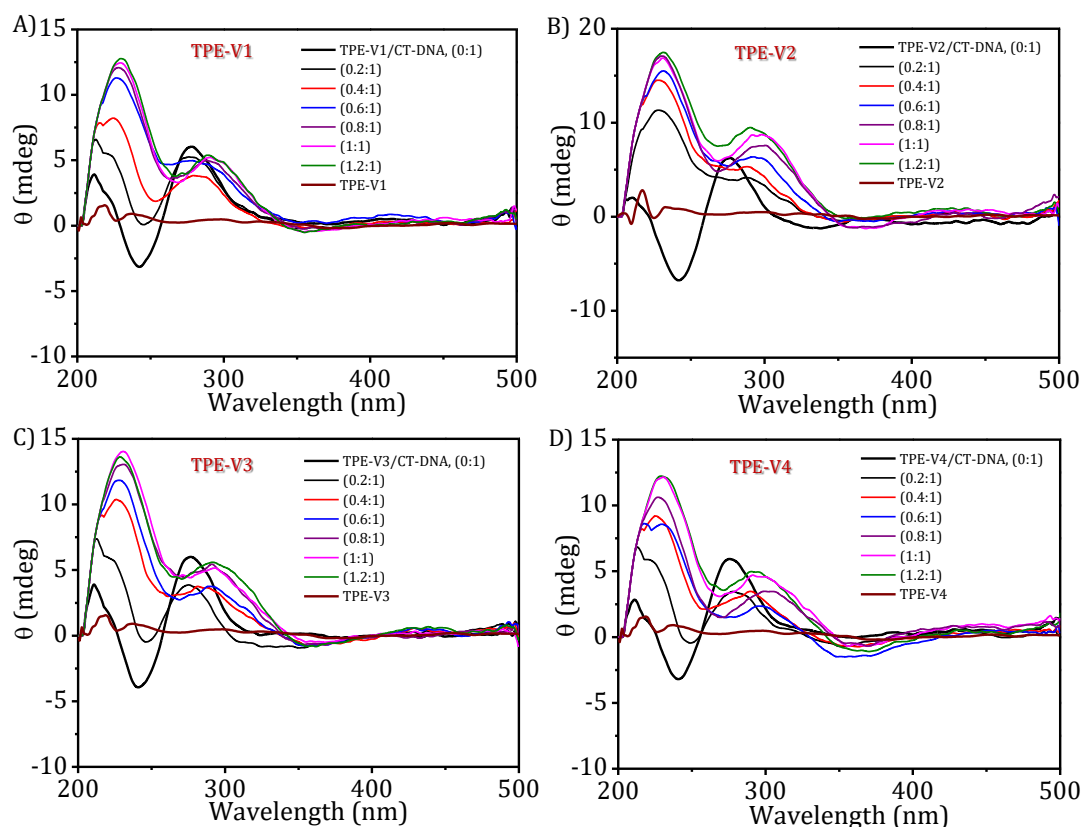


Figure 4.13. Changes in the circular dichroism spectra of CT-DNA (100 μ M) in presence of varying concentrations (0, 20, 40, 60, 80, 100 and 120 μ M) of A) **TPE-V1**, B) **TPE-V2**, C) **TPE-V3** and D) **TPE-V4**.

This considerable change observed in the characteristic CD signal of B-form CT-DNA to a signal above 300 nm indicates the condensation of DNA into particles which can scatter light.⁴¹ In addition, this newly formed induced circular dichroism (ICD) band in the region of the absorption of **TPE-V** derivatives, where **TPE-V** derivatives alone doesn't show any CD signal also suggests the chiral organization of **TPE-V** derivatives on CT-DNA template, indicative of the DNA groove binding.

4.3.5. Ethidium bromide displacement assay

Fluorescence displacement assay using ethidium bromide (EB) as the DNA probe is a suitable method to identify the mode of binding between small molecules and DNA. EB shows enhancement in the fluorescence intensity upon intercalation between the base-pairs of duplex DNA structure and thereby provides the structural information about DNA. In addition, several examples of interaction of cationic ligands with EB/DNA complexes resulting in DNA condensation and subsequent displacement of EB from the DNA complex with quenching of EB fluorescence are also reported in the literature.^{42,43}

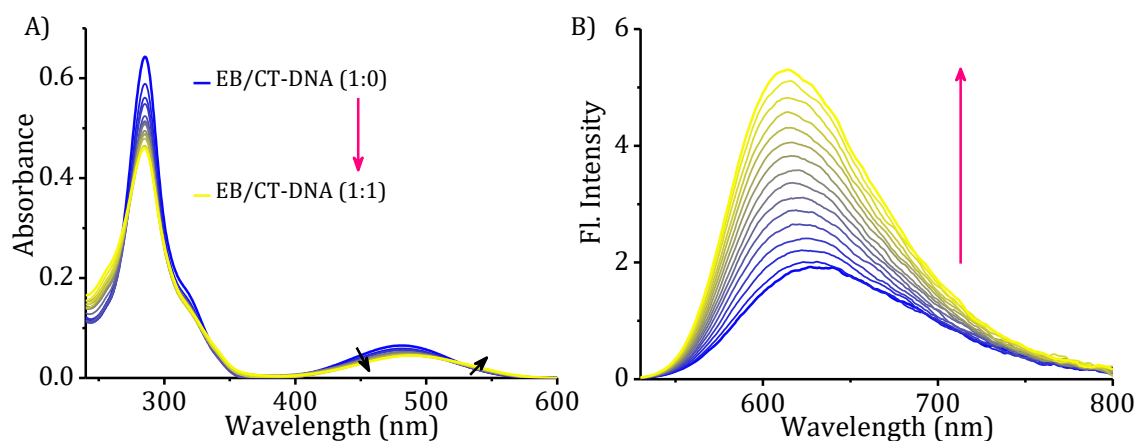


Figure 4.14. Changes in the A) absorption and B) emission spectra of EB (15 μM) in presence of increasing concentrations of CT-DNA (0-15 μM).

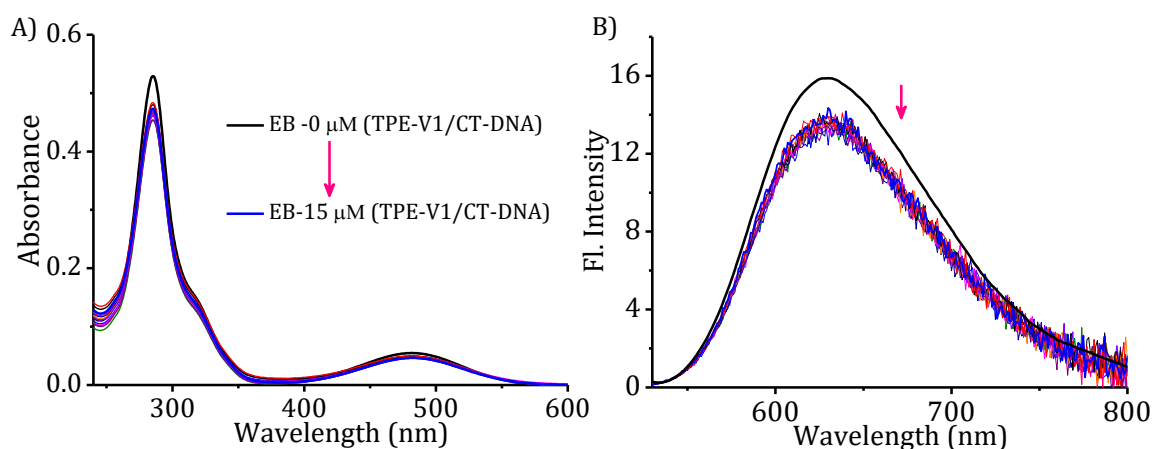


Figure 4.15. Changes in the A) absorption and B) emission spectra of EB (15 μM) in presence of increasing concentrations of **TPE-V1/CT-DNA** (1:1 complex, 0-15 μM).

Here, we carried out the above-mentioned experiments to understand the structural changes and mode of binding in **TPE-V/CT-DNA** complexes. Figures 4.14A & 4.14B represent a typical titration experiment of CT-DNA against EB, which shows the enhancement in fluorescence intensity upon intercalation of EB into CT-DNA. Similar titration experiment performed with **TPE-V1/CT-DNA** complex against EB showed only negligible changes in the absorption spectra with an initial marginal decrease in the fluorescence emission spectra (Figures 4.15A & 4.15B), up to 1:1 equivalent addition of **TPE-V1/CT-DNA** complex to EB. Results indicate the inability of EB to intercalate between the base-pairs of CT-DNA in **TPE-V1/CT-DNA** complex. Likewise, intercalation studies of EB with **TPE-V2**, **TPE-V3** and **TPE-V4** complexes of CT-DNA (Figures 4.16A-C) also displayed only slight decrease

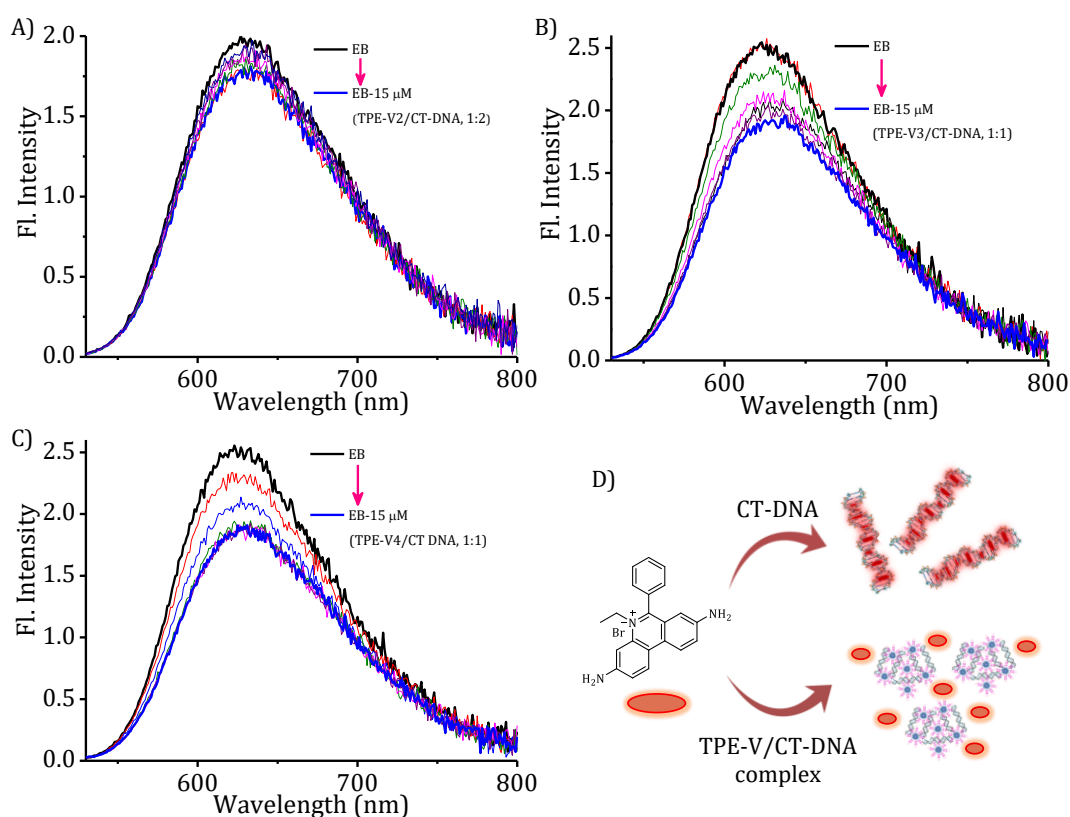


Figure 4.16. Changes in the fluorescence emission spectra of EB (15 μM) in presence of increasing concentrations of A) **TPE-V2/CT-DNA** (1:2 complex, 0-15 μM), B) **TPE-V3/CT-DNA** (1:1 complex, 0-15 μM) and C) **TPE-V4/CT-DNA** (1:1 complex, 0-15 μM). D) Schematic representation of the interaction of EB with CT-DNA alone and **TPE-V/CT-DNA** complexes.

in the fluorescence emission, instead of the expected intercalation prompted enhancement in fluorescence intensity. Therefore, failure of EB to intercalate between the base-pairs of CT-DNA in the **TPE-V/CT-DNA** complexes suggest conformational changes in long double helical DNA structure upon interaction with **TPE-V** derivatives (Figure 4.16.D; schematic representation of this experiment).

Next, we have studied the interaction of **TPE-V** derivatives with CT-DNA by titrating **TPE-V** derivatives against a preincubated solution of EB/CT-DNA complex (EB: CT-DNA; 1:2, 15 μ M:30 μ M). As observed in the above experiment (Figure 4.14), the fluorescent intensity of EB increases upon incubation with CT-DNA and shows a 4-fold enhancement at 1:2 equivalent ratio. Figures 4.17A & 4.17B shows the changes in the absorption and emission spectra of EB, upon titrating **TPE-V1** against EB/CT-DNA (1:2) complex. Addition of **TPE-V1** in to EB/CT-DNA complex showed gradual quenching of the EB fluorescence, which suggest the displacement of intercalated EB from CT-DNA due to DNA conformational changes upon interaction with **TPE-V1**.

Similarly, the addition of **TPE-V2**, **TPE-V3** and **TPE-V4** molecules also displayed quenching of the fluorescence intensity of EB/CT-DNA complex (Figures 4.17C-E). The results of ethidium bromide displacement assays strongly support the possible condensation of the double helical DNA structure of CT-DNA upon interactions with positively charged **TPE-V** derivatives. Though, quenching in fluorescence intensity was observed with all the four **TPE-V** derivatives, the extent of quenching was different, which can be taken as the measure of DNA condensation ability of these ligands. Figure 4.17.F shows the changes in fluorescence intensity of EB/CT-DNA complex at 612 nm upon addition of **TPE-V** derivatives, constructed by plotting the concentration of **TPE-V** against I/I_0 . Compared to **TPE-V1**, other three

TPE-V derivatives completely quench the fluorescence intensity of EB/CT-DNA complex at relatively lower concentrations, which implies the enhanced DNA interaction and condensation ability of **TPE-V2**, **TPE-V3** and **TPE-V4**.

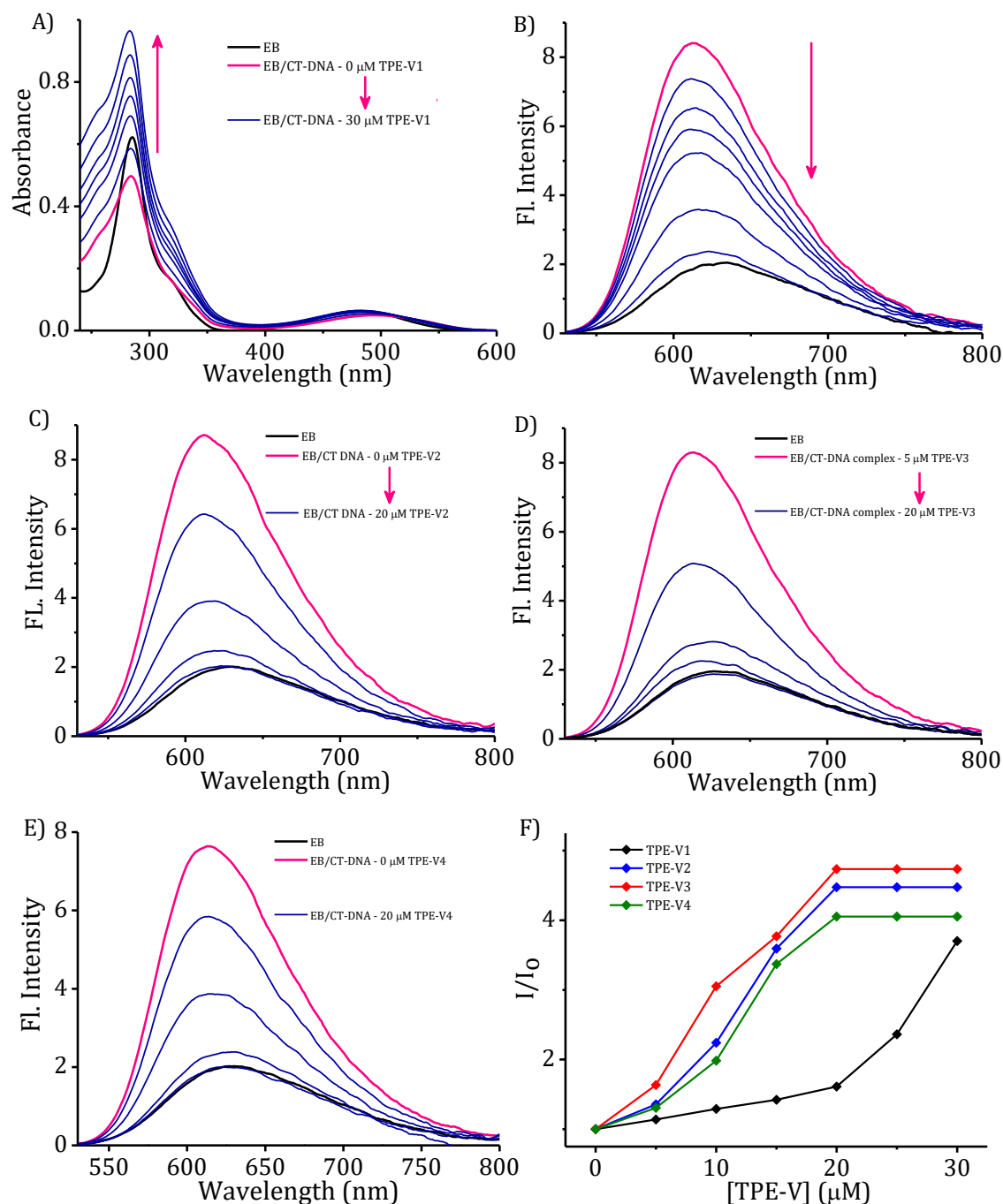


Figure 4.17. Changes in the A) absorption and B) fluorescence emission spectra of EB (15 μM), EB/CT-DNA complex (1:2) and addition of **TPE-V1** (5 μM sequential) in to EB/CT-DNA complex. Changes in the emission spectra of EB/CT-DNA complex upon addition of C) **TPE-V2**, D) **TPE-V3** and E) **TPE-V4**. F) Changes in the fluorescence intensity of EB/CT-DNA complex at 612 nm, I/I_0 against concentration of **TPE-V** derivatives.

4.3.6. Morphological studies

The formation of ICD band in the CD spectra of CT-DNA in presence of **TPE-V** derivatives, signifying the groove binding of chromophores aided by electrostatic interaction and expulsion of intercalated EB from EB/CT-DNA complex in presence of **TPE-V** derivatives, suggesting the DNA condensation process were further investigated in detail by monitoring the changes in the morphologies of CT-DNA and **TPE-V** derivatives using AFM, TEM and DLS techniques. Sample concentrations in the micro molar range used for the UV-visible absorption studies were chosen for AFM and TEM analysis. Whereas, higher concentrations used for CD studies were chosen for DLS analysis.

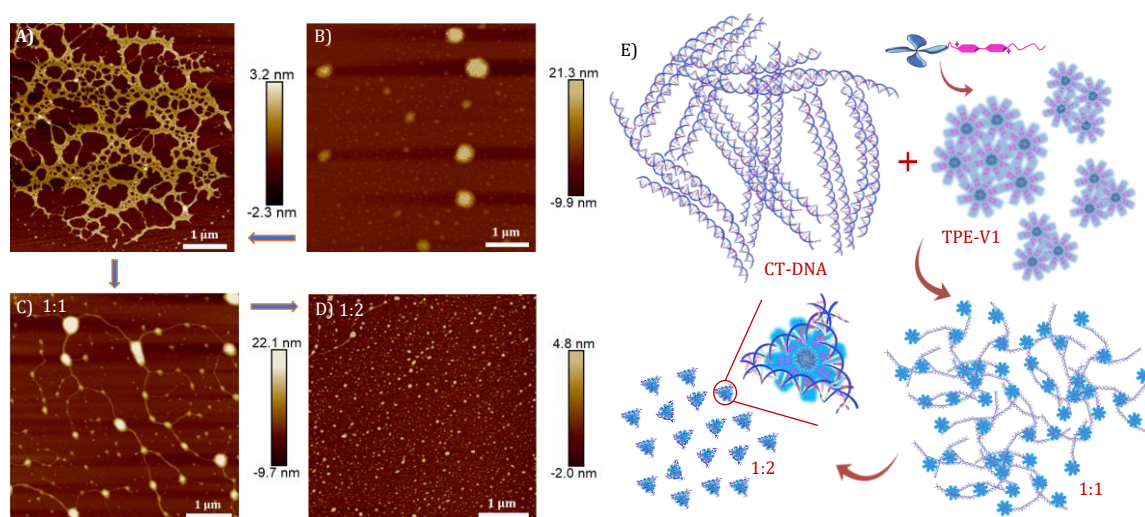


Figure 4.18. AFM images of A) CT-DNA (15 μM), B) **TPE-V1** (15 μM) and **TPE-V1/CT-DNA** complex at different CT-DNA to **TPE-V1** ratios, C) 1:1 & D) 1:2. E) Schematic representation of the DNA interaction and condensation process by **TPE-V1**.

To understand the changes observed in the UV-visible absorption, fluorescence and CD properties at different CT-DNA to **TPE-V** molar ratios, we have carried out the AFM analysis of samples with two different molar equivalents of **TPE-V** in **TPE-V/CT-DNA** complex on a freshly cleaved mica surface. Figure 4.18A-D shows the morphologies of CT-DNA, **TPE-V1**, 1:1 **TPE-V1/CT-DNA** and 1:2 **TPE-**

V1/CT-DNA complexes (In all the morphology studies, the ratios 1:1 and 1:2 represent CT-DNA:**TPE-V** molar ratio). CT-DNA alone displayed fibrous network like structures with 200-300 nm width (Figure 4.18A), while **TPE-V1** alone displayed random, spherical aggregates with 350 nm diameter for the largest aggregate (Figure 4.18B). On the other hand, **TPE-V1/CT-DNA** complex at 1:1 ratio displayed a hybrid morphology of **TPE-V1** and CT-DNA, exhibiting a “beads on a string” type arrangement (Figure 4.18C), similar to the structure of chromatin fibers found in the chromosomes of eukaryotic cells. The strings (fibers) showed an average width of 80 nm while the beads (spherical aggregates on fibers) had an average width of 110 nm. Further, at higher concentrations of **TPE-V1** in **TPE-V1/CT-DNA** complex (1:2), the AFM images showed spherical aggregates with an average diameter of 50 nm (Figure 4.18D), indicating complete condensation of the complex.

The observed AFM results could be explained as follows. At initial, lower **TPE-V1** concentrations, the electrostatic interactions between positively charged viologen moiety of aggregated **TPE-V1** and fibrous network of negatively charged CT-DNA structures, lead to the separation of fibrous DNA networks and disruption of larger **TPE-V1** aggregates to smaller ones. Under these conditions, the electrostatically bound **TPE-V1** aggregates tend to form bead type structures on the long CT-DNA templates. While at higher concentration of **TPE-V**, complete condensation of CT-DNA is observed due to effective charge neutralization. Thus, upon increasing the concentration of **TPE-V1** in **TPE-V1/CT-DNA** complex to 1:2, the interaction possibilities between DNA and molecule increases which lead to the disruption of larger aggregates of **TPE-V1** along with complete charge neutralization of the negatively charged DNA back bone. As a consequence, the 'beads on a string' structure with DNA chains and **TPE-V1** aggregates completely condense into

spherical structures of 40-50 nm in size. Figure 4.18E shows the schematic representation of the proposed mechanism of DNA condensation process by **TPE-V1**. The morphological changes observed at different ratios of **TPE-V1** to CT-DNA validate the observed ICD band in the CD spectra. Up to 1:1 equivalent ratio, the 'beads on a string' type structures are formed through a combination of electrostatic and groove binding interactions of **TPE-V1** aggregates with chiral DNA template which induce chirality to **TPE-V1**. With the addition of higher amounts of **TPE-V1**, complete DNA condensation takes place and hence no further changes were observed in the ICD signal of **TPE-V1/CT-DNA** complex.

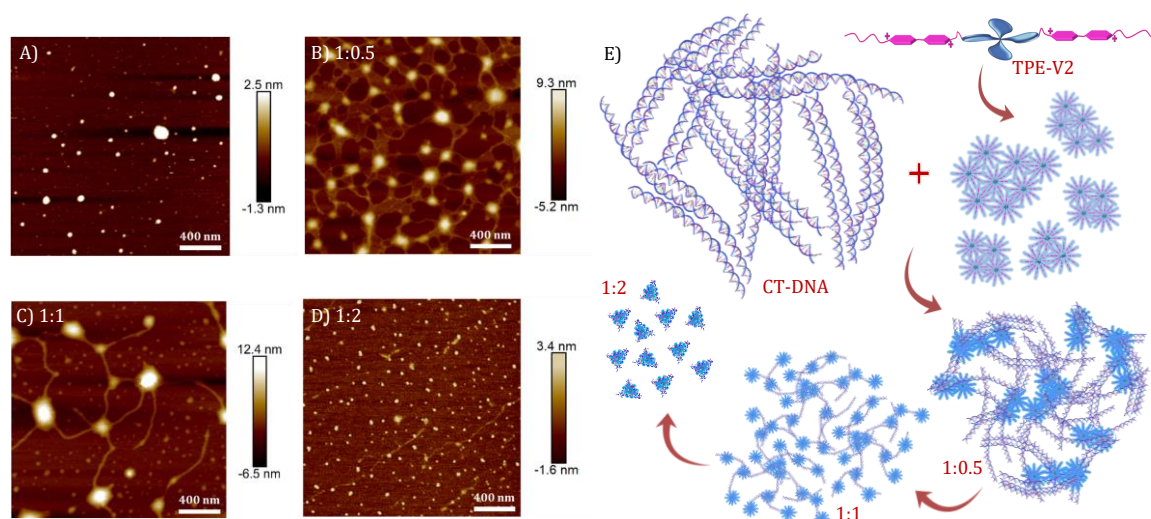


Figure 4.19. AFM images of A) **TPE-V2** (10 μM) and **TPE-V2/CT-DNA** complex at different CT-DNA to **TPE-V2** ratios, B) 1:0.5, C) 1:1 and D) 1:2. E) Schematic representation of the CT-DNA interaction and condensation process by **TPE-V2**.

Similarly, the morphologies of **TPE-V2/CT-DNA** complex at different **TPE-V2** to CT-DNA ratios displayed initial formation of intertwined network structures at 1:0.5 ratio, while beads on a string (1:1) and condensed spherical structures (1:2) are formed at higher **TPE-V2** concentrations. In detail, the AFM morphologies at 1:0.5 ratios of **TPE-V2/CT-DNA** complex showed the disruption of the fibrous network structures of CT-DNA (Figure 4.18A) to intertwined network structures

(Figure 4.19B) with morphological features of both CT-DNA and **TPE-V2** (Figure 4.19A). Upon further increasing the concentration of **TPE-V2** in **TPE-V2/CT-DNA** complex, enhanced disruption of CT-DNA fibrous structures by **TPE-V2** leading to a 'beads on a string' type of arrangement (Figure 4.19C) at 1:1 ratio and completely condensed spherical **TPE-V2/CT-DNA** structures at 1:2 ratio (Figure 4.19D) was observed in the AFM images. Figure 4.19D shows the schematic representation of morphological changes observed in CT-DNA and **TPE-V2** upon interaction with each other at different molar ratios of **TPE-V2/CT-DNA**.

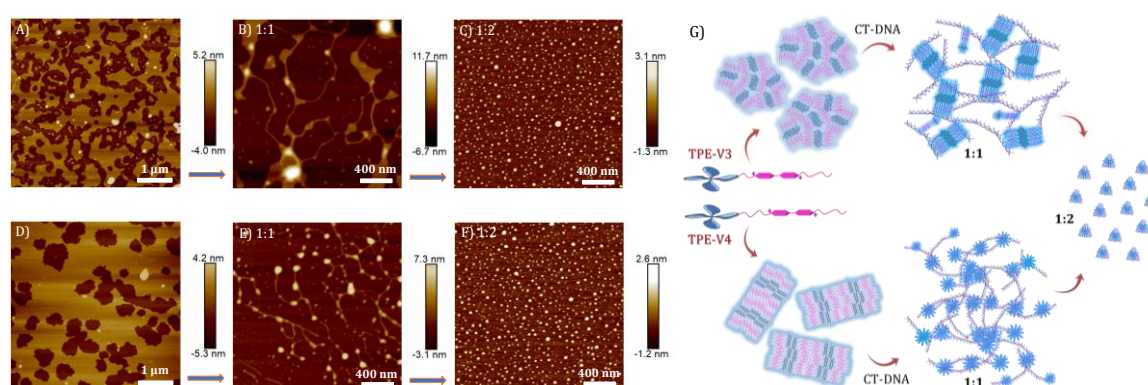


Figure 4.20. AFM images of A) **TPE-V3** (15 μM), and **TPE-V3/CT-DNA** complex at different CT-DNA to **TPE-V3** ratios; B) 1:1 and C) 1:2. AFM images of D) **TPE-V4** (15 μM), and **TPE-V4/CT-DNA** complex at different CT-DNA (15 μM) to **TPE-V4** ratios; E) 1:1 and F) 1:2. G) Schematic representation of the CT-DNA interaction and condensation process by **TPE-V3** and **TPE-V4**.

AFM analysis of **TPE-V3** and **TPE-V4** (drop cast from Tris solutions) showed the formation of sheet like aggregates with nano to micro-meter width (Figures 4.20A and 4.20D), inferring an enhanced aggregation tendency of these derivatives in Tris buffer, compared to that in pure water. Upon interactions with CT-DNA, these derivatives also show a transition from sheet to 'beads/sheets on string' type structures at 1:1 ratio (Figures 4.20B & 4.20E) and to completely condensed spherical structures of **TPE-V/CT-DNA** (Figures 4.20C & 4.20F) with 40-50 nm size at higher **TPE-V** concentrations, as expected. Figure 4.20G shows the schematic

representation of CT-DNA condensation mechanisms upon interaction with **TPE-V3** and **TPE-V4** at different CT-DNA to **TPE-V** ratios.

The morphological changes observed in AFM analysis were further confirmed using TEM analysis of **TPE-V2/CT-DNA** samples. TEM image of CT-DNA (Figure 4.21A) and **TPE-V2** (Figure 4.21B) displayed networked fibrous structures and random aggregated structures, respectively as observed in AFM analysis. Similarly, in agreement with AFM morphologies the **TPE-V2/CT-DNA** complex with increasing concentrations of **TPE-V2** showed the structural transition from the networked fibrous CT-DNA structure to condensed spherical structures of **TPE-V2/CT-DNA** complex with 30-40 nm in size (Figures 4.21C-E). Further, EDAX analysis of **TPE-V2/CT-DNA** complex at 1:2 ratio of CT-DNA to **TPE-V2** spots the occurrence of P atoms (Figure 4.21F), confirming the presence of DNA in the condensed spherical structures observed in TEM.

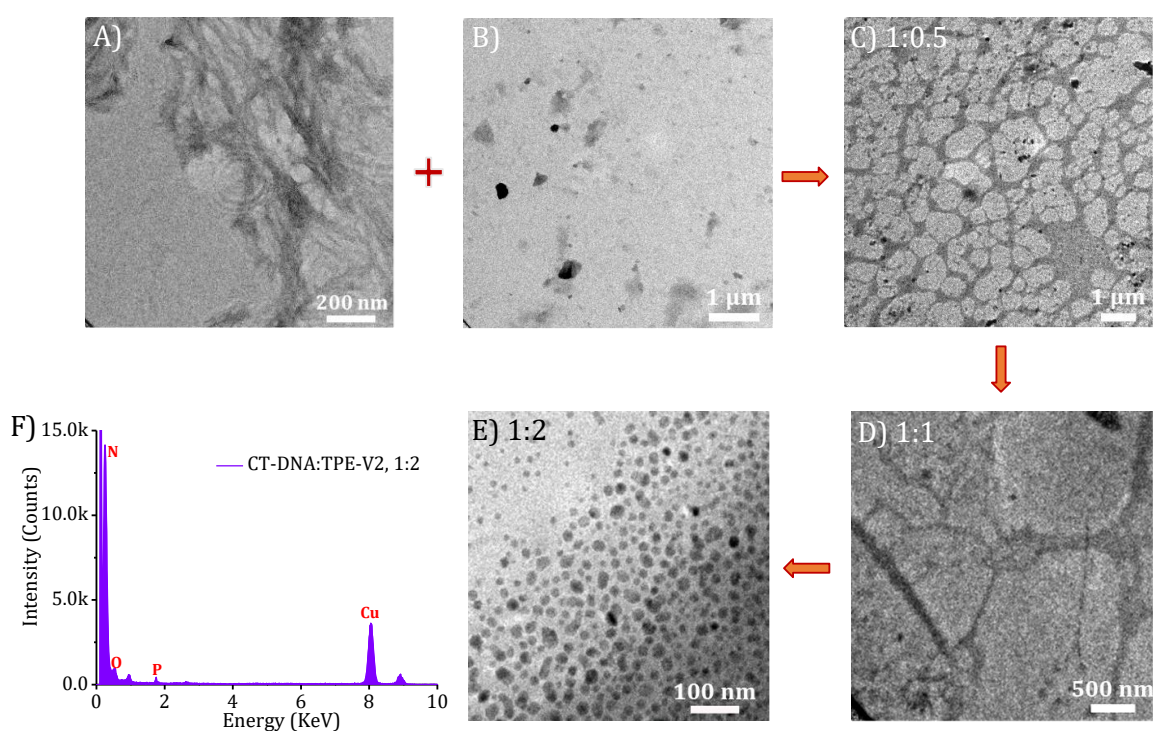


Figure 4.21. TEM images of A) CT-DNA (20 μM), B) TPE-V2 (10 μM) and TPE-V2/CT-DNA complex at different CT-DNA to TPE-V2 ratios, C) 1:0.5, D) 1:1 and E) 1:2. F) EDAX spectra of TPE-V2/CT-DNA at 1:2 ratio.

To get further insight into the DNA condensation process, dynamic light scattering (DLS) measurements were carried out to understand the zeta-potential and size changes accompanying the process (Figure 4.22A & 4.22B). 100 μM samples of CT-DNA were used for DLS studies, since the lower concentrations used in morphological studies doesn't show any significant changes in zeta-potential and hydrodynamic size. CT-DNA alone in Tris buffer showed (-35) to (-40) mV zeta potential and 700-750 nm hydrodynamic radius. With the sequential addition of **TPE-V** derivatives, the zeta-potential values showed gradual increase towards positive values and hydrodynamic size showed steady decrease to 100-200 nm. Since, CT-DNA is a highly networked structure, the hydrodynamic radius we observe here only gives a rough estimate of size in solution. But it still can indicate the changes upon CT-DNA-**TPE-V** interaction leading to spherical condensates. This opposite trends in zeta-potential and size further supports the charge neutralization directed DNA condensation resulting in **TPE-V/CT-DNA** complexes.

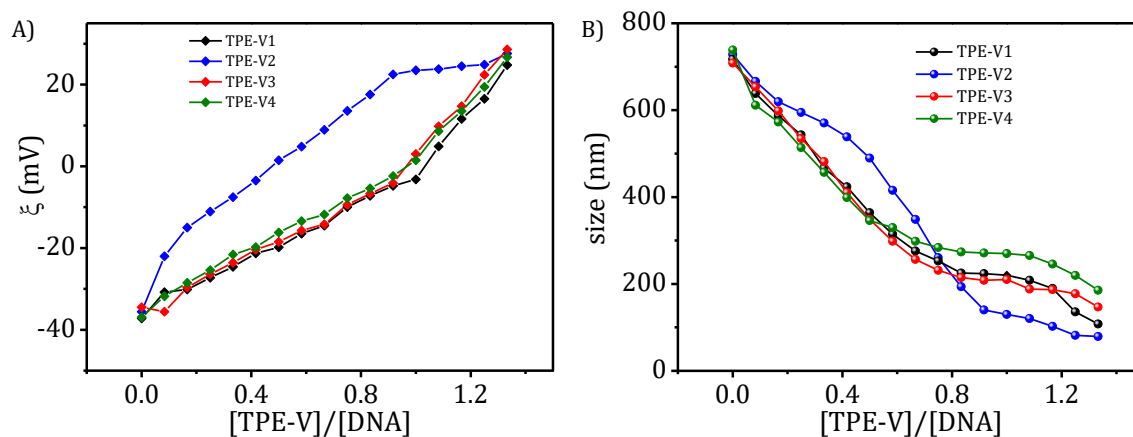


Figure 4.22. Changes in the A) zeta-potential and B) hydrodynamic size of CT-DNA (100 μM) with increasing concentrations of **TPE-V** derivatives.

Compared to other three **TPE-V** derivatives, **TPE-V2** displayed deviation in the values of zeta-potential and hydrodynamic size. These deviations in the values can be attributed to the presence of positively charged di-viologen units enhancing

the electrostatic interaction possibilities between **TPE-V2** molecules and CT-DNA, resulting in a relatively enhanced changes in the zeta-potential and hydrodynamic size. In short, the DLS experiments further supports the optical and morphological results of electrostatic interaction directed CT-DNA condensation by positively charged **TPE-V** derivatives.

4.3.7. Interactions of Cucurbit[8]uril/TPE-V complexes with CT-DNA

To get further insight into the interacting units in **TPE-V** derivatives with CT-DNA, DNA binding experiments were carried out in presence of Cucurbit[8]uril (CB[8]). CB[8] is a well-known host for viologen guests, with the ability to completely encapsulate the guest inside its cavity. Strong complexation with CB[8], results in complete masking of viologen units in the CB[8]/**TPE-V** complex, preventing the binding of viologen moiety with CT-DNA through electrostatic and groove binding interactions. For this experiment, we titrated CT-DNA against preformed CB[8]/**TPE-V** host-guest complex to understand the binding interactions. The UV-visible absorption spectra of CB[8]/**TPE-V1** (1:1) complex showed slightly lower absorbance values at 255 nm and 315 nm compared to **TPE-V1** alone (Figure 4.23A), and an enhanced fluorescence emission (Figure 4.23B). Sequential addition of CT-DNA to this complex showed negligible changes in the UV- visible absorption and fluorescence emission, as expected. Similarly, the absorption and fluorescence spectra of CB[8]/**TPE-V2** (2:1) complex also was not affected by sequential addition of CT-DNA, except for the initial decrease in absorption and enhancement in fluorescence emission of CB[8]/**TPE-V2** (2:1) complex compared to **TPE-V2** (Figures 4.23C & 4.23D). These results indicate that CT-DNA interaction and subsequent condensation observed with **TPE-V** derivatives are primarily due to the

presence of positively charged viologen groups, which interact with CT-DNA through electrostatic and groove binding interactions. The CB[8] complexes of other two derivatives (**TPE-V3** & **TPE-V4**) were prone to precipitation upon addition of CT-DNA and hence were not studied in detail.

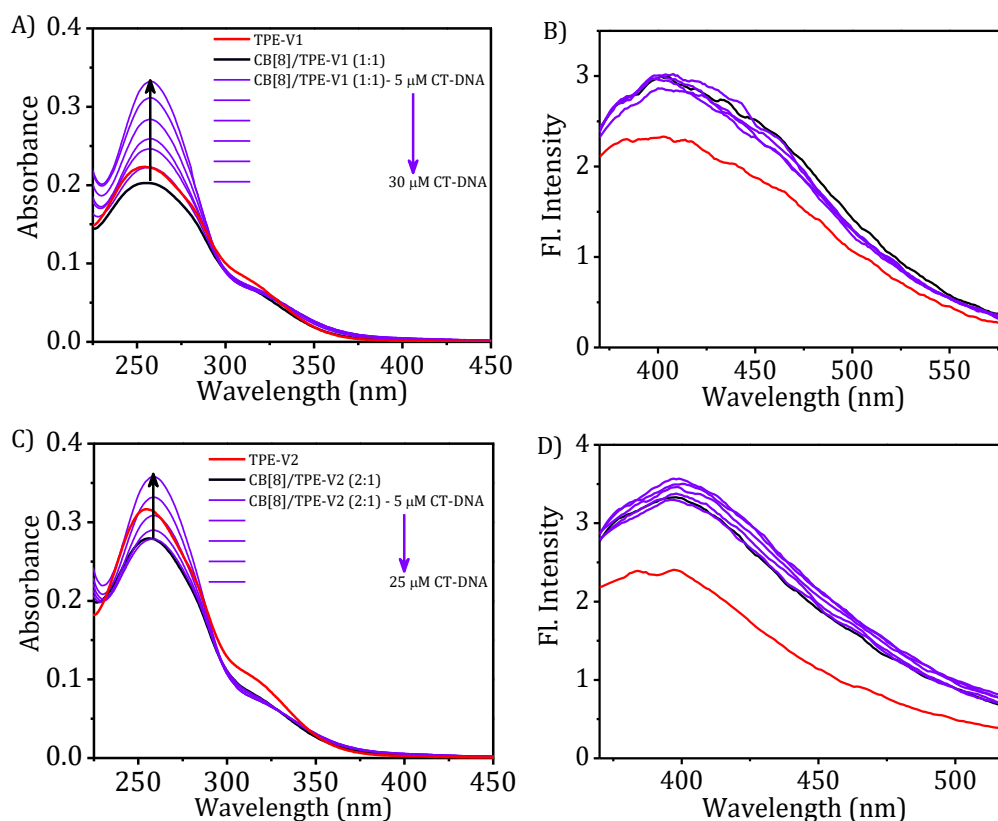


Figure 4.23. Changes in the UV-visible absorption and fluorescence emission spectra of A) and B) CB[8]/**TPE-V1** (1:1, 15 μM), and C) and D) CB[8]/**TPE-V2** (2:1, 20 μM :10 μM) with sequential addition of CT-DNA.

4.3.8. Cytotoxicity studies

An important initial study to check the biological *in vitro* applicability of drugs and chemicals is cytotoxicity analysis, which gives information about the toxicity of these chemicals on cells. A cytotoxicity value greater than 90% gives an indication of its biocompatibility and potential in intracellular drug and gene delivery, whereas a lower value implies cell death, with the potential for cancer therapy. To check the cytotoxicity of our **TPE-V** condensing agents, MTT assay was

conducted. The cytotoxicity of **TPE-V/CT-DNA** condensates were studied with A549 and WI-38, cancer and normal cells, respectively. Figures 4.24A-D shows the cell viabilities of CT-DNA, **TPE-V** aggregates and **TPE-V/CT-DNA** complexes at two different ratios (1:1 and 1:2 of CT-DNA to **TPE-V**) after 24 h and 48 h incubation. The concentrations of CT-DNA and **TPE-V** derivatives are same as that we used for absorption, emission and morphological studies.

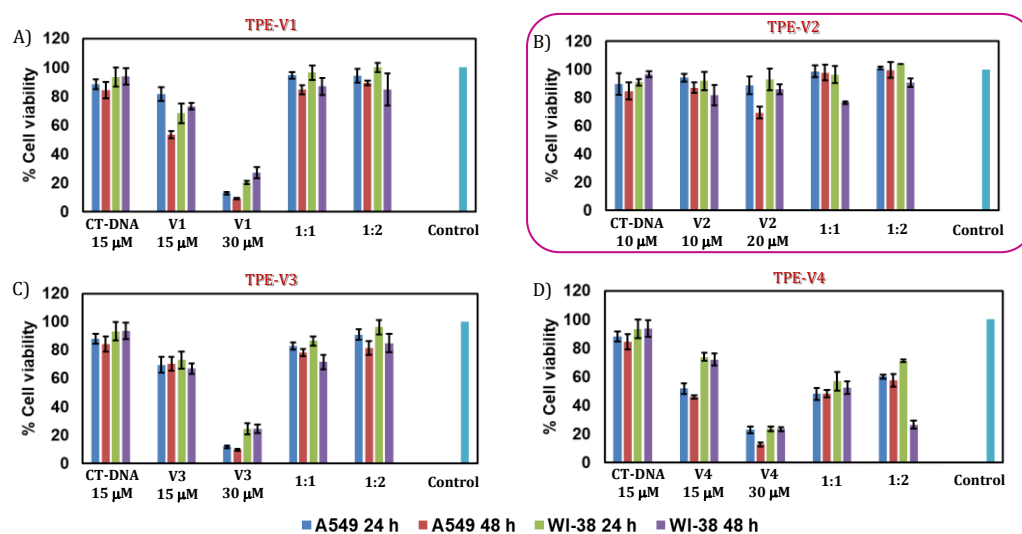


Figure 4.24. Cell viability assay of A549 and WI-38 cells in presence of the four **TPE-V/CT-DNA** assemblies and their control experiments after 24 h and 48 h incubation.

At these concentrations, CT-DNA, **TPE-V2** and the complexes of **TPE-V1**, **TPE-V2** and **TPE-V3** with CT-DNA displayed less cytotoxicity with more than 75 % cell viability in both cell lines. Whereas **TPE-V1**, **TPE-V2**, **TPE-V3** alone and **TPE-V4/CT-DNA** complex were found to be cytotoxic. Results suggest, the “beads on a string” type assembly (1:1) and spherical condensates (1:2) of **TPE-V(1-3)/CT-DNA** have superior cell viabilities compared to the **TPE-V4/CT-DNA** assemblies. Among the afore-mentioned three, **TPE-V2/CT-DNA** complexes displayed a comparatively higher cell-viability in both cells, which could be attributed to the higher solubility and improved electrostatic interaction capability of **TPE-V2** aggregates compared to other derivatives.

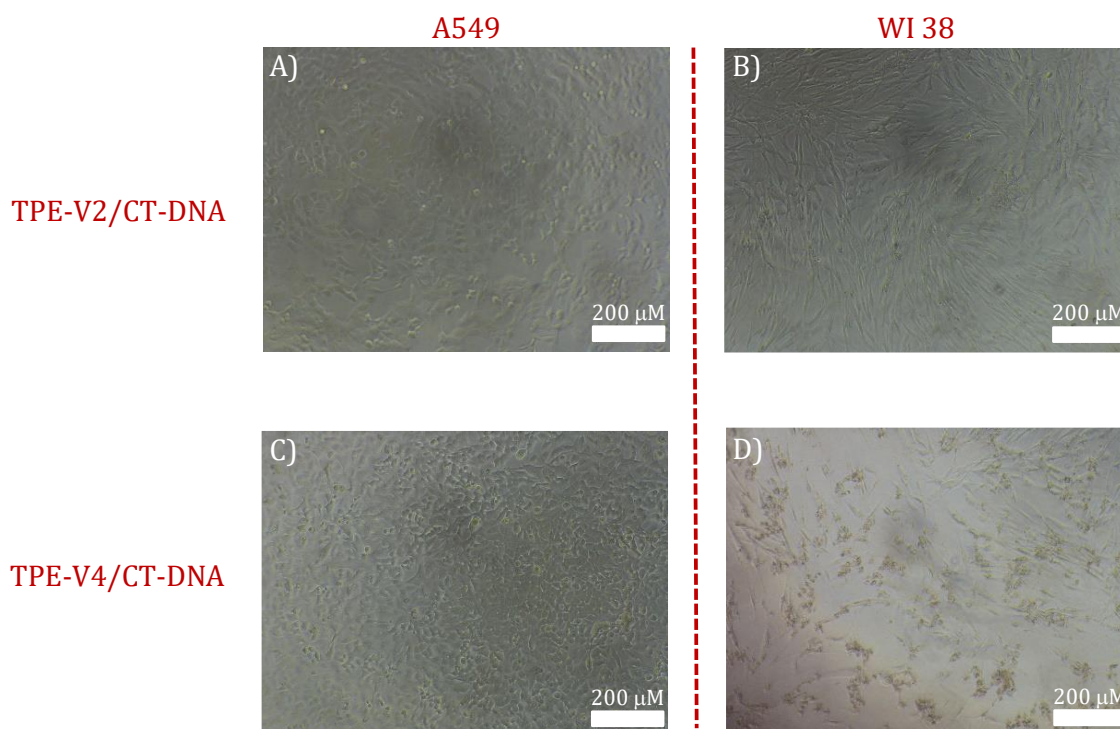


Figure 4.25. Optical microscopic images of A549 and WI-38 cells after 24 hours of incubation with 1:2 complex of A) & B) **TPE-V2/CT-DNA**, and C) & D) **TPE-V4/CT-DNA**.

In agreement with MTT assay, the optical microscopic bright field images of A549 and WI-38 cells, incubated with **TPE-V2/CT-DNA** condensates in a 1:2 ratio after 24 hours displayed the presence of healthy cells (Figures 4.25A & 4.25B). Whereas, under similar conditions, optical microscopic images of A549 and WI-38 cells incubated with **TPE-V4/CT-DNA** condensates showed cell death related morphological changes (Figures 4.25C & 4.25D), confirming the cytotoxic nature of **TPE-V4/CT-DNA** condensates. Therefore, from the above cytotoxicity studies we can conclude that DNA condensates of **TPE-V1**, **TPE-V2**, **TPE-V3** are non-toxic and hence, these three derivatives of **TPE-V** are reasonably good DNA condensing agents for non-viral gene-delivery applications, and among them **TPE-V2** molecule is a better candidate.

4.4. CONCLUSIONS

In summary, we have synthesized four novel viologen functionalized tetraphenylethylene (**TPE-V**) derivatives, which can replace the common DNA condensing agents like counter ions, cationic polymers, polyamines, etc., with an additional property of fluorescence-based tracking of the DNA condensation and gene-delivery process. In this chapter, we have demonstrated the CT-DNA binding, subsequent DNA condensation and cytotoxicity studies of these four **TPE-V** derivatives using optical, morphological and MTT assay techniques. UV-visible absorption studies showed a characteristic decrease in the 315 nm absorbance and slight enhancement in the fluorescence emission of **TPE-V** with the addition of CT-DNA up to a particular molar equivalent ratio, indicating the interaction of CT-DNA with **TPE-V** derivatives. In addition, the enhanced stability observed in the thermal denaturation studies and ICD band observed in the CD studies of CT-DNA in presence of **TPE-V** derivatives suggested the DNA condensation process. Further, the corresponding morphological analysis revealed the synergistic dis-assembly of the random aggregates of **TPE-V** derivatives and the fibrous CT-DNA structure in to an initial, partially condensed “beads on a string” type assembly at lower concentrations of **TPE-V**, and completely condensed compact DNA nanoparticles of 40-50 nm in size at higher concentrations of **TPE-V**. The role of positively charged viologen units in directing the DNA condensation process were verified by zeta-potential measurements and CB[8] encapsulation studies, which further confirmed the electrostatic interaction and groove binding induced effective DNA condensation process by **TPE-V** derivatives. The *in vitro* biological pertinence of **TPE-V/CT-DNA** condensates tested by performing MTT assay on A549 cancer and WI-38 normal cells revealed the non-toxic nature of **TPE-V1**, **TPE-V2** and **TPE-V3** CT-DNA

condensates, which implies the use of these **TPE-V** derivatives as non-viral DNA compaction agents in gene delivery applications. In short, this work highlights the development of small fluorescent organic chromophores, which can bind with DNA through non-covalent interactions like groove binding, electrostatic binding, etc., to achieve fluorescence-based tracking of the DNA condensation process and non-viral gene delivery.

4.5. EXPERIMENTAL SECTION

4.5.1. Materials and methods

All chemicals and solvents used for organic synthesis were purchased from Sigma Aldrich, Spectrochem and TCI, and were used without further purification. DMEM medium, Fetal Bovine Serum and Antibiotics used for growing cells were purchased from HiMedia and, MTT and HBSS used in MTT assay was purchased from Sigma Aldrich. A549 (human lung carcinoma) and WI-38 (Human normal lung fibroblast) were obtained from American Type Culture Collection (ATCC). TLC analysis were performed with Merck silica gel plates on aluminium sheets and column chromatography were performed using 230-400 mesh silica gel. ^1H NMR (500 MHz) and ^{13}C NMR (125 MHz) were performed in deuterated chloroform, methanol and DMSO with tetramethylsilane (TMS) ($\delta = 0$ ppm for ^1H and $\delta = 77$ ppm for ^{13}C) as an internal standard using Bruker Avance DPX spectrometer. Deionized Milli Q water (18.2 M Ω .cm) was used for all the studies.

CT-DNA samples were prepared by dissolving the commercially available (Sigma Aldrich) white fibrous mass in de-ionized Milli Q water. Initially, the solution was vortexed for 2-3 minutes and allowed to stand overnight at 0-4 °C to completely

dissolve the fibrous structure. Later, the samples were filtered through 0.45 mm syringe filters and concentrations were calculated using the average ϵ value ($6600 \text{ M}^{-1} \text{ cm}^{-1}$) of single nucleotide at 260 nm. All the DNA-binding studies described in this work are carried out in 10 mM Tris buffer containing 2mM NaCl.

The UV-visible absorption and fluorescence measurements were performed on Shimadzu UV-2600 spectrophotometer and SPEX FLUOROLOG-3 (FL3-221) spectrofluorimeter equipped with a 450 W Xenon arc lamp, respectively. All the optical measurements were carried out in 1 cm quartz cuvette at 25 ± 1 °C. UV-visible absorption and fluorescence emission studies of DNA binding experiment were carried out by the sequential addition of CT-DNA samples in to **TPE-V** derivatives in buffer. Ethidium bromide intercalation/displacement assays were performed in two ways. Initially by the sequential addition of **TPE-V/CT-DNA** complexes into EB solutions to check the intercalation possibilities of EB into CT-DNA structures in the **TPE-V/CT-DNA** complexes. And later by the addition of **TPE-V** derivatives into a EB intercalated CT-DNA complex to verify the condensation abilities of **TPE-V** derivatives. Fluorescence emission spectra of EB experiments were recorded using an excitation wavelength of 515 nm.

CD studies were performed at room temperature using Jasco J-810 spectropolarimeter and DLS analysis of the hydrodynamic size and zeta potential measurements were performed using Zetasizer (Malvern Nano ZS) operating with a He-Ne laser at a wavelength of 633 nm. 100 mM samples of CT-DNA and corresponding concentration ratios of **TPE-V** derivatives were used for CD and DLS measurements. In DLS analysis, each measurement was performed in triplicate, with 10-15 measurements in each run and the mean value is used to construct the plot of size, zeta-potential versus concentration of **TPE-V**.

4.5.2. AFM/TEM sample preparations

Samples for AFM analysis were prepared by drop-casting 5-7 μL solution over freshly cleaved mica surface, followed by slow air drying. The images were recorded at ambient conditions using a BRUKER MULTIMODE AFM operating in the tapping mode. NT-MDT-NSG series, TiN cantilever tips with 299 kHz resonance frequency was used for the analysis. TEM samples were prepared by drop-casting 20-30 μL samples over carbon coated copper grid (400 meshes, Ted Pella) and air dried for 2 days at ambient conditions followed by vacuum drying before imaging. TEM images were recorded with JEOL-JEM0310 microscope with an accelerating voltage of 100 kV and the samples were imaged using a Hamamatsu ORCA charge-coupled device (CCD) camera.

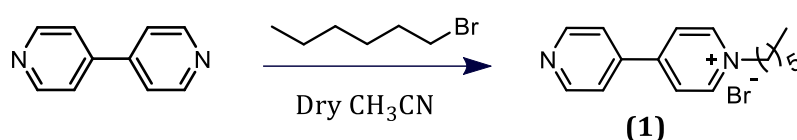
4.5.3. MTT assay

The cells were seeded at a density of 10000 cells per well in 100 μL complete DMEM medium, treated with 10% Fetal Bovine Serum and Antibiotic Antimycotic (100x diluted to 1x) in a flatbottom microtiter plate (96 well) and incubated for 24 hrs at 37 °C with 5 % CO_2 for cells to adhere. Later, cells were treated with 100 μL samples of CT-DNA (10 μM and 15 μM), **TPE-V1**, **TPE-V3** and **TPE-V4** (15 μM and 30 μM), **TPE-V2** (10 μM and 20 μM), 1:1 and 1:2 CT-DNA condensates of **TPE-V** derivatives (diluted in serum free DMEM medium) followed by further incubation for 24 hrs and 48 hrs separately. Afterwards, these cells were treated with 100 μL MTT (3-(4,5-dimethylthiazol-2-yl)-2,5-diphenyl tetrazolium bromide) solution in HBSS (Hanks' Balanced Salt solution, 0.5 mg/ml). After 3 hrs, the solution in the wells were removed and 100 μL DMSO was added to dissolve the formazan crystals formed in the wells. Formazan crystals were completely dissolved by giving a gentle

rocking to the culture plates for 20 minutes and using a microplate reader the optical density at 570 nm was measured. Using these values of optical density obtained from different wells, the relative cell viability was calculated (Absorbance of [treated/control] x 100).

4.5.4. Synthetic procedures and characterization details

4.5.4.1. Synthesis of 1-hexyl-([4, 4'-bipyridine]-1-ium)bromide, (1)⁴⁴

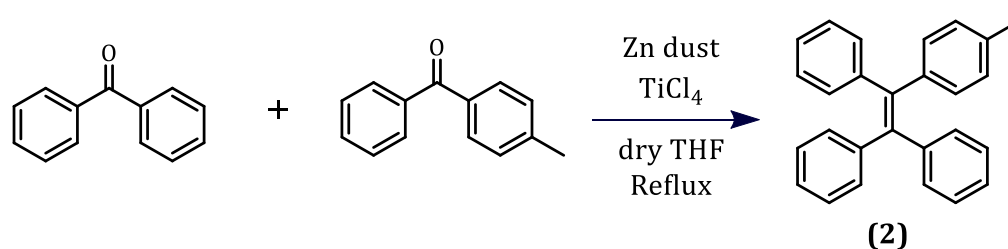


To a solution of 4,4'-bipyridine (2 g, 12.8 mmol) dissolved in 20 mL acetonitrile, 1-bromohexane (0.597 mL, 4.26 mmol) was added. The resultant solution was refluxed at 81 °C for 24 hrs. After cooling, the yellow precipitate formed was filtered and suspended in hot DMF. The mono alkylated product got dissolved in DMF, while the yellow insoluble di-alkylated product was removed by filtration. Ether was then added to the cooled solution of DMF to precipitate the pale-yellow mono-alkylated salt. Yield = 32% (0.8826 g).

¹H NMR (500 MHz, CD₃OD), δ (ppm): 9.032 (d, J = 5.5 Hz, 2H) 8.755 (d, J = 5.5 Hz, 2H), 8.438 (d, J = 6.5 Hz, 2H), 7.907 (d, J = 4.5 Hz, 2H), 4.607-4.578 (m, 2H), 2-1.955 (m, 2H), 1.360-1.202 (m, 6H), 0.860-0.833 (m, 3H). ¹³C NMR (125 MHz, CH₃OD), δ (ppm): 154.30, 150.41, 147.32, 142.89, 125.76, 122.16, 61.40, 31.04, 30.90, 25.49, 22.07, 12.86. HRMS (ESI): m/z calcd., for C₁₆H₂₁N₂, 241.17 [M]; found, 241.17 [M]⁺.

4.5.4.2. Synthesis of (2-(p-tolyl)ethene-1,1,2-triyl)tribenzene, (2)⁴⁵

Into a 250 ml three necked RB flask, 4-methylbenzophenone (3.0116 g, 15.2 mmol), benzophenone (2.8191 g, 15.2 mmol) and Zn dust (8.906 g, 136 mmol) were added. The flask was evacuated and flushed with argon 3 times. After the addition of dry THF (150 mL), reaction mixture was cooled in ice bath to 0 °C and TiCl₄ (7.5 mL, 68.4 mmol) was slowly injected. The mixture was stirred at room temperature for 30 minutes and then refluxed under argon condition for 48 hrs. The mixture was then extracted with ethyl acetate and organic part was dried over anhydrous Na₂SO₄. The crude product was purified by silica column chromatography using hexane as eluent to give a white solid. Yield = 73% (3.8796 g).

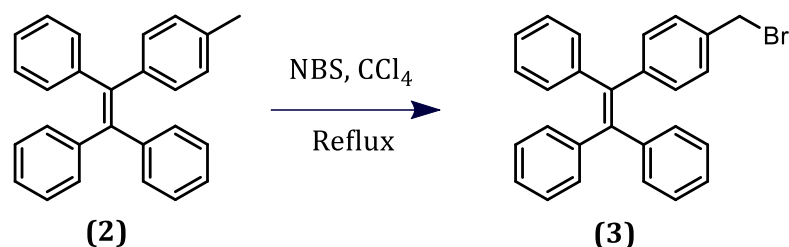


¹H NMR (500 MHz, CDCl₃), δ (ppm): 7.90 (s, 9H), 7.03-7.01 (m, 6H), 6.91-6.88 (m, 4H), 2.25 (s, 3H). ¹³C NMR (125 MHz, CDCl₃), δ (ppm): 143.72, 140.92, 140.72, 140.39, 136.05, 131.34, 128.37, 127.64, 126.4, 21.18. HRMS (ESI): m/z calcd., for C₂₇H₂₂, 346.46 [M]; found 346.17 [M]⁺.

4.5.4.3. Synthesis of (2-(4-(bromomethyl)phenyl)ethene-1,1,2-triyl)tribenzene, (3)

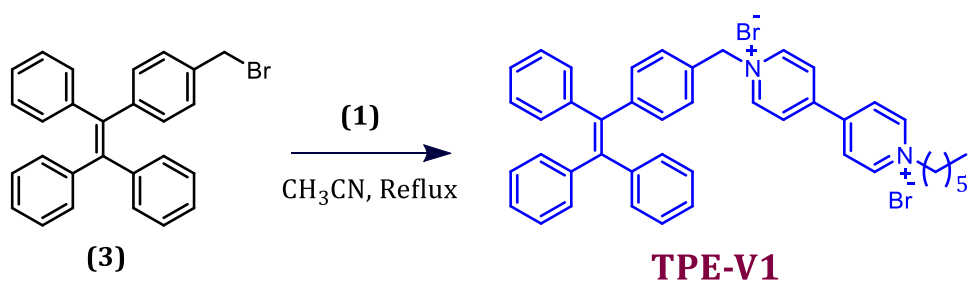
1 (1.5825 g, 4.4 mmol), freshly recrystallized NBS (0.9936 g, 5.1 mmol) and catalytic amount of BPO (0.015 g) were taken in a 100 mL RB flask and 60 mL of CCl₄ was added. The solution was refluxed for 24 hours before it was cooled to room temperature. The precipitate was filtered and washed with dichloromethane. The filtrate was extracted with dichloromethane, and the organic fraction was dried

under reduced pressure. The crude product thus obtained was further purified with silica gel (230-400 mesh) column chromatography using 2% ethyl acetate-hexane as eluent to yield a white solid. Yield = 28% (0.5381 g).



^1H NMR (500 MHz, CDCl_3), δ (ppm): 7.107-7.105 (m, 11H), 7.018-7.011 (m, 8H), 4.414 (s, 2H). ^{13}C NMR (125 MHz, CDCl_3), δ (ppm): 131.68, 131.34, 131.30, 128.42, 127.93, 127.75, 127.73, 127.66, 126.55, 33.65. HRMS (ESI): m/z calcd., for $\text{C}_{27}\text{H}_{21}\text{Br}$, 425.36 [M]; found 426.36 [M+1] $^+$.

4.5.4.4. Synthesis of [1-hexyl-1'-(4-(1,2,2-triphenylvinyl)phenyl)-(4,4'-bipyridine)-1,1'-dium] dibromide, (TPE-V1)

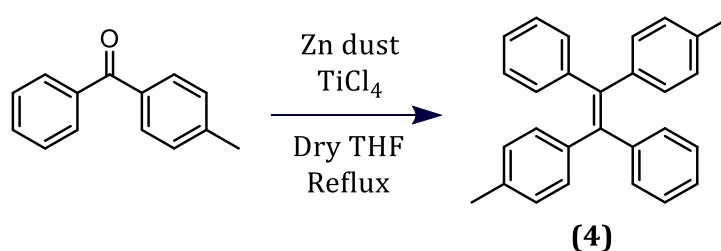


To a solution of **3** (0.538 g, 1.26 mmol) in acetonitrile (20 mL), **1** (0.3059 g, 1.26 mmol) was added and refluxed at 84 °C for 24 hrs. After cooling to room temperature, precipitated product was filtered, washed with acetonitrile and dried to give the product as pale-yellow powder. Yield = 79% (0.59 g).

^1H NMR (500 MHz, DMSO-d_6), δ (ppm): 9.412-9.355 (m, 4H), 8.755-8.724 (m, 4H), 7.325 (d, $J = 8$ Hz, 2H), 7.135-7.106 (m, 9H), 7.061 (d, $J = 8$ Hz, 2H), 6.979-6.965 (m,

2H), 6.950-6.936 (m, 4H), 5.834 (s, 2H), 4.681-4.652 (m, 2H), 1.958 (s, 2H), 1.292 (s, 6H), 0.872-0.859 (s, 3H). ^{13}C NMR (125 MHz, DMSO- d_6), δ (ppm): 146.16, 143.26, 131.78, 131.56, 131.34, 131.03, 130.97, 128.72, 123.54, 128.40, 128.31, 127.58, 127.19, 71.9, 61.8, 31.14, 31.01, 25.52, 22.32, 14.29. HRMS (ESI): m/z calcd., for $\text{C}_{43}\text{H}_{42}\text{N}_2^{2+}$, 586.33 [M]; found 745.16 [M+2Br+1] $^+$.

4.5.4.5. Synthesis of (E)-1,2-diphenyl-1,2-di-p-tolylolethene, (4)⁴⁶



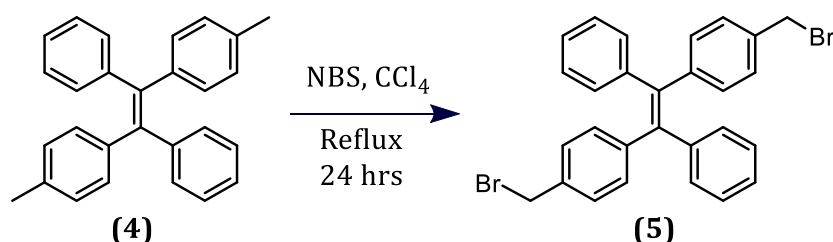
Reaction follows the same McMurry coupling procedure detailed as in the synthesis of **2**. 4-methylbenzophenone (2.01 g, 10 mmol), Zn dust (6.093 g, 91 mmol), TiCl_4 (5.02 mL, 45 mmol) and 120 mL of dry THF were used for this reaction. Using hexane as eluent, the crude product was purified by silica column chromatography to give the product as white solid. Yield = 53% (3.87 g).

^1H NMR (500 MHz, CDCl_3), δ (ppm): 7.01-6.93 (m, 10H), 6.84-6.81 (m, 8H), 2.19 (d, J = 10 Hz, 6H). ^{13}C NMR (125 MHz, CDCl_3), δ (ppm): 143.11, 139.87, 134.87, 130.33, 130.14, 127.35, 127.35, 126.57, 125.15, 20.18. HRMS (ESI): m/z calcd., for $\text{C}_{28}\text{H}_{24}$, 360.19 [M]; found 360.18 [M] $^+$.

4.5.4.6. Synthesis of (E)-1,2-bis(4-(bromomethyl)phenyl)-1,2-diphenylethene, (5)⁴⁶

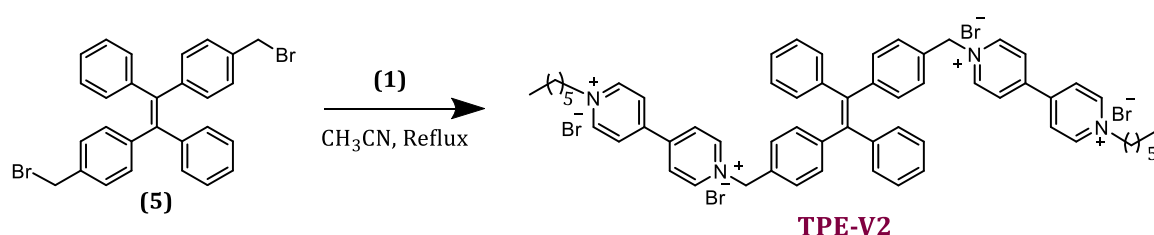
4 (1.532 g, 4.16 mmol), freshly recrystallized NBS (1.6095 g, 9.1 mmol) and catalytic amount of BPO (0.03 g) in 70 mL of CCl_4 were refluxed for 24 hrs. After

cooling, the precipitate was filtered and washed with DCM. The filtrate was extracted with DCM and concentrated under reduced pressure. The crude product was then purified using silica gel column (230-400 mesh) with hexane-ethyl acetate as an eluent to yield product as white solid. Yield = 12% (0.260 g).



^1H NMR (500 MHz, CDCl_3), δ (ppm): 7.108 (m, 10H), 7.000-6.966 (m, 8H), 4.411 (d, $J = 7$ Hz, 4H). ^{13}C NMR (125 MHz, CDCl_3), δ (ppm): 143.79, 143.19, 140.79, 135.83, 131.65, 131.31, 128.43, 127.84, 126.75, 33.60. HRMS (ESI): m/z calcd., for $\text{C}_{28}\text{H}_{22}\text{Br}_2$, 516.01 [M]; found 556.98 [M+K⁺⁺+1]⁺.

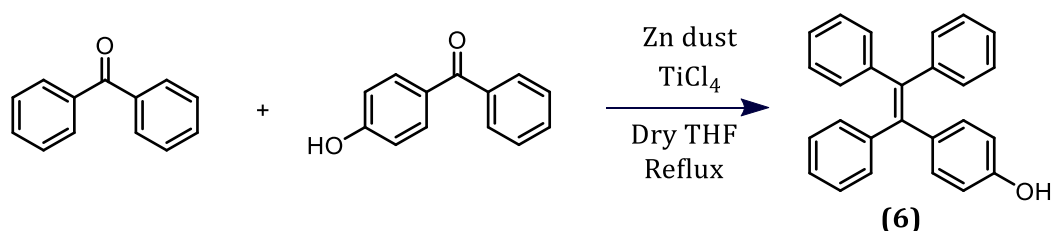
4.5.4.7. Synthesis of (E)-1',1'''-(((1,2-diphenylethene-1,2-diyl)bis(4,1-phenylene))bis(methylene))bis(1-hexyl-[4,4'-bipyridine]-1,1'-dium) tetrabromide, (TPE-V2)



A solution of **5** (0.241 g, 0.46 mmol) and **1** (0.168 g, 0.7 mmol) dissolved in dry acetonitrile (15 mL) was refluxed for 24 hrs. After cooling, precipitated product was filtered, washed with acetonitrile and dried to give product as bright yellow solid. Yield = 83% (0.325 g).

^1H NMR (500 MHz, DMSO- d_6), δ (ppm): 9.437 (d, $J = 16$ Hz, 8H), 8.799 (s, 8H), 7.348-7.126 (m, 8H), 7.109-7.033 (m, 3H), 6.979-6.912 (m, 7H), 5.861 (s, 4H), 4.688 (s, 4H), 1.962 (s, 4H), 1.292 (s, 12H), 0.871-0.858 (d, $J = 6.5$ Hz, 6H). ^{13}C NMR (125 MHz, DMSO- d_6), δ (ppm): 149.63, 146.33, 141.21, 140.03, 137.61, 134.32, 132.67, 128.74, 128.41, 128.5, 127.60, 127.19, 71.82, 61.36, 31.17, 31.04, 25.54, 22.34, 14.31. HRMS (ESI): m/z calcd., for $\text{C}_{60}\text{H}_{64}\text{N}_4^{4+}$, 840.51 [M]; found 886.79 [M+2Na] $^+$.

4.5.4.8. Synthesis of 4-(1,2,2-triphenylvinyl)phenol, (6)

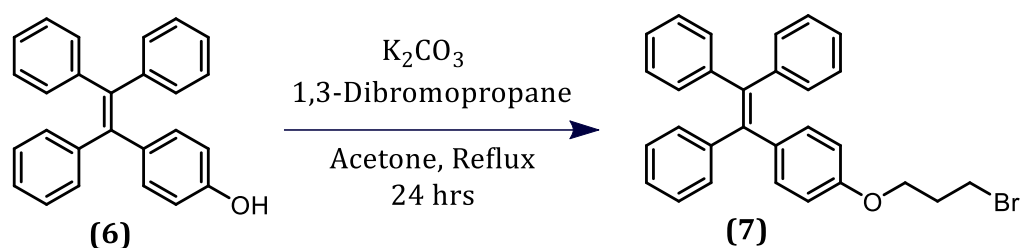


Similar procedure as in the synthesis of **2** was followed using benzophenone (4 g, 21.9 mmol) and 4-hydroxybenzophenone (4.32 g, 21.9 mmol) as the two coupling ketones for this McMurry reaction. Zinc dust (12.8 g, 190 mmol), TiCl₄ (10.738 mL, 98 mmol) and dry THF (180 mL) were added. After reaction, the crude product was purified by silica column chromatography using 10% ethyl acetate-hexane as the eluent to give an off white solid. Yield = 31% (2.359 g).

^1H NMR (500 MHz, CDCl₃), δ (ppm): 7.117-7.072 (m, 9H), 7.038-6.997 (m, 6H), 6.895 (d, $J = 8.5$ Hz, 2H), 6.571 (d, $J = 8$ Hz, 2H), 4.755 (s, 1H). ^{13}C NMR (125 MHz, CDCl₃), δ (ppm): 154.05, 144.00, 143.90, 140.43, 140.19, 136.35, 132.73, 131.36, 131.32, 127.70, 127.60, 126.38, 126.26, 114.58. HRMS (ESI): m/z calcd., for $\text{C}_{26}\text{H}_{20}\text{O}$, 348.15 [M]; found, 348.15 [M] $^+$.

4.5.4.9. Synthesis of (2-(4-(3-bromopropoxy)phenyl)ethene-1,1,2-triyl)tri-benzene, (7)

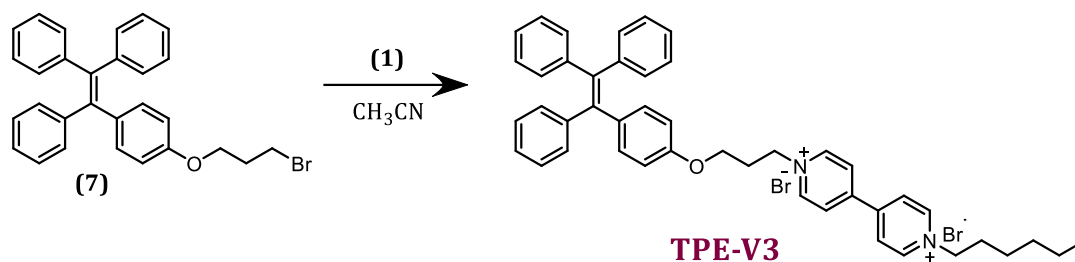
Into a 100 mL two-necked RB flask **6** (0.75 g, 2.15 mmol), K_2CO_3 (0.891 g, 6.45 mmol) and 30 mL acetone was added and stirred for 30 minutes at room temperature. 1,3-Dibromopropane (0.2195 mL, 2.15 mmol) was added dropwise to this mixture and refluxed for 24 hrs. After the reaction mixture was cooled to room temperature, K_2CO_3 was filtered off and the crude product was purified using silica column chromatography using 2% ethyl acetate-hexane as the eluent to give pale yellow viscous oil. Yield = 40% (0.4 g).



^1H NMR (500 MHz, CDCl_3), δ (ppm): 7.073-7.035 (m, 9H), 7.020-6.999 (m, 6H), 6.936 (d, $J = 8.5$ Hz, 2H), 6.641 (d, $J = 9$ Hz, 2H), 4.033-4.010 (m, 2H), 3.589-3.563 (m, 2H), 2.300-2.251 (m, 2H). ^{13}C NMR (125 MHz, CDCl_3), δ (ppm): 157.21, 144.01, 143.96, 140.47, 140.19, 136.41, 132.56, 131.38, 131.32, 127.73, 127.60, 126.36, 126.27, 113.64, 65.16, 32.48, 29.71. HRMS (ESI): m/z calcd., for $\text{C}_{29}\text{H}_{25}\text{BrO}$, 468.11 [M]; found, 468.10 [M] $^+$.

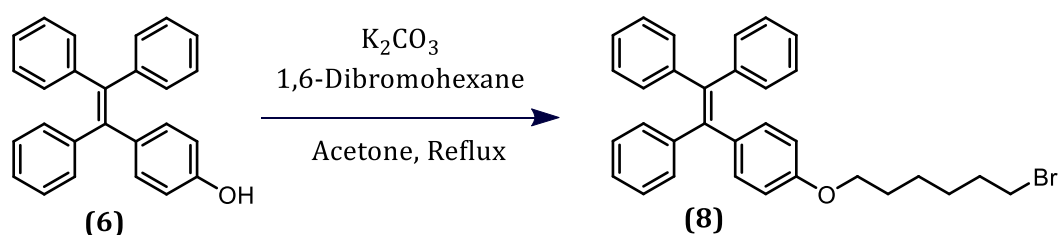
4.5.4.10. Synthesis of [1-hexyl-1'-(3-(4-(1,2,2-triphenylvinyl)phenoxy)propyl)-[4,4'-bipyridine]-1,1'-dium] dibromide, (TPE-V3)

To a solution of **7** (0.4 g, 0.854 mmol) in 15 mL acetonitrile, **1** (0.246 g, 1.02 mmol) was added and refluxed at 84 °C for 72 hrs. Precipitated product was filtered, washed with acetonitrile and dried to give a sandy powder. Yield = 27% (0.144 g).



^1H NMR (500 MHz, DMSO- d_6), δ (ppm): 9.409-9.361 (m, 4H), 8.739 (s, 4H), 7.145-7.067 (m, 9H), 6.951-6.904 (m, 6H), 6.824 (d, $J = 8.5$ Hz, 2H), 6.560 (d, $J = 8.5$ Hz, 2H), 4.850 (m, 2H), 4.689-4.660 (m, 2H), 4.050 (m, 2H), 3.463 (m, 2H), 1.964 (m, 2H), 1.301-1.294 (m, 6H), 0.861 (m, 3H). ^{13}C NMR (125 MHz, DMSO- d_6), δ (ppm): 146.57, 146.22, 143.89, 143.84, 143.78, 140.49, 140.27, 136.17, 132.35, 131.10, 128.35, 128.27, 127.07, 126.98, 126.90, 126.83, 114.04, 65.37, 61.36, 59.59, 31.20, 31.04, 30.41, 25.55, 22.35, 14.32. HRMS (ESI): m/z calcd., for $\text{C}_{45}\text{H}_{46}\text{N}_2\text{O}_2^{2+}$, 630.36[M]; found, 630.36 [M] $^+$.

4.5.4.11. Synthesis of (2-(4-((6-bromohexyl)oxy)phenyl)ethene-1,1,2-triyl)tri benzene, (8)

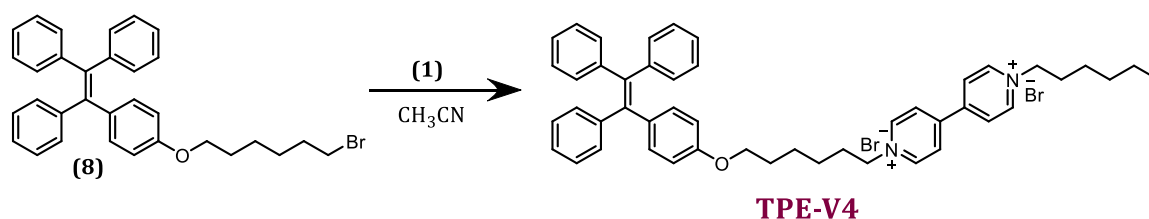


Into a 100 mL two-necked RB flask **6** (1 g, 2.87 mmol), K_2CO_3 (1.19 g, 8.61 mmol) and 35 mL acetone was added and stirred for 30 minutes. 1,3-Dibromohexane (0.441 mL, 2.87 mmol) was introduced dropwise into this mixture and refluxed for 24 hrs. After the mixture was cooled to room temperature, excess K_2CO_3 was removed by filtration and the crude reaction mixture was purified using

silica column chromatography using 2% ethyl acetate-hexane as the eluent to give a pale-yellow viscous oil. Yield = 41% (0.595 g).

^1H NMR (500 MHz, CDCl_3), δ (ppm): 7.104-7.084 (m, 9H), 7.071-7.035 (m, 6H), 6.924 (d, $J = 8.5$ Hz, 2H), 6.626 (d, $J = 8.5$ Hz, 2H), 3.890-3.865 (m, 2H), 3.431-3.403 (m, 2H), 1.896-1.868 (m, 4H), 1.764-1.736 (m, 2H), 1.286-1.253 (m, 2H). ^{13}C NMR (125 MHz, CDCl_3), δ (ppm): 157.61, 144.07, 144.02, 140.59, 140.04, 136.01, 132.52, 131.40, 131.36, 127.71, 127.59, 126.33, 126.21, 113.58, 67.54, 33.77, 32.69, 29.13, 27.95, 25.32. HRMS (ESI): m/z calcd., for $\text{C}_{32}\text{H}_{31}\text{BrO}$, 510.15 [M]; found, 510.15 [M] $^+$.

4.5.4.12. Synthesis of [1-hexyl-1'-(6-(4-(1,2,2-triphenylvinyl)phenoxy)hexyl)-[4,4'-bipyridine]-1,1'-diium] dibromide, (TPE-V4)



To a solution of **8** (0.595 g, 1.17 mmol) in 20 mL acetonitrile, **1** (0.338 g, 1.40 mmol) was added and refluxed at 84 °C for 72 hours. Precipitated product was filtered, washed with acetonitrile and dried to give the product as sandy colored powder. Yield = 17 % (0.133 g).

^1H NMR (500 MHz, DMSO-d_6), δ (ppm): 9.365 (d, $J = 5$ Hz, 4H), 8.758 (d, $J = 6.5$ Hz, 4H), 7.138-7.081 (m, 9H), 6.972-6.915 (m, 6H), 6.847 (d, $J = 8.5$ Hz, 2H), 6.666 (d, $J = 8.5$ Hz, 2H), 4.684-4.655 (m, 4H), 3.874-3.849 (m, 2H), 1.999-1.969 (m, 4H), 1.678-1.651 (m, 2H), 1.493-1.424 (m, 2H), 1.366-1.351 (m, 2H), 1.294 (m, 6H), 0.875-0.848 (m, 3H). ^{13}C NMR (125 MHz, DMSO-d_6), δ (ppm): 157.59, 149.15, 146.17, 143.98, 143.90, 143.84, 140.64, 140.17, 135.76, 132.35, 131.08, 128.33, 128.24, 127.09,

126.95, 126.85, 114.12, 67.54, 61.45, 61.40, 31.15, 31.01, 28.89, 25.66, 25.53, 25.45, 22.31, 14.28, 2.25. HRMS (ESI); m/z calcd., for $C_{48}H_{52}N_2O_2^{2+}$, 672.40 [M]; found, 672.40 [M]⁺.

4.6. REFERENCES

- 1) Bloomfield, V. A. DNA condensation. *Curr. Opin. Struct. Biol.* **1996**, *6*, 334-341.
- 2) Bloomfield, V. A. DNA condensation by multivalent cations. *Biopolymers.* **1997**, *44*, 269-282.
- 3) Estévez-Torres, A.; Baigl, D. DNA compaction: fundamentals and applications. *Soft Matter.* **2011**, *7*, 6746-6756.
- 4) Gonzalez-Perez, A.; Dias, R. S. Different strategies for controlling DNA conformation: compaction and decompaction. *Frontiers in bioscience (Elite edition).* **2009**, *1*, 228-241.
- 5) Arakawa, H.; Ahmad, R.; Naoui, M.; Tajmir-Riahi, H. A. A comparative study of calf thymus DNA binding to Cr(III) and Cr(VI) ions. Evidence for the guanine N-7-chromium-phosphate chelate formation. *J. Biol. Chem.* **2000**, *275*, 10150-10153.
- 6) Gosule, L. C.; Schellman, J. A. Compact form of DNA induced by spermidine. *Nature.* **1976**, *259*, 333-335.
- 7) Baigl, D.; Yoshikawa, K. Dielectric Control of Counterion-Induced Single-Chain Folding Transition of DNA. *Biophys. J.* **2005**, *88*, 3486-3493.
- 8) Cao, M.; Wang, Y.; Zhao, W.; Qi, R.; Han, Y.; Wu, R.; Wang, Y.; Xu, H. Peptide-Induced DNA Condensation into Virus-Mimicking Nanostructures. *ACS Appl. Mater. Interfaces.* **2018**, *10*, 24349-24360.
- 9) Huang, Y.-C.; Su, C.-J.; Chen, C.-Y.; Chen, H.-L.; Jeng, U. S.; Berezhnoy, N. V.; Nordenskiöld, L.; Ivanov, V. A. Elucidating the DNA-Histone Interaction in Nucleosome from the DNA-Dendrimer Complex. *Macromolecules.* **2016**, *49*, 4277-4285.
- 10) Fan, Y.; Wang, H.; He, C.; Qiao, F.; Wang, S.; Wang, Y. DNA Condensation Induced by a Star-Shaped Hexameric Cationic Surfactant. *ACS Appl. Mater. Interfaces.* **2017**, *9*, 23333-23341.

- 11) Ganguli, M.; Babu, J. V.; Maiti, S. Complex Formation between Cationically Modified Gold Nanoparticles and DNA: An Atomic Force Microscopic Study. *Langmuir*. **2004**, *20*, 5165-5170.
- 12) Liu, Y.; Yu, Z.-L.; Zhang, Y.-M.; Guo, D.-S.; Liu, Y.-P. Supramolecular Architectures of β -Cyclodextrin-Modified Chitosan and Pyrene Derivatives Mediated by Carbon Nanotubes and Their DNA Condensation. *J. Am. Chem. Soc.* **2008**, *130*, 10431-10439.
- 13) Gupta, S.; Tiwari, N.; Munde, M. A Comprehensive Biophysical Analysis of the Effect of DNA Binding Drugs on Protamine-induced DNA Condensation. *Sci. Rep.* **2019**, *9*, 5891.
- 14) Matulis, D.; Rouzina, I.; Bloomfield, V. A. Thermodynamics of Cationic Lipid Binding to DNA and DNA Condensation: Roles of Electrostatics and Hydrophobicity. *J. Am. Chem. Soc.* **2002**, *124*, 7331-7342.
- 15) Zinchenko, A. A.; Yoshikawa, K.; Baigl, D. Compaction of Single-Chain DNA by Histone-Inspired Nanoparticles. *Phys. Rev. Lett.* **2005**, *95*, 228101.
- 16) Zinchenko, A. A.; Sakaue, T.; Araki, S.; Yoshikawa, K.; Baigl, D. Single-Chain Compaction of Long Duplex DNA by Cationic Nanoparticles: Modes of Interaction and Comparison with Chromatin. *J. Phys. Chem. B.* **2007**, *111*, 3019-3031.
- 17) Hayakawa, K.; Santerre, J. P.; Kwak, J. C. T. Study of surfactant-polyelectrolyte interactions. Binding of dodecyl- and tetradecyltrimethylammonium bromide by some carboxylic polyelectrolytes. *Macromolecules*. **1983**, *16*, 1642-1645.
- 18) Marchetti, S.; Onori, G.; Cametti, C. DNA Condensation Induced by Cationic Surfactant: A Viscosimetry and Dynamic Light Scattering Study. *J. Phys. Chem. B.* **2005**, *109*, 3676-3680.
- 19) Dias, R.; Rosa, M.; Pais, A. C.; Miguel, M.; Lindman, B. DNA-Surfactant Interactions. Compaction, Condensation, Decompaction and Phase Separation. *J. Chin. Chem. Soc.* **2004**, *51*, 447-469.
- 20) Diguët, A.; Mani, N. K.; Geoffroy, M.; Sollogoub, M.; Baigl, D. Photosensitive Surfactants with Various Hydrophobic Tail Lengths for the Photocontrol of Genomic DNA Conformation with Improved Efficiency. *Chem. Eur. J.* **2010**, *16*, 11890-11896.

- 21) Rudiuk, S.; Yoshikawa, K.; Baigl, D. Enhancement of DNA compaction by negatively charged nanoparticles. Application to reversible photocontrol of DNA higher-order structure. *Soft Matter*. **2011**, *7*, 5854-5860.
- 22) Cassell, A. M.; Scrivens, W. A.; Tour, J. M. Assembly of DNA/Fullerene Hybrid Materials. *Angew. Chem. Int. Ed.* **1998**, *37*, 1528-1531.
- 23) Nitta, H.; Minami, K.; Harano, K.; Nakamura, E. DNA Binding of Pentaamino [60]fullerene Synthesized Using Click Chemistry. *Chem. Lett.* **2015**, *44*, 378-380.
- 24) Mondal, J. H.; Pramanik, B.; Shinde, M. N.; Khurana, R.; Barooah, N.; Bhasikuttan, A. C.; Das, D.; Mohanty, J. DNA-Induced Novel Optical Features of Ethyl Viologen-Tethered Perylenediimide Triad. *J. Phys. Chem. C*. **2018**, *122*, 18061-18069.
- 25) Minami, K.; Okamoto, K.; Doi, K.; Harano, K.; Noiri, E.; Nakamura, E. siRNA delivery targeting to the lung via agglutination-induced accumulation and clearance of cationic tetraamino fullerene. *Sci. Rep.* **2014**, *4*, 4916.
- 26) Yan, H.; Li, Z.-F.; Guo, Z.-F.; Lu, Z.-L.; Wang, F.; Wu, L.-Z. Effective and reversible DNA condensation induced by bifunctional molecules containing macrocyclic polyamines and naphthyl moieties. *Biorg. Med. Chem.* **2012**, *20*, 801-808.
- 27) Liu, Y.; Yu, L.; Chen, Y.; Zhao, Y.-L.; Yang, H. Construction and DNA Condensation of Cyclodextrin-Based Polypseudorotaxanes with Anthryl Grafts. *J. Am. Chem. Soc.* **2007**, *129*, 10656-10657.
- 28) Nakamura, E.; Isobe, H. In vitro and in vivo gene delivery with tailor-designed aminofullerenes. *Chem. Rec.* **2010**, *10*, 260-270.
- 29) Minami, K.; Okamoto, K.; Harano, K.; Noiri, E.; Nakamura, E. Hierarchical Assembly of siRNA with Tetraamino Fullerene in Physiological Conditions for Efficient Internalization into Cells and Knockdown. *ACS Appl. Mater. Interfaces*. **2018**, *10*, 19347-19354.
- 30) Vittala, S. K.; Saraswathi, S. K.; Joseph, J. Fullerene Cluster Assisted Self-Assembly of Short DNA Strands into Semiconducting Nanowires. *Chem. Eur. J.* **2017**, *23*, 15759-15765.
- 31) Vittala, S. K.; Saraswathi, S. K.; Ramesan, A. B.; Joseph, J. Nanosheets and 2-D Networks by Mutually Assisted Self-Assembly of Fullerene Clusters and DNA Three-way Junctions. *Nanoscale Adv.* **2019**.
- 32) Kulala Vittala, S.; Joseph, J. Chiral self-assembly of fullerene clusters on CT-DNA templates. *Faraday Discuss.* **2018**, *207*, 459-469.

- 33) Zhang, R.; Kwok, R. T. K.; Tang, B. Z.; Liu, B. Hybridization induced fluorescence turn-on of AIEgen-oligonucleotide conjugates for specific DNA detection. *Rsc Adv.* **2015**, *5*, 28332-28337.
- 34) Lou, X.; Leung, C. W. T.; Dong, C.; Hong, Y.; Chen, S.; Zhao, E.; Lam, J. W. Y.; Tang, B. Z. Detection of adenine-rich ssDNA based on thymine-substituted tetraphenylethene with aggregation-induced emission characteristics. *Rsc Adv.* **2014**, *4*, 33307-33311.
- 35) Krishnan, N.; Golla, M.; Thelu, H. V. P.; Albert, S. K.; Atchimnaidu, S.; Perumal, D.; Varghese, R. Self-assembly of DNA-tetraphenylethylene amphiphiles into DNA-grafted nanosheets as a support for the immobilization of gold nanoparticles: a recyclable catalyst with enhanced activity. *Nanoscale.* **2018**, *10*, 17174-17181.
- 36) Rothenbühler, S.; Iacovache, I.; Langenegger, S. M.; Zuber, B.; Häner, R. Supramolecular assembly of DNA-constructed vesicles. *Nanoscale.* **2020**, *12*, 21118-21123.
- 37) Geng, W.-C.; Liu, Y.-C.; Zheng, Z.; Ding, D.; Guo, D.-S. Direct visualization and real-time monitoring of dissipative self-assembly by synchronously coupled aggregation-induced emission. *Mater. Chem. Front.* **2017**, *1*, 2651-2655.
- 38) Zhang, T.; Sun, S.; Liu, F.; Pang, Y.; Fan, J.; Peng, X. Interaction of DNA and a series of aromatic donor-viologen acceptor molecules with and without the presence of CB[8]. *PCCP.* **2011**, *13*, 9789-9795.
- 39) Hvastkovs, E. G.; Buttry, D. A. Minor Groove Binding of a Novel Tetracationic Diviologen. *Langmuir.* **2006**, *22*, 10821-10829.
- 40) Joseph, J.; Eldho, N. V.; Ramaiah, D. Control of Electron-Transfer and DNA Binding Properties by the Tollyl Spacer Group in Viologen Linked Acridines. *J. Phys. Chem. B.* **2003**, *107*, 4444-4450.
- 41) Kypr, J.; Kejnovská, I.; Renčíuk, D.; Vorlíčková, M. Circular dichroism and conformational polymorphism of DNA. *Nucleic Acids Res.* **2009**, *37*, 1713-1725.
- 42) Szumilak, M.; Merez, A.; Strek, M.; Stanczak, A.; Inglot, T. W.; Karwowski, B. T. DNA Interaction Studies of Selected Polyamine Conjugates. *Int. J. Mol. Sci.* **2016**, *17*, 1560.
- 43) Cain, B. F.; Baguley, B. C.; Denny, W. A. Potential antitumor agents. 28. Deoxyribonucleic acid polyintercalating agents. *J. Med. Chem.* **1978**, *21*, 658-668.

-
- 44) Causin, V.; Saielli, G. Effect of asymmetric substitution on the mesomorphic behaviour of low-melting viologen salts of bis(trifluoromethanesulfonyl) amide. *J. Mater. Chem.* **2009**, *19*, 9153-9162.
- 45) Ma, L.; Wang, S.; Li, C.; Cao, D.; Li, T.; Ma, X. Photo-controlled fluorescence on/off switching of a pseudo[3]rotaxane between an AIE-active pillar[5]arene host and a photochromic bithienylethene guest. *Chem. Commun.* **2018**, *54*, 2405-2408.
- 46) Liang, J.; Shi, H.; Kwok, R. T. K.; Gao, M.; Yuan, Y.; Zhang, W.; Tang, B. Z.; Liu, B. Distinct optical and kinetic responses from E/Z isomers of caspase probes with aggregation-induced emission characteristics. *J. Mater. Chem. B.* **2014**, *2*, 4363-4370.

ABSTRACT

Name of the Student: **Ms. Sajena K. S.**
Faculty of Study: Chemical Sciences
AcSIR academic centre/CSIR Lab: CSIR-National
Institute for Interdisciplinary Science
and Technology (CSIR-NIIST)

Registration No.: 10CC15A39003
Year of Submission: 2021

Name of the Supervisor: Dr. Joshy Joseph

Title of the thesis: **DNA-Interactions, Self-Assembly and Photophysical Properties of DNA Three-way Junction Templated Fluorescent Silver Nanoclusters and Functional Tetraphenylethylene Derivatives**

Development of functional materials with precision and programmability in the molecular level is accomplished by following the nature's concept of using non-covalent interactions to achieve complexity. The unique double helical structure and hydrogen bonding property of DNA and its building blocks makes them superior over other various biological templates used in the bottom-up construction of functional supramolecular assemblies. In the **First Chapter**, we summarize the recent progress in the construction of self-assembled structures from DNA and nucleobase derivatives, the key challenges in this area, origin and major objectives of the present thesis.

Cytosine rich DNA templated fluorescent AgNCs are promising fluorophores in sensing and bioimaging applications. In the **Second Chapter**, we describe the construction of a DNA-3WJ with a central cytosine loop for templating AgNCs, which offers the free duplex branches for multi-templating applications. **3WJ20-C12** comprising of 12 cytosine bases in the center of DNA-3WJ, forms fluorescent AgNCs with 630 nm emission maxima and 12% fluorescence quantum yield. On the other hand, **3WJ20-C6** and the ones without cytosine loop, **3WJ20** failed to form fluorescent AgNCs, confirming the requirement of central unhybridized cytosine bases to stabilize AgNCs. In addition, we also demonstrate, (i) the influence of the size of duplex arms and size of cytosine-loop on the fluorescent properties of AgNCs, and (ii) the selectivity of **3WJ20-C12/AgNCs** towards Hg²⁺ ions.

In the **third Chapter**, we employed the precise hydrogen bonding property of nucleobase and nucleobase analogues for the construction of ordered 1D assemblies of the AIE active TPE chromophore, which otherwise could result in the formation of random aggregates. In **Part A**, we describe the synthesis, AIE properties in THF-water system and self-assembly of a diaminotriazine functionalized TPE derivative, **TPE-1**. In dodecane, **TPE-1** self-assembles through cooperative pathway and forms blue emissive 1D-fibers with characteristic 307 nm absorption 430 nm emission band at lower concentrations and forms transparent supramolecular gels at higher concentrations. We also demonstrate the competitive complementary H-bonding assisted transition of the blue emissive aggregates to green emissive aggregates using a thymine derivative, **T-C12**. Detailed characteristics and mechanism of self-assembly are explained in this chapter. In **Part B**, to verify the proposed mechanism of this **TPE-1** self-assembly, three more TPE-DAT derivatives (**TPE-2**, **TPE-3** and **TPE-4**) were synthesized by changing the alkoxy substitutions, and their optical, morphological, gelation properties and interactions with dT₂₀ were investigated and explained in detail.

Development of small organic chromophores with DNA interaction, subsequent DNA condensation and absorbance/fluorescence-based tracking of the gene delivery process are in the emerging stages. In **Chapter four**, we describe the synthesis, AIE properties, CT-DNA interaction and condensation properties of four novel viologen functionalized TPE derivatives (**TPE-V1-4**). Optical and morphological studies revealed the electrostatic interaction of positively charged **TPE-V** derivatives with negatively charged CT-DNA, leading to the condensation of its fibrous network structure to an initial "beads on a string type" assembly and subsequent change to 40-50 nm sized spherical **TPE-V/CT-DNA** condensates. Moreover, cytotoxicity studies performed on normal and cancer cell lines with the CT-DNA condensates of **TPE-V1**, **TPE-V2** and **TPE-V3** disclosed the non-toxic nature of these **TPE-V** derivatives and hence could be employed as non-viral gene-delivery vectors.

List of Publications

Related to Thesis

1. **Sajena K. Saraswathi**, Sandeepa K. Vittala, Mathews K. Manayani, Joshy Joseph*, Sequence Programmed DNA Three-Way Junctions for Templated Assembly of fluorescent Silver Nanoclusters. *J. Photochem. Photobiol. B, Biol.*, **2020**, *207*, 111886.

Manuscripts Under Preparation

1. **Sajena K. Saraswathi** and Joshy Joseph*, 1D-Organization of a Diaminotriazine Appended Tetraphenylethylene-Derivative: Thymine-Induced Transition of Blue to Green emissive Molecular Aggregates.
2. **Sajena K. Saraswathi** and Joshy Joseph*, DNA Condensation Triggered by the Synergistic Self-assembly of Tetraphenylethylene-viologen Aggregates and CT-DNA.

From Other Related Works

1. Sandeepa K. Vittala, **Sajena K. Saraswathi**, Anjali Bindu Ramesan, and Joshy Joseph*, Nanosheets and 2D-Nanonetworks by Mutually Assisted Self-Assembly of Fullerene Clusters and DNA Three-way Junctions. *Nanoscale adv.*, **2019**, *1*, 4158-4165.
2. Sandeepa K. Vittala, **Sajena K. Saraswathi** and Joshy Joseph*, Fullerene Cluster Assisted Self-Assembly of Short DNA Strands into Semiconducting Nanowires. *Chem. Eur. J.*, **2017**, *1*, 15759-15765.

Book Chapter

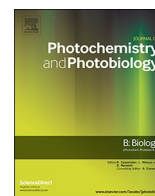
1. Sandeepa K. Vittala, **Sajena K. Saraswathi** and Joshy Joseph*, Self-assembled Functional Fullerenes and DNA Hybrid Nanomaterials for Various Applications. Chapter 8., Editor: T. Govindaraju, 'Templated DNA Nanotechnology: Functional Nucleic Acid Nanoarchitectures'. *Jenny Stanford Publishing.*, 1st edition, **2019**.

List of Posters and Papers Presented in Conferences

1. One-Dimensional Self-Assembly of Tetraphenylethylene Derivatives and Thymine Induced Transition of their Molecular Aggregates. **Sajena K. S.** and Joshy Joseph. **Paper** presented for MRSI-International Symposium on Advanced Materials (ISAM-2021) through MS Teams online platform, March 26-27, 2021.
2. Tuning the Self-Assembly and Aggregation Induced Emission Behaviour of Tetraphenylethylene Derivatives. **Sajena K. S.** and Joshy Joseph. **Paper** presented for International Conference on Materials for the Millennium (MatCon-2021) through Zoom online platform, March 15-19, 2021.
3. Water Soluble Tetraphenylethylene-Viologen Derivatives: Interactions with CT-DNA. **Sajena K. S.**, Kavya. J. M. and Joshy Joseph. **Poster** presented at the 15th DAE-BRNS Biennial Trombay Symposium on Radiation & Photochemistry (TSRP-2020), DAE Convention Centre, BARC, Mumbai, January 5-9, 2020.
4. Design, Synthesis and Investigation of the Nucleotide Assisted Self-assembly of Tetraphenylethylene-Diaminotriazine Derivatives. **Sajena K. S.**, Navaneetha P. and Joshy Joseph. **Poster** presented at the Inter Institutional Students Conference on Sustainable Chemistry for Health, Environment and Materials (Su-CHEM YUVA 2019), CSIR- Indian Institute of Chemical Technology, Hyderabad, July 24-26, 2019.
5. Fluorescent Silver Nanoclusters Templated by DNA Three-way Junction Nanostructures: Synthesis, Characterization and Applications. **Sajena K. S.**, Sandeepa K. V., Sreejith M. and Joshy Joseph. **Poster** presented at the First Indian Materials Conclave and 30th AGM of MRSI, Indian Institute of Science, Bangalore, February 12-15, 2019.
6. Design, Synthesis and Investigation of Hydrogen Bonding Directed Supramolecular Self-assembly of Tetraphenylethylene-Diaminotriazine Derivatives. **Sajena K. S.** and Joshy Joseph. **Poster** presented at the Second International Symposium on New Trends in Applied Chemistry (NTAC-2019), Sacred Heart College, Thevara, January 14-15, 2019.

7. DNA Three-Way Junction Templated Fluorescent Silver Nanoclusters: A Selective Label Free Sensor for Mercury (II) ions. **Sajena K. S.**, Sandeepa K. V., Sreejith M. and Joshy Joseph. **Paper** presented at the International Conference on Recent Trends in Materials Science and Technology (ICMST 2018), Indian Institute of Space Science and Technology, Thiruvananthapuram, October 10-13, 2018.

8. Fluorescent silver nanoclusters templated by DNA three-way Junction for selective detection of mercury ions. **Sajena K. S.** and Joshy Joseph. **Poster** presented at the 13th Kerala Science Congress, Government Brennen College, Kannur, January 28-30, 2017.



Sequence programmed DNA three-way junctions for templated assembly of fluorescent silver nanoclusters

Sajena Kanangat Saraswathi^{a,b}, Sandeepa Kulala Vittala^{a,b}, Mathews Kuruville Manayani^{a,b},
Joshy Joseph^{a,b,*}

^a Photosciences and Photonics Section, CSIR-National Institute for Interdisciplinary Science and Technology, Thiruvananthapuram 695 019, India

^b Academy of Scientific and Innovative Research (AcSIR), Ghaziabad 201002, India

ARTICLE INFO

Keywords:

DNA-3WJs
Sequence programming
Cytosine loop
Fluorescent AgNCs
DNA
Nanotechnology

ABSTRACT

Fluorescent silver nanoclusters (AgNCs) templated by DNA are promising label free fluorophores with excellent photostability and tunable optical properties. Most of the reported DNA-nanocluster fluorescent tags comprise of programmed strands for the cluster formation either on the edges as overhangs or as loops on the duplex strands. Herein, we report a design strategy for sequence programmed, DNA three-way junctions (DNA-3WJ), comprising of unhybridized cytosine nucleobases in the 3WJ-center, capable of binding to silver ions and stabilizing the AgNCs. The formation of AgNCs in these DNA-3WJs were confirmed by various spectroscopic and microscopic techniques. 3WJ20-C12 comprising of 12 cytosine bases in the center of the DNA-3WJ, form fluorescent nanoclusters with an emission maximum around 630 nm and 12% fluorescence quantum yield. Control DNA-3WJs with six cytosine bases in the center (3WJ20-C6) and ones without cytosine bases (3WJ20) failed to form fluorescent AgNCs confirming the requirement of central, unhybridized cytosine bases for the stabilization of the nanoclusters. Further, the duplex arms of DNA-3WJs were shown to influence the fluorescent properties of AgNCs by varying the size and stability of the cytosine-loop structure of DNA-3WJs. Metal ion interaction studies shows the selectivity of the 3WJ20-C12/AgNCs towards Hg^{2+} with sensitivity in the nanomolar range.

1. Introduction

Fluorescent metal nanoclusters comprising 2–20 metal atoms in the sub-nanometer size are emerging competitors for typical fluorophores like organic dyes, quantum dots and fluorescent proteins [1,2]. Metal nanoclusters, because of its small size have discrete electronic energy levels like molecules and displays distinct optical spectra, strong fluorescence emission and well separated highest occupied molecular orbital - lowest unoccupied molecular orbital (HOMO-LUMO) [3]. Among the various metal nanoclusters (Au, Ag, Pt, Cu etc), silver nanoclusters (AgNCs) possess low toxicity, superior water solubility, easy synthesis and suitable photophysical properties, which make them useful candidates for various applications in optoelectronics [4], catalysis [5], bioimaging and biosensing [6–8]. However, stabilization of these metal nanoclusters, particularly AgNCs from oxidation and aggregation to larger nanoparticles is a key challenge in this field. Previously, various stabilizing agents like small organic molecules, dendrimers, inorganic matrices, synthetic polymers, biopolymers, DNA, etc., were used in the construction of metal nanoclusters [9–11]. Since the pioneering work by

Dickson and coworkers on the fluorescence emission of cytosine rich DNA stabilized AgNCs [10], numerous DNA stabilized AgNCs with tunable fluorescence emission were developed using single strand oligonucleotides as templates [12]. The important features of DNA templated AgNCs (DNA-AgNCs), such as sequence dependent fluorescence emission [13], neighbouring sequence directed fluorescence modulation [14,15] and straightforward synthesis has stimulated the use of these fluorophores in bioimaging, sensing of DNA, RNA, proteins, metal ions, small molecules and cancer cells [16–24]. In addition, several reports have demonstrated the structural and sequence dependence of DNA on the origin and fluorescence modulation of AgNCs [25–31].

The unique property of programmable DNA hybridization, allows the construction of various AgNCs templated by secondary DNA structures such as duplex [14], triplex [32], hairpin loop [33], G-quadruplex [34], i-motifs [35], branched DNA junctions etc. [36] Among these secondary structures, branched DNA junction templated AgNCs have been used for multifunctional applications [36,37]. For example, Wang and coworkers developed a target-induced grafting technique to engineer the DNA-3WJ with multifunctional catalytic and fluorescent properties for the

* Corresponding author at: Photosciences and Photonics Section, CSIR-National Institute for Interdisciplinary Science and Technology, Thiruvananthapuram 695 019, India.

E-mail address: joshy@niist.res.in (J. Joseph).

<https://doi.org/10.1016/j.jphotobiol.2020.111886>

Received 6 December 2019; Received in revised form 17 February 2020

Available online 25 April 2020

1011-1344/ © 2020 Elsevier B.V. All rights reserved.

detection of DNA, thrombin and ATP [36]. Willner et al. demonstrated the formation of fluorescent DNA hydrogels by the successful incorporation of AgNCs in the sequence-specific loops of the Y-shaped DNA units [37]. Recently from our group, we have shown the formation of 2D-nanonetworks by the mutually assisted self-assembly of fullerene nanoclusters and DNA-3WJs with AgNCs stabilized in the cytosine rich overhang [38]. These reports highlight the stabilization of AgNCs either on one of the duplex strands of DNA-3WJs with a single strand overhang or by creating hairpin loops on the duplex strand. The overhang/hair pin modifications in the duplex arms, used in these strategies impose structural restrictions in building extended multifunctional sensor conjugates and hence limit their practical applications in biological sensing and imaging. Herein, we report the construction of a DNA-3WJ for templating AgNCs, without modification at the duplex branches. Instead, a cytosine loop has been inserted at the center of DNA-3WJ using mismatch single strand DNA (ssDNA) sequences. Although AgNCs templated by DNA-3WJs have been previously reported [36–38], to the best of our knowledge this is the first report of DNA-3WJ design with programmable cytosine loop in the center of Y-shaped DNA for stabilizing AgNCs. The DNA-3WJs with central cytosine loops were shown to act as efficient templates, which stabilize the formation of AgNCs. Multiple DNA-3WJ structures were used to demonstrate the sequence dependence of the central loop region and duplex arms, on the formation and stabilization of AgNCs. Further, the fluorescence of the synthesized AgNCs was used to probe Hg^{2+} ions in aqueous solutions in subnanomolar concentrations.

2. Materials and Methods

2.1. Materials

Short oligonucleotide sequences used in this work (Table S1) were synthesized by solid phase oligonucleotide synthesis using K&A Laboratory H-6/H-8 DNA/RNA/LNA synthesizer. Phosphoramidites used for the solid-phase DNA synthesis were purchased from Glen Research (<http://www.glenresearch.com/index.php>). Anhydrous acetonitrile and all other reagents required for DNA synthesis were purchased from Sigma Aldrich. The synthesized oligonucleotides sequences were purified by LC-6AD Shimadzu Reverse Phase-High Performance Liquid Chromatography (RP-HPLC) with an Inertsil ODS-3, 5 mm, 10×250 mm reverse phase column. Deprotection and hybridization of ssDNAs were performed on IKA® dry block heater. Ammonium hydroxide (28% NH_3 in H_2O , 99.99%), ethidium bromide (EB), silver nitrate ($AgNO_3$, 99.0%), sodium borohydride ($NaBH_4$, 98.0%), sodium chloride ($NaCl$, 99%), sodium phosphate dibasic anhydrous (Na_2HPO_4) and sodium phosphate monobasic monohydrate ($NaH_2PO_4 \cdot H_2O$) were purchased from Sigma Aldrich. All the metal salts used in this work are of analytical grade and used as received without further purification. Water used for all the experiments was de-ionized Milli Q (18.2 $M\Omega \cdot cm$). All optical measurements were carried out in buffer solution (10 mM sodium phosphate buffer, pH = 7.4 and 150 mM NaCl) using 1 cm cuvettes at room temperature (25 ± 1 °C), unless otherwise mentioned.

2.2. UV/Visible and Photoluminescence Spectroscopy

The UV/Vis absorption spectra and melting temperature measurements were performed on Shimadzu UV-2600 Spectrophotometer. Steady state fluorescence emission spectra were recorded on a SPEX FLUOROLOG-3 (FL3–221) Spectrofluorimeter, equipped with a 450 W Xenon arc lamp and a slit width of 5 nm. The quantum yield of 3WJ20-C12/AgNCs was measured by a relative comparison method using cresyl violet ($\Phi_F = 57\%$ in methanol) as the fluorescent standard [39]. The fluorescence life time measurements of 3WJ20-C12/AgNCs were done using a picosecond single photon counting system (Horiba, DeltaFlex) employing 510 nm laser as excitation source using picosecond photon detection module (PPD-850) as a detector. The fluorescence

decay profile was deconvoluted using EzTime software and fitted with multi exponential decay of chi-square value 1 ± 0.1 .

2.3. Circular Dichroism (CD) Spectroscopy

CD spectra of DNA-3WJs were obtained at ambient temperatures using JASCO J-810 spectropolarimeter having Peltier controlled thermostatic cell holder with an accumulation of 2 and scan speed of 200 nm/min.

2.4. High Resolution-Transmission Electron Microscopy (HR-TEM)

The samples for TEM imaging were prepared by drop casting 5 μL samples on the top of carbon-coated copper grid (400 meshes, Ted Pella). The as-prepared samples were initially dried on copper grid by slow evaporation and subjected to vacuum drying for 2 days before analysis. HR-TEM characterization and Energy Dispersive X-ray spectroscopy (EDAX) were performed with JEOL-JEM0310 microscope with an accelerating voltage of 100 kV and the samples were imaged using a Hamamatsu ORCA charge-coupled device (CCD) camera.

2.5. Dynamic Light Scattering (DLS) Measurements

Particle size distributions were calculated using a Zetasizer (Malvern Nano ZS) operating with a He-Ne laser at a wavelength of 633 nm. Each analysis was performed in triplicate and the mean value is reported. In each run, 10–15 measurements were made. Purified samples of 3WJ20-C12/AgNC, Ag nanoparticles formed in presence of 3WJ20 (15 μM) and in the absence of DNA were used for hydrodynamic size measurements

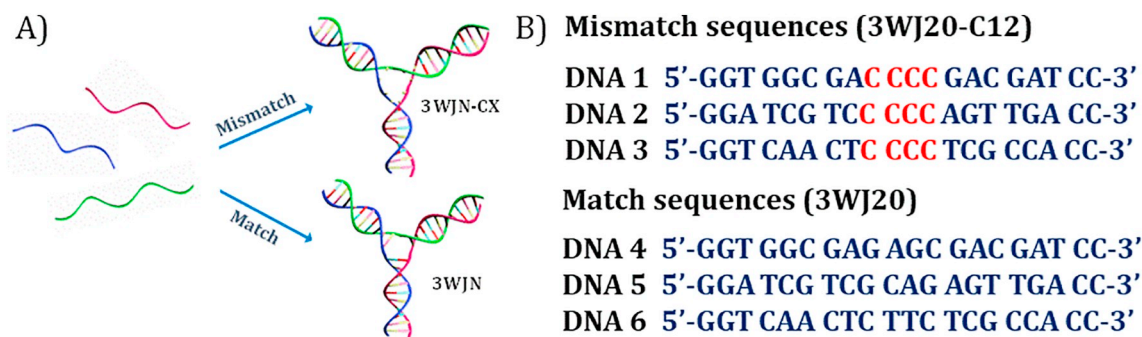
2.6. X-ray Photoelectron Spectroscopy (XPS)

XPS analysis of dried samples were performed using PHI 5000 Versa Probe II (ULVAC-PHI Inc., USA) equipped with microfocused (200 μm , 15 kV) monochromatic Al-K α X-Ray source ($h\nu = 1486.6$ eV). Survey scans were recorded with X-ray source power of 50 W and pass energy of 187.85 eV. High-resolution spectrum of the Ag was recorded at 46.95 eV pass energy.

2.7. Synthesis of Sequence Specific DNA-3WJs

Two different types of DNA-3WJs, 3WJN-CX and 3WJN used in this work were assembled from corresponding ssDNA sequences (Table S1 & Scheme 1A), following the typical hybridization protocols. The short ssDNA sequences (with 20 bases and 30 bases) were synthesized by solid phase oligonucleotide synthesis. The synthesis was carried out on a 1.0 μmol solid support, CPG (Controlled pore-glass, 1000 Å pore size) using commercial phosphoramidites. Required oligonucleotide sequences were prepared with automated synthesis, which follows the stepwise addition of nucleoside 3'-phosphoramidite monomers to the 5'-end of resin bound nucleoside. The oligonucleotides were cleaved from the solid support and deprotected using standard conditions (28% NH_4OH , 10h at 60 °C on a dry block heater). The synthesized oligonucleotides were purified by RP-HPLC. A binary gradient system of triethylammonium acetate (TEAA) buffer (0.05 mM, pH = 7) and acetonitrile were used as eluents. The purified oligonucleotide samples were concentrated under vacuum, desalted using Sep-Pak C18 cartridge and concentrations were determined by monitoring the UV absorbance at 260 nm. The samples were then stored at below 4 °C and used as required to assemble into corresponding DNA-3WJs.

Hybridization of ssDNA sequences into corresponding DNA-3WJs were achieved by following the standard hybridization protocols. Equimolar mixture of three complementary ssDNAs in buffer solution were annealed at 90 °C for 10 min. All of the DNA-3WJs mentioned in this work were assembled by this procedure and stored at 4 °C. 1 μM



Scheme 1. A) Schematic illustration of the hybridization of mismatched ssDNA in to 3WJN-CX and matched ssDNA in to 3WJN. B) ssDNA Sequences used for the construction of 3WJ20-C12 and 3WJ20.

samples of DNA-3WJs were used for thermal denaturation and circular dichroism studies. EB intercalation studies were performed by sequential addition of 10 μ L, 100 μ M samples of DNA-3WJ into 30 μ M, 1 mL EB in buffer solution.

2.8. Synthesis of 3WJ/AgNCs

Fluorescent AgNCs were synthesized according to the modified literature reports described by Dickson et al. [10,12] For the preparation of AgNCs templated by 3WJN-CX and 3WJN, 45 μ L, 2 mM AgNO₃ solution was added to a freshly prepared sample of 15 μ M DNA-3WJs in buffer solution to provide a DNA-3WJ to Ag⁺ molar ratio of 1:6 (final volume of 1 mL solution). After vortexing the sample for 10 min at room temperature, the mixture was reduced by quickly adding 45 μ L, 2 mM of NaBH₄ (freshly prepared) under vigorously shaking conditions for 2 min. Final concentrations were fixed to 15 μ M for the DNA-3WJ template, 90 μ M for AgNO₃, 90 μ M for NaBH₄ in a molar ratio 1, 6, 6, respectively. The reaction mixture was kept in the dark at 4 °C for another 8 h before optical measurements. The purification of 3WJN-CX/AgNCs from AgNPs and aggregates was achieved using Amicon® Ultra Ultracel®-10k centrifugal filters. A similar procedure was followed for all the AgNCs synthesis mentioned in this work. The 3WJ-AgNCs concentration is referred to the concentration of DNA-3WJ unless mentioned otherwise. 15 μ M samples of 3WJ/AgNCs in buffer solution was used for UV-visible absorption, fluorescence emission, quantum yield (ϕ) and fluorescence lifetime measurements.

2.9. Selectivity and Sensitivity Measurements of 3WJ20-C12/AgNCs

The selectivity of 3WJ20-C12/AgNC system for various metal ions were studied by monitoring the changes in fluorescence intensity of this system with the addition of common cations like K⁺, Li⁺, Ca²⁺, Mg²⁺, Hg²⁺, Cu²⁺, Zn²⁺, Cd²⁺, Al³⁺ and Fe³⁺. For selectivity experiment, 10 μ L, 60 μ M metal ions in acetonitrile was added to 1 mL, 1.5 μ M 3WJ20-C12/AgNCs in buffer solution. The sensitivity of this 3WJ20-C12/AgNCs system towards Hg²⁺ was studied by adding increasing concentrations of Hg²⁺ (0, 1–10, 100, and 200 nM) to 6 μ M 3WJ20-C12/AgNCs. Fluorescence changes in a range of Hg²⁺ concentrations from 0 to 5 nM was used for limit of detection (LOD) calculation. LOD is determined from standard deviation of response of the curve (Sy) and slope of calibration curve (S), according to the formula LOD = 3.3 (Sy/S). The standard deviation of response can be determined from the standard deviation of y-intercepts of regression lines [40].

3. Results and Discussion

3.1. Assembly and Characterization of DNA-3WJs

In the initial design, three ssDNAs, DNA 1, 2 & 3 (Scheme 1B), each containing 20 nucleobases with four cytosines in the center were used,

which upon hybridization form a DNA-3WJ with an unpaired, 12-cytosine loop at the center of the 3WJ (hereafter referred as 3WJ20-C12, Scheme S1). On the other hand, DNA 4, 5 & 6 (Scheme 1B) hybridize to form a 3WJ without a cytosine loop at the center and is used as a control 3WJ (3WJ20) [41]. In general, the DNA-3WJs with and without the central cytosine loops, used in this work are defined as 3WJN-CX and 3WJN, respectively where N represents the total number of nucleobases in one ssDNA and X represents the total number of unpaired, cytosines in the central loop region of the 3WJ. All the ssDNA sequences, corresponding DNA-3WJs, HRMS and melting temperature (T_m) values obtained are tabulated in Table S1.

Thermal denaturation properties of 3WJ20-C12 and 3WJ20 were studied by monitoring the absorbance at 260 nm as a function of temperature. 3WJ20-C12 dissociates into ssDNA at 32 °C whereas the fully hybridized 3WJ20 melts at 41 °C. The decrease in the T_m value of 3WJ20-C12 compared to 3WJ20 (Fig. S1) is due to the relative destabilization of the 3WJ in the presence of the twelve unpaired cytosine nucleobases in the central loop region. Circular dichroism analysis showed a bisignated CD signal centered at 260 nm, with a positive band at 275 nm and a negative band at 248 nm (Fig. S2), which indicates the B-form duplex structure of the arms in the DNA-3WJs. The duplex nature of the 3WJ arms and presence of cytosine loop in 3WJ20-C12 were further analyzed by ethidium bromide (EB) intercalation studies (Fig. S3A and S3B, Fig. S4A and S4B of 3WJ20-C12, 3WJ20, respectively). Upon excitation at 515 nm, an enhancement in the monomeric fluorescence emission of EB with successive addition of DNA-3WJs was observed. A ~ 30% relative enhancement in the fluorescence emission of EB in presence of fully hybridized 3WJ20 compared to 3WJ20-C12 (Fig. S5) indicates the presence of unpaired nucleobases in 3WJ20-C12. Thus, the DNA melting, CD and EB displacement studies verify the presence of 3WJ branches with duplex structures and cytosine loop in 3WJ20-C12.

3.2. DNA-3WJ Templated Fluorescent AgNCs

3.2.1. Absorption and Photoluminescence Study

To demonstrate our strategy of stabilizing AgNCs on cytosine loop inserted at DNA-3WJ center, silver ions were added to DNA-3WJs in buffer solution, followed by reduction using NaBH₄ (Schematic illustration; Fig. 1A and 1B). UV-visible absorption spectra of 3WJ20-C12/AgNC (AgNC formed in the presence of 3WJ20-C12) showed a characteristic absorption band at 510 nm along with the surface plasmonic resonance band of silver nanoparticles (AgNPs) around 400 nm [42]. The 510 nm absorption band is characteristic of the DNA templated AgNCs as reported in the literature [43]. Control AgNC synthetic experiments in the absence of 3WJs or in the presence of 3WJ20, showed only the 400 nm surface plasmonic resonance band with no evidence of 510 nm band (Fig. 1C). These results clearly indicate that, only the samples with DNA, templates and stabilizes Ag nanoparticles. Whereas, the one without stabilizing agent results in the formation of more

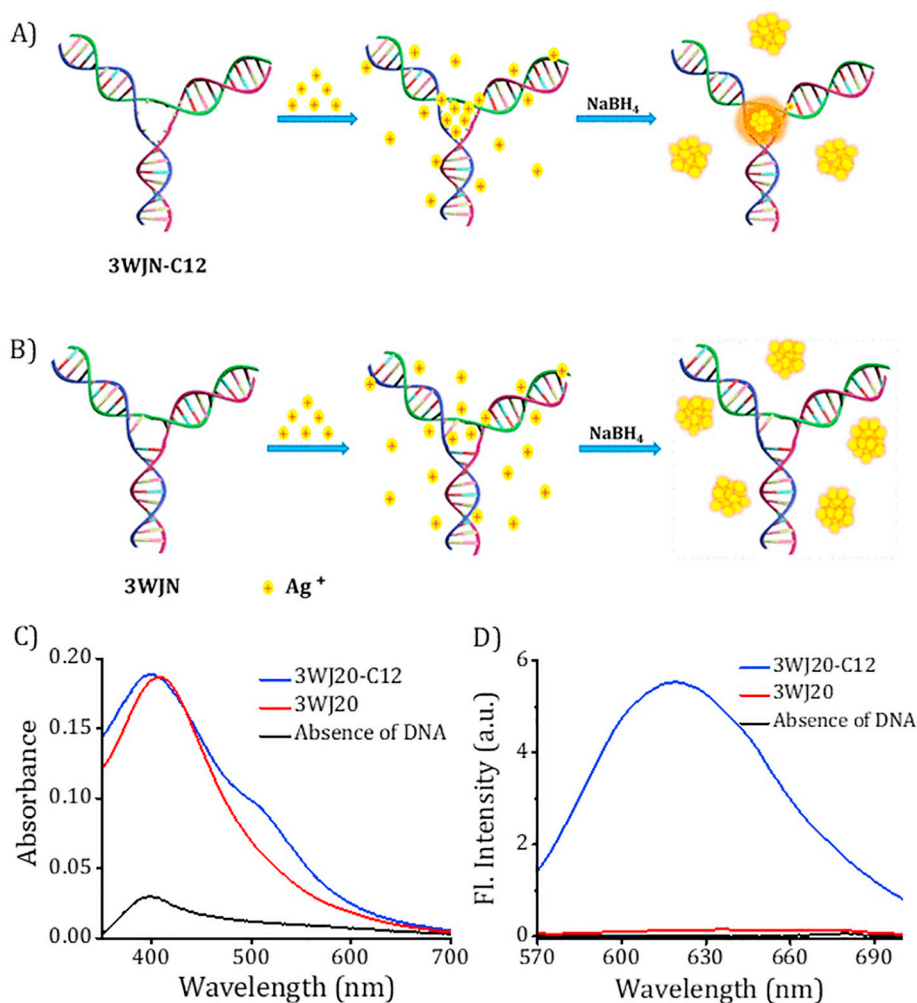


Fig. 1. Schematic illustration of the strategy for the preparation of fluorescent AgNCs in presence of A) 3WJN-C12 and B) 3WJN, C) UV-visible absorption spectra and D) corresponding fluorescence emission spectra of AgNCs prepared with 3WJ20-C12, 3WJ20 and in the absence of DNA ($\lambda_{\text{exc}} = 510$ nm).

aggregated Ag nanostructures than AgNPs, responsible for the observed surface plasmon band. In addition, fluorescence emission spectra of 3WJ20-C12/AgNC showed characteristic emission band at 630 nm ($\lambda_{\text{exc}} = 510$ nm) which was not observed in the control experiments (Fig. 1D). This distinctive absorption and fluorescence behaviour of 3WJ20-C12/AgNC indicates efficient cytosine- Ag^+ interaction only in the 3WJs with central cytosine loop leading to the formation and stabilization of fluorescent AgNCs upon reduction, which otherwise results in the formation of aggregated AgNPs.

The formation of 3WJ20-C12/AgNCs was monitored by recording the time dependent changes in UV-visible absorption and fluorescence emission spectra. The plasmon absorption of the AgNPs around 400 nm along with a small shoulder band around 510 nm corresponding to the AgNCs started to appear within 10 min of the addition of NaBH_4 to a mixture of 3WJ20-C12 and silver ions (Fig. S6A). The absorption band at 510 nm due to the formation of AgNCs gradually increased up to 8 h, beyond which it got saturated (inset of Fig. S6A). Similar to the absorption spectra, a characteristic fluorescence emission band appeared at 630 nm and showed significant emission within 2 h, with slight enhancement in the fluorescence emission up to 8 h and gets saturated (Fig. 2A, Fig. S6B). The observed red fluorescence compares well with the fluorescence of AgNCs, reported with 12-cytosine as ssDNA template or as a part of ssDNA/hairpin loop structures. [44–46] The quantum yield (Φ_f) of as-synthesized 3WJ20-C12/AgNCs was found to be 12% in PBS buffer at pH 7.4, (Fig. S7A). Fluorescence lifetime measurements of these 3WJ20-C12/AgNCs showed triexponential

decay with an average fluorescence lifetime of 1.64 ns (Fig. S7B). Purification of 3WJ20-C12/AgNCs from AgNPs was achieved using Ultracel®-10k centrifugal filters by the continuous washing of sample with buffer solution (Fig. S8A and S8B). Purified samples of 3WJ20-C12/AgNCs showed slight yellow color under day light and intense red emission under 365 nm UV light (Fig. 2B, cartoonic representation of purified 3WJ20-C12/AgNCs, Fig. 2C and 2D). Further, the purified 3WJ20-C12/AgNCs showed higher stability in terms of fluorescence emission compared to the unpurified samples, as evidenced by the fluorescence emission over 72 h (Fig. S9A and S9B).

3.2.2. HR-TEM, DLS, EDAX and XPS Study

HR-TEM analysis was used to visualize the size and shape of Ag nanoparticles formed in the presence of different DNA-3WJs. Purified samples of 3WJ20-C12/AgNCs showed 2–3 nm sized clusters, supporting the effective stabilization of AgNCs inside the 3WJ center (Fig. 2E). Whereas, the sample drop cast before purification showed a combination of AgNCs, AgNPs and aggregated nanostructures (Fig. S10A). The structure of the 3WJ with 4 unpaired cytosine bases per strand at the 3WJ center (total 12 cytosines) is highly dynamic and hence the exact nature of the 3WJ center is unknown. However, the diameter of the 3WJ center calculated based on regular B-like structure for the duplex arms with central unpaired cytosines in random coil structure ranges between 2.5 nm to 4.5 nm and the AgNC complexation could bring this to shorter diameters and more rigid structures. EDAX spectrum of purified 3WJ20-C12/AgNCs, shows peaks corresponding to

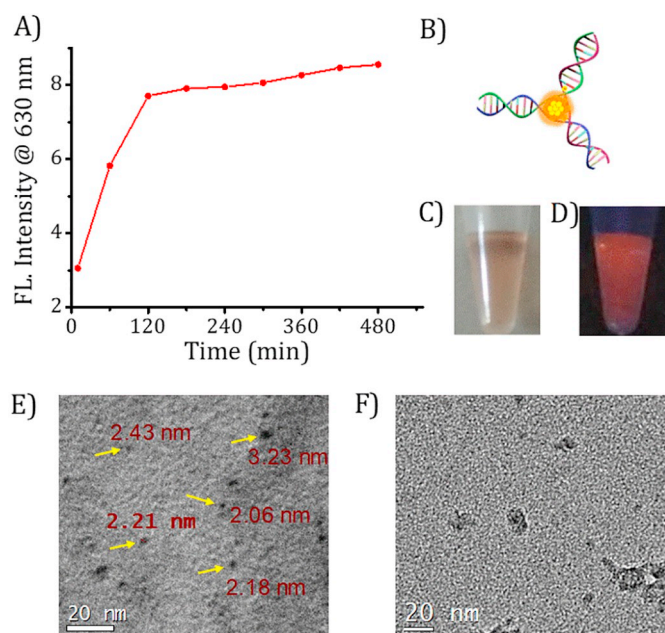


Fig. 2. A) Plot of fluorescence intensity of 3WJ20-C12/AgNC with reaction time, obtained by monitoring fluorescence emission at 630 nm ($\lambda_{\text{exc}} = 510$ nm); B) cartoonic representation of purified 3WJ20-C12/AgNC; photographs of purified 3WJ20-C12/AgNC under the exposure of C) day light and D) UV light ($\lambda_{\text{exc}} = 365$ nm) and TEM images of E) purified 3WJ20-C12/AgNCs (The formation of 2–3 nm sized 3WJ20-C12/AgNCs are indicated by yellow arrow mark) and F) AgNPs formed in the presence of 3WJ20. (For interpretation of the references to color in this figure legend, the reader is referred to the web version of this article.)

Ag and phosphorous validating the presence of AgNCs and DNA (Fig. S11) [47].

Under similar conditions, HR-TEM analysis of the AgNPs formed in the presence of 3WJ20 or in the absence of any DNA, showed 10–12 nm sized AgNPs and aggregated AgNPs (Fig. 2F and Fig. S10B). DLS measurements of the AgNCs (or AgNPs) prepared under similar reaction conditions in presence of 3WJ20-C12, 3WJ20 and in the absence of any DNA, provide an estimation of the hydrodynamic size of various nanostructures (Fig. S12). Purified 3WJ20-C12/AgNCs showed a lower hydrodynamic size of ~20 nm compared to the AgNPs formed in the presence of 3WJ20 (> 60 nm) and in the absence of DNA (> 100 nm, aggregates of AgNPs). Further, the elemental analysis and surface composition obtained from the XPS spectrum (Fig. S13A) of 3WJ20-C12/AgNCs confirmed the presence of Ag, phosphorous, oxygen and nitrogen. Expanded Ag 3d region of XPS spectrum shows two peaks at 368.29 and 374.3 eV characteristic of the AgNCs (Fig. S13B) [42]. Thus, HR-TEM and XPS analysis confirms that emissive AgNCs with 2–3 nm size are formed only in the presence of mismatched 3WJ20-C12 template with cytosine loop and validates our proposed strategy.

3.2.3. Sequence Dependence on the Formation and Fluorescence Properties of AgNCs

Alterations in the formation of AgNCs and corresponding fluorescence emission was inspected by programming the ssDNA sequences as represented in Table S1 & Fig. 3A–B. In the first instance, the duplex branch length of DNA-3WJ was increased from 8 to 13 to obtain 3WJ30-C12 and 3WJ-30, with and without the central cytosine loop, respectively. In the second example, the central, cytosine loop size was reduced from 12 to 6 cytosines to obtain 3WJ20-C6. DNA-3WJs were prepared from the corresponding ssDNAs and T_m values obtained are tabulated (Table S1, Fig. S14A and Fig. S14B). A comparison of the T_m values of 3WJ30-C12 (51 °C) and 3WJ20-C12 (32 °C) demonstrate the additional stability offered by the extended duplex arms in the case of

3WJ30-C12. AgNCs prepared in presence of 3WJ30-C12 showed a characteristic emission at 578 nm ($\lambda_{\text{exc}} = 490$ nm), with a blue shift and relatively enhanced emission compared to 3WJ20-C12/AgNCs (Fig. 3B). This shift in the emission spectrum could be attributed to the presence of higher number of nearby nucleobases and less flexibility of 3WJ30-C12 compared to 3WJ20-C12 [48]. Control experiments with 3WJ30 doesn't show any characteristic emission as expected, thereby validating the requirement of cytosine loop in the 3WJ center for stabilizing AgNCs. Likewise, attempts to prepare AgNCs with 3WJ20-C6 doesn't show the formation of emissive AgNCs, indicating that, a 6 cytosine loop is not enough for stabilization of the emissive AgNCs (Table S2 in supporting information shows the different DNA-3WJ structures and corresponding changes in the fluorescence emission). These results of fluorescence emission were further supported with HR-TEM analysis. 3WJ30-C12/AgNCs showed the presence of 3–4 nm sized AgNCs whereas 3WJ30 and 3WJ20-C6 showed the formation of AgNP aggregates (Fig. S15A, S15B and Fig. S15C).

3.2.4. Metal Ion Interaction Studies

Interestingly, the 3WJN-C12/AgNCs exhibited highly selective and sensitive interactions with Hg^{2+} ions and hence can be employed in the detection of trace amounts of Hg^{2+} ions in aqueous solutions by a fluorescence turn-off mechanism. For example, the fluorescence of 3WJ20-C12/AgNC, showed significant quenching in the presence of 1–200 nM Hg^{2+} ions as shown in Fig. S16A. The sensitive detection is characterized by a significantly low, LOD value of 0.7 nM, calculated by monitoring the changes in fluorescence intensity as a function concentration of Hg^{2+} ions (Fig. 3C). Similarly, the selectivity of 3WJ20-C12/AgNC for Hg^{2+} ions was analyzed using various metal ions (K^+ , Li^+ , Ca^{2+} , Mg^{2+} , Cu^{2+} , Zn^{2+} , Cd^{2+} , Al^{3+} , Hg^{2+} and Fe^{3+} , Fig. S16B) and the results are summarized in Fig. 3D. Other metal ions, even at 300 times higher concentrations compared to Hg^{2+} , failed to show significant fluorescence quenching. A review of existing literature shows that the silver nanoclusters (AgNCs) stabilized by DNA strands and other small molecules are shown to exhibit a highly selective and sensitive interaction with Hg^{2+} , leading to significant fluorescence changes. [46,49] The leading mechanisms proposed for the selective interaction of AgNCs with Hg^{2+} ions are; (i) d^{10} – d^{10} metallophilic interactions and (ii) redox reactions involving Hg^{2+} and Ag leading to the oxidation of Ag atoms in the cluster to Ag(I) ions, which perturb the fluorescence properties. The highly sensitive fluorescence quenching of 3WJ20-C12/AgNCs in presence of Hg^{2+} ions could be attributed to the possible oxidation of Ag(0) to Ag^+ ions, which also explains the selectivity of the interactions in this case.

To get a better insight into the fluorescence quenching mechanism of AgNCs by Hg^{2+} , thermal denaturation studies of 3WJ20-C12 in presence of Ag^+ ions, AgNCs and AgNC/ Hg^{2+} were conducted (Fig. S17). The addition of 6 equivalents of Ag^+ to 3WJ20-C12 stabilizes the 3WJ DNA by 3 °C and the corresponding AgNCs (obtained by reduction of the same solution using 6 equivalents of NaBH_4) by 4 °C. Subsequent addition of Hg^{2+} to the 3WJ20-C12/AgNC resulted in the destabilization of 3WJ20-C12/AgNC. These results further supports the proposed redox mechanism for the fluorescence quenching in 3WJ20-C12/AgNCs in the presence of Hg^{2+} . [17]

4. Conclusion

In summary, we present a novel design of branched DNA-3WJ with a cytosine loop at the center for stabilizing AgNCs, which can replace the process of modifying DNA branches for AgNCs used in multi-functional applications. The potential of this strategy to template AgNC is verified using a standard DNA-3WJ. The formation of AgNCs inside this loop was characterized with photophysical, microscopic and surface analysis techniques. Sequence length and central cytosine loop size dependent changes on the formation and fluorescence properties were also examined. Results suggest that, AgNCs templated by DNA-3WJ

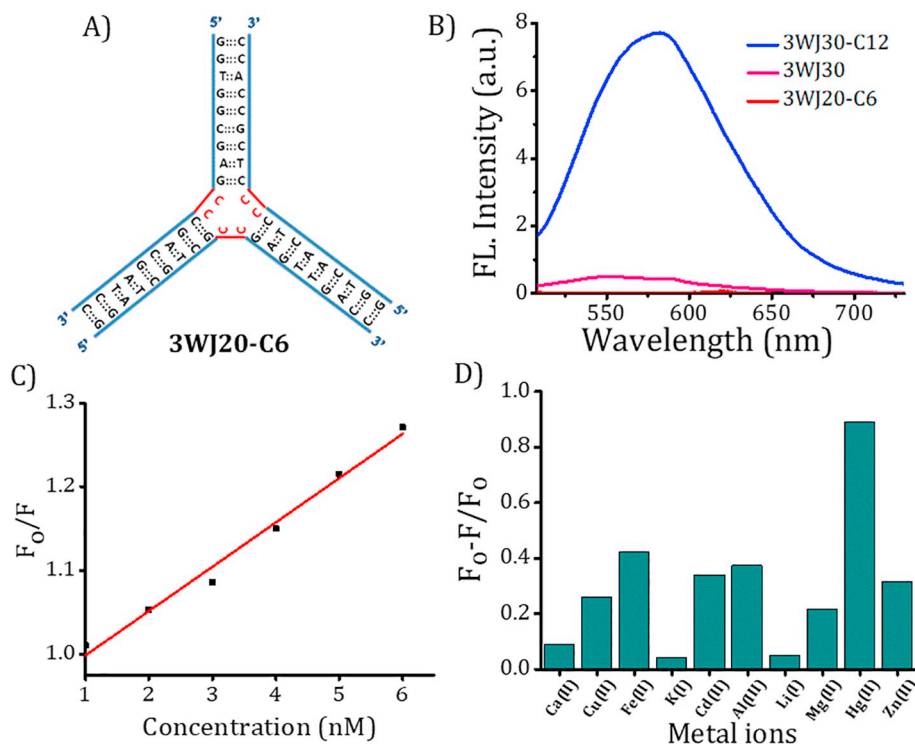


Fig. 3. A) Representation of 3WJ20-C6; B) Fluorescence emission spectra of AgNCs prepared in the presence of 3WJ30-C12, 3WJ-30 and 3WJ20-C6 ($\lambda_{exc} = 490$ nm); C) F_0/F versus concentration plot of fluorescence quenching of 3WJ20-C12/AgNC with increasing the Hg^{2+} from 1 to 6 nM and D) Fluorescence quenching of 3WJ20-C12/AgNC, $(F_0-F)/F_0$ at 630 nm with addition of 60 μM different metal ions in acetonitrile.

with a 12 cytosine loop is a reasonably good template with fluorescence properties compared to its 6 cytosine analogue. The length of duplex 3WJ branch shows significant influence on fluorescence properties of AgNCs. The selectivity and sensitivity studies with metal ions demonstrates the ability of 3WJN-C12/AgNCs to sense Hg^{2+} ions in aqueous solutions with detection limit in nanomolar range. Therefore, this novel design of AgNCs templated by branched DNA structure can be used as a fluorescent nanotag, which offers a better programmability of the duplex branches for multifunctional applications over the normal DNA-3WJ templated fluorophores reported.

Declaration of Competing Interest

There are no conflicts to declare.

Acknowledgements

The work is supported by CSIR (HCP-0012 & MLP0027) and DST-SERB (RJN-19/2012), & UGC (Research Fellowships for SKS & SKV), Government of India.

Appendix A. Supplementary Data

Supplementary data to this article can be found online at <https://doi.org/10.1016/j.jphotobiol.2020.111886>.

References

- Y. Tao, M. Li, J. Ren, X. Qu, Metal nanoclusters: novel probes for diagnostic and therapeutic applications, *Chem. Soc. Rev.* 44 (2015) 8636–8663.
- L. Shang, S. Dong, G.U. Nienhaus, Ultra-small fluorescent metal nanoclusters: synthesis and biological applications, *Nano Today* 6 (2011) 401–418.
- A. Mathew, T. Pradeep, Noble metal clusters: applications in energy, environment, and biology, *Part. Part. Syst. Charact.* 31 (2014) 1017–1053.
- J. Kondo, Y. Tada, T. Dairaku, Y. Hattori, H. Saneyoshi, A. Ono, Y. Tanaka, A metallo-DNA nanowire with uninterrupted one-dimensional silver array, *Nat. Chem.* 9 (2017) 956–960.
- N. Wang, Y. Hu, Z. Zhang, Sustainable catalytic properties of silver nanoparticles supported montmorillonite for highly efficient recyclable reduction of methylene blue, *Appl. Clay Sci.* 150 (2017) 47–55.
- S. Pan, W. Liu, J. Tang, Y. Yang, H. Feng, Z. Qian, J. Zhou, Hydrophobicity-guided self-assembled particles of silver nanoclusters with aggregation-induced emission and their use in sensing and bioimaging, *J. Mater. Chem. B* 6 (2018) 3927–3933.
- V. Kumar, R.K. Gundampati, D.K. Singh, D. Bano, M.V. Jagannadham, S.H. Hasan, Photoinduced green synthesis of silver nanoparticles with highly effective antibacterial and hydrogen peroxide sensing properties, *J. Photochem. Photobiol. B Biol.* 162 (2016) 374–385.
- L. Meng, Q. Zhu, J.-H. Yin, N. Xu, Polyethyleneimine protected silver nanoclusters luminescence probe for sensitive detection of cobalt (II) in living cells, *J. Photochem. Photobiol. B Biol.* 173 (2017) 508–513.
- I. Díez, R.H.A. Ras, Fluorescent silver nanoclusters, *Nanoscale* 3 (2011) 1963–1970.
- J.T. Petty, J. Zheng, N.V. Hud, R.M. Dickson, DNA-templated Ag nanocluster formation, *J. Am. Chem. Soc.* 126 (2004) 5207–5212.
- A. Quaranta, S. Carturan, M. Bonafini, G. Maggioni, M. Tonzzer, G. Mattei, C. de Julián Fernandez, G. Della Mea, P. Mazzoldi, Optical sensing to organic vapors of fluorinated polyimide nanocomposites containing silver nanoclusters, *Sensors Actuators B Chem.* 118 (2006) 418–424.
- C.I. Richards, S. Choi, J.-C. Hsiang, Y. Antoku, T. Vosch, A. Bongiorno, Y.-L. Tzeng, R.M. Dickson, Oligonucleotide-stabilized Ag nanocluster fluorophores, *J. Am. Chem. Soc.* 130 (2008) 5038–5039.
- W. Guo, J. Yuan, Q. Dong, E. Wang, Highly sequence-dependent formation of fluorescent silver nanoclusters in hybridized DNA duplexes for single nucleotide mutation identification, *J. Am. Chem. Soc.* 132 (2010) 932–934.
- R. Lin, G. Tao, Y. Chen, M. Chen, F. Liu, N. Li, Constructing a robust fluorescent DNA-stabilized silver nanocluster probe module by attaching a duplex moiety, *Chem. Eur. J.* 23 (2017) 10893–10900.
- Y.-A. Chen, H.T. Vu, Y.-L. Liu, Y.-I. Chen, T.D. Nguyen, Y.-A. Kuo, S. Hong, Y.-A. Chen, S. Carnahan, J.T. Petty, H.-C. Yeh, Improving NanoCluster Beacon performance by blocking the unlabeled NC probes, *Chem. Commun.* 55 (2019) 462–465.
- S. Lu, S. Wang, J. Zhao, J. Sun, X. Yang, Fluorescence light-up biosensor for MicroRNA based on the distance-dependent photoinduced electron transfer, *Anal. Chem.* 89 (2017) 8429–8436.
- K. Morishita, J.L. MacLean, B. Liu, H. Jiang, J. Liu, Correlation of photobleaching, oxidation and metal induced fluorescence quenching of DNA-templated silver nanoclusters, *Nanoscale* 5 (2013) 2840–2849.
- B. Han, E. Wang, Oligonucleotide-stabilized fluorescent silver nanoclusters for sensitive detection of biothiols in biological fluids, *Biosens. Bioelectron.* 26 (2011) 2585–2589.
- L. Feng, L. Wu, F. Xing, L. Hu, J. Ren, X. Qu, Novel electrochemiluminescence of silver nanoclusters fabricated on triplex DNA scaffolds for label-free detection of biothiols, *Biosens. Bioelectron.* 98 (2017) 378–385.
- W.-Y. Mu, R. Yang, A. Robertson, Q.-Y. Chen, A near-infrared BSA coated DNA-AgNCs for cellular imaging, *Colloids Surf. B: Biointerfaces* 162 (2018) 427–431.
- I.M. Khan, S. Zhao, S. Niazi, A. Mohsin, M. Shoabi, N. Duan, S. Wu, Z. Wang, Silver nanoclusters based FRET aptasensor for sensitive and selective fluorescent detection of T-2 toxin, *Sensors Actuators B Chem.* 277 (2018) 328–335.
- R. Zou, F. Zhang, C. Chen, C. Cai, DNA-programming multicolor silver nanoclusters for sensitively simultaneous detection of two HIV DNAs, *Sensors Actuators B Chem.*

- 296 (2019) 126608.
- [23] R. Cheng, J. Xu, X. Zhang, Z. Shi, Q. Zhang, Y. Jin, A selective and label-free strategy for rapid screening of telomere-binding ligands via fluorescence regulation of DNA/silver nanocluster, *Sci. Rep.* 7 (2017) 42629.
- [24] J. Ai, J. Li, L. Ga, G. Yun, L. Xu, E. Wang, Multifunctional near-infrared fluorescent nanoclusters for simultaneous targeted cancer imaging and photodynamic therapy, *Sensors Actuators B Chem.* 222 (2016) 918–922.
- [25] M.L. Neidig, J. Sharma, H.-C. Yeh, J.S. Martinez, S.D. Conradson, A.P. Shreve, Ag K-edge EXAFS analysis of DNA-templated fluorescent silver nanoclusters: insight into the structural origins of emission tuning by DNA sequence variations, *J. Am. Chem. Soc.* 133 (2011) 11837–11839.
- [26] E.G. Gwinn, P. O'Neill, A.J. Guerrero, D. Bouwmeester, D.K. Fygenson, Sequence-dependent fluorescence of DNA-hosted silver nanoclusters, *Adv. Mater.* 20 (2008) 279–283.
- [27] J.T. Petty, C. Fan, S.P. Story, B. Sengupta, M. Sartin, J.-C. Hsiang, J.W. Perry, R.M. Dickson, Optically enhanced, near-IR, silver cluster emission altered by single base changes in the DNA template, *J. Phys. Chem. B* 115 (2011) 7996–8003.
- [28] D.J.E. Huard, A. Demissie, D. Kim, D. Lewis, R.M. Dickson, J.T. Petty, R.L. Lieberman, Atomic structure of a fluorescent Ag₈ cluster templated by a multistranded DNA scaffold, *J. Am. Chem. Soc.* 141 (2019) 11465–11470.
- [29] E. Thyraug, S.A. Bogh, M.R. Carro-Temboury, C.S. Madsen, T. Vosch, D. Zigmantas, Ultrafast coherence transfer in DNA-templated silver nanoclusters, *Nat. Commun.* 8 (2017) 15577.
- [30] H. Liu, F. Shen, P. Haruehanroengra, Q. Yao, Y. Cheng, Y. Chen, C. Yang, J. Zhang, B. Wu, Q. Luo, R. Cui, J. Li, J. Ma, J. Sheng, J. Gan, A DNA Structure Containing AgI-Mediated G:G and C:C Base Pairs, 56 (2017), pp. 9430–9434.
- [31] Y. Chen, M.L. Phipps, J.H. Werner, S. Chakraborty, J.S. Martinez, DNA templated metal nanoclusters: from emergent properties to unique applications, *Acc. Chem. Res.* 51 (2018) 2756–2763.
- [32] L. Feng, Z. Huang, J. Ren, X. Qu, Toward site-specific, homogeneous and highly stable fluorescent silver nanoclusters fabrication on triplex DNA scaffolds, *Nucleic Acids Res.* 40 (16) (2012) e122.
- [33] J. Chen, X. Ji, P. Tinnefeld, Z. He, Multifunctional dumbbell-shaped DNA-templated selective formation of fluorescent silver nanoclusters or copper nanoparticles for sensitive detection of biomolecules, *ACS Appl. Mater. Interfaces* 8 (2016) 1786–1794.
- [34] J. Ai, W. Guo, B. Li, T. Li, D. Li, E. Wang, DNA G-quadruplex-templated formation of the fluorescent silver nanocluster and its application to bioimaging, *Talanta* 88 (2012) 450–455.
- [35] B. Sengupta, K. Springer, J.G. Buckman, S.P. Story, O.H. Abe, Z.W. Hasan, Z.D. Prudowsky, S.E. Rudisill, N.N. Degtyareva, J.T. Petty, DNA templates for fluorescent silver clusters and I-motif folding, *J. Phys. Chem. C* 113 (2009) 19518–19524.
- [36] L. Zhang, S. Guo, J. Zhu, Z. Zhou, T. Li, J. Li, S. Dong, E. Wang, Engineering DNA three-way junction with multifunctional moieties: sensing platform for bioanalysis, *Anal. Chem.* 87 (2015) 11295–11300.
- [37] W. Guo, R. Orbach, I. Mironi-Harpaz, D. Seliktar, I. Willner, Fluorescent DNA hydrogels composed of nucleic acid-stabilized silver nanoclusters, *Small* 9 (2013) 3748–3752.
- [38] S.K. Vittala, S.K. Saraswathi, A.B. Ramesan, J. Joseph, Nanosheets and 2D-nanoneetworks by mutually assisted self-assembly of fullerene clusters and DNA three-way junctions, *Nanoscale Adv.* 1 (2019) 4158–4165.
- [39] M. Brouwer Albert, Standards for photoluminescence quantum yield measurements in solution (IUPAC Technical Report), *Pure Appl. Chem.* 2011, p. 2213.
- [40] S. Mangalath, S. Abraham, J. Joseph, pH-responsive fluorescence enhancement in graphene oxide–naphthalimide nanoconjugates: a fluorescence turn-on sensor for acetylcholine, *Chem. Eur. J.* 23 (2017) 11404–11409.
- [41] A.L. Benvin, Y. Creeger, G.W. Fisher, B. Ballou, A.S. Waggoner, B.A. Armitage, Fluorescent DNA nanotags: supramolecular fluorescent labels based on intercalating dye arrays assembled on nanostructured DNA templates, *J. Am. Chem. Soc.* 129 (2007) 2025–2034.
- [42] X. Zhang, Y. Qian, X. Ma, M. Xia, S. Li, Y. Zhang, Thiolated DNA-templated silver nanoclusters with strong fluorescence emission and a long shelf-life, *Nanoscale* 10 (2018) 76–81.
- [43] M.R. Carro Temboury, V. Paolucci, E.N. Hooley, L. Latterini, T. Vosch, Probing DNA-stabilized fluorescent silver nanocluster spectral heterogeneity by time-correlated single photon counting, *Analyst* 141 (2016) 123–130.
- [44] S.Y. New, S.T. Lee, X.D. Su, DNA-templated silver nanoclusters: structural correlation and fluorescence modulation, *Nanoscale* 8 (2016) 17729–17746.
- [45] S.L. Brown, E.K. Hobbie, S. Tretiak, D.S. Kilin, First-principles study of fluorescence in silver nanoclusters, *J. Phys. Chem. C* 121 (2017) 23875–23885.
- [46] P.R. O'Neill, L.R. Velazquez, D.G. Dunn, E.G. Gwinn, D.K. Fygenson, Hairpins with poly-C loops stabilize four types of fluorescent Ag_n:DNA, *J. Phys. Chem. C* 113 (2009) 4229–4233.
- [47] S.K. Vittala, S.K. Saraswathi, J. Joseph, Fullerene cluster assisted self-assembly of short DNA strands into semiconducting nanowires, *Chem. Eur. J.* 23 (2017) 15759–15765.
- [48] J. Li, X. Jia, D. Li, J. Ren, Y. Han, Y. Xia, E. Wang, Stem-directed growth of highly fluorescent silver nanoclusters for versatile logic devices, *Nanoscale* 5 (2013) 6131–6138.
- [49] Y. Zhou, J. Wang, G. Yang, S. Ma, M. Zhang, J. Yang, Cysteine-rich protein-templated silver nanoclusters as a fluorometric probe for mercury(II) detection, *Anal. Methods* 11 (2019) 733–738.